

AD-A181 324

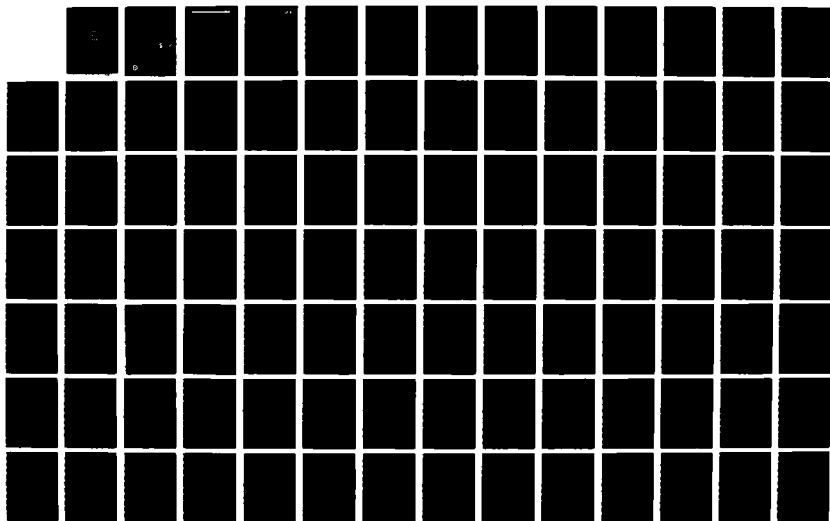
MICROMECHANISMS OF FRACTURE AND CRACK ARREST IN TWO  
HIGH STRENGTH STEELS(U) DAVID W TAYLOR NAVAL SHIP  
RESEARCH AND DEVELOPMENT CENTER ANN J P GUDAS FEB 87  
DTNSRDC/SNE-87-28

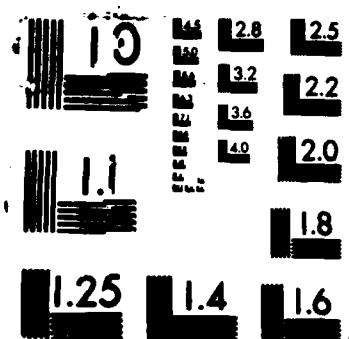
1/4

UNCLASSIFIED

F/G 11/6 1

NL





DTIC FILE COPY

(12)

**David W. Taylor Naval Ship Research and Development Center**

Bethesda MD 20884-5000

**AD-A181 324**

DTNSRDC/SME-87-20 February 1987

Ship Materials Engineering Department  
Research and Development Report

MICROMECHANISMS OF FRACTURE AND CRACK ARREST  
IN TWO HIGH STRENGTH STEELS

by

J.P. Gudas

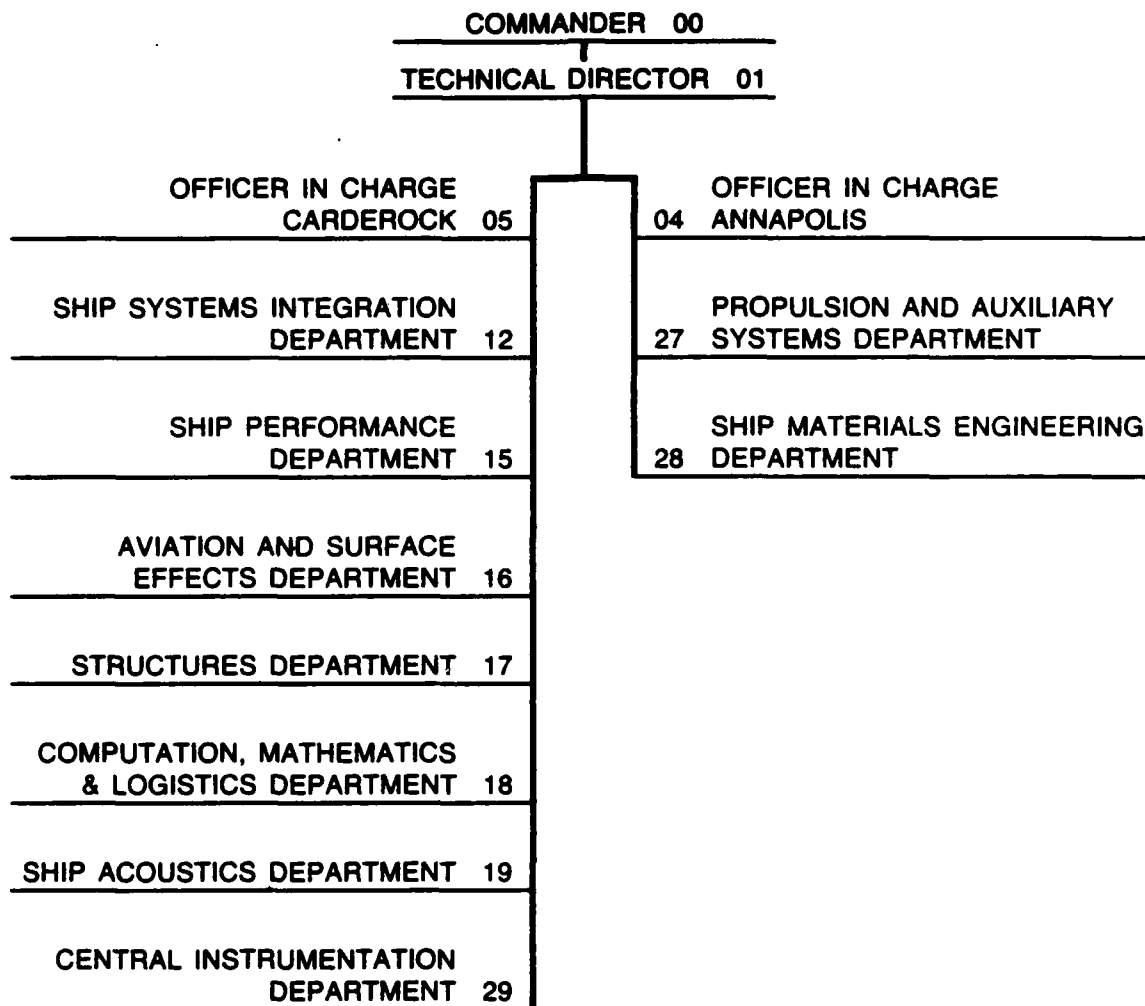
DTIC  
ELECTE  
JUN 18 1987  
S A D

Approved for public release; distribution  
unlimited.



DTNSRDC/SME-87-20 MICROMECHANISMS OF FRACTURE AND CRACK ARREST IN TWO HIGH STRENGTH STEELS

# MAJOR DTNSRDC TECHNICAL COMPONENTS



**DESTRUCTION NOTICE** — For **classified** documents, follow the procedures in DOD 5220.22M, Industrial Security Manual, Section II-9, or DOD 5200.1-R, Information Security Program Regulation, Chapter IX. For **unclassified**, limited documents, destroy by any method that will prevent disclosure of contents or reconstruction of the document.



UNCLASSIFIED

SECURITY CLASSIFICATION OF THIS PAGE

## REPORT DOCUMENTATION PAGE

1a. REPORT SECURITY CLASSIFICATION UNCLASSIFIED			1b. RESTRICTIVE MARKINGS <b>A181384</b>		
2a. SECURITY CLASSIFICATION AUTHORITY			3. DISTRIBUTION/AVAILABILITY OF REPORT Approved for public release; distribution unlimited.		
2b. DECLASSIFICATION/DOWNGRADING SCHEDULE					
4. PERFORMING ORGANIZATION REPORT NUMBER(S) DTNSRDC/SME-87-20			5. MONITORING ORGANIZATION REPORT NUMBER(S)		
6a. NAME OF PERFORMING ORGANIZATION DTNSRDC		6b. OFFICE SYMBOL (If applicable) Code 2814		7a. NAME OF MONITORING ORGANIZATION	
6c. ADDRESS (City, State, and ZIP Code) Bethesda, MD 20084-5000			7b. ADDRESS (City, State, and ZIP Code)		
8a. NAME OF FUNDING/SPONSORING ORGANIZATION DTNSRDC		8b. OFFICE SYMBOL (If applicable) 012		9. PROCUREMENT INSTRUMENT IDENTIFICATION NUMBER	
8c. ADDRESS (City, State, and ZIP Code) Bethesda, MD 20084-5000			10. SOURCE OF FUNDING NUMBERS		
PROGRAM ELEMENT NO. 62234N		PROJECT NO. 5 RS34550		TASK NO. WORK UNIT ACCESSION NO. DN778013	
11. TITLE (Include Security Classification) (U) MICROMECHANISMS OF FRACTURE AND CRACK ARREST IN TWO HIGH STRENGTH STEELS					
12. PERSONAL AUTHOR(S) J.P. Gudas					
13a. TYPE OF REPORT R&D		13b. TIME COVERED FROM Sep 84 TO Oct 85		14. DATE OF REPORT (Year, Month, Day) February 1987	
15. PAGE COUNT 308					
16. SUPPLEMENTARY NOTATION 1-2803-175-08, RF4.2/24					
17. COSATI CODES			18. SUBJECT TERMS (Continue on reverse if necessary and identify by block number)		
FIELD	GROUP	SUB-GROUP	crack arrest, crack initiation, cleavage fracture, structural steel		
19. ABSTRACT (Continue on reverse if necessary and identify by block number) An investigation of fracture properties of a quenched and tempered martensitic steel (3-Ni Steel) and a copper precipitation strengthened low carbon ferritic steel (ASTM A710 Gr. A Cl. 3) possessing similar yield strengths was conducted. The objective included evaluation of fracture toughness, and explanation of metallurgical mechanisms causing changes in relative fracture performance. A crack arrest toughness test procedure was developed to obtain full plate thickness, lower bound measurements of dynamic fracture toughness at various test temperatures. Micromechanisms of fracture processes were described using metallurgical analysis techniques. ASTM A710 Gr. A Cl. 3 steel displayed superior ductile fracture toughness due to reduced inclusion and carbon content. This led to ductile cracking through coalescence of inclusion-initiated voids, whereas 3-Ni Steel steel showed ductile cracking due to interrupted void growth by fracture of shear bands along sheets of carbides.					
CONTINUED ON REVERSE					
20. DISTRIBUTION/AVAILABILITY OF ABSTRACT <input type="checkbox"/> UNCLASSIFIED/UNLIMITED <input checked="" type="checkbox"/> SAME AS RPT. <input type="checkbox"/> DTIC USERS			21. ABSTRACT SECURITY CLASSIFICATION UNCLASSIFIED		
22a. NAME OF RESPONSIBLE INDIVIDUAL M.T. Kirk			22b. TELEPHONE (Include Area Code) (301) 267-2368		22c. OFFICE SYMBOL DTNSRDC 2814

DD FORM 1473, 84 MAR

83 APR edition may be used until exhausted.

All other editions are obsolete

SECURITY CLASSIFICATION OF THIS PAGE

U.S. Government Printing Office: 1988-039-012

0102-LF-014-6602

UNCLASSIFIED

# 19. CONTINUED

When temperature was reduced and degree of constraint increased, 3-Ni Steel displayed ductile fracture at significantly lower temperatures, and higher fracture toughness in the transition regime. The relatively high cleavage initiation temperature of ASTM A710 Gr. A Cl. 3 steel was attributed to the size and distribution of cementite particles. Estimations of critical fracture stress based on carbide size differences clearly pointed to this factor as sufficient to cause the observed differences in cleavage initiation temperatures.

For the first time, evaluation of crack arrest toughness in a steel showing substantial low temperature toughness was made possible with the compact crack arrest test developed in this study. The crack arrest toughness of 3-Ni Steel is displaced from static fracture toughness values by 60 to 70°C (108 to 126°F) toward higher temperatures, and was shown to merge with, and extend previous measurements of dynamic fracture toughness from impact tests. The ASTM A 710 Gr. A Cl. 3 steel showed reduced ability to sustain dynamic crack propagation without catastrophic crack branching.

Cleavage crack arrest at low temperatures and low levels of driving force occurred in response to reduction of the instantaneous K level. At temperatures higher on the  $K_{IC}$  transition curve, mixed modes of cleavage and ductile tearing were observed, and related to loss of constraint due to local plastic deformation.



Approved For	
By	<input checked="" type="checkbox"/>
Date	<input type="checkbox"/>
Approved	<input type="checkbox"/>
Distribution	
By	
Date	
Approved	Codes
Approved 3/or	
Date	
A1	

## ABSTRACT

An investigation of fracture properties of a quenched and tempered martensitic steel (HY-80), and a copper precipitation strengthened low carbon ferritic steel (ASTM A710 Gr. A Cl. 3) possessing similar yield strengths was conducted. The objective included evaluation of fracture toughness, and explanation of metallurgical mechanisms causing changes in relative fracture performance. A crack arrest toughness test procedure was developed to obtain full plate thickness, lower bound measurements of dynamic fracture toughness at various test temperatures. Micromechanisms of fracture processes were described using metallurgical analysis techniques.

ASTM A710 Gr. A Cl. 3 steel displayed superior ductile fracture toughness due to reduced inclusion and carbon content. This led to ductile cracking through coalescence of inclusion-initiated voids, whereas HY-80 steel showed ductile cracking due to interrupted void growth by fracture of shear bands along sheets of carbides.

When temperature was reduced and degree of constraint increased, HY-80 displayed ductile fracture at significantly lower temperatures, and higher fracture toughness in the transition regime. The relatively high cleavage initiation temperature of ASTM A710 Gr. A Cl. 3 steel was attributed to the size and distribution of cementite particles. Estimations of critical fracture stress based on carbide size differences clearly pointed to this factor as sufficient to cause the

observed differences in cleavage initiation temperatures.

For the first time, evaluation of crack arrest toughness in a steel showing substantial low temperature toughness was made possible with the compact crack arrest test developed in this study. The crack arrest toughness of HY-80 is displaced from static fracture toughness values by 60 to 70°C (108 to 126°F) toward higher temperatures, and was shown to merge with, and extend previous measurements of dynamic fracture toughness from impact tests. The ASTM A 710 Gr. A Cl. 3 steel showed reduced ability to sustain dynamic crack propagation without catastrophic crack branching.

Cleavage crack arrest at low temperatures and low levels of driving force occurred in response to reduction of the instantaneous K level. At temperatures higher on the  $K_a$  transition curve, mixed modes of cleavage and ductile tearing were observed, and related to loss of constraint due to local plastic deformation.

#### ACKNOWLEDGEMENTS

My sincere appreciation is extended to Professor Robert B. Pond for his guidance, motivation, and personal encouragement, and to Professor Robert E. Green for his continued support. The guidance and commitment of Professor George R. Irwin is gratefully acknowledged.

The cooperation and diligent assistance of Mr. Joseph Waskey, Mr. Mark Kirk and Mr. Rich Hays is appreciated. Special thanks is also expressed to Messrs. Jack Saveleski, Tom Montemarano, Ernie Czyryca, Fred Dersch, Paul Ditta, Rob Meiklejohn, III, Mrs. MarjorieAnn Natishan, Mrs. Catherine Wong, Dr. Tom Scoonover, and Mrs. Carol Hartman for technical advice and assistance. The professional support of Mr. George Wacker was key to the completion of this research.

#### ADMINISTRATIVE INFORMATION

This report was prepared as part of the Surface Ship and Craft Materials Block under the sponsorship of Messrs. C. Zanis (NAVSEA 05R25) and I. Caplan (DTNSRDC 012.5). This effort was was performed at this Center under Program Element 62234N, Task Area RS345S50, Work Unit 1-2814-175-08. This report satisfies milestone RF 4.2/24.

## TABLE OF CONTENTS

	page
ABSTRACT.....	iii
ACKNOWLEDGEMENTS.....	v
ADMINISTRATIVE INFORMATION.....	v
TABLE OF CONTENTS.....	vii
LIST OF TABLES.....	viii
LIST OF FIGURES.....	ix
INTRODUCTION.....	1
TECHNICAL REVIEW	
Steels Investigated.....	5
Crack Arrest Testing and Analysis.....	22
Micromechanisms of Cleavage, Ductile Fracture and Crack Arrest.....	76
EXPERIMENTAL DESIGN	
Materials.....	146
Mechanical Property Tests.....	147
Crack Arrest Testing.....	151
Metallographic and Fractographic Examination.....	157
RESULTS AND DISCUSSION	
Mechanical Properties.....	159
Fracture Toughness.....	165
Crack Arrest Toughness.....	172
Metallurgical Examination.....	181
SUMMARY AND CONCLUSIONS.....	206
REFERENCES.....	213

## TABLES

1. Specification Compositions and Properties of HY-80 and ASTM A710 Gr. A Cl. 3 Steels
2. Chemical Composition of HY-80 and ASTM A710 Gr. A Cl. 3 Steels
3. Room Temperature Mechanical Properties of HY-80 and ASTM A710 Gr. A Cl. 3 Steels
4. Results of True Stress/True Strain Tests of HY-80 and ASTM A710 Gr. A Cl. 3 Steels
5. Charpy V-notch Impact Toughness Test Results for HY-80 Steel
6. Charpy V-notch Impact Toughness Test Results for ASTM A710 Gr. A Cl. 3 Steel
7. Results of 5/8-inch Dynamic Tear Tests of HY-80 and ASTM A710 Gr. A Cl. 3 Steels
8. Fracture Toughness Test Results for HY-80 Steel
9. Fracture Toughness Test Results for ASTM A710 Gr. A Cl. 3 Steel
10. Crack Arrest Toughness Test Results for HY-80 Steel
11. Crack Arrest Toughness Test Results for ASTM A710 Gr. A Cl. 3 Steel
12. Summary of Inclusion and Carbide Size Measurements in HY-80 and ASTM A710 Gr. A Cl. 3 Steels

## FIGURES

1. Schematic Drawing, Robertson Crack Arrest Test Specimen
2. Typical Results of Robertson Crack Arrest Test
3. SOD (ESSO) Wide Plate Crack Arrest Specimen Design and Test Arrangement
4. Typical Results of SOD (ESSO) Wide Plate Crack Arrest Tests, ASTM-A285 Gr. C Steel
5. Crack Arrest Toughness Values for ARALDITE B Double Cantilever Beam Specimens from Optical Method of Caustics Measurements
6. Crack Velocity as a Function of the Instantaneous Stress Intensity Factor for HOMALITE-100
7. Crack Arrest Toughness Plotted as a Function of Initiation Toughness for MRL and BCL Specimens of SA533 B-1 Steel Tested at 0°C (32°F)
8. Double Tension Test Specimen Geometry
9. Results of Double Tension Crack Arrest Tests
10. Drawing of Tensile Specimen used for Room Temperature Tests
11. Drawing of Tensile Specimen used for True Stress/True Strain Tests
12. Drawing of Charpy V-Notch Test Specimen
13. Schematic Drawing of Plate Showing Specimen Orientations
14. Drawing of 5/8-inch Dynamic Tear Impact Toughness Specimen
15. Drawing of Modified 1T Compact Specimen for Fracture Toughness Tests
16. Drawing of Compact Crack Arrest Test Specimen
17. Schematic Drawing of Compact Crack Arrest Specimen Test Arrangement
18. Optical Photomicrographs of HY-80 Steel
19. Optical Photomicrographs of ASTM A710 Gr. A Cl. 3 Steel



20. Plot of Yield Strength as a Function of Temperature for HY-80 and ASTM A710 Gr. A Cl. 3 Steels
21. Plot of Yield Strength as a Function of Temperature for HY-80 Steel
22. Charpy V-Notch Impact Toughness Results for HY-80 and ASTM A710 Gr. A Cl. 3 Steels
23. Percent Shear Fracture from Charpy V-notch Tests of HY-80 and ASTM A710 Gr. A Cl. 3 Steels
24. Lateral Expansion from Charpy V-notch Tests of HY-80 and ASTM A710 Gr. A Cl. 3 Steels
25. Results of 5/8-inch Dynamic Tear Tests of HY-80 and ASTM A710 Gr. A Cl. 3 Steels
26. Load versus Load-line Displacement Results for 1TCT Specimens of HY-80 Steel
27. Typical Results of J-integral Tests of HY-80 Steel
28. Load versus Load-line Displacement Results for 1TCT Specimens of ASTM A710 Gr. A Cl. 3 Steel
29. Typical Results of J-integral Tests of ASTM A710 Gr. A Cl. 3 Steel
30. Results of Fracture Toughness Tests of HY-80 Steel
31. Results of Fracture Toughness Tests of ASTM A 710 Gr. A Cl. 3 Steel
32. Results of Fracture Toughness Tests of HY-80 and ASTM A710 Gr. A Cl. 3 Steels
33. Ratios of Yield Strength and Fracture Toughness versus Room Temperature Values of These Properties for HY-80 and ASTM A710 Gr. A Cl. 3 Steels
34. Typical Temperature Gradient Data from Compact Crack Arrest Specimen Tests
35. Typical Load versus Crack Opening Displacement Results from Compact Crack Arrest Specimen Tests
36. Photograph of Fracture Surface of HY-80 Compact Crack Arrest Specimen FYB CCA-2
37. Photograph of Fracture Surface of HY-80 Compact Crack Arrest Specimen FYB-1A

38. Photograph of Fracture Surface of HY-80 Compact Crack Arrest Specimen FYB-1B
39. Photograph of Fracture Surface of HY-80 Compact Crack Arrest Specimen FYB-3A
40. Results of Fracture Toughness and Crack Arrest Toughness Tests of HY-80 Steel
41. Results of Fracture Toughness, Crack Arrest Toughness, and Reported Dynamic Fracture Toughness Measurements of HY-80 Steel
42. Results of Fracture Toughness and Crack Arrest Toughness Tests of ASTM A 710 Gr. A Cl. 3 Steel
43. Scanning Electron Micrographs of HY-80 Steel (2% Nital Etch)
44. Optical Photomicrograph of HY-80 Steel (4% Picral Etch)
45. Scanning Electron Micrographs of HY-80 Steel (4% Picral Etch).
46. Scanning Electron Micrographs of ASTM A710 Gr. A Cl. 3 Steel (2% Nital Etch)
47. Optical Photomicrograph of ASTM A710 Gr. A Cl. 3 Steel (4% Picral Etch)
48. Scanning Electron Micrograph of ASTM A710 Gr. A Cl. 3 Steel (4% Picral Etch)
49. Scanning Electron Micrographs of ASTM A710 Gr. A Cl. 3 Steel (4% Picral Etch)
50. Optical Photomicrographs of HY-80 and ASTM A710 Gr. A Cl. 3 Steels
51. Optical Photomicrographs of Crack Paths in HY-80 1TCT Specimens FYB 42 and FYB 45
52. Optical Photomicrographs of Crack Paths in HY-80 1TCT Specimens FYB 57 and FYB 44
53. Optical Photomicrograph of Crack Path in HY-80 1TCT Specimen FYB 59
54. Scanning Electron Fractograph of HY-80 1TCT Specimen FYB 43

55. Scanning Electron Fractographs of HY-80 1TCT Specimen  
FYB 42
56. Scanning Electron Fractograph of HY-80 1TCT Specimen  
FYB 42
57. Optical Photomicrograph of Crack Path in 1TCT Specimens  
GGO-9 and GGO-1 of ASTM A710 Gr. A Cl. 3 Steel
58. Optical Photomicrographs of Crack Paths in 1TCT Specimens  
of ASTM A710 Gr. A Cl. 3 Steel
59. Scanning Electron Fractograph of ASTM A710 Gr. A Cl. 3  
Steel 1TCT Specimen GGO-3
60. Scanning Electron Fractographs of ASTM A710 Gr. A Cl. 3  
Steel 1TCT Specimens
61. Scanning Electron Fractographs of ASTM A710 Gr. A Cl. 3  
Steel 1TCT Specimen GGO-3
62. Scanning Electron Fractographs of Cleavage Fracture in  
HY-80 Steel 1TCT Specimen FYB-51
63. Scanning Electron Fractographs of Cleavage Fracture in  
ASTM A710 Gr. A Cl. 3 Steel 1TCT Specimen GGO-2
64. Scanning Electron Fractographs of Cleavage Fracture in  
ASTM A710 Gr. A Cl. 3 Steel 1TCT Specimen GGO-18
65. Optical Photomicrograph of Arrested Crack Tip in HY-80  
Compact Crack Arrest Specimen FYB CCA-2
66. Scanning Electron Fractographs Near Arrested Crack Tip in  
HY-80 Compact Crack Arrest Specimen FYB CCA-2
67. Scanning Electron Fractograph of Crack Path of HY-80  
Compact Crack Arrest Specimen FYB-2 Located 12 mm Behind  
Arrested Crack Tip
68. Optical Photomicrograph of Arrested Crack Tip in HY-80  
Compact Crack Arrest Specimen FYB-1A
69. Scanning Electron Fractographs of Arrested Crack Tip in  
HY-80 Compact Crack Arrest Specimen FYB-1A
70. Optical Photomicrograph of Arrested Crack Tip in HY-80  
Compact Crack Arrest Specimen FYB-1B
71. Scanning Electron Fractograph of Arrested Crack Tip in  
HY-80 Compact Crack Arrest Specimen FYB-1B

72. Optical Photomicrograph of Arrested Crack Tip in HY-80 Compact Crack Arrest Specimen FYB-3A
73. Optical Photomicrograph of Arrested Crack Tip in HY-80 Compact Crack Arrest Specimen FYB-3A
74. Low Magnification Scanning Electron Fractographs of HY-80 Compact Crack Arrest Specimen FYB-3A
75. Scanning Electron Fractographs of Arrested Crack Tip of HY-80 Compact Crack Arrest Specimen FYB-3A
76. Scanning Electron Fractographs of Arrested Crack Tip of HY-80 Compact Crack Arrest Specimen FYB-3A at Various Tilt Angles
77. Optical Photomicrograph Across the Crack Path of HY-80 Compact Crack Arrest Specimen FYB-3A on Plane Located 12 mm Behind Arrested Crack Tip
78. Photograph of Fracture Surface of ASTM A710 Gr. A Cl. 3 Compact Crack Arrest Specimen GGO-2
79. Optical Photomicrograph of Arrested Crack Tip of ASTM A710 Gr. A Cl. 3 Compact Crack Arrest Specimen GGO-2
80. Scanning Electron Fractographs of Arrested Crack Tip of ASTM A710 Gr. A Cl. 3 Compact Crack Arrest Specimen GGO-2
81. Comparison of Fracture Surfaces of HY-80 Compact Crack Arrest Specimens FYB-1B, FYB-1A and FYB-3A

## INTRODUCTION

The fracture properties of high strength steels are important to their successful utilization in most structural applications. The fracture toughness of a steel is keyed to its transition from ductile to brittle cracking modes as temperature is lowered, degree of constraint is increased, or loading rate is increased. The relative levels of toughness of steels may change as these factors are varied, hence materials selections must be linked to realistic service conditions.

This transition in fracture properties has formed the basis for extensive fracture mechanics test method and analysis development, and micromechanical modelling to predict trends in fracture toughness, principally related to test temperature. Tests include simple impact toughness, fracture toughness, and crack arrest toughness. The latter has been shown to provide the lowest, hence most conservative, measure of fracture toughness because it incorporates dynamic crack propagation, and is typically performed in thick section tests which can approach or exceed constraint levels in certain structural details.

Micromechanical modelling of the fracture process in steels has proceeded simultaneously with the development of fracture mechanics, and has used fracture mechanics on a micro-scale to predict trends in linear elastic and more recently elastic-plastic fracture. For the most part, these models have been applied to relatively high carbon steels ranging from spherodized mild steel to reactor pressure vessel plate

and forging steels. Current clean steel technology has made high strength, high toughness, easily welded steels available for structural applications, many of which are in extreme service environments regarding temperature, loading rate and section thickness. Many of these low carbon ferritic steels exhibit ductile fracture toughness which is superior to traditional quenched and tempered martensitic steels, but are seen in some cases to initiate transition to cleavage fracture at higher temperatures, and display inferior low temperature toughness properties. An improved understanding of mechanical and micro-mechanical aspects of the fracture process of high strength low alloy ferritic steels and traditional quenched and tempered martensitic steels is necessary to allow their safe utilization in high performance structures.

The objective of this investigation is two-fold. The first is to quantify the fracture properties of a quenched and tempered martensitic steel and a low-carbon ferritic steel with similar yield strength levels in the range 585 MPa (85 ksi), and which are seen to reverse in relative toughness level as various loading factors are changed. Because temperature, constraint and loading rate are all to be considered, crack arrest testing is included as a major element in this characterization of the steels. This required the development of a crack arrest test procedure which would be applicable to steels exhibiting high levels of toughness at low test temperatures. The second objective of this investigation was to conduct metallurgical examinations of the mechanisms

of fracture in search of factors which might explain the relative changes in fracture performance of the steels.

The steels selected for this study included HY-80 and ASTM A710 Grade A Class 3 alloys. These were selected because HY-80 has shown superior low temperature fracture performance compared to most steels, and because ASTM A710 Gr. A Cl. 3 steel has shown upper shelf fracture properties which are superior to HY-80 and to most quenched and tempered martensitic steels. Besides crack arrest performance, impact toughness, quasi-static fracture toughness, and stress-strain properties of these steels were evaluated over a broad temperature range. Detailed metallographic and fractographic examinations were conducted to describe the fracture processes which occurred in these steels under various testing conditions.

Because this investigation addresses both the mechanics and metallurgy of fracture and crack arrest, a review of the metallurgy and properties of the two steels will first be presented. This will be followed by a review of crack arrest technology which will introduce the concepts of such testing and analysis, and identify key factors which led to the experimental design used in this study. The micromechanisms of cleavage and ductile fracture in steels will then be reviewed, with a focus on the microstructural details which control both types of cracking. Details of the test program will then be presented. Results will be developed first in terms of the mechanical property, fracture mechanics and crack arrest tests, and properties

of both steels under various loading conditions will be established and compared. Metallurgical observations will then be presented first in terms of the ductile, then brittle fracture processes, and the mechanisms of fracture will be discussed. Finally, the mechanisms of crack arrest will be described, and related to previous observations from fracture toughness tests.



## STEELS INVESTIGATED

This investigation of the micromechanisms of fracture and crack arrest includes two high strength steels. HY-80 is a martensitic steel which obtains its strength and toughness through traditional quench and temper heat treatment. ASTM A 710 Grade A Class 3 steel is a low carbon ferritic alloy which principally utilizes precipitation strengthening. A brief review of the metallurgy and properties of both steels will now be presented.

### HY-80 STEEL

HY-80 steel is a 551 MPa (80 ksi) yield strength alloy developed in the late 1940's based on Krupp armor steel formulation [Heller, et al. 1965]. Table 1 lists the specification limits for this alloy and the minimum mechanical properties. HY-80 is a quenched and tempered steel where heat treatment practice is left to the manufacturer except for the requirement to temper above 593°C (1100°F), and to achieve mid-thickness martensite content not less than 50%. According to Heller, et al. [1965], typical heat treatment consists of austenitization in the range 843 to 899°C (1550 to 1650°F), followed by a water quench, and tempering in the range 621 to 677°C (1150 to 1250°F).

The metallurgical design of HY-80 was keyed to providing low temperature toughness at the minimum prescribed yield strength. The principal strengthening in this alloy is derived from carbon, the upper content of which is set at 0.18%. The mechanism of martensitic strengthening by carbon involves the trapping of carbon atoms in the body centered tetragonal structure following

transformation from the fcc austenite structure. The tetragonality of the martensite laths has been shown to be affected by the carbon content [Reed-Hill, 1964]. The carbon atoms thus contribute to straining the martensite lattice and impeding slip. Dislocation movement in martensite is also impeded by the formation of fine crystals with many orientations, and the macroscopic shear transformation which deforms the matrix surrounding the platelets.

Because of its strength, martensite in steels is typically brittle. In HY-80, alloying with Ni, and tempering heat treatment serve to recover the toughness lost in obtaining the quenched martensite structure. Nickel has been shown to be a solid solution strengthener in ferrite, and also reduces the transformation temperature causing refinement of the transformation products [Orton, 1977; DePaul and Kitchen, 1970; Tanaka, et al. 1977; Pickering, 1977]. Jolley [1968] evaluated the toughness behavior of nickel in carbide free iron and determined that the toughening behavior resides solely in its influence in the ferrite matrix. He showed that nickel decreased the temperature and strain rate dependence of the lower yield stress of alpha-iron, and suggested that the improved toughness attainable with Ni alloying is attributable to these reductions, and their effect on slip behavior of alpha-iron.

The manganese content of this steel was set primarily to control the sulphur content rather than provide strengthening [Heller, et al. 1965]. The Cr and Mo contents, with manganese, contribute to increase the hardenability of this steel. All of

these three elements have been shown to have large hardenability factors, and serve to guarantee that the required materials properties are obtained in plate thicknesses which may exceed 50mm.

#### PROPERTIES OF HY-80 STEEL

The early studies of properties of HY-80 centered on attainment of adequate toughness at low temperature while achieving the 551 MPa (80 ksi) minimum yield strength. Heller, et al. [1965] reported typical Charpy impact toughness curves for this steel and showed that the transition temperature was well below  $-18^{\circ}\text{C}$  ( $0^{\circ}\text{F}$ ). They also reported that upper shelf energy levels were obtained at that temperature, and that transverse Charpy impact toughness energies were above 68 J (50 ft-lb). Results of explosion bulge and crack starter explosion bulge tests of HY-80 were also reported and compared to Charpy transition curves. These results showed that the amount of cracking decreases with increasing temperature and CVN impact energy, and the depth of bulging and plastic deformation increases. The flat break shattering type of fracture in this test occurred at temperatures below  $-90^{\circ}\text{C}$  ( $-130^{\circ}\text{F}$ ). At  $-40^{\circ}\text{C}$  ( $-40^{\circ}\text{F}$ ), which corresponded to the attainment of upper shelf Charpy energy, only short tears occurred in these large scale tests.

Shoemaker and Rolfe [1969] conducted static and dynamic low temperature fracture toughness tests of HY-80 steel. Results of tests of 25.4mm (1-inch) plate showed that the dynamic  $K_{Ic}$  increased rapidly above  $-129^{\circ}\text{C}$  ( $-200^{\circ}\text{F}$ ). A maximum valid dynamic

fracture toughness of approximately 88 MPa/m (80 ksi/in) was achieved at  $-101^{\circ}\text{C}$  ( $-150^{\circ}\text{F}$ ), but a non-valid value of 155 MPa $\sqrt{\text{in}}$  (141 ksi $\sqrt{\text{in}}$ ) was also obtained at this temperature. These results also showed that  $K_{IC}$  values decrease with increasing strain rate at constant temperature. Shoemaker and Rolfe concluded that the drop weight NDT temperature correctly represents the upper limit at which plane-strain crack toughness occurs under dynamic conditions for this alloy.

Dolby and Knott [1972] conducted a variety of furnace heat treatments of HY-80 steel to produce martensitic microstructures from various austenite grain sizes, and to produce microstructures containing various proportions of bainite for a single austenite grain size. Crack Opening Displacement (COD) tests of three-point bend specimens were conducted over the temperature range  $-196^{\circ}\text{C}$  to  $200^{\circ}\text{C}$  ( $-321$  to  $392^{\circ}\text{F}$ ). Their results showed that an increase in mean prior austenite grain size from 8 to 95  $\mu\text{m}$  had little effect on fracture toughness above  $-40^{\circ}\text{C}$  ( $-40^{\circ}\text{F}$ ), but progressively decreased toughness at lower temperatures. Typical upper shelf CTOD values of 0.1mm (0.004-inch) were obtained. Metallographic examination showed that the width of the individual martensite lath was not markedly dependent on changes in austenite grain size, but that colony width increased to a much greater extent for the same increase in grain size. Martensitic colony boundaries often coincided with changes in direction of the fracture profile. For ductile cracking, the microvoid size appeared smaller for smaller austenite grain size, and microvoids nucleated at particles

including sulphides and possibly large undissolved carbides. Autotempered carbides did not nucleate microvoids. Dolby and Knott also showed that the increasing proportion of bainite progressively decreased the fracture toughness at test temperatures less than  $-50^{\circ}\text{C}$  ( $-58^{\circ}\text{F}$ ). Between  $-50^{\circ}\text{C}$  and  $20^{\circ}\text{C}$  ( $-58$  and  $68^{\circ}\text{F}$ ), bainite had no marked effect on toughness. Above room temperature, the fracture toughness of both martensitic and martensitic-bainitic steels fell.

Werchniak [1972] conducted an investigation of effects of static prestrain on the low cycle fatigue properties of HY-80. Notched cantilever beam specimens 25.4mm (1-inch) in thickness were prestrained to selected nominal stress in the range -1171 to 1102 MPa ( $-170$  to  $+160$  ksi) in bending, and then subjected to cyclic bending at a selected stress level. When stress cycling was conducted below the yield strength of this steel, tensile prestrain increased the fatigue life in proportion to the level of prestrain. At stress levels above the yield strength, tensile prestress had little effect on fatigue life. Compressive prestress was found to be detrimental to fatigue life regardless of stress levels at which fatigue tests were run.

Novack [1973] evaluated effects of prior uniform plastic tensile prestrain on mechanical properties of HY-80. Tests of Charpy impact toughness, tensile properties and stress corrosion cracking susceptibility were conducted on materials after plastic strain levels of 1, 3, and 5% were achieved in tensile blanks. Results showed that the increasing levels of plastic strain

increased the tensile and CVN properties. Although HY-80 was immune to stress corrosion cracking, tensile prestrain was shown to decrease the K level at which overload fracture occurred in precracked cantilever bend tests.

Hancock and Mackenzie [1976] conducted notched tensile tests of HY-80 steel in the long and short transverse orientations with different notch geometries. Tests were stopped after different levels of plastic strain and specimens were sectioned longitudinally near the center plane. In specimens examined before a drop in average stress, there were discrete voids, whereas after the drop in average stress the voids had joined over a length of approximately 200  $\mu\text{m}$ . In the short transverse orientation microcracking between large elliptical holes was observed whereas larger voids almost growing to coalescence were observed in the long transverse orientation.

Harding [1977] evaluated effects of temperature and strain rate on strength and ductility of HY-80. Tests were conducted at nominal values of mean plastic strain rate ranging from 20 to 2500 per second, and at temperatures of  $-196$ ,  $-118$  and  $-48^{\circ}\text{C}$  ( $-321$ ,  $-180$  and  $-54^{\circ}\text{F}$ ). For the slowest strain rate, the yield strength varied from 593 to 994 MPa (86 to 144 ksi) as temperature was decreased. At  $2^{\circ}\text{C}$  ( $36^{\circ}\text{F}$ ), the yield strength increased from 593 MPa to 1145 MPa (86 to 166 ksi) as strain rate was increased from 0.001 to 2500 per second.

Clayton and Knott [1976] studied the effects of compressive prestrain on the COD of HY-80 steel. Prestrain levels ranging

from 0 to 20% in direct compression were developed, and four-point bend tests were conducted. The COD required to produce ductile crack initiation was reduced by 10% up to the 5% nominal prestrain level, then decreased rapidly at higher levels of prestrain to a level approximately 40% of that obtained in the unstrained metal. Studies of the fracture mechanism showed differences in the shear decohesion behavior as a function of prestrain.

Hasson and Joyce [1981] evaluated the effects of loading rate on the  $J_{IC}$  versus temperature transition of HY-80 steel. Tensile tests and J-integral tests were conducted over a temperature range of 192 to 23°C (-314 to 73°F). High rate servo-hydraulic loading of tensile and compact specimens were carried out over this temperature range. The yield strength of the HY-80 varied from 624 MPa to 1024 MPa (91 to 149 ksi) as temperature decreased over the test range. At room temperature, the faster strain rate caused only a 3% increase of lower yield stress, but at -192°C (-314°F), a 20% increase in yield stress was observed. The mid-transition CVN impact toughness temperature was -115°C (-175°F). At conventional displacement rates, the fracture toughness initially increased from an average of 130 kJ/m<sup>2</sup> (740 in-lb/in<sup>2</sup>) at room temperature to 188 kJ/m<sup>2</sup> (1070 in-lb/in<sup>2</sup>) at -140°C (-220°F), then fell to 45 kJ/m<sup>2</sup> (256 in-lb/in<sup>2</sup>) at -192°C (-314°F). Specimens in the transition regime showed ductile tearing followed by cleavage, although temperatures bounding this type of fracture were not explicitly reported.

You and Knott [1982] conducted COD tests with HY-80 steel to assess the effects of test specimen crack length on fracture toughness. They found that as the ratio of crack length to specimen depth increased from 0.1 to 0.5, the critical COD fell from 0.58 to 0.22 mm (0.023 to 0.009-inch). The increase of fracture toughness at short crack length was ascribed to hydrostatic stress relaxation at the top surface of the specimen allowing greater crack opening displacement prior to initiation of tearing.

#### ASTM A 710 STEEL DEVELOPMENT

The low carbon ferritic steel included in this investigation is designated ASTM A710 Grade A steel. Table 1 presents the composition specification for this alloy. This high strength low alloy steel was originally developed by the International Nickel Company under the designation IN-787 [Hydrean, et al. 1972]. It is a modification of the Ni-Cu-Nb steels developed by the International Nickel Company in the early 1960's. These steels contained nominally 0.04% C, 1.4% Cu, 1.4% Ni and 0.03% Nb [Hurley and Shelton, 1966]. Depaul and Kitchen [1970] investigated the separate and combined additions of Ni, Cu and Nb in a low carbon base steel and found the as hot-rolled properties were elevated on the order of 69 MPa (10 ksi) with Ni and Nb, and 138 MPa (20 ksi) with Cu. They suggested that the increase in strength by addition of Ni and Nb results from solid solution strengthening and grain refinement, with an added increment due to aging. The increase in strength of Cu-bearing alloys was attributed to solid solution strengthening



and grain refinement, plus aging during cooling, or auto-aging. Depaul and Kitchen [1970] pointed out that the strength increase realized on aging of these Ni-Cu-Nb steels was entirely due to Cu-precipitation, and was on the order of 103 MPa (15 ksi).

Hurley and Shelton [1966] discussed the roles of each of these alloying elements of the Ni-Cu-Nb age-hardenable steels. The 1.3% Cu was seen to provide optimum strengthening, while the Ni was included to prevent hot shortness, and provide increased toughness. The Nb addition resulted in ferrite grain size reduction from ASTM 8.5 to 10.5. Nb was also seen to decrease the austenite transformation temperature.

The development of ASTM A710 steel as IN-787 followed these Ni-Cu-Nb steels, and was originally targeted for pipe-line applications, hence direct aging from hot rolling was to provide adequate strength and low temperature toughness. Small amounts of Cr and Mo were added to retard autoaging on cooling after hot rolling. Hydrean, et al. [1972] reported that the hot rolling of IN-787 required low finishing temperatures for optimum properties in the direct-aged condition. However, they reported that either normalizing or water quenching prior to aging increased the toughness in this alloy, and eliminated the need for close control of hot-rolling schedules. The first commercial production of IN 787 occurred in 1970.

#### METALLURGY OF Ni-Cu-Nb-Cr-Mo (ASTM A710) STEEL

The principal alloying element in ASTM A710 steel related to strengthening is the 1.00 to 1.3% copper which provides substantial

age hardening. The maximum solubility of Cu in alpha-iron is 1.4%, but decreases with increasing temperature to 0.35% below 649°C (1200°F) [ASM, 1948]. The Fe-Cu-C ternary eutectoid point has been reported at approximately 700°C (1298°F) to have a composition of approximately 0.9% C and 1.9% Cu [ASM, 1948], and 0.65% Cu and 0.8% C at 710°C (1310°F) [Rivlin, 1984]. This relates to the observation that most steels containing more than 0.6% Cu can be precipitation hardened.

Smith and Palmer [1933] reported that the elevation of tensile properties first occurs at 0.7% Cu in iron, and reaches a maximum with 1.5% Cu. They also showed that for the case of low carbon steels, cooling through the precipitation range at a rate exceeding approximately 25°C (45°F) per minute kept copper in solution. They also showed that the time to reach maximum hardness ranged from 0.25 to 18 hours as the reheat temperature was decreased through the range 600 to 450°C (1100 to 840°F).

On aging, the supersaturated ferrite contains coherent copper-enriched clusters which subsequently transform into epsilon-phase copper particles near peak hardness [Hornbogen, 1964; Goodman, et al. 1973a; Krishnadev, et al. 1983]. Goodman, et al. used a field ion microscope (FIM) atom probe to assess the size and number density of precipitates formed during the early stage of precipitation in Fe-1.4%Cu. They found that this alloy peak aged after approximately three hours at 500°C (932°F). At the peak aged condition, electron micrographs showed no evidence of

precipitation due to similarity of scattering for factor iron and copper, and negligible strains produced by the precipitate.

However, the FIM methods identified particles with diameters as low as 8 angstroms, and they concluded that particles below 50 angstroms in size showed such little structural detail that the state of coherency could not be determined. Goodman, et al. [1973a, 1973b] also examined the shape and composition of precipitate particles and showed that nearly all are spherical from the earliest stage of observation. Few particles were rod-shaped, and may have nucleated in dislocations. Cutler and Krishnadev [1982] reported that overaging produced a coarser, but uniformly distributed dispersion of much larger spherical as well as rod-shaped precipitates. It has also been shown that copper particles larger than 100 angstroms are nearly pure epsilon-copper phase, whereas particles produced below peak aging conditions contained on the order of 44-51% Cu. Goodman et al. [1973b] suggested that precipitates in peak aged and underaged Fe-Cu alloys are zones of highly supersaturated solid solution, and the strengthening effects of these zones may be much greater than that of nearly pure copper.

It is known that greater than approximately 0.4% copper causes hot shortness in steels[Speller, 1933; Lorig, 1933; Cox and Winn, 1965; Hurley and Shelton, 1966]. Because of the selective oxidation of iron, copper tends to concentrate at the surface beneath the scale when such steels are heated in oxidizing atmospheres, where at sufficiently elevated temperatures, melting

of copper and penetration of grain boundaries occurs which leads to surface checking. Nickel raises the temperature at which checking occurs, and it has been suggested that copper-bearing steels should be alloyed with nickel in proportions of at least 1/3 the copper content. Hydrean, et al. [1971] found that 0.7 to 1.0% Nickel was adequate to prevent hot shortness due to 1.25% Copper in a Cu-Nb steel. They observed that the amount of copper phase and degree of grain boundary penetration decreased rapidly with Ni addition until the copper-phase was present only in the oxide, and eventually eliminated.

Besides this role in preventing hot-shortness, nickel also plays a role in increasing the strength and toughness of this steel. This is due to solid solution strengthening and the role of nickel in reducing the transformation temperature and thus contributing to grain refinement as earlier discussed.

The ASTM A710 alloy contains a minimum of 0.02% niobium. This element (with V and Ti) has limited solubility in austenite and is a strong carbide and nitrate former. DeArdo, et al. [1984] provided a review of the metallurgy of Nb in steels where they pointed out that in most steels, niobium is in solution at static reheating temperatures, but when present in excess, acts to refine the austenite. It is seen as the most effective grain refiner for hot-rolled microalloyed steels. In these steels, Nb-carbon-nitride precipitates retard the motion of subgrain boundaries associated with static recrystallization and grain growth after hot deformation [DeArdo, et al. 1984; Baumgardt, et al. 1984; Meyer, et al.

1977]. In the austenite, the precipitation rate is sensitive to the level of strain imparted prior to aging. Niobium has also been shown to inhibit the static recrystallization of austenite [Tanaka, et al. 1977; DeArdo, et al. 1984].

The ASTM A 710 steel contains 0.6 to 0.9% Cr and 0.15 to 0.25% Mo. These elements were added to this Ni-Cu-Nb steel to retard auto-aging on cooling after hot rolling, and take better advantage of the copper precipitation strengthening [Hydrear, et al. 1972]. Baumgardt, et al. [1984] pointed out that Cr and Mo play an important role in microalloyed steels, especially in controlling the transformation behavior and formation of carbides. Both Cr and Mo have been shown to depress the austenite-ferrite transformation temperature [Pickering 1977; Jesseman and Murphy 1984], and this is key to this copper-bearing steel because the precipitation and growth of epsilon-copper on cooling after rolling is retarded.

#### PROPERTIES OF ASTM A 710 GRADE A CLASS 3 STEEL

ASTM A 710 Grade A steel is provided in three conditions including as-rolled and precipitation heat treated (Class 1), normalized and precipitation heat treated (Class 2), and quenched and precipitation heat treated (Class 3). The Class 3 heat treatment which is used in this study, calls for austenitization in the range 870-930°C (1600-1700°F) followed by water quenching. Aging is conducted in the range 540 to 665°C (1000-1225°F), followed by air cooling.

The initial studies of properties of IN 787 steel were performed by Hydrean, et al. [1972] on plate in the thickness range 9.5 to 19mm (3/8 to 3/4-inch). They found that water quenching plates after austenitization, then aging at 699°C (1200°F) raised the yield point of these plate thicknesses to the range 594 to 661 MPa (86 to 96 ksi). Kelley, [1974] studied the aging response of IN 787 plate, and optimum strength was obtained following aging at 593°C (1100°F), while low temperature toughness was improved most following aging in the range 593 to 704°C (1100 to 1300°F). Jesseman and Smith [1975] evaluated the effects of 3% plastic strain on the tensile and toughness properties of IN 787 plate. They found that the introduction of this level of strain in quenched plate increased the 68 J (50 ft-lb) Charpy impact toughness by approximately 61°C (110°F), and increased the yield point. A stress relief heat treatment of 621°C (1150°F) which followed a 288°C (550°F) aging reduced the yield stress to that normally obtained with aged plate, but the 68 J (50 ft-lb) Charpy temperature did not recover.

Cutler and Krishnadev [1982] performed an evaluation of the effects of aging on as-rolled 19mm (0.75-inch) thick ASTM A710 Grade A plate. Although austenitization and quenching were not performed, the results are pertinent to the description of fracture properties of this alloy. They found that overaging increased the slip band height, and observed that slip bands maintained a similar orientation over distances exceeding the ferrite grain size. For cleavage fracture of overaged, as-rolled plate, the

fracture consisted of many fine cleavage facets separated by pronounced tear ridges. The calculated process zone size corresponded to groupings of cleavage facets with similar orientations. Cutler and Krishnadev postulated that since slip bands have similar orientations over many ferrite grains in the overaged condition, low temperature fracture occurs by ductile tearing of ligaments between microcracks of similar orientation. For the case of ductile crack initiation in overaged as-rolled ASTM A710 Grade A steel, regions of dimples existed in a wide relatively undefined stretch zone. Following the Green and Knott model, Cutler and Krishnadev suggested that the plastic zone beneath the notch is much larger in this condition, and thus requires voids to form and grow before ligaments between voids become unstable and crack growth occurs. For the overaged as-rolled plate, the strength, cleavage fracture and slip behavior were postulated to be controlled by the copper precipitates.

Miglin [1982] and Miglin, et al. [1983] conducted a study of the ferrite grain size and size of Cu and NbCN precipitates on the fracture toughness of 12.7mm (0.5-inch) thick ASTM A710 Grade A plate. These variations in microstructure and precipitate characteristics were induced by a complex series of heat treatments including varying the austenitization temperature and time, aging temperature and time, and cooling rate from austenitization. Refinement of ferrite grain size and size of NbCN precipitates increased the yield properties, but did not change the ductile-brittle transition temperature (DBTT). Overaging was shown to

lower both the yield strength and the DBTT. At  $-196^{\circ}\text{C}$  ( $-321^{\circ}\text{F}$ ),  $K_{IC}$  values were similar, and were not changed by heat treatment. These authors concluded that the triggering particles for fracture at low temperature are sulphides or other nonmetallic inclusions which are minimally affected by heat treatment. For upper-shelf fracture at room temperature, voids initiated at oxide and sulphide inclusions, and cracked elongated sulphides were observed in some voids. Some of these inclusion-related voids impinged on each other, otherwise they were linked by sheets of submicron size void sheets where the scanning electron microscope examination did not resolve the initiation sites. The spacing of these voids was similar to that of the NbCN precipitates which nucleated in the austenite. Miglin, et al. [1982, 1983] concluded that the microstructural variables which directly affect fracture toughness of the ASTM A 710 Grade A steel are those associated with inclusions. The direct effects of the hardening particles are mainly seen through their influence on work hardening rate and yield strength, and indirectly these particles affect grain size, or their participation in the shear localization process on a micro-scale.

Hicho, et al. [1984] evaluated the sensitivity of 31.8mm (1.25-inch) thick ASTM A710 plate to heat treatment variations which may occur in production of thick plate Class 3 product. Austenitizing time at  $899^{\circ}\text{C}$  ( $1650^{\circ}\text{F}$ ) was varied from 60 to 90 minutes, and aging treatments were conducted over the temperature range  $482$  to  $649^{\circ}\text{C}$  ( $900$ – $1200^{\circ}\text{F}$ ) for periods of 30, 60 and 90



minutes. They found that peak aging occurred at 482°C (900°F), and all other temperatures led to decreases of the tensile properties. Small angle neutron scattering tests showed that 90-minute aging at 482°C (900°F) did not result in complete precipitation in plate of this thickness. This led to the conclusion that this thickness of plate is supplied in the overaged condition when conventionally aged. Results of this investigation also showed that the grain size of this plate was not affected by the narrow range of heat treatment variables examined, and variations on the order of 30 minutes in austenitizing time at 879°C (1650°F) had little effect on mechanical properties.

Montemarano, et al. [1984] conducted an evaluation of the tensile, impact toughness, fracture toughness, fatigue, stress corrosion cracking and weldability of ASTM A710 Grade A Class 3 steel plate in thicknesses ranging from 4.8 to 31.8mm (0.17 to 1.25-inch). The yield strength of all of these plates exceeded 552 MPa (80 ksi). Low temperature impact toughness was quite high in some cases, but heat to heat variability was noted. High impact toughness was generally obtained where carbon content was less than 0.044%, and sulphur less than 0.008%. Inclusion shape control treatment using calcium injection was found effective in improving low temperature impact toughness. Room temperature fracture toughness tests produced  $J_{IC}$  values in the range 299 to 580 kJ/m<sup>2</sup> (1700 to 3300 in-lb/in<sup>2</sup>).

## CRACK ARREST TESTING AND ANALYSIS

The history of crack arrest testing and analysis dates to World War II efforts to solve the problem of unacceptably high failure rates in Liberty Ship structures. Robertson [1953] developed a large single edge notched tensile test with an imposed temperature gradient to establish the critical combination of stress and temperature leading to brittle crack propagation and arrest in ship steels. Feely, et al. [1954, 1955] developed a modification of the Robertson test to reproduce conditions associated with hydrostatic test failures of large oil storage tanks. Pellini developed a series of small scale laboratory tests to identify the critical temperature for crack initiation and arrest. All of these early approaches involved the transition temperature approach to fracture control in steel structures.

Irwin and Wells [1965] first suggested the appropriateness of fracture mechanics in crack arrest analysis. Nordell and Hall [1965], and subsequently Crosley and Ripling [1969, 1971], made the first attempts to evaluate crack arrest toughness using the critical stress intensity approach. This triggered over two decades of active experimental and analytical research which addressed test method development, analysis approaches to dynamic fracture and arrest, and materials characterization to set limits for service application. In order to introduce the crack arrest testing performed in this investigation, the early transition temperature investigations will be reviewed. A discussion of analysis concepts pertaining to dynamic fracture and arrest will

be presented. This will be followed by reviews of attempts to develop standard crack arrest test methods, and wide plate crack arrest testing.

#### ROBERTSON CRACK ARREST TEST

T.S. Robertson developed the first large scale crack arrest test in order to address cases of catastrophic failures of welded ship hulls [Robertson, 1953]. In these failures, he determined that one or both of two conditions were present, specifically reduced ambient temperature, and storm conditions (or conditions of high stress). Robertson felt that notched bar tests failed to adequately assess arrest toughness because they did not simulate practical conditions for crack propagation, and because local yield is necessary to initiate a cleavage crack, which in turn is driven into this yielded field. He designed his test of steels in terms of crack resisting properties. Specifically, this called for a test where the crack started in a test piece carrying a known stress transverse to the crack propagation direction, and in which the crack arrests because it propagates into material of increasing toughness.

Figure 1 is a schematic drawing of the Robertson crack arrest specimen. It consists of a test piece which is a maximum of 50mm (2-inches) thick, and approximately 254mm (10-inches) in length. One end contained a 25.4mm (1-inch) diameter hole with a 4.8mm (3/16-inch) long saw cut slot emanating from it toward the width of the specimen. The specimen was welded to plates with lugs, and placed in a large capacity tensile testing machine.

Liquid nitrogen was used to cool the notch to approximately  $-60^{\circ}\text{C}$  ( $-76^{\circ}\text{F}$ ), and the opposite end of the specimen was heated to approximately  $60^{\circ}\text{C}$  ( $140^{\circ}\text{F}$ ). A large mass was placed against the warm end of the test piece to resist loading forces, and prevent bending. A tensile stress was applied, and a bolt gun was used to deliver a high speed blow against the end of the specimen containing the machined hole. This started a running crack which either propagated the entire length of the specimen, or arrested at some length short of complete separation. In some tests at high stress levels, the cracks started, arrested, restarted, and again arrested. General yield of the steel took place in the zones between arrests. The arrest temperature and crack length correlations were made from broken specimens where the tip of the crack was used in assessment of results.

A typical result of the Robertson Crack Arrest Test is shown in Figure 2 which shows two distinct regions. There is a region where arrest occurs by yield of the crack tip at essentially the same temperature, independent of the applied stress level. This single temperature was named the "ductile arrest temperature". When the temperature of arrest fell below this temperature, there was a critical relation between stress and temperature. Robertson [1953] reported that arrests in this region were not associated with plasticity, and were much more abrupt.

Robertson evaluated 29 plates of four qualities of mild steel using this test procedure [Robertson, 1953]. Each of the qualities of plate showed a decided decrease in ductile arrest temperature

with decreasing plate thickness. A series of tests with a single plate of a fine-grained ferritic steel was conducted where the test pieces were machined to thicknesses of 20mm (0.8-inch) and 15mm (0.6-inch) and compared to the original 25mm (1-inch) thick specimen tests. Again the results showed a decrease in arrest temperature, and Robertson concluded that there was a well defined thickness effect due to geometry alone.

A series of constant temperature tests at a constant stress level was conducted with one steel plate to evaluate the validity of the arrest temperature developed under a temperature gradient. Local cooling was applied to the crack tip to assist in crack initiation. This series of tests produced either separation of the specimen below the ductile arrest temperature, or arrest. The sum of the tests exactly reproduced the arrest temperature predicted from temperature gradient tests. Finally, Robertson used high speed photography and conducting strips to establish the velocity of running cracks. It was found that a stress of 137.9 MPa (20 ksi) gave an apparent crack velocity of 1829 m/sec (6000 ft/sec), and when stress was reduced to 82.7 MPa (12ksi) the observed velocity was 1219 m/sec (4000 ft/sec). Near arrest, crack speeds fell to approximately 457 m/sec (1500 ft/sec).

#### ESSO WIDE-PLATE CRACK ARREST TEST

In the spring of 1952, two large oil storage tanks failed during hydrostatic testing in England. Feely, et al. [1954, 1955] with the Standard Oil Development Company (later changed to ESSO Corporation) undertook a series of experiments to simulate the

conditions at the time of the tank failures. They noted that Robertson was unable to initiate brittle crack propagation at a stress below 69 MPa (10 ksi), and they also attempted to design a specimen which would avoid transient wave reflections.

Figure 3 is a drawing of the crack arrest specimen developed by Feely, et al. It is essentially a large tensile specimen which contains a sharp crack on one side, and a corresponding saw cut on the other. The test section was uniformly cooled, and a known tensile stress was applied to the specimen through loading pins. The crack was initiated by impacting a hardened steel wedge into the previously prepared notch. Under this test format, either crack arrest occurred, or the specimen was completely fractured. A plot of stress versus temperature for a set of standard test conditions is shown in Figure 4. The authors identified the temperature where the breaking stress began to increase markedly as the "SOD Transition Temperature".

In their early work, Feely, et al. [1954] evaluated the effects of notch sharpness, notch length, impact energy, test plate geometry and size. They found that sharp cleavage cracks resulted in lower breaking stress than saw-cut or wire-cut notches. They also found that crack lengths ranging from 19mm to 51mm (3/4-to 2-inches) in specimens where width varied from 152mm to 406mm (6-to 16-inches) indicated no effect of crack length at any temperature. Fracture stress was lowered with increasing impact energy until a plateau was reached, whereupon further increase in energy did not lower the stress. Finally, it was shown that

below the SOD Temperature, variations in width, length, size and shape of plates had no effect on breaking stress. At higher temperatures, the brittle breaking stress fell off as the length/width ratio increased, and approached a limiting stress asymptotically.

In their later work toward a crack arrest test procedure, Feely, et al. [1955] further evaluated the effects of impact energy and plate size on the limiting fracture stress. They tested plate specimens up to 1829mm (6-feet) in width, and found that large plates yielded lower critical temperatures than did the smaller specimens. It was also shown that brittle behavior occurred at the same stress in the 1800mm wide plates as that to which results from smaller specimens extrapolated. It was also determined that in tests carried out at a constant stress of 124 MPa (18 ksi), the temperature below which failure occurred, but above which it did not occur, agreed with data from Robertson tests, and service experience. Thus the crack arrest test was standardized by the production of specimens which were 1829mm (6-feet) in length, 254mm (10-inches) wide, and 25mm (1-inch) thick. A fixed stress level of 124 MPa (18 ksi) was set which related to storage tank design minimums. The "ESSO Brittle Temperature" was defined as the lowest temperature at which the crack did not propagate across the plate using these standard test conditions.

An evaluation of the ESSO Brittle Temperature for 29 carbon steels showed a trend indicating that lower carbon content resulted

in better performance when compared with high-carbon steels. Feely, et al. [1955] also correlated the ESSO tests with Charpy V-notch results, and recommended minimum impact energy levels for various classes of steels. They also emphasized that the temperature aspect of these correlations was more important than the energy level chosen.

#### DROP-WEIGHT TEAR TESTING

In the early 1950's, Pellini [1976] identified the need for a simple, natural crack test for laboratory use to assess crack arrest temperatures. This led to the development of the Drop-Weight Tear test to determine the nil-ductility transition temperature (NDT). These specimens have a brittle weld which contained a saw cut to localize the fracture at the center of the specimen. The brittle weld in turn fractures under dynamic loading of a dropped weight. The drop-weight tear test is conducted by loading the specimen as a simply supported beam, and determining the highest temperature of nil ductility breaks using a series of specimens. This is defined as the NDT temperature.

Pellini correlated results of Drop Weight NDT tests and Robertson crack arrest tests and determined that the latter have a fixed relationship to NDT. He thus developed an empirical correlation between the tests. For 50% yield stress level, the conservative index of the crack arrest temperature is  $NDT+16.7^{\circ}C$  ( $NDT+30^{\circ}F$ ), and a similar index for yield stress level loading is  $NDT+33.3^{\circ}C$  ( $NDT+60^{\circ}F$ ).



## FRACTURE MECHANICS ANALYSIS OF CRACK ARREST

In 1965, Irwin and Wells [1965] theorized that arrest of running cracks are simple time scale reversals of possible plane-strain initiation events. They suggested that there must be a material property which governs crack arrest in the same sense that  $K_{Ic}$  governs crack initiation.

Nordell and Hall [1965] applied the Irwin crack extension force concept to analyze the role of residual stresses and materials properties, and primary fracture arrest in 19, 25, and 41mm (0.75, 1.0 and 1.625-inch) thick plates of welded A 212 GR. B steel. In this series of experiments, both stress analysis and fracture mechanics analysis were applied to two-stage fracture where an initially short crack was arrested, then completely fractured at a higher load. Wide plate specimens measuring 914mm (36-inches) in height, and 610mm or 914mm (24 or 36-inches) wide were tested with centerline notches placed across weldments and through the plate. This test series included investigations of residual stress levels, and effects of mechanical and thermal stress relieving.

Nordell and Hall [1965] first evaluated the results of these wide plate tests at different temperatures to attempt to establish a critical value of stress for crack arrest. The data for primary fracture stress where cracks propagated completely across the plate in either single stage or secondary fracture, and results for arrested cracks were plotted against test temperature. These results identified an apparent critical value of applied stress

which must be exceeded for full fracture on the order of 34.5 MPa (5 ksi) for all plate thicknesses. The critical stress level for arrested fracture rose to approximately 690 MPa (10 ksi) at  $-1^{\circ}\text{C}$  ( $30^{\circ}\text{F}$ ), then turned up sharply. It was also determined that slightly different critical stress-arrest temperature relationships existed for the different thicknesses tested.

Nordell and Hall [1965] conducted the fracture mechanics analysis of these wide plate test results utilizing the Westergaard method and a stress function of a central crack in an infinite plate with a pair of opposing forces located symmetrically about the crack region. Stress intensity solutions were derived for arbitrary stress distributions, including residual stresses. In the welded plates used in this study, the value of the stress intensity,  $K$ , for low stress fracturing was large for small crack lengths due to the high longitudinal tensile stresses in the weld, but decreased as the crack length increased because the tensile residual stresses decreased.  $K$  was evaluated at arrest with intentions of providing an estimate of the fracture toughness of the A 212 GR B steel. The values of  $K$  at arrest were in good agreement for all specimens of various thicknesses. Between the temperature range  $-40$  to  $+4^{\circ}\text{C}$  ( $-40$  to  $+40^{\circ}\text{F}$ ), the arrest  $K$  increased gradually. Above  $4^{\circ}\text{C}$  ( $40^{\circ}\text{F}$ ), the value of  $K$  at arrest increased rapidly indicating an apparent increase in fracture toughness. Nordell and Hall [1965] concluded that the possibility of low stress single-stage fracture could occur in this steel at temperatures as high as  $-1$  to  $-4^{\circ}\text{C}$  ( $30$ - $40^{\circ}\text{F}$ ).

Crosley and Ripling evaluated the crack arrest toughness of ASTM A 533 B steels using contoured double cantilever beam specimens [1969,1971]. They reasoned that crack arrest toughness involved a more conservative design practice than fracture control based on initiation because of rate sensitivity of intermediate strength steels, and the need to address larger cracks following an arrest event. Crosley and Ripling defined crack arrest toughness,  $K_{Ia}$ , as the value of the stress intensity factor based on the length of the arrested crack and load established immediately after crack arrest [1971]. They recognized that the high velocity of a propagating crack precludes the use of static analysis during the interval of crack propagation prior to arrest. They postulated that the static analysis is applicable after the crack had arrested, and their original experiments explored the value of  $K$  measured after different crack jump distances.

The Crosley and Ripling experiments [1969, 1971] utilized tapered double cantilever beam specimens which allowed for measurement of  $K$  from applied load only. Specimens were tested in either a closed-loop servo-hydraulic test machine, or a drop-weight test device, and loading time to fracture ranged from 1000 sec. to 1 msec. Specimens were tested at either constant temperature, or with a temperature gradient going from cold to hot as the crack length increased. Separate oscilloscope traces of load versus load-line deflection, and load versus time were obtained for each test. The typical load-deflection records were linear until the onset of rapid fracture. As the crack ran, the load

dropped too abruptly to produce a trace, but the load deflection trace resumed when the crack had arrested and the load on the specimen again increased. The start of this increase defined the crack arrest load, hence,  $K_{Ia}$ .

The  $K_{Ia}$  values measured with this procedure over various crack jump lengths were constant for the first arrest event, but increased after successive jumps. Thus, Crosley and Ripling felt that artificially lowering the initiation value for a fast running crack would make it possible to measure crack arrest toughness at higher temperatures. They conducted dynamically loaded TDCB tests with temperature gradient of 0.33 to 0.44°C/mm (15 to 20°F/inch). A large number of tests resulted in crack arrest at temperatures from 24 to 46°C (75 to 115°F) with arrest values clustering around a single value, but also displaying some dependence on crack jump length. Crosley and Ripling [1971] concluded that it appeared feasible to characterize crack arrest toughness in terms of  $K_{Ia}$ , based on the load and crack length immediately following crack arrest. They also pointed out that this is a conservative design number, the practical importance of which is greatest above NDT where it is significantly less than both static  $K_{Ic}$ , and dynamic initiation toughness.

#### STATIC AND DYNAMIC ANALYSIS

In 1973, Hahn, et al. reported preliminary results of crack speed and arrest measurements conducted using a wedge-loaded double cantilever beam (DCB) specimen. The material employed in this investigation was 4340 steel with a Rockwell hardness of 55.

Their analysis employed a beam-on-elastic-foundation model which was extended to account for inertia forces. This specimen was loaded with a wedge, and static  $K$  values were calculated from measurements of crack opening displacement taken a fixed distance from the loading pins. Crack velocity was measured with a grid of conducting strips insulated from the specimen surface. A blunt notch was employed to allow the specimen to sustain a stress intensity prior to onset of crack extension which is greater than the fracture toughness.

The analysis employed in these experiments addressed the dynamic crack propagation where the time variable appears explicitly. The beam-on-elastic-foundation model was augmented by entering the lateral inertia forces into the equations of motion, but neglecting (at this point) shearing deformation and rotary inertia. The model allowed for calculation of crack length versus time, strain energy and kinetic energy versus crack length for assumed geometric parameters and assumed ratio of initiation fracture toughness to dynamic fracture toughness, and the value of the stress intensity factor required to advance the crack dynamically. It was assumed that  $K_d$ , the dynamic fracture toughness was a constant, independent of crack speed and position after some amount of crack growth beyond the blunted crack tip.

Results of their experiments showed that the crack propagated essentially at a constant velocity until shortly before crack arrest. Hahn, et al. [1973] reported that the velocity increased with the initiation  $K$  value,  $K_q$ , associated with the blunt starter

notch. No crack branching was observed in these experiments. The calculated crack-length versus time curves for the model predicted a steady state propagation rate as seen in the experiment. However, there was a factor of two discrepancy between the steady state velocity predictions and measurements, with the actual measurements being lower. The authors attributed this discrepancy to the method of simulating the blunt notch, neglect of shear deformation and rotational inertia terms, and assumption of velocity independence of  $K_d$ . Nevertheless, they felt that this model gave a far better representation of the crack propagation event when compared to the static calculation.

Using this analysis, Hahn, et al. [1973] determined that more than half the stored energy released by the propagating crack in the initial stages of growth is converted to kinetic energy, which is a source of fracture energy late in propagation. They suggested that the appropriate crack arrest criterion is one based on the concept that kinetic energy of the system is largely recovered. Their calculations showed that kinetic energy remaining after crack arrest is less than 4% of the total energy dissipated by fracture. Hahn, et al. also noted that using the DCB specimen to obtain a wide range of constant crack velocities would provide an attractive vehicle to evaluate dynamic toughness.

Hahn, et al. [1974] extended the measurements of unstable crack propagation and arrest in 4340 steel DCB specimens to a range of crack velocities from 180 to 860 m/sec (590 to 2821 ft/sec). The authors discussed the differences between the

static and dynamic approaches to crack propagation in terms of the stress field energy release rate, or crack driving force  $G$ . This is evaluated as follows for the running crack [Hahn, et al., 1974; Irwin, 1977]:

$$G = \frac{dw}{da} - \frac{du}{da} - \frac{dT}{da} \quad (1)$$

where:  $da$  = Increment of new separational area;

$W$  = Work performed on structure by surroundings;

$U$  = Total strain energy in stress field;

$T$  = Total kinetic energy in stress field.

Hahn, et al. [1974] equated  $G$  with the energy dissipated in the vicinity of the crack tip per unit of crack extension ( $R$ ) and allowed as how it can be a function of crack speed. They concluded that prediction of crack speed or likelihood of arrest entailed a fully dynamic analysis and knowledge of velocity dependence of  $R$ . In the static analysis, the kinetic energy release rate can be neglected. Hahn, et al. stated that this implied a crack arrest toughness which is controlled by  $G$  or  $K$  at arrest, and is a single materials property independent of crack speed or crack length. Their experiments were intended to test these assumptions.

The experimental procedure employed by Hahn, et al. [1974] was similar to that of Hahn, et al. [1973]. The steel tested was 4340 which was quenched and tempered to a yield strength of 1379 MPa (200 ksi), and tested using 12.7mm (0.5-inch) thick DCB specimens. The root radius of the starting notch was changed to vary crack initiation  $K(K_0)$ , and electro-polishing techniques were used to

reduce scatter in initiation toughness. The beam on elastic foundation model was again employed, and this described the crack length, crack velocity, time variation of displacements of the arms of the specimen, and length of the crack at arrest as functions of  $R$ , dynamic  $K$ , specimen dimensions, elastic modulus, density and crack initiation  $K$ . This analysis again predicted the region of constant velocity crack propagation which was observed experimentally. The analysis also showed that of the maximum amount of kinetic energy generated, 85% is recovered during the latter 2/3 of the crack growth increment, with less than 10% of the total strain energy released remaining as unrecovered kinetic energy.

All specimens tested exhibited an extensive region of constant velocity propagation, followed by rapid deceleration and arrest. The dynamic fracture toughness,  $K_d$ , was calculated from measured velocity, and from the crack length at arrest following the assumption of total recovery of kinetic energy. These two calculations showed good agreement, and showed that the toughness almost doubled between the static value and the highest velocity attained. The results also showed that crack velocity depended on  $K$  at initiation. Hahn, et al. also measured the static crack arrest toughness and found it to increase slightly with  $K$  and crack velocity in the range 0 to 200 m/sec (0 to 656 ft/sec), then remained constant over the remaining range of  $K_Q$  values. They suggested that this is a consequence of the increase of  $K_d$  with crack velocity rather than an indication of the invariance of  $K_a$ .



They suggested that  $K_a$  from static calculations is not a materials property. Finally, Hahn, et al. concluded that the fully dynamic analysis only provides the best description of the relation between crack velocity and crack length at arrest.

Hahn, et al. [1975] discussed three different theories of crack arrest. The static analysis for  $K_{Ia}$  assumes that the kinetic energy term in the calculation of  $G$  can be neglected as discussed above. The second theory relates crack arrest toughness to dynamically loaded stationary crack toughness. This approach assumes that the time variation of stress in the elastic field in front of a crack is the same for a stationary crack loaded at a given  $K$ -rate, and a crack propagates with a given velocity. This velocity- $K$  rate equivalence exists only at one specific point ahead of the crack tip. Further, the strain rate in the plastic zone is not the same as in the crack tip region, and this differs from the case for the stationary crack. The third approach is that of the fully dynamic analysis of crack propagation and arrest such as that previously developed for the DCB specimen. These authors argued that specimen dimensions prescribe a specific relation between crack velocity and arrest length, and as such,  $K_{Ia}$  is a function of test piece geometry, and depends on history of energy dissipation and kinetic energy recovery throughout the propagation event. Hahn, et al. [1975] stated that results of dynamic studies suggest that  $K_{Ia}$  from laboratory test pieces cannot be equated a priori with  $K_{Ia}$  values for a crack arrest event in a structure of entirely different geometry. The common

property between specimen and structure is the dynamic K-crack velocity dependence.

Hahn, et al. [1976] evaluated the dynamic fracture toughness  $K_{ID}$  versus crack velocity and temperature for a number of steels with the wedge loaded DCB specimen using the beam-on-elastic-foundation analysis. For the case of 4340 steel, O-1 tool steel, and 9-Ni steel tested at  $-196^{\circ}\text{C}$  ( $-321^{\circ}\text{F}$ ), results indicate that  $K_D$  is only slightly velocity dependent. This investigation also included an analysis of specimen/test machine interaction during tensile loading of the DCB specimen. The initial prediction of steady state crack velocity was seen in experiment, but then was followed by a temporary halt in crack growth, and reinitiation prior to final arrest. These events were attributed to additional energy input from the load train as transmitted by arm motion. From this, it was concluded arrest behavior depends on loading system as well as on the material toughness. These authors concluded that the material property governing both crack propagation and arrest is the fast fracture toughness  $K_D$ , the value of which and velocity dependence depends on micromechanism of fracture. Further they suggested that the lowest value of  $K_{ID}$  at the appropriate service temperature provides a materials property which defines the ability of a steel to arrest a fast running crack.

Crosley and Ripling [1977a] discussed several issues related to the use of plane strain crack arrest toughness  $K_{Ia}$ . The proposed definition of  $K_{Ia}$  is the value a short time interval

(about 1 msec) following an arrest segment of crack extension. It was assumed that the test conditions permit establishment of a nearly static stress state in the test specimen in a time less than the 1 msec interval. According to Crosley and Ripling the major question associated with  $K_{Ia}$  is in defining limits over which crack arrest capability of real structural components can be predicted by measurements made in relatively small laboratory test specimens. The analysis of real structures and even laboratory specimens containing running cracks is extremely difficult requiring treatment of such considerations as energy loss occurring remote from the crack tip, including damping at specimen corners, loading points and notches. They suggested that the only feasible method to establish the usefulness of the  $K_{Ia}$  method and analysis is by measuring  $K_{Ia}$  with as many different test procedures as possible to determine whether the measured values are independent of test method. Results of crack arrest tests of ASTM A 533 B steel conducted with contoured double cantilever beam specimens, single edge notched (SEN) specimens, and duplex uniform double cantilever beam (UDCB) specimens were presented and compared. The results of the SEN and UDCB specimens were seen to provide similar results to those obtained with TDCB specimens.

Crosley and Ripling [1977c] proposed a chronology of a run-arrest segment of crack extension which would justify the invariance of  $K_{Ia}$ . It assumes that for each material and temperature, there is a unique dependence of crack tip velocity on driving force  $K$ . At high crack velocities, large increases in  $K$  cause small increases

in crack velocity, where at low velocities, small increases in  $K$  cause large increases in crack velocity.  $K_{Im}$  is defined as the minimum value of  $K$  at which a crack can extend. The second assumption is that the range of crack initiation toughness,  $K_0$ , can be varied by loading rate or the use of blunt notch starter cracks. Under this proposed scenario, after initiation the cracks accelerate to the value associated with  $K_a$ . If the specimen or structure shape and loading are such that  $K$  decreases with crack length, then the instantaneous value of  $K$  moves along the  $K$  versus crack velocity curve until  $K_{Im}$  is reached, and arrest occurs.

Irwin [1977] reviewed the basic definitions and concepts applicable to linear elastic analysis of dynamic fracture. He discussed the fact that separational behavior in the fracture process zone is controlled by the local environmental strain across the fracture process zone. To produce a running crack, the surrounding elastic field must produce a plastic strain continually near the advancing crack tip adequate for the separational process. An increase in  $K$  can enlarge the plastic strain field, increase the size of segments of crack extension, and produce a higher crack speed. He postulated that limitations on the speed of propagation of the crack tip plastic zone are a major factor in fixing the upper limit of crack velocity of a running crack in structural metals. Using this rationale for the shape of the  $K$  versus crack velocity curve ( $\dot{a}$ - $K$  curve), Irwin defined  $K_{Im}$  as the minimum value of the curve. Any reduction of  $K$

below this value would result in crack arrest. Rapid load initiation toughness,  $K_{Id}$ , and static arrest toughness,  $K_{Ia}$ , were seen as natural choices for simplified experiments to determine  $K_{Im}$ . Irwin suggested that since  $K_{Ia}$  values for ASTM A 533 B steel developed in the range  $NDT + 50^{\circ}C$  ( $90^{\circ}F$ ) gave lower average results than  $K_{Id}$ , acceptance of  $K_{Ia}$  as a lower bound  $K_{Im}$  would appear to represent sensible engineering practice. He recognized uncertainties in the  $K_{Ia}$  analysis, particularly related to dynamic stress field analysis, and suggested that such uncertainty could be reduced by restricting the length of the run-arrest in the  $K_{Ia}$  measurement.

Kanninen, et al. extended the previously developed dynamic analysis of crack propagation and arrest in the DCB specimen to treat contoured specimens and machine loading conditions [1977]. This was done to address inertia forces, kinetic energy contribution to crack growth, and fracture process energy dependence on crack speed. The beam-on-elastic-foundation model was generalized to treat the zero-taper rectangular DCB specimen, positive and negative-taper straight sided DCB specimens, and contoured DCB shapes. For each shape, a wedge-loaded and machine-loaded calculation was performed. Here again,  $K_D$  was assumed to be constant and equal to  $K_C$ . Results of the calculations for the tapered and contoured DCB specimen shapes were similar to those obtained for the rectangular DCB specimen shape. In all of these, the cracks began to propagate at full speed, and continued at essentially constant velocity over most of the event, and arrest was fairly

abrupt. For rigid wedge loading, reinitiation of growth typically did not occur. For machine loading systems, the crack usually restarted after a period of time, propagating and arresting, and repeating this sequence several times. The loading system was seen to have a more significant effect on crack history than specimen geometry. The use of wedge loading was seen to offer advantages over more compliant tensile loading. Kanninen, et al. [1977] also showed that  $K_a$  systematically decreased as  $K_q$  increased. For modest  $K_q$  values  $K_a$  values from contoured specimens were reasonably good approximations of  $K_D$ . It was suggested that the calculated variation of  $K_a$  with  $K_q$  showed that  $K_a$  is not basically a correct crack arrest criterion.

As seen to this point, the analysis of the crack arrest toughness requires knowledge of the stress intensity-crack velocity relationship for materials of interest. Experiments with wedge-loaded DCB specimens which were performed by investigators at Battelle Columbus Laboratories included crack velocity measurements from grids of conducting strips. Crosley and Rippling [1977b] applied ladder gages in side grooves of tapered DCB specimens to measure crack velocity, and response of the specimen to crack advance and arrest. For tests of ASTM A 533 B steel conducted in the vicinity of the NDT temperature, the crack attained a high velocity in the range 400 to 600 m/sec (1312 to 1968 ft/sec) shortly after crack initiation, then decelerated to a low velocity prior to crack arrest on the order of 100 m/sec (328 ft/sec). The cracks were observed to grow continuously, without halts. From

strain gage measurements in the arms of these specimens, it was observed that the strain dropped abruptly over time intervals of fast crack extension, then oscillated with a low amplitude, and period of 50 to 150  $\mu\text{sec}$ . This oscillation started before crack extension was completed, and continued after arrest. When compared to strain gage measurements based on condition of static equilibrium, the largest difference between dynamic and static strains occurred at the end of fast crack extension. While the crack extended slowly, the strains in the arms increased, then oscillated with a low amplitude about the eventual static value, suggesting that a static calculation of  $K$  near the end of an arrest segment is an adequate approximation of the actual value of  $K$ .

Kalthoff, et al. [1977] evaluated the influence of dynamic effects on the crack arrest process in wedge-loaded DCB specimens produced from an epoxy resin, Araldite B. Actual dynamic stress intensity factors were measured by the shadow optical method of caustics. Cracks were initiated from blunted notches at initiation stress intensity factors larger than the fracture toughness,  $K_{Ic}$ . As seen in earlier experiments of Hahn, et al. [1973,1974], the measured velocities were constant over a broad extent of crack growth then decreased prior to crack arrest. The maximum velocities increased with initiation value,  $K_Q$ , reflecting the level of elastic stored energy in the specimen.

The dynamic stress intensity factors from shadow optical caustics measurements were compared with static calculations and these results are reproduced as Figure 5. At the beginning of

crack propagation, the dynamic K value is greater than the static value, and at the end of crack propagation, this relation is reversed. It was observed that only after arrest did the dynamic stress intensity factor approach the static value. Differences between static and dynamic K values were reduced at lower maximum crack velocities. Post arrest behavior of cracks was also investigated, and results showed a damped oscillation of dynamic K around the static fracture toughness at arrest. Kalthoff, et al. [1977] observed that the frequency of the oscillation had the same order of magnitude as that of vibration of a cantilever beam corresponding to a half of the cracked specimen. The crack arrest toughness points determined from static analysis were observed to depend on crack velocity, with faster crack extension resulting in lower toughness values. The observed dynamic crack arrest toughness values scattered about a horizontal line and did not depend on crack velocity. The authors concluded that these results supported the concept of recovered kinetic energy contributing to the arrest process. They suggested that stress waves emanating from the crack tip carry kinetic energy which after being reflected at the finite boundaries of the specimen contributes to actual dynamic stress intensity factors associated with the crack during run and arrest. They concluded further that the dynamic crack arrest toughness seems to be a more fundamental property than that determined with the static analysis.

Popelar and Kanninen extended the study of dynamic crack propagation and arrest in polymeric, model materials to determine



the importance of viscoelastic constitutive behavior [1980]. They employed the beam-on-elastic-foundation analysis of the DCB specimen, under the assumption that the specimens were wedge-loaded under infinitely slow loading. The model materials included an elastic material, and four polymers with viscoelastic properties. The results showed that while the crack is in motion, the deformation is controlled by the short time, viscoelastic modulus, and up to the point of crack arrest, true viscous energy dissipation is seen to be negligible. They concluded correlation between elastic-dynamic events and viscoelastic dynamic crack propagation/arrest can be made using only short time and long time viscoelastic moduli. They also concluded that for long crack jump lengths, no connection exists between the dynamic value of the crack driving force at the instant of crack arrest, and the static value corresponding to the arrest state.

Gehlen, et al. developed a method of extracting fracture toughness measurements from compact tension specimen tests [1979]. This reference-curve technique allowed inference of fracture toughness as a function of crack speed from measurements of the crack opening displacement at initiation of crack growth, and the total crack extension. The basis for this approach was the extensive series of modelling and experiments with the DCB specimen which showed that the total amount of crack extension as a function of average crack speed was relatively insensitive to the exact fracture toughness/crack speed relationship for a fixed ratio of initial crack length to specimen depth. Then, if  $K_{ID}$  is identified

with the average crack speed fracture resistance, the dependency of  $K_D$  on  $K_Q$  and crack jump distance is relatively insensitive to the crack-speed fracture toughness relationship. From calculations (using reference curves) of crack velocity versus crack extension, and  $K_{ID}/K_Q$  versus crack extension, the average crack speed and associated fracture resistance can be calculated from test measurements of  $K_Q$  and crack jump length. Gehlen, et al. [1979] detailed their calculation approach and produced reference curves for ordinary and duplex compact specimens, and discussed their utilization in calculating  $K_{ID}$  from this geometry of test piece.

Crosley and Ripling [1980a] discussed the static and dynamic approaches to crack arrest methodologies in the context of developing a standard test procedure. They pointed out that both the static crack arrest toughness ( $K_{IA}$ ) approach, and dynamic ( $K_{ID}$ ) calculations assume a material property,  $K_{Im}$ , which is the lowest value of the stress intensity factor which will support continued propagation of a running crack. The  $K_{IA}$  approach asserts that the stress intensity factor achieved in static conditions following crack arrest is a reasonable approach to  $K_{Im}$ . The dynamic analysis allows values of crack speed and running crack toughness to be inferred from a laboratory test, and by determining  $K_{ID}$  as a function of velocity, the minimum value may be found. Crosley and Ripling stated that  $K_{ID}$  and  $K_{IA}$  approaches are measuring different things, and except for the case of the very short crack jump, they are not expected to be compatible approaches to  $K_{Im}$  measurement. Only if there is a reason for identifying  $K_{ID}$

as the minimum value (from direct measurements of  $K$  versus crack velocity) can  $K_{Ia}$  be compared to  $K_{ID}$  to determine which is a more meaningful parameter.

Hahn, et al. [1981] reviewed the complications associated with dynamic effects when analyzing crack arrest. They noted that the first involves the variation of the dynamic fracture toughness with crack velocity. A second is the departure of the instantaneous value of  $K$  for a propagating or arresting crack from the static equilibrium value for a static crack of the same length. The departure is caused by the inertia of the cracked body which can lead to the conversion of kinetic energy to fracture energy causing the crack to propagate while the static fracture toughness is less than the dynamic fracture toughness. These authors stated that the difference between the minimum dynamic fracture toughness and the static arrest toughness is the departure from static equilibrium. A third dynamic effect is the oscillation of the cracked component immediately after arrest as the result of the kinetic energy trapped in the body. Hahn, et al. [1981] stated that the magnitude of the dynamic effects from these three sources depends on the relative amount of kinetic energy which is consumed or converted to fracture energy. They postulated three cases to illustrate conservation of kinetic energy. The first involved no conservation when the amount of kinetic energy imparted to the fracturing body is small relative to the fracture energy and/or becomes widely dispersed. The departure from static equilibrium is negligible, and is seen to pertain when crack jumps are small

relative to dimensions of the specimen or cracked body. Partial conservation occurs in a case where relatively large amounts of kinetic energy is imparted, and the  $K_{ID}$  value is rate insensitive. Because of the little time for damping in the short time intervals involved, substantial departure from equilibrium is obtained and large oscillations follow crack arrest as kinetic energy must be returned. This hypothetical case corresponds to large crack jumps (compared with body dimensions) and  $K_{ID}$  velocity curves which are rate insensitive at lower velocities. The third case of nearly complete energy conservation was postulated for the case of a large amount of kinetic energy coupled with a material displaying a strong rate sensitivity of the  $K_{ID}$  versus crack velocity curve. This combination provides smaller departure from static equilibrium at arrest, smaller oscillations after arrest, and more complete kinetic energy conservation.

Kalthoff, et al. [1980] performed an experimental analysis of dynamic effects in several crack arrest test specimen geometries using the shadow optical method of caustics. The specimens considered included the longitudinal wedge-loaded rectangular DCB, machine-loaded tapered DCB, and the transverse wedge-loaded compact specimen. These specimens were produced from Araldite B, an epoxy resin. For all types of specimens, there was a gradual decrease of the crack velocity prior to the arrest event. Kalthoff, et al. found that the stability of the crack propagation event in the tapered DCB and compact specimens was much greater than for the rectangular DCB configuration. As seen earlier, the dynamic

stress intensity factor showed an oscillation after arrest. The observed amplitude and frequency varied from specimen type to specimen type, and in all cases the frequency was roughly correlated to the frequency of vibration of a beam corresponding to one-half of the cracked specimen. The compact specimen displayed the lowest amplitude of oscillation, where the rectangular DCB showed a very large amplitude oscillation of the dynamic K value after arrest. In comparing the influence of the dynamic effects with the rectangular DCB specimen, the tapered DCB specimen was seen to be less affected by a factor of two, and the compact specimen by a factor of four. Kalthoff, et al. concluded that the smaller amounts of kinetic energy are recovered in the compact and tapered DCB specimens during the arrest process. They attributed this to the reduced interaction of elastic stress waves with the arresting crack tip due to stronger attenuation of reflections in response to differences in configuration in comparison with the rectangular DCB specimen. They also suggested that errors in applying static analysis of crack arrest to the tapered DCB and compact specimens would be smaller than those experienced with the rectangular DCB specimen.

In following up these experiments with model materials, Kalthoff, et al. [1980] evaluated the dynamic effects on crack arrest of a high strength steel using rectangular DCB specimens. The optical method of caustics was used in reflection to determine the dynamic stress intensity factor as a function of crack length. It was found that the crack velocity behavior for the steel

specimen was similar to that of the Araldite B in that there was a large phase of constant velocity, followed by a gradual decrease prior to arrest. In the steel specimens, arrest was typically characterized by multiple arrest/reinitiation events. The dynamic fracture toughness values for the high strength steel showed large variations which these authors attributed to higher frequency vibrations or higher frequency stress-wave interaction with the crack. The post-arrest oscillations of dynamic  $K$  did not show a simple harmonic as seen with the Araldite B specimens. The amplitude of the oscillation increased with increasing crack jump distance, and the oscillation was considerably less attenuated than for the case of epoxy specimens. It was observed that a static condition at the tip of an arrested crack could be established only for times considerably longer than 1 msec after arrest.

Nakano and Katyama [1981] evaluated the stress intensity factor during dynamic crack propagation in ESSO-type specimens using the half value width of the X-ray diffraction intensity curve from the fracture surface after completion of the test. The broadening of the X-ray diffraction intensity curve from the brittle fracture surface was used to evaluate the degree of change in microstructure of the steel beneath the fracture surface due to plastic deformation caused by crack propagation. A calibration curve from J-integral fracture toughness in three-point bend specimens was developed to relate  $J$  (and  $K$ ) to the breadth of the X-ray diffraction intensity curve. For tests of compact specimens

of ASTM A 533 B steel which were 250mm (9.8-inches) thick, the dynamic stress intensity factor was shown to decrease with crack extension, then oscillate until arrest. It was observed that arrest of a brittle crack did not necessarily occur when the dynamic K value was at a minimum. It was also observed that the dynamic K values were in good agreement with static K values at arrest.

Nakano extended this type of experimental measurement of dynamic stress intensity factors to 1000mm (39.4-inches) wide, 250mm (9.8-inches) thick ESSO specimens with temperature gradients [1981a]. The dynamic stress intensity was observed to increase strongly in the early stages of crack extension because the ESSO test is a K-increasing test. After reaching an upper limit, the dynamic K value decreased with crack extension, and then gradually decreased with oscillations. For short crack jumps, there was no significant difference between dynamic K at arrest and  $K_{Ia}$ . As crack jump length increased, the dynamic K value at arrest became greater than  $K_{Ia}$ .

Besides efforts to characterize and directly measure the K values associated with the arrest event, there has been substantial experimental effort to determine the crack velocity-dynamic stress intensity ( $\dot{a}$ -K) relationships for model materials and high strength steels. The basis for this research is the fact that the analysis of the arrest event is keyed to the assumption that a unique  $\dot{a}$ -K relationship exists for materials, and that the mechanics of the arrest event are defined in relation to the

minimum of this relationship.

Kobayashi and Dally [1977] conducted an experimental investigation of the dynamic behavior of crack propagation in two birefringent polymers. They recorded photoelastic isochromatic fringe patterns associated with events in single edge notch (SEN) specimens which were pin-loaded. The size and shape of the isochromatic fringe lines were employed to evaluate instantaneous values of the stress intensity factor by matching analytical and experimental results. For Homalite 100, it was shown that there was a minimum value of  $K$  associated with crack arrest. Small increases in  $K$  above this level resulted in large increases in crack velocity. A transition region existed where the stress intensity had to be doubled to achieve a significant change in velocity. For even higher velocities, substantial increases in  $K$  were required to achieve further increase in crack speed. This result is reproduced in Figure 6. Kobayashi and Dally concluded that there appeared to be a unique relation between stress intensity and crack velocity for Homalite 100.

Dahlberg, et al. [1980] conducted a series of crack propagation experiments on four different geometries of 0.5mm (0.02-inch) sheets of cold rolled carbon steel plate where the yield strength was 1500 MPa (218ksi). All four specimen geometries were rectangular single edge notch configurations where the width was 406mm (16-inches) and the height ranged from 200 to 1600mm (7.9 to 63-inches). Specimens were tested to fracture under load control. Finite element calculations were performed to evaluate the stress



intensity factor during dynamic crack extension. As input to the finite element method (FEM) program, the times and external loads when the crack tip passed the nodal points were used to calculate  $K$  and crack velocity and crack tip accelerations. Results for specimens where the height/width ratio ranged from 0.25 to 0.75 taken at low velocities showed that there was very good agreement between  $\dot{a}$ - $K$  curves. At higher loads, scatter substantially increased, and the curves tended to show a maximum in velocity, then turn backwards. Dahlberg, et al. concluded that this was due to the high nominal stress levels required. The  $\dot{a}$ - $K$  curves for specimens with height/width ratio of 2.0 deviated somewhat from the three other specimen geometries, but these authors concluded that their results did not invalidate the hypothesis of a unique  $\dot{a}$ - $K$  relationship, or the hypothesis of a geometry-independent crack arrest toughness. For high  $K$  levels, the differences between the  $\dot{a}$ - $K$  curves gradually increased, and the crack propagation toughness decreased with decreasing height of the specimen. This is consistent with the assumption that a non-unique  $\dot{a}$ - $K$  relationship exists with non-elastic deformations in these specimens.

Kobayashi and Dally [1980] carried out an investigation to determine the crack velocity- $K$  relationship for 4340 steel. They utilized dynamic photoelastic determinations from birefringent coatings applied to compact specimens. Results for these tests showed that at high crack velocity levels, the instantaneous  $K$  value oscillates, and the changes in  $K$  did not markedly affect the

crack tip velocity. One instance of multiple crack arrest and reinitiation was noted, and it was observed that the instantaneous value of  $K$  at arrest was the same for each event. A crack velocity- $K$  curve was constructed and displayed a vertical stem as seen in the earlier work by these authors with Homalite 100. It was observed that the slope of the stem was higher in the steel than observed with the model material.

Ravi-Chander and Knauss [1983] investigated the processes of dynamic fracture in Homalite 100 using an electromagnetic loading device to apply dynamic loads to edge-cracked specimens. The optical method of caustics was used to determine the stress intensity factor at the crack tip. Their results differed from those of Dally in that they observed significant changes in stress intensity factor while the crack velocity remained constant. They also found that the velocity of propagation depended on the stress intensity factor at initiation, and that the discontinuous changes in velocity were found to be caused by stress waves interacting with propagating cracks.

Kobayashi and Mall [1978] evaluated dynamic fracture toughness measurements of Homalite 100 and Araldite B from dynamic photoelastic techniques and the optical method of caustics. They compared results for Homalite 100 with those of Kobayashi and Dally, and found that the dynamic fracture toughness measurements agreed well, particularly in the low velocity regime. However, Kobayashi and Mall did not establish a definitive  $\dot{a}$ - $K$  curve because of their experience with dynamic finite element analyses.

Specifically, they pointed up that an elastic crack must run in intermittent crack velocities in order for a smoothly varying  $\dot{a}$ -K relationship to prevail, or alternatively, the dynamic fracture toughness must vary intermittently to maintain smoothly varying crack velocity. They felt that the dynamic photoelastic measurements, caustics measurements, and crack velocity measurements were not sufficiently accurate to resolve these questions.

Fourney, et al. [1983] summarized results of dynamic photoelastic determinations of the crack velocity K relationship for Homalite 100 using six different types of fracture specimens. These included single-edge notched, compact tension, modified compact tension, rectangular DCB, contoured DCB, and a ring segment. These results were obtained with four batches of Homalite 100, and included four different investigations conducted over a five-year period. Fourney, et al. concluded that there was satisfactory agreement between the crack velocity-K relations for these different geometries to argue a unique relationship.

Kalthoff [1983] presented results of measurements of dynamic K versus crack velocity for Araldite B epoxy resin obtained with the optical method of caustics in transmission. In this case, experiments were carried out under practically identical conditions with DCB and SEN specimens. These results showed two clearly separated  $\dot{a}$ -K curves, where the DCB specimens showed significantly higher values than the SEN specimen. Kalthoff speculated that K versus crack velocity curves are not unique, but are dependent on specimen geometry.

Rosakis, et al. [1983] carried out a series of dynamic crack propagation experiments with AISI 4340 steel using rectangular DCB specimens. The optical method of caustics in reflection was employed. Curves of crack length and  $K$  versus time showed oscillations, and peaks and jumps in these curves occurred at different instances for different tests, depending on the velocity history of the crack tip. Plots of dynamic  $K$  versus crack length showed that the oscillations occurred in phase, and suggested a relationship between dynamic  $K$  and crack tip velocity. The plot of  $K$  versus velocity showed that for values of crack tip speed less than 700 m/sec (2296 ft/sec), the dynamic fracture toughness is nearly independent of velocity. For velocities greater than 800 m/sec (2624 ft/sec), the dynamic toughness increased sharply with velocity, but did not indicate a limiting or asymptotic value. These authors concluded that the observed  $K$  versus crack velocity relationship is a good description for a high strength, low ductility metal which fails in a locally ductile manner, and whose fracture is well described by a ductile failure criterion such as critical level of plastic strain ahead of a crack.

Nakano [1981b] measured the dynamic stress intensity in compact specimens and ESSO wide plate tests of SA 533 B steel using half value breadth of the x-ray diffraction curve as introduced earlier. The value of dynamic  $K$  in the compact specimen increased as the crack velocity increased. A relation between dynamic  $K$  and crack velocity in the temperature range evaluated could be represented by a single curve. The results of  $\dot{a}$ - $K$

measurements in ESSO specimens tested at  $-40$  and  $-90^{\circ}\text{C}$  ( $-40$  and  $-130^{\circ}\text{F}$ ) were in good agreement with compact specimens tested at  $-60^{\circ}\text{C}$  ( $-76^{\circ}\text{F}$ ). The ESSO test results indicated that dynamic  $K$  at a given velocity is greater at a higher temperature than obtained with the compact specimen. Nakano concluded that the velocity dependence of the strain intensity factor is dependent on temperature, but not on test method. This conclusion is difficult to support in examining the results of Nakano [1981b].

This analysis of crack velocity-dynamic stress intensity dependence does not conclusively point to, or negate the existence of a unique material property which is independent of test specimen geometry. The bulk of the experimental work, which is difficult to obtain, has been performed with model materials, and tests of metallic materials are very limited. Erdogan [1983] concluded that the existence of a unique  $K$  versus crack velocity material property does not appear likely. He further suggested that in solids which are not ideally brittle (where the zone of energy dissipation around the propagating crack tip possesses sizeable value), the global energy balance must be satisfied for crack growth to occur. The geometries and loading conditions in real structural materials undergoing dynamic fracture are seen to affect the size and shape of the energy dissipation zone around the crack front as well as the dimensions of the plastic wake. Consequently, Erdogan concluded that fracture energy should also depend on the medium, current crack size, nature of external loads, environmental conditions (mainly temperature), as well as

crack velocity. Erdogan concluded therefore that it was unrealistic to expect the dynamic fracture resistance of such a material would be characterized by a single  $\dot{a}$ -K relationship. He also suggested that in certain practical applications, a proper  $\dot{a}$ -K curve which may be parameterized with respect to environmental and test conditions may be useful.

This review of the theoretical aspects of crack arrest (and dynamic fracture) is intended to introduce the various test procedures employed to evaluate crack arrest toughness. The fact that there is no current, recognized standard to evaluate this property reflects to a great extent the controversy which existed and continues in the area of analysis of dynamic fracture and arrest. Recently, Irwin [1984] suggested that the development of test methods for crack arrest toughness and the study of fast fracture with the aid of dynamic analysis computations are mutually supportive topics with somewhat different goals. Crack arrest toughness evaluation emphasizes simplicity and minimum cost. This is seen to conflict directly with extensive dynamic computation which must derive crack arrest K values from the limited data provided by the simple laboratory test. Irwin concluded that the value of K at crack arrest can plausibly be estimated using small specimen tests without need for dynamic analysis computations.

Kanninen and Popelar [1985] have recently suggested that an accommodation exists between the two opposing crack arrest criteria (static and kinetic). This is based on the treatment of two complications admitted by the kinetic analysis, specifically,

inertia forces and reflected stress waves. The statically determined value,  $K_{Ia}$ , will be exactly equal to the minimum dynamic  $K$  for crack propagation ( $K_{Im}$ ) if there are no reflected stress waves. They also suggest that  $K_{Ia}$  is a legitimate fracture parameter provided that it is measured in a short crack jump arrest test before reflected waves can impinge on the crack tip. For larger crack jumps,  $K_{Ia}$  may still be useful because it provides a lower bound, conservative estimate of the true crack arrest toughness.

#### DEVELOPMENT OF A STANDARD CRACK ARREST TOUGHNESS TEST METHOD

As previously introduced, the first attempts to utilize fracture mechanics concepts to characterize crack arrest were accomplished by Nordell and Hall [1965] and Crosley and Ripling [1969]. By 1971, Crosley and Ripling suggested that a standardized test procedure was a realistic goal based on results with the tapered double cantilever beam measurements. These authors pursued the evaluation of crack arrest toughness in a variety of steels using procedures previously detailed [Crosley and Ripling; 1969, 1971].

In 1977, Crosley and Ripling presented a review of details of  $K_{Ia}$  testing using tapered DCB specimens which would contribute to the successful development of a test standard [1977a]. Stress intensity and load relationships for the tapered DCB specimen were presented, and a method for scaling different thickness specimens was suggested. The test procedure for measuring crack arrest involved loading fatigue precracked specimens in a conventional

tension test machine, and obtaining records of load versus displacement and load versus time. These test records define the equilibrium situation preceding rapid crack extension, and the equilibrium situation following the run-arrest segment, and critical loads associated with crack initiation and crack arrest. Crack arrest toughness,  $K_{Ia}$ , was based on static analysis and was defined as the value of the stress intensity factor determined a short time after a run-arrest segment of crack extension. This time interval was set on the order of 1 msec and was seen as the time for setting up a static condition. Specific size criteria were also proposed to obtain plane strain arrest toughness measurements.

Besides these details of the test procedure, Crosley and Ripling [1977a] reviewed general considerations related to crack arrest testing of metals. The suitability of conducting tests with specimens displaying a decreasing  $K$  field was recognized, and the requirements for a stiff loading system were developed. The use of face grooves was recommended to eliminate undue edge influences in the arrest process. An analysis of the change of specimen compliance with crack length for the tapered DCB, DCB and compact tension specimens was presented. For the compact specimen, it was determined that possible use of wedge loading was likely required because the ratio of  $K_{Ia}/K_q$  increased faster with crack length than with the DCB specimen geometry.

Simultaneous with the development of the  $K_{Ia}$  test procedure, and following the original work of Hahn and coworkers at Battelle Columbus Laboratories, a crack arrest measuring procedure for  $K_{Im}$ ,



$K_{ID}$ , and  $K_{Ia}$  properties was developed by Hoagland, et al. [1977]. This procedure employed dynamically stiff, wedge loading with the focus on the DCB specimen. In discussing specimen shape, Hoagland, et al. suggested that main factors for specimen choice included size of the crack jump which must be accommodated, and crack path stability. For the case of the stiff wedge loading, and a given volume of material, the rectangular DCB specimen accommodated the largest crack jump, the compact specimen was intermediate, and the single-edge-notch-bend was the least efficient. However, the tendency for the crack path to deviate was highest in the rectangular DCB, and deep side grooves were seen as a method to restrict both crack branching and crack path instabilities, increase the measurement capacity of the specimen, and inhibit shear lip formation. The specimen dimensions for cases of homogenous and duplex specimens with welded brittle crack starters were discussed. Because specimen size requirements are set by the yield strength of the starter section, the measurement capacity of the duplex specimen was shown to increase substantially over the homogenous specimen, or conversely, the minimum thickness was reduced. A minimum crack jump length of two-times the net thickness was recommended.

The method of loading was examined in light of the crack driving force at the onset of crack extension. For the case where the driving force originates entirely from elastic strain energy stored in the specimen, the crack velocity and propagation distance in the specimen were seen as related uniquely to  $K$  and

specimen geometry. When elastic energy is allowed to enter the specimen from the load train, both the driving force and crack extension distance are modified, and the effect would be an underestimation of the inherent crack resistance. For the DCB specimen, a tie-down device to reduce the strain energy in the loading pins was presented and discussed.

The analysis methods proposed by Hoagland, et al. [1977] employed reference curves of  $K_{ID}/K_Q$  versus crack extension and crack velocity to allow calculation of  $K_{ID}$  from measurements of crack jump after the test, and  $K_Q$  prior to initiation. These results were limited to the rectangular DCB specimen, but the approach was seen applicable to single-edge-notch and compact specimens with additional modelling. Utilizing these measurements of  $K_{ID}$ , it was proposed that any measurement of this property is equivalent to  $K_{Im}$ , where the crack jump distance is small. The static calculation for  $K_{Ia}$  was also included in this procedure, and seen as valid where the minimum of the  $K_{ID}$  versus crack velocity curve occurs at zero crack velocity. This was described as the small crack jump  $K_{Ia}$  approach. However, it was pointed up that this approach is inherently limited because of the difficulty in obtaining small crack jumps, inapplicability to duplex specimens, and the inapplicability of  $K_{Ia}$  corresponding to the cases of high crack velocity.

In 1977, Crosley and Rippling of Materials Research Laboratory (MRL) and Hoagland of Battelle Columbus Laboratories (BCL) proposed new tests for measuring crack arrest toughness which employed

split-pin wedge loading of compact specimen geometries [Hahn, et al. 1980a]. A task group of ASTM Committee E 24.01.07 undertook a multi-laboratory cooperative test program to acquaint potential users with the two test procedures, and assess reproducibility of measurements, and identify questions associated with the interpretation of data. The two test procedures were very similar in that they employed the compact specimen design common to plane strain fracture toughness testing as detailed in ASTM Method E 399. Both procedures called for loading the specimens by transverse wedge loading using a split pin arrangement. Both specimens employed measurement of crack length at arrest, and evaluation of displacement at the onset of fracture, and after arrest in the MRL method. The MRL specimen employed a 3mm (0.12-inch) diameter brittle weld bead at the crack starter slot, while the BCL specimen employed a massive, hardened AISI steel starter section electron beam welded to the test section. The MRL procedure called for measurement of crack mouth displacement and inference of load-line displacement, while the duplex BCL specimen employed direct load line displacement measurement. The MRL procedure used a static analysis for crack arrest, while the BCL procedure used a dynamic analysis to account for kinetic energy, but neglected damping prior to arrest. Hahn, et al. pointed that in principle, both analyses could be applied to either procedure [1980]. The cooperative test program called for the testing of 10 specimens by each participating laboratory. These included four weld-embrittled specimens of ASTM A 533 B steel, and two weld embrittled

specimens of AISI 1018 steel following the MRL procedure. Four duplex specimens of ASTM A 533 B steel were supplied for tests following the BCL procedure. Two tests of the ASTM A 533 B steel were to be performed following each procedure at 0°C (32°F) and room temperature. The 1018 steel specimens were provided for practice testing which were to be performed at room temperature. The test temperatures for the ASTM A 533 B steel were determined to be approximately 40 and 20°C (22 and 11°F) above RTNDT.

Partial results of the cooperative test program were reported by, Hahn, et al. [1980a] and Crosley and Rippling [1980a]. In gathering and analyzing the data, errors in each test procedure were detected, and extensive reanalysis of the test results was required. This was performed and reported by Crosley, et al. [1983]. The corrections to the procedures included the experimental compliance calibrations and modifications of the  $K$  versus load relationship for single-hole crack line loading of the compact specimen. Hence the 290 tests from 29 participating laboratories were completely re-analyzed, and the original results were deleted. It was also determined that test results from 1018 steel were satisfactory, and these were included in the analysis.

The report of the cooperative test program results included the derivation of experimentally based expressions for  $K_Q$ ,  $K_{Ia}$ , and  $K_{ID}$  for both the MRL and BCL specimens. The  $K_{ID}$  calculations employed expressions derived from the calibration curves for compact specimens which were developed by Gehlen, et al. [1979]. These calculations involved measurements of  $K_Q$  and crack jump

distance. The  $K_{Ia}$  and  $K_{ID}$  results for all test specimens, steels and temperatures were plotted against  $K_Q$ . It was recognized that  $K_Q$  in the duplex specimens is a reflection of the load required to produce crack extension in the 4340 steel starter section, and in the weld-embrittled specimen likely reflected the toughness of the weld or heat affected zone. Nevertheless, it was felt that  $K_Q$  was an appropriate independent variable with the higher values of  $K_Q$  resulting in more crack extension prior to arrest. It was theorized that an appropriate parameter should result in a constant value of arrest toughness, independent of  $K_Q$ .

For a given test condition including material and test temperature, Crosley, et al. [1983] found that the MRL and BCL specimens yielded similar  $K_{Ia}$  values, and that  $K_{ID}$  measured with the duplex BCL specimen was higher than  $K_{ID}$  measured with the MRL test. This was attributed to the fact that the BCL specimen results included initiations at higher  $K_Q$  values, hence higher crack velocities resulted.  $K_{Ia}$  showed no dependence on  $K_Q$ , while  $K_{ID}$  showed a distinct, systematic increase with  $K_Q$ . The results for ASTM A 533 B steel specimens tested at 0°C (32°F) illustrating these points are shown in Figure 7. The statistical analysis included calculations of mean values and standard deviations for arrest K values. These analyses showed that for  $K_{Ia}$ , the horizontal line fit is at least as good as the linear fit relating  $K_{Ia}$  to  $K_Q$ . The  $K_{ID}$  data were fitted much better by a straight line with a positive slope. It was also noted that at a given  $K_Q$  value, the scatter in  $K_{ID}$  was about half that in  $K_{Ia}$  measurements.

An analysis of potential scatter in  $K_{Ia}$  measurements was conducted. It was determined that laboratory-to-laboratory variations did not have a significant effect, and there was no evidence that extremes of crack jump length affected the results. Positions through the thickness of the ASTM A 533 B steel plate had no effect, and regions of high and low  $K_{Ia}$  were generally not clearly defined or localized. It was concluded that the observed scatter in  $K_{Ia}$  reflected inherent toughness variations in the material. Crosley, et al. [1983] further concluded that the  $K_{Ia}$  procedure yielded a better estimate of lower bound crack arrest toughness than  $K_{ID}$ . They recommended that methods of initiation of crack extension at a given K level be improved, and effects of size of the plastic zone be evaluated, and that proper size requirements for a valid crack arrest crack arrest toughness specimen be determined.

As both static and dynamic crack arrest test methodologies were being developed, the Oak Ridge National Laboratory was conducting a series of thermal shock experiments with large cylinders. Two of these experiments (TSE-4 and TSE-5) were focused on crack arrest, and included extensive laboratory evaluations of  $K_{Ia}$  and  $K_{ID}$ , in some cases following methods employed in the ASTM Cooperative Test Program. Hahn, et al. [1981] and Cheverton, et al. [1985] reported the details of these tests and their analysis. ASTM A 508 Cl 2 steel was used in the tests, and the initial flaws were shallow, sharp cracks extending the full length of the cylinder. The cylinder for experiment TSE-4 had an outside

diameter of 533mm (21-inches), wall thickness of 152mm (6-inches), and length of 914mm (36-inches). The cylinder for the TSE-5 experiment had an outside diameter of 991mm (39-inches), wall thickness of 152mm (6-inches) and length of 1220mm (48-inches). The steels were heat treated to provide high transition temperatures. Thermal shocks were achieved by heating the test cylinders uniformly, then rapidly cooling the inner surface. The TSE-4 experiment resulted in an initiation and arrest event where the crack grew 12mm (0.5-inch). Calculated arrest toughness measurements for the cylinder were compared with  $K$  measurements from DCB specimens, and it was shown that the  $K$  data deduced from the thermal shock experiment agreed very well with laboratory data. The TSE-5 experiment with a stronger thermal transient resulted in a series of three initiation and arrest events, with the second crack jump progressing through 43% of the wall thickness. The  $K_{Ia}$  values corresponding to these arrests were approximately equal to values produced using wedge-loaded compact specimens and  $K_{Ia}$  calculations. From these results, Hahn, et al. [1981] concluded that for steels which display  $K_{ID}$  curves which increase sharply with velocity (as expected for this steel), experimentally measured  $K_{Ia}$  values can be adequate for predicting the extent of crack propagation, and are most appropriate to small crack jumps in large structures.

Kalthoff [1983] and Beinert and Kalthoff [1984] designed a crack arrest specimen to minimize errors resulting from neglected dynamic effects. This "reduced dynamic effects" specimen contains

edges and boundaries which were shaped to defocus reflected waves and reduce wave reflections in the body of the test piece. Damping material and additional weights were attached to the arms of the specimen to absorb kinetic energy and increase the period of oscillations and thereby reduce the recovery of kinetic energy. Analysis of the RDE specimen showed that it resulted in substantially less dependence of arrest  $K$  on crack jump length when compared with the compact specimen. Beinert and Kalthoff concluded that this test concept combined the advantages of both the static and dynamic approaches in that dynamic effects are incorporated into specimen rather than in the analysis.

Rosenfield, et al. [1984] presented results of investigations of miniature compact specimens to assess the crack arrest toughness of reactor pressure vessel steels, and compare these results with thermal shock experiments. Compact specimens measuring 50mm by 50mm (2-inch by 2-inch), 100mm by 100mm (3.9-inch by 3.9-inch) and 150mm by 150mm (5.9-inch by 5.9-inch) were evaluated with thicknesses ranging from 50.9mm (2-inch) to 6.3mm (0.25-inch). Side grooves ranging from 25 to 40% in total depth were also employed. These results, when plotted within the scatter bands of two standard deviations of typical crack arrest data, showed that the thinnest specimens with the smallest face dimension were seen to lower the data trend, although the significance of this departure was not clear to the authors. A key observation of these tests was that ligation of the fracture surfaces decreased with decreasing specimen thickness.



In 1984, a task group of ASTM Committee E 24.01.06 initiated a testing round robin to evaluate a draft  $K_{Ia}$  test standard. The materials include ASTM A 514, A 588, and A 533 B steels. The test procedure is a modification of the BCL and MRL procedures used in the Cooperative Test Program. In this case the brittle weld notch starter is detailed, but the duplex specimen is allowed. Results of the program are not currently available, and formal adoption of a crack arrest test standard by the ASTM will not be completed until the results of this program are analyzed.

#### WIDE PLATE CRACK ARREST TESTING

Earlier, the investigations of Feeley, et al. [1954, 1955] which were directed to establishing the stress/temperature relationship for crack arrest using wide plate tests with wedge impact loading were discussed. Such testing persisted in the United States into the mid-1960's as evidenced by the work of Nordell and Hall [1965]. However, the focus of crack arrest testing and analysis in the United States shifted to the problem of arrest in nuclear pressure vessels, and test method development was focused on small-scale laboratory specimens, and the appropriate analysis approach. Wide plate crack arrest investigations were principally undertaken in Japan.

Yoshiki and Kanazawa modified the ESSO wide plate test specimen to include an initial part in which the crack is started by static tension so as to reach the body of the specimen which was separately loaded [1957]. This specimen configuration is shown in Figure 8, and was named the Double Tension Test. Again, the purpose of the test was to determine the various combinations

of tensile stress and temperature under which cracks propagated through the test piece or arrested. Yoshiki and Kanazawa theorized that once a brittle crack was initiated, it will propagate indefinitely at low temperature and high stresses because stored energy in the cracked plate decreases with increasing crack length. At higher temperatures, and lower stresses, a minimum in energy occurs for a definite crack length, and hence a critical stress and temperature may be defined for crack arrest. Yoshiki and Kanazawa evaluated a 12mm (0.5-inch) thick rimmed steel plate using the double tension test procedure over an extensive matrix of applied stress and test temperature, and showed a stress versus temperature curve defining the results which was similar to that of Robertson. Specifically, there was a low temperature region where arrest temperature and stress were dependent, and a critical temperature above which the arrest stress did not show temperature dependence.

Akita and Ikeda [1959] conducted ESSO tests of normalized and killed steels of various plate thicknesses. Crack velocity was measured by wire speed detectors, and dynamic stress was calculated by strain gage measurements. They determined that crack speed increases with decreasing temperature when the average stress and plate thickness are constant. The crack speed also increased with average stress, and with plate thickness. However, above 45mm (1.8-inches) in thickness, crack speed was seen to be invariant at a fixed stress level. They also showed that surface plastic energy decreased with decreasing temperature.

Akita and Ikeda [1962] developed a theoretical analysis of the ESSO test. They determined that the factors most affecting the brittleness of steels are the yield stress, the plastic surface energy, and the thickness of the plastic layer adjacent to the fracture surface. Akita and Ikeda subsequently conducted an extensive series of ESSO wide plate tests with temperature gradients to assess factors governing arrest of brittle fracture [1962]. They determined that the amount of impact energy used in crack initiation has an influence on crack propagation only within 100mm (3.9-inches) from the front edge of the specimen. Thus they assumed that crack velocity versus crack length curve in the ESSO test with a temperature gradient is the same as that for the Robertson test. ESSO tests of 400mm (15.7-inches) wide plates of three ship steels were conducted in the presence of a linear temperature gradient, and strain gages were used to measure crack velocity. The propagating cracks arrested in the higher temperature zone. As remote stress was increased, the observed crack velocities increased. The total thickness of shear lip increased with stress and crack length. To assess the role of shear lip formation in brittle crack propagation, these authors hardened the surface of plates along the intended crack path by hammer peening. They found that the crack speed and arresting temperature were higher, and the crack front straighter with the peened specimens in comparison to similar test conditions with standard specimens. Thus they concluded that plastic surface energy for shear lip formation is one of the most fundamental

factors governing brittle fracture. They estimated that plastic surface energy for shear lip formation is 100 times that for cleavage.

By the mid-1960's, Japanese investigators began to include fracture mechanics analysis into the wide plate (ESSO and Double Tension) tests of steels. Kanazawa and Machida [1967] reviewed studies of crack arrest studies in Japan and stated that the double tension test had emerged as the most standardized test for evaluating crack propagation characteristics of steels. Single edge notch tension solutions with back-wall corrections were employed for evaluating  $K$  for both types of wide plate tests. These results are typically plotted as  $\log K_a$  versus  $1/T$  as shown in Figure 9.

Kanazawa, et al. [1964a, 1964b] and Yoshiki, et al. [1965] conducted an investigation of conditions governing brittle crack arresters for welded steel structures beginning in 1964. Using the double-tension test, they analyzed the  $K$  values for two simple crack arrester models including single or double riveted holes, located near the crack propagation line, and a riveted seam. They determined that arrest will occur when the  $K$  value of a running crack falls below the critical  $K$  for arrest for the particular steel developed in normal double-tension tests. They saw the role of crack arresters of these configurations as providing a minimum in the  $K$  field of a running crack. Yoshiki, et al. (1965) extended this work to double tension test specimens with patch and riveted stiffener crack arresters. Again, experimental evidence of arrest

corresponded closely with the decrease of the  $K$  field below  $K_a$  measurements from previous double-tension tests of the subject steels.

Kanazawa, et al. [1967a,b] evaluated the arrest performance of stiffener type crack arresters. Calculation of  $K$  for various stiffener configurations were performed, and double-tension tests of plates containing stiffeners were conducted. These investigations also included methods of stiffener attachment. Kanazawa [1973] reviewed studies of brittle crack propagation in Japan. This included a discussion of ESSO tests with various weld joint geometries to assess the crack path in response to residual stresses. Analytical and experimental investigations of the effects of test machine rigidity were carried out with specimens of different aspect ratios and different test machines using the double-tension test. The arrest toughness values for specimens with larger aspect ratios were lower than those with smaller aspect ratios, as more elastic energy participated in the run-arrest process. When the results were corrected by accounting for the effects of aspect ratio and test machine compliance, the scatter was considerably reduced.

Kanazawa [1973] reviewed the basic concept of crack arrest and discussed the strong influence that formation of shear lips had in the arrest of brittle cracks. Studies of crack arresters for complicated steel structures (some of which were discussed earlier) were reviewed. The analytical and experimental studies of various arrester geometries were discussed. Tests related to welded ship

crack arrester plates were detailed. From this work it was concluded that a crack would be arrested if the stress intensity factor falls below the toughness value for propagation arrest obtained from such tests as the double-tension or ESSO test. This was based on the consideration that the dynamic aspects of the stress intensity factor can be neglected in so far as the crack length is relatively small, and that crack speed is below a critical velocity just prior to arrest. It was stated that the static arrest concept would only be valid for running cracks shorter than 200-300mm (7.9-11.8-inches).

In light of this conclusion, results of a series of ESSO and double-tension tests of plates with widths ranging from 500 to 2400mm (19.7 to 94.5inches) were reviewed [Kanazawa, et al. 1977; Kanazawa, 1983]. The arrest K values obtained from wide plate specimens in which the length of the crack was approximately 1200 to 1800mm (47.2 to 70.9-inches) were significantly larger than those obtained with standard double tension test specimens. Correction of this data in terms of "effective crack length" and "effective stress intensity" were reviewed, and speculation about the significance of such parameters was discussed.

In 1983, Kanazawa, et al. again reviewed studies of brittle crack propagation and arrest conducted in Japan. This paper focused on the dynamic analysis formulated to address crack arrest [Kanazawa, et al. 1983]. A mass-spring model of crack advance was introduced, and an expression for  $K_D$  was formulated. Additionally, a modification of the static approach was introduced

for solution of stationary crack propagation in an infinite plate. A simplified expression for  $K_D$  was introduced, and a series of tests of duplex double-tension specimens was conducted and analyzed. Characteristic  $K_D$  versus crack velocity curves were produced for the steels tested, and scenarios for crack arrest and complete fracture of specimens were correlated with observation.

Nakano and Tanaka [1982] conducted an investigation of crack arrest in three steels using compact, ESSO, and DCB tests. The results of these tests showed that static arrest toughness from compact and ESSO test specimens were similar over the temperature range tested. It was also shown that the relation between  $K_{ID}/K_{Ia}$  and  $K_{ID}/K_{IQ}$  could be represented by a single curve. The  $K_{ID}/K_{Ia}$  value approached unity as  $K_{ID}/K_{IQ}$  did. This is expected since this limits the analyses to the case of short crack jumps and lower crack velocities.

## MICROMECHANISMS OF CLEAVAGE, DUCTILE FRACTURE AND CRACK ARREST CLEAVAGE FRACTURE

### CLEAVAGE FRACTURE

The first theories for micromechanisms of cleavage fracture centered on the role of dislocations in the nucleation of micro-cracks. Zener [1948] proposed a model where crack initiation occurred at the heads of slip bands stopped by grain boundaries or hard precipitate particles. He suggested that a slip band consists of a linear array of dislocations, the density of which is greatest at the ends of the bands where obstacles prevent further dislocation movement. As stress is increased, the dislocation concentration increases with coalescence of crack nuclei occurring. A crack thus formed was postulated to extend throughout the region of high stress concentration then stop, unless its length was above the critical value for crack propagation. Zener pointed up that the fracture history of a crack may depend on the hydrostatic component of the stress system.

Petch [1953] studied the tensile fracture of unnotched specimens of mild steel (0.155% C), ingot iron (0.036% C) and spectrographic iron (0.07%C). Tests were performed at liquid nitrogen temperature, and the variation of cleavage strength as a function of ferrite grain size was evaluated. Results for all materials showed a linear dependence of cleavage strength on the inverse square root of the ferrite grain size ( $d^{-1/2}$ ). Petch postulated that this grain size dependence could be explained by identifying Griffith cracks with glide planes in which dislocation movement has been held up by blockage at a grain boundary. The resulting



very high tensile stress at the head of such an array could attain the level of the theoretical cleavage strength, and fracture then initiated from these sites. An expression was developed which provided a  $d^{-1/2}$  dependence of theoretical cleavage strength, and which keyed the cleavage strength in ferrite to the fracture of one grain under the influence of dislocations in another grain. Petch observed and predicted that theoretical cleavage strength was independent of carbon content. He concluded that the cleavage strength of ferritic polycrystal is controlled by the theoretical cleavage strength in the vicinity of the grain boundaries, and by the grain size which determines the magnitude of the grain boundary stress concentration due to dislocations. He recognized potential effects of chemical composition in the vicinity of grain boundaries related to the separation of yield and cleavage strength and strain hardening changes, and he limited the model to situations where precipitates did not interact and become the controlling stress concentration.

Stroh [1954, 1955, 1957], following the work of Zener, postulated that a crack could be formed by an array of dislocations piled up at a grain boundary. Near the pile-up, the stresses were seen to be large, and fracture would be expected in a polycrystalline material on grains which are oriented favorably in response to these stresses. Stroh [1954] concluded that a crack should form when the group consisted of approximately 1000 dislocations piled up under a stress of the magnitude occurring in a cold-worked metal. He further suggested that the formation of

microcracks was the controlling factor in the cleavage process.

Mott [1956] developed a theoretical analysis which showed that an active slip plane containing dislocations behaves like a freely slipping crack which will serve to raise the stress in a polycrystal. He discounted the role of Griffith cracks in cleavage fracture initiation, and modeled the slip initiation process. Brittle fracture was postulated in cases where a slip line crosses a grain, if the crack which initiates is not blunted by plastic flow, and the tensile stress is great enough to make it spread. The conditions for crack initiation included the existence of barriers to stop spreading of slip lines and allow for the building of high tensile stress, and the spread of the crack formed at the end of the slip line. Mott suggested that when dislocation sources are locked, cleavage cracks cannot spread, and he suggested that carbon, nitrogen and hydrogen can serve this locking function, even in very pure polycrystalline materials.

Cottrell [1958] critically examined the conclusions of Stroh [1957] that the tensile stress necessary to nucleate a crack at the tip of a slip band is more than sufficient to propagate that crack. Cottrell argued that results of tests with various thickness specimens indicated that hydrostatic tension plays a part in increasing the apparent brittleness of metals. He therefore concluded that the growth of a crack nucleus is the more difficult step in the fracture process (compared to crack nucleation), and that at the critical stage in the fracture process, a crack must

already be present in order for hydrostatic stress to exert an influence. Cottrell [1958] postulated a mechanism for cleavage crack formation in which the crack is formed at the intersection of slip bands in two  $[110]$  planes with two burgers vectors of the form  $a/2 [111]$  coalescing to form a new dislocation. An accumulation of such dislocations at the intersection point served to open a cleavage crack. A requirement of this model was that two intersecting slip bands were required, but it did not require the presence of a grain boundary.

Biggs and Pratt [1958] determined the stresses for slip, twinning and cleavage of single crystals of alpha-iron through tensile tests conducted at  $-183^{\circ}\text{C}$  ( $-297^{\circ}\text{F}$ ). Single crystals were produced by the strain-anneal method in 2mm ARMCO iron wire. The wires were initially decarburized, and after production of single crystals, re-carburized to obtain carbon contents in the range 0.003 to 0.007%. A limited number of crystals were prestrained at room temperature in order to suppress twinning at the test temperature, and allow determination of yield stress for slip at the reduced test temperature. Such prestraining eliminated brittle fracture at the low test temperature. The annealed single crystals with orientations away from the  $(011)-(111)$  line deformed mainly by mechanical twinning, and failed by cleavage after a small amount of plastic deformation. Crystals oriented near the  $(011)-(111)$  line formed only a few twins in the early stages of deformation, and then deformed in a ductile manner, with fracture occurring by slipping off after deformation. Examination of the

cleavage fracture surfaces showed a well defined rectangular block structure produced by twinning in the (001) cleavage plane. Existence of many nucleation sites and apparently discontinuous fracture was noted. Biggs and Pratt concluded that twin boundaries act as the necessary boundaries to describe fracture according to dislocation theory. Once initiated, a cleavage crack was seen to cause repeated twinning ahead of itself, but such twinning was unable to stop crack advance. Elimination of twinning was seen as a way to eliminate brittle fracture.

Hull [1960] evaluated thin sheet single crystals of 3% silicon iron which were strained in tension at  $-196^{\circ}\text{C}$  ( $-321^{\circ}\text{F}$ ) in the [010] crystallographic direction in order to evaluate the effects of twinning. He found that all but two of the 20 cleavage cracks in the crystals examined originated at the intersection of twins. Hull proposed that there are two factors affecting the formation and propagation of a cleavage crack, including the shear stress operating in the twins to produce the crack, and the direct tensile stress across the crack embryo. He concluded that the controlling factor governing brittle fracture depends on whether the resolved shear stress to produce a crack from a twin intersection is greater than the tensile stress to propagate the newly formed crack.

Allen, et al. [1953] evaluated the tensile and impact properties of low carbon content iron-carbon and iron-carbon-manganese alloys. High purity alloys of iron with carbon ranging from 0.0025% to 0.177%, and C-Mn alloys where the carbon content was

in the range 0.03% to 0.05%, and manganese ranged from 0.46 to 2.00% were produced. Heat treatments consisting of furnace cooling, air cooling and water quenching from 950°C and 700°C (1742 and 1292°F) were carried out. Tensile tests were conducted at room temperature and at -196°C (-321°F). Charpy impact tests employing an Izod notch were conducted over a broad temperature range. A key result from this work was the close connection between impact transition temperature and the appearance of carbides in the microstructure. Specifically, when the formation of carbides was suppressed either due to reduced carbon content, or by a change in cooling rate, transition temperature was reduced. Where carbides were observed to form such as in ferrite/pearlite constituent, or as grain boundary carbides, the transition temperature increased with increasing carbon content. Careful microscopic examination showed that existence of cracks had occurred in some of the carbide films situated in grain boundaries or enveloping pearlitic areas. It was also noted that cracking of the carbides was more extensive in regions of the Charpy specimen which deformed substantially. This led to the postulation that deformation of the ferrite was possibly necessary to cause cracking of the carbide. These authors also proposed that cracks produced in the carbides resulted in the development of high triaxial stresses in the immediate neighborhood which would be effective in promoting cleavage.

Low [1954] discussed the application of the Griffith criterion to the case of cleavage of polycrystalline metals. The Griffith

criterion relates to a critical stress for complete fracture for the case of homogeneous, isotropic solids such as glass. The critical stress is as follows:

$$\sigma_c = \left[ \frac{2 E T}{\pi C} \right]^{1/2} \quad (2)$$

where E= Young's Modulus

T= Surface tension of solid

C= Half-width of any flaws present.

Difficulty in applying this criterion to metal polycrystals was attributed to the fact that energy terms for crack propagation must include surface energy of new surfaces created, plus a large amount of energy to accomplish the local plastic deformation which occurs in unfavorably oriented grains. Low showed several examples where microcracks were produced well prior to fracture in thin sheets of a low carbon rimmed steel tested in bending. The Orowan modification of the Griffith expression was introduced which included an energy term for the plastic deformation involved in fracture, and he suggested that this term far outweighs the surface energy term. Low suggested that the distance term in the modified Griffith expression might be equal to or proportional to grain size, and an inverse square root dependence of fracture stress on grain diameter is expected. Results of tensile tests of a low carbon rimmed steel tested at  $-195^{\circ}\text{C}$  ( $-319^{\circ}\text{F}$ ) were obtained using various grain sizes produced by straining and annealing the specimens. Below a certain grain size ( $d=0.16 \text{ mm}$ ), the Griffith-Orowan equation was satisfied in that

$$\sigma_c = \text{constant} \times d^{-1/2}$$

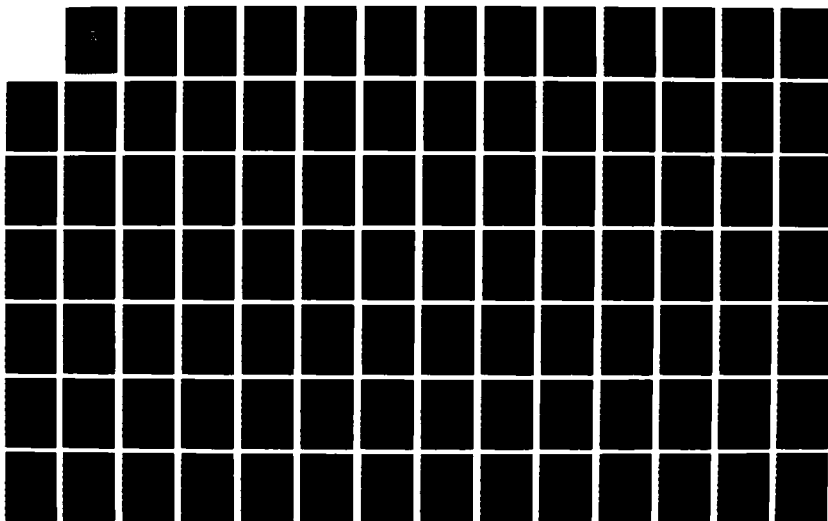
AD-A181 324

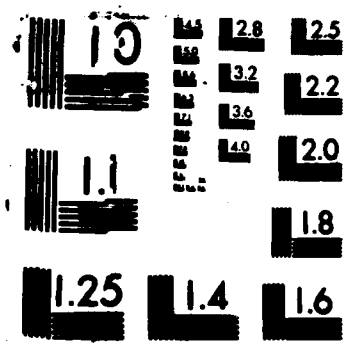
MICROMECHANISMS OF FRACTURE AND CRACK ARREST IN TWO  
HIGH STRENGTH STEELS(U) DAVID W TAYLOR NAVAL SHIP  
RESEARCH AND DEVELOPMENT CENTER ANN J P GUDAS FEB 87  
DTNSRDC/SME-87-20 F/G 11/6 1

2/4

UNCLASSIFIED

NL







Low interpreted these results with a two-step model of the cleavage process. The first step involves the formation of microcracks after some slip occurs, that is, above the yield stress. The propagation of these microcracks depends on their size and applied stress at the time they form. This model was the first which applied a crack growth criterion to the cleavage fracture process, rather than the crack initiation criterion suggested by previous dislocation models. Owen, et al. [1958] investigated the brittle fracture of a clamped steel subjected to wide variety of heat treatments. Tensile tests at  $-196^{\circ}\text{C}$  ( $-321^{\circ}\text{F}$ ) were carried with polished strip specimens on which light scribe marks were placed. Tests were carried out at various crosshead rates. Examination of the polished surfaces indicated that each specimen fracture was located within a Luders band, even for the fastest crosshead speed. Microcracks were observed in the Luders' bands of all specimens, and they usually transversed only one or two ferrite grains. However, there were instances where an assembly of microcracks across five or more grain occurred where the microcracks were joined by severe deformation. Owen, et al. could not determine the origin of the microcracks. They did not find any smaller than one grain diameter. They observed evidence of numerous markings indicating slip at variance with the predominant slip orientation producing exceptional slip line height. Their conclusions, which were limited to this steel, indicated that fracture occurred by a two-step process first involving the formation of grain diameter microcracks. These

cracks were seen to spread subsequently across a number of grains incorporating severe deformation, and finally an assembly of cracks was seen to reach a critical size and propagated rapidly to failure. They also concluded that fracture is always preceded by gross yielding. Finally, Owen, et al. suggested that their results were compatible with the critical Griffith-Orowan crack growth criterion previously suggested by Low [1954].

McMahon and Cohen [1965a] conducted an investigation of the origin of cleavage cracking in two polycrystalline irons which differed primarily in the amount of carbide precipitate they contained. The approach included tensile tests conducted from room temperature to  $-195^{\circ}\text{C}$  ( $-319^{\circ}\text{F}$ ) in which the sides of the flat specimens were electropolished. Observations of the numbers of microcracks on each face were made after test, and in some cases, plastic film replicas were used during interrupted loading to trace the microcracking sequence throughout tensile deformation. Metallographic examination of specimens was conducted with sequential grinding to establish the origins of microcracks. The materials tested included 0.035% and 0.007% carbon ferrites which were austenitized and furnace cooled to produce coarse-grained structures. The higher carbon material contained discontinuous films of iron carbide along the grain boundaries, plus patches of pearlite and well distributed carbide particles. The lower carbon ferrite contained carbides which were located only at the grain boundaries, and were finer and more widely dispersed than in the higher carbon containing alloy.

The results of the tensile tests of McMahon and Cohen as temperature was lowered showed the onset of mechanical twinning and the coincident elimination of discontinuous yielding. From a fracture standpoint, the ductility transition temperature of the higher carbon ferrite was approximately 70°C (126°F) above that of the other alloy. Microcracks were observed and counted, and they tended to lie normal to the tensile axis. For each alloy, the number of observed microcracks over the gage length went through a maximum as temperature was lowered. The carbide particles in both materials were severely fragmented, even in specimens tested at room temperature. The carbide cracks often acted as a source of cleavage microcracking in the ferrite. The interrupted loading replication experiments showed that most microcracks formed during the strain hardening portion of the stress-strain curve, and new microcracks continued to form up to the point of fracture. McMahon and Cohen found that microcrack formation was not necessarily connected with discontinuous yielding. Their three-dimensional metallographic examination showed that over 90% of the observed surface microcracks originated in cracked carbides. Microcrack propagation was most often arrested by preexisting twins or grain boundaries.

McMahon and Cohen [1965a] postulated that the formation of a cleavage microcrack in ferrite involves first the cracking of a carbide following some plastic deformation of the surrounding ferrite, and propagation across the carbide as a Griffith crack. When the crack arrives at the cementite-ferrite interface, two

possibilities occur. A Griffith type crack will occur if the ferrite cannot respond plastically to the stress concentration at the tip of the carbide crack. The crack will enter the ferrite and propagate until it encounters barriers strong enough to stop it, or until sufficient slip or twinning occurs. If on the other hand, the ferrite yields locally, a microcrack will not form in the ferrite. McMahon and Cohen concluded that a dislocation initiation mechanism in the ferrite did not have to be postulated to account for cleavage, and they also concluded that twin intersections were of no consequence in initiating microcracks in polycrystalline ferrite. They also suggested that the initiation of cleavage is a statistical event as evidenced by the very large number of carbide microcracks and relatively small number of cleavage microcracks.

In an extended discussion of their examination of microcrack formation in polycrystalline iron, McMahon and Cohen [1965b] suggested that the probability of cleavage fracture could be considered as the product of the separate probabilities of crack initiation and propagation. They concluded that crack sources from built-in distributions of brittle particles such as carbides or inclusions require lower applied stresses than do sources arising from plastic deformation such as twins or slip-band intersections. Once initiation takes place, the question of fracture was seen as one of propagation, and the various surface energy terms in the Griffith equation were discussed. The barriers to microcleavage propagation in polycrystalline

materials in order of decreasing effectiveness included grain boundaries, preexisting mechanical twins, and initiation of slip bands or twins at the tip of an advancing crack. Orientation distribution of grains was also seen as affecting the probability of easy cleavage path existence.

Smith [1966] examined the nucleation and growth of cleavage microcracks in mild steel and addressed the critical event in the fracture process. He concluded after examining available data that growth of cleavage cracks across a grain boundary is frequently the critical event in the fracture process. Smith cited three deficiencies in the Cottrell-Petch models for dislocation based calculations of stress required to spread a crack across a grain, including lack of a mechanism for increase in effective surface energy with crack growth, lack of consideration of gradual formation of wedge crack due to dislocation coalescence, and lack of accounting for effects of microstructure on the cracking mechanism. Smith [1966] then developed a model based on the initiation of failure within second phase particles, and the difficulty in crack growth of a precipitate-size crack into the ferrite matrix which is associated with a value of effective surface energy greater than that required for a crack to traverse a precipitate. This model included the dislocation pileup contribution to the stress field required for crack nucleation, and assumed a plastic work term to propagate a crack into the ferrite matrix which is significantly higher than the plastic work term for cleavage

crack initiation in a hard particle. By examining the change in energy with crack length, Smith calculated the cleavage fracture stress as follows:

$$\left(\frac{C_0}{d}\right) \sigma_f^2 + \left[ \tau_e^2 \left( 1 + \frac{4}{\pi} \left(\frac{C_0}{d}\right)^{1/2} \frac{\tau_l}{\tau_e} \right)^2 \right] \geq \frac{4E\gamma_p}{\pi(1-\nu^2)d} \quad (4)$$

where:  $C_0$  = the thickness of the grain boundary carbide;

$\sigma_f$  = the tensile stress required to propagate the nucleus;

$\tau_l$  = lattice friction stress;

$\tau_e$  = the effective shear stress;

$d$  = the average grain diameter;

$\gamma_p$  = the effective surface energy of ferrite.

This relation shows a predicted dependence between fracture stress and grain size which was subsequently examined by Curry and Knott [1978]. They substituted the Hall-Petch relationship for the effective shear stress term, and modified this expression as follows:

$$\sigma_f^2 + \left(\frac{k_y S}{C_0}\right)^2 \left[ 1 + \frac{4}{\pi} \sqrt{C_0} \frac{\tau_l}{k_y} \right]^2 \geq \frac{4E\gamma_p}{\pi(1-\nu^2)C_0} \quad (5)$$

where  $k_y$  is the slope of the Hall-Petch yield relationship in shear. This predicted a microstructural dependence only on carbide width. Curry and Knott examined data from the literature and showed that the critical fracture stress was dependent on ferrite grain size in an apparent conflict with the Smith theory. By again examining the literature, these authors showed that there was a relationship between the ferrite grain size and the largest observed grain boundary carbide in mild steels where

a decrease in grain size was followed by a decrease in carbide diameter. This ratio of carbide thickness to grain diameter was also seen to decrease with increasing ferrite grain size. Using this relationship, and taking the value of effective surface energy in Equation 5 to be  $14 \text{ J/m}^2$  provided the best fit of previously published data relating cleavage fracture stress to the inverse square root of the ferrite grain size. This value of the effective surface energy was noted to be seven times higher than the true surface energy of iron.

Knott [1978] explored the basis for this difference in effective surface energy required to correlate results and that of the elastic work of fracture of iron. He developed a model addressing crack tip bond separation in a two-dimensional linear chain of atoms. Knott examined the model of fracture due to crack tip bond separation versus displacement controlled fracture criteria. He concluded that in bcc iron, the difference between yield and fracture was such as to require crack tip dislocation movement before attainment of critical crack opening displacement of each successive crack tip bond. He estimated that this energy was provided by a five-fold increase in the effective surface energy term, and thus agreed with observation.

Knott [1966] examined the deformation and fracture of notched and smooth specimens of two C-Mn steels to explain the differences obtained in the transition temperature region, where in the smooth bar tests the fracture is ductile, but brittle behavior is observed in the notched tests. Specifically, he examined the postulate

attributed to Cottrell that brittle fracture is produced at a critical tensile stress which is not very dependent on temperature. This theory predicts that there is a temperature regime where the critical fracture stress is below the general yield stress for a notched bar, and brittle fracture occurs when this stress is exceeded. Knott produced notched bars of a 0.20% and 0.06% carbon steels and conducted four-point bend tests over a temperature range from 25°C to -160°C (77 to -256°F). Experiments were performed with notches where the included angle was varied from 45° to 105°. The key result of these experiments was the determination of the temperature for each notch geometry where fracture occurred at general yield. Calculated values of the maximum tensile stress beneath each notch geometry at the temperature where fracture was coincident with general yield (from slip-line field theory) were plotted versus temperature. These stress values were identified as experimental values of the critical stress criterion, and were shown to be only slightly temperature dependent. Knott [1966] concluded that this result supported a critical tensile stress criterion for cleavage fracture, provided that yield has first occurred.

Smith [1968] reviewed experimental evidence pertaining to the cleavage process in mild steel, and concentrated on the role of second phase particles. He concluded that plastic deformation always precedes fracture, and that cleavage crack formation is directly associated with the inhomogeneous nature of plastic flow. Smith concentrated on defining the critical event in the



fracture process, specifically addressing nucleation versus growth processes. After reviewing the evidence in the literature, he concluded that the critical event was cleavage crack growth, and further, that the critical stage in the growth process occurs when the crack length is very small when compared to grain size. In formulating a physical model for the cleavage process, Smith [1968] suggested that any such model should take into account the inhomogeneous plastic deformation responsible for the nucleation of cleavage cracks, the criticality of the crack growth event, and the effect which hard particles have on the cleavage phenomenon. He proposed a model which included first the nucleation of a cleavage crack within a grain boundary particle in response to inhomogeneous deformation in a ferrite grain due to slip or a twin band. The particle is completely cracked because of its inherent inability to deform plastically. The surrounding ferrite is then presented with a crack of length equal to the particle thickness, and complete fracture was predicted by cleavage if the applied stress and stress due to dislocations from deformation processes are sufficient. Smith explained that his model did not imply that the cleavage cracks will never form unless particles are present, but rather that the particles provide a means by which a crack can spread a sufficient distance such that the applied stress can act on it.

Groom and Knott [1975] examined changes in the local fracture stress ahead of a notch as a function of prestrain in a mild steel. A 0.7% C steel was austenitized and air-cooled to produce uni-

form grain size where the largest portion of the grain boundary carbides were  $3\mu\text{m}$  or less in thickness. Uniform prestrains varying from 2.5% to 75% were introduced under conditions of direct compression, and test pieces were produced under conditions where the temperature after prestrain did not rise above  $-40^{\circ}\text{C}$  ( $-40^{\circ}\text{F}$ ), or after an aging treatment at  $230^{\circ}\text{C}$  ( $446^{\circ}\text{F}$ ). Notched test pieces for four-point bending were produced containing several V-notch depths and included angles. Yield stress in the strained and aged material was determined from fractured halves of the notched bars, whereas tensile yield stress from the unaged steel was determined from square test pieces containing prestrain introduced by lateral compression. The values of the critical tensile stress were measured as function of prestrain, and these led to the calculation of effective surface energy for propagation of a crack either in the matrix using the Cottrell [1958] model, or from the carbide using the Smith model [1966]. Results for the unaged and aged materials showed that the local fracture stress increased with prestrain, and fracture was more difficult. Metallographic examination of specimens tested at temperatures where fracture coincided with general yield showed no apparent effect of prestrain on the number of micro-cracks observed, and prestrain greater than 2.5% effectively inhibited twinning at the lower test temperature. A high incidence of single grain microcracks was observed near the fracture surface of all specimens. Curved fracture facets were also observed, but it was concluded that these were the result of ductile

deformation after passage of the main crack. To attempt to explain the increase in effective surface energy with prestrain, Groom and Knott suggested that propagation of a crack occurs when a critical displacement is attained at its end. In prestrained material, the applied fracture stress would be increased because of flow-stress elevation would result in higher applied stress to achieve the critical displacement. Despite the post fracture metallographic evidence, it was concluded that the propagation of a nucleus from a grain boundary carbide was the critical event in the fracture process.

Ritchie, et al. [1973] developed a correlation of the critical value of the tensile stress for unstable cleavage related to the attainment of maximum principal stress over a critical characteristic distance ahead of the crack tip. This model was used to predict the variation of  $K_{IC}$  with temperature for a high nitrogen steel under plane stress conditions where cleavage fracture occurred. The basis for this model was the Orowan critical stress concept for cleavage fracture. The key feature suggested by Ritchie, et al. was the introduction of a size scale over which the critical stress fracture criterion must be met.

The fracture toughness of a high nitrogen mild steel (0.07% C) supplied in the form of 24 mm (0.94-inch) square hot-rolled bar was evaluated using 20 mm (0.79-inch) square single edge notch fatigue precracked bars over a temperature range of -150 to +150°C (-238 to 302°F). Tensile properties from smooth specimens were also evaluated over the same temperature range. At tempera-

tures less than  $-95^{\circ}\text{C}$  ( $-139^{\circ}\text{F}$ ), fracture in the bend bars occurred prior to general yield by slip-induced cleavage leading to immediate catastrophic failure. At temperatures above  $-95^{\circ}\text{C}$  ( $-139^{\circ}\text{F}$ ), crack initiation occurred after general yield, and above  $-60^{\circ}\text{C}$  ( $-76^{\circ}\text{F}$ ), was described as occurring in a non-catastrophic cleavage mode. Fracture occurred by microvoid coalescence above  $+90^{\circ}\text{C}$  ( $194^{\circ}\text{F}$ ). The value of the critical stress where fracture was coincident with general yield was calculated from slip line field theory and shown to be similar to previously reported values for the same steel with a slightly larger grain size. Calculations of  $K_{IC}$  were carried out from tests over the temperature range  $-150$  to  $-75^{\circ}\text{C}$  ( $-238$  to  $-103^{\circ}\text{F}$ ). Linear elastic fracture mechanics validity criteria were met at temperatures below  $-115^{\circ}\text{C}$  ( $-175^{\circ}\text{F}$ ), and above this temperature, a plastic zone correction was employed.

The model for temperature dependence of  $K_{IC}$  was based on the postulated requirement that the maximum principal stress at the crack tip equals or exceeds the critical tensile stress criterion over a microstructurally significant size scale. Stress distributions ahead of the crack tip for the case of small scale yielding for hardening and non-hardening materials were evaluated. Ritchie, et al. felt that it was necessary to supplement the critical stress criterion because this value could be exceeded very close to the crack tip even by small applied loads. Hence they supposed that the critical stress must be attained at some fixed distance ahead of a crack tip. Further, Ritchie, et al. postulated that insufficient stress would be generated across the second grain if

the critical stress is achieved only at the first grain boundary, hence they suggested that a characteristic distance greater than one grain diameter is likely.

Calculations of  $K_{Ic}$  employing the critical stress value from these experiments and the flow stress at specific temperatures using a power-hardening solution were carried out. The predicted values of fracture toughness represented the value of  $K$  at which the critical stress was achieved at arbitrary distances ahead of the crack tip of 60 $\mu$ m and 120 $\mu$ m respectively for temperatures of -150 and -75°C (-238 and -103°F). For a characteristic distance of two grain diameters, agreement was very close to the experimentally determined values of  $K_{Ic}$ . Thus, Ritchie, et al. [1973] concluded that unstable cleavage failure in a coarse grained mild steel is governed by attainment of a critical stress over a distance of two grain diameters.

Curry and Knott [1976] studied the microstructural significance of the characteristic distance concept by evaluating the critical tensile stress and fracture toughness variation with grain size in a mild steel. A high nitrogen, 0.10% carbon mild steel was produced in a hot forged condition, and then heat treated at various austenitization temperatures and quench/cooling rates to vary the ferrite grain size. The resultant ferrite grain size ranged from 12 to 85 $\mu$ m, and cementite was present in all samples as both grain boundary films, and pearlitic regions. Three-point bend fracture toughness specimens were produced, and tests were carried out at -120°C (-184°F), where 100% cleavage fracture

occurred without shear-lip formation. The fracture stresses were determined by deforming notched specimens in four-point bending at  $-120^{\circ}\text{C}$  ( $-184^{\circ}\text{F}$ ), and uniaxial tensile properties were also determined at this temperature.

Curry and Knott found that the tensile properties and cleavage fracture stress varied linearly with the reciprocal square root of the ferrite grain size. To determine the characteristic distance, a stress analysis developed by Tracey was employed to calculate the stress intensification ahead of the crack tip. The characteristic distance following the Ritchie-Knott-Rice [1973] model was the distance over which the stress intensification ahead of the crack exceeded the ratio of the cleavage fracture stress to the uniaxial yield stress. At large grain diameters, the characteristic distance increased with grain size, but remained constant at small grain diameters less than  $40\text{ }\mu\text{m}$ . Curry and Knott [1976] explained this result in terms of particle size associated with cleavage crack initiation. Their premise was that the cracked carbides provide incipient microcracks which propagate under the influence of local stress due to dislocation pileup and applied stress following the Smith model [1966]. They suggested that cleavage fracture is likely to be initiated by the largest carbide particle found in the crack tip region subject to tensile stress elevation. Because tensile stress varies rapidly at a fatigue crack tip, the actual site for initiation is likely determined by competition between thinner carbides in a small region of higher stress and less numerous thicker carbides in a

larger region of lower critical stress. They concluded that because of the distribution of carbide sizes, it was difficult to place simple physical significance on the characteristic distance. Further, Curry and Knott suggested that a-priori calculation of fracture toughness from known values of cleavage fracture stress and yield stress is possible only with a detailed knowledge of the frequency distribution of carbide particle thickness.

Rawal and Gurland [1977] evaluated the Ritchie-Knott-Rice [1973] criterion using a number of spherodized carbon steels tested at low temperatures. Fatigue precracked circumferentially notched round bars were tested at temperatures ranging from  $-196$  to  $-110^{\circ}\text{C}$  ( $-320$  to  $-166^{\circ}\text{F}$ ). Metallographic examination showed that the preferential location of cleavage crack concentration and propagation was the cementite particles. Application of the Ritchie, et al. [1973] model was carried out where  $\sigma_0$  was taken to be equal to the yield stress, the strain hardening exponent was taken to be equal to 0.2, and effective surface energy was taken as  $14 \text{ J/m}^2$ . They found that this model worked well for predicting  $K_{Ic}$  in specimens fractured at temperatures up to  $-150^{\circ}\text{C}$  ( $-238^{\circ}\text{F}$ ) where cleavage crack propagation was observed near the fatigue crack tip. They found an average critical distance of 1.3 grain diameters in these steels.

Curry and Knott [1978] undertook the study of several spherodized steels to assess the dependence of the fracture stress on carbide diameter and demonstrate that a Griffith-type relationship was followed. Three plain carbon steels containing 0.3, 0.7, and

1.15% C respectively were spherodized by a three stage heat treatment, and a 0.9% C tool steel was oil-quenched and subjected to various tempering treatments. Single-edge notch specimens measuring 12.7 mm (0.5-inch) square were tested in four-point bending at  $-143^{\circ}\text{C}$  ( $-202^{\circ}\text{F}$ ) and compression specimens were tested at this temperature as well. Carbide particle radius distributions were determined from quantitative metallographic measurements. Calculated values of the critical fracture stress were plotted against the reciprocal square root of the 90th and 95th percentile carbide radii, and in turn compared to the Griffith criterion for through-thickness and penny-shaped defects. Curry and Knott concluded that the 95th percentile carbide value is a reasonable estimate of the crack nucleus size, and that the nucleus should be treated as being penny-shaped in these spherodized steels.

Ritchie, et al. [1979] investigated the feasibility of applying the Ritchie-Knott-Rice [1973] model to predict the variation of lower shelf static and dynamic fracture toughness of SA 533B-1 and SA 302 B ferritic steels. The microstructure of these steels was primarily acicular tempered upper bainite with a small volume fraction of proeutectoid ferrite. Plane strain fracture toughness data for these steels were obtained from the EPRI data bank, and various Heavy Section Steel Technology Program reports. Critical fracture stress values for cleavage were determined from slow bend and impact four-point bend tests on 45-degree V-notched bars at  $-73$ ,  $-129$  and  $-193^{\circ}\text{C}$  ( $-99$ ,  $-200$ ,  $-315^{\circ}\text{F}$ ). At these temperatures, fracture occurred catastrophically by cleavage



prior to general yield. The nominal bending stress and critical values of maximum principal stress at the crack tip were computed. Fractographic examination showed that cleavage facets in both steels were of the order of the prior austenitic grain size rather than the bainitic packet size. Hence, characteristic distances were chosen between two and four times the prior austenitic grain size. The temperature dependence of the static fracture toughness was calculated for these characteristic distances based on calculated temperature dependence of yield strength, the measured critical cleavage stress which was assumed to be temperature independent, an assumed work hardening exponent, and the assumption of plane strain crack tip stresses. It was shown that the Ritchie, et al. [1973] model provided a very good description of lower shelf fracture toughness behavior for temperatures up to the nil-ductility transition temperature. Above this temperature, the prediction tended to level off due to the temperature variation of yield strength, and hence underestimated the data. However, Ritchie, et al. [1979] concluded that a priori prediction of fracture toughness from such models were not possible because of uncertainties in the magnitude of the microstructurally significant distance.

Curry and Knott [1979] developed a statistical fracture model to estimate the cleavage fracture toughness of a steel containing spheroidized carbide particles based on a knowledge of a carbide particle radius distribution in quenched and tempered steels. The steels included a 1% C tool steel, and a 0.38% C low alloy

steel. Different tempering treatments were employed to impart a range of spherodized microstructures, and one set of the carbon steel specimens was heat treated to give a constant microstructure. Single edge notch bend fracture toughness tests were performed over the temperature range  $-196$  to  $-60^{\circ}\text{C}$  ( $-320$  to  $-76^{\circ}\text{F}$ ) with the carbon steel specimens of constant microstructure, and at  $-196^{\circ}\text{C}$  ( $-320^{\circ}\text{F}$ ) with the carbon steel specimens of varying microstructure. The carbon tool steel specimens of varying microstructure were tested at  $-113^{\circ}\text{C}$  ( $-171^{\circ}\text{F}$ ). Quantitative metallographic examination was performed to estimate the mean interparticle spacing. Post-test fractographic examination of the fracture toughness test specimens showed no evidence of either ductile tearing or intergranular fracture. No shear lips were formed at any test temperature, and only the two highest temperatures showed offset of the load-displacement records. The yield stress for both steels showed a linear dependence on the inverse square root of the mean interparticle spacing. The carbon tool steel showed the typical variation of fracture toughness with test temperature, with an increasing rate of elevation with temperature above  $-100^{\circ}\text{C}$  ( $-148^{\circ}\text{F}$ ).

Curry and Knott [1979] then developed a model which was based on their previous investigation [Curry and Knott; 1978] which showed that carbide cracks propagate into the ferrite matrix as penny-shaped Griffith defects (for spherodized microstructures), and where the effective surface energy of the ferrite matrix was taken to be  $14 \text{ J/m}^2$ . This allowed calculation of the critical

fracture stress to cause failure from the Griffith expression where the carbide particle radius was the microstructural distance term. For a range of carbide particle radii, the cleavage fracture stress value was calculated and related to the stress intensification required to produce fracture of a given carbide. Through appropriate stress analysis, the required stress intensification was converted into critical distance value for the fracture of a cracked carbide of a given radius. Curry and Knott then introduced the calculations for the probability that at least one carbide particle of a given radius is within an arbitrary distance from the crack tip using the frequency distribution of the carbide particle radii and a shape factor related to the areal zone considered. They then introduced a calculation for the probability of a carbide particle of a given radius causing fracture through introduction of a factor to account for particle orientation and the probability that the particle is cracked. Curry and Knott proposed that the probability of fracture due to any carbide size is obtained by summing these probabilities over all carbide radii. The calculation of the probability summations required by this model was accomplished by rearranging the experimentally determined frequency distribution to give the probability that a carbide particle possessing a given radius would fall within arbitrary limits of carbide size. The normalized distance parameter for critical stress intensification was determined from the finite element analysis of Tracey, where the work hardening exponent was taken to be 0.2. The statistical summation was

determined by multiplying the square of the critical distance parameter by the probability of a given particle radius interval, the values of which were summed over all carbide radii intervals obtained with each specimen. A numerical constant was required to allow for the probability of any particle being cracked with its crack plane perpendicular to the principle stress axis, and the shape factor given the areas enclosed with contours of equal maximum stress. For an arbitrary value of this constant equal to 3, Curry and Knott showed very good agreement between experimental fracture toughness and prediction as related to temperature for the carbon tool steel, and related to mean interparticle spacing at a single temperature for both steels.

Curry and Knott [1979] defended this two-dimensional model based on their observations that fracture tended to be more or less sympathetic across the crack front. For these steels, no thickness dependence of fracture toughness was observed in subsidiary experiments. Further, a carbide radius cutoff was imposed during the summation such that any radii less than 5% probability of occurring was neglected. It was further assumed that the carbide particle distribution was homogenous on the basis of the statistical sampling. Finally, Curry and Knott pointed out that this model was proposed to illustrate the nature of the statistical competition at the crack tip leading to an observed fracture toughness. They cautioned against the extension of this model beyond a priori prediction of trends.

Curry [1978] combined an analytical crack tip stress

distribution with the Ritchie, et al. [1973] model to provide an expression for fracture toughness in terms of microstructurally determined properties. Using an asymptotic small scale yielding solution by Hutchinson for the stress at the crack tip in a material obeying a Ramberg-Osgood stress-strain law, he determined the maximum principal stress at any point ahead of a crack tip of a given length. He then rearranged this solution to incorporate the prediction that fracture stress over a characteristic distance. He then substituted the reported Hall-Petch dependence of yield and fracture stress and produced the following expression:

$$K_{Ic} = \beta^{-[(N+1)/2]} X_0^{1/2} \frac{(K_f d^{-1/4})^{(N+1)/2}}{(\sigma_0 + K_y d^{-1/2})^{(N-1)/2}} \quad (6)$$

where:  $\beta$  = Calculated value of singularity amplitude;

$N$  = Work hardening exponent;

$K_f$  = Hall-Petch constant in fracture stress/grain  
size relation;

$d$  = Grain size;

$\sigma_0$  = Internal friction  
stress;

$K_y$  = Hall-Petch constant in yield stress/grain  
size relation;

$X_0$  = Characteristic distance.

With this expression, Curry suggested that the magnitude of the fracture toughness as a function of grain size could not be directly predicted because of the inherent errors in calculation of the singularity amplitude. However, he concluded that this expression would point to the grain size dependence trends ob-

served. This expression then was shown to predict a maximum toughness with grain size, and with increasing temperature. Thus, Curry predicted that an optimum grain size specified at one temperature may give less than optimum toughness at another. Curry also used this expression to question the approaches in HSLA steel processing toward ultra-refined microstructures in the sense that this practice could ultimately reduce toughness if such processing did not significantly change the carbide particle distribution.

Curry [1980a] extended this model to investigate the temperature and strain rate dependence of the cleavage fracture toughness of ferritic steels. This was accomplished by analyzing the temperature dependence of the various terms in Equation 6. By utilizing appropriate expressions for these terms which reflect their temperature dependency (or lack of dependency), Curry predicted the trends of  $K_{IC}$  versus temperature reported by Ritchie, et al. [1973]. He determined that most of these results were outside the range of applicability of his expression because the characteristic distance exceeded the plastic zone size at low temperatures. However, Curry was able to match the measured  $K_{IC}$  versus temperature data by Curry and Knott [1979]. Thus he concluded that this model could successfully be used to predict temperature dependence of fracture toughness for the case of ferritic steels failing by slip-induced fracture, and further he concluded that this analysis was not appropriate at low temperatures where the fracture is mechanism controlled.

Brozzo, et al. [1977] examined the microstructure and cleavage resistance of low-carbon (0.05%) 2Mn-3Cr bainitic steels. The focus of this effort was toward the question of the applicability of models for mild steels with low dislocation density and containing carbides when considering low carbon bainitic steel with sub-boundaries, high dislocation density, and the occasional absence of carbides. Fracture stress was chosen as the parameter of interest because of the general acceptance of the critical stress criterion, and the availability of critical cleavage stress data for mild steels. The basic composition of the steels investigated was 2% Mn-3%Cr with two carbon and sulphur contents (0.025% and 0.050% C, and 0.005 and 0.014% S). The steels were vacuum melted and hot-rolled to 12mm (0.5-inch) thick plates. Critical cleavage stress values were determined by three-point bend tests on Charpy V-notch specimens at quasi-static displacement rates in the temperature range -146 to 23°C (-231 to 73°F). Load deflection diagrams were obtained, and the temperature at which the general yield curve intercepted the fracture load curve was taken as the nil-ductility temperature. Conventional Charpy V-notch impacttoughness tests were also included using transverse specimens of three of the steels. A plot of critical cleavage fracture stress as a function of the inverse square root of the bainitic packet size was produced and resulted in a straight line. Brozzo, et al. examined the two theories which account for this dependence of critical fracture stress, namely that of Cottrell which assumes that the critical stage of the fracture

process is the growth of a microcrack within each microstructural unit, and Griffith-Orowan theory assuming that the critical step is the propagation of a microcrack from one microstructural unit to another. These authors concluded that the use of the Cottrell theory led to calculated values of the effective surface energy equal to the true surface energy of ferrite. The Griffith-Orowan theory led to the calculation of an effective surface energy of  $120 \text{ J/m}^2$  which was in agreement with previously reported values for low Mn steels with polygonal ferrite microstructures. Metallographic analysis of the crack profile showed that secondary microcracks existed below the fracture surface, with length approximately twice the diameter of the bainitic packets. Unit crack path measurements on the surface of specimens showed that this value was approximately 1.3 times the bainitic packet size. This led Brozzo, et al. [1977] to conclude that the bainitic co-varient packet was the microstructural unit which controlled the cleavage fracture mechanism in low carbon bainite.

Naylor [1979] studied the influence of lath morphology on the yield stress and transition temperature of martensitic bainitic steels. This analysis showed that for fine grain sizes as encountered in bainite and martensite, macroscopically heterogeneous deformation tends to vanish. Naylor showed that the ductile-brittle transition temperature is reduced when packet diameter and lath width decreases, and that major cleavage crack deviations occur at packet boundaries. He formulated a quasi-cleavage model which permitted small angle deviations of crack path across laths, and



the establishment of another fracture plane at a packet boundary involving plastic tearing. Further, Naylor developed a Griffith-type of fracture criterion in terms of this plastic tearing which resulted in a logarithmic function of the inverse square root of the product of the packet diameter and lath width.

Wallin, et al. [1984] and Saario, et al. [1984] developed a two-dimensional model assuming statistically distributed carbides control fracture toughness. The fracture criterion utilized the Griffith crack advancement expression and fracture was assumed to occur when the tensile stress ahead of the crack tip at the site of a carbide having a radius  $r$  exceeds the Griffith critical fracture stress. This led to an expression for critical carbide radius which would lead to cleavage fracture for a given stress condition. The probability of fracture was then calculated for the probability of a carbide having a radius equal to or greater than the critical radius.

Wallin, et al. [1984] and Saario, et al. [1984] evaluated this model with a 0.16% C-Cr-Mo-V bainitic steel with a known size distribution of Cr-rich carbides which were rod-shaped, and found to be located at packet boundaries. From previously reported values of the critical fracture stress for cleavage determined from bend tests, an estimated value of the Griffith-Orowan effective energy term was  $8.8 \text{ J/m}^2$ . Saario, et al. [1984] attributed this value to the much higher dislocation density of the bainitic microstructure over that found in spherodized ferritic microstructures.

Hagiwara and Knott [1981] evaluated the fracture toughness of martensitic and mixed martensitic-bainitic microstructures of HY-80 steel. The objective of the study was to determine the micro-mechanism of cleavage fracture of mixed microstructure by evaluating the variation of fracture toughness with volume fraction of bainite in martensite. HY-80 steel specimens were austenitized and quenched to produce 100% martensite, or isothermally transformed to give varying amounts of upper bainite in the ferrite matrix. Single-edge notch bend specimens with a thickness of 23mm (0.9inch) were produced and tests were performed over a temperature range from -196 to -60°C (-320 to -76°F). Four-point bend specimens were also tested to determine the critical fracture stress. Fractographic examination showed that all specimens tested below -139°C (-218°F) fractured completely in quasi-cleavage. The quasi-cleavage was associated with bainite, and the microvoid coalescence with martensite. At small proportions of bainite, the fracture toughness decreased rapidly with increase of bainite content, and at greater than 50% bainite, fracture toughness remained constant. The critical fracture stress decreased rapidly when a small proportion of bainite was introduced in martensite, and remained constant for bainite content greater than 40%. Hagiwara and Knott examined these results in terms of bimodal Gaussian distributions of fracture toughness in martensite and upper bainite assuming the same standard deviation in each case. Agreement between estimated and experimental results was obtained using an arbitrary "cleavage fracture sensitivity factor" of

bainite compared with martensite. SEM fractographic examination showed that the mean diameter of the cleavage facets in martensite was 10  $\mu\text{m}$ , and 39  $\mu\text{m}$  in bainite. Following the work of Brozzo, et al. [1977], the cleavage fracture sensitivity factor was calculated for the case of cracks propagating into adjacent packets, and this compared well with previously calculated values. Further, from fractographic examination, these authors noted that the fracture toughness of mixed microstructures was affected by proportion of bainite and its location ahead of the crack tip, specifically the probability of coarse bainite in regions of high stress. In this sense, the Curry and Knott [1979] largest particle argument refers to the bainitic packets rather than carbide particles.

Curry [1982] performed experiments to identify the influence of hydrostatic tension on the cleavage fracture of ASTM A 508 C1 2 bainitic pressure vessel steel. Microstructures of fully tempered bainite and as-transformed upper bainite were examined. Sets of 12.7mm (0.5-inch) square SEN specimens were machined with various included angles in the notch (30 to 105 degrees) and constant root radii. Tests were carried out over the temperature range -188 to -136°C (-306 to -213°F). Tensile tests were also performed over this range. The range of temperatures within which fracture and general yield coincided were determined. The results showed a large amount of scatter, but Curry concluded that at most, the maximum tensile stress at fracture was weakly dependent on hydrostatic tension, and further that cleavage

fracture for both of these microstructures was predominantly tensile stress controlled. The critical fracture stress from slip-line field theory and stress analysis was constant at temperatures above  $-160^{\circ}\text{C}$  ( $-256^{\circ}\text{F}$ ), but increased as temperatures decreased below this value. This was attributed to an increase in effective surface energy due to the work done in moving dislocations at low temperatures. Examination of the fracture surfaces showed cleavage facets the same size as the bainite packets, with little evidence of large changes in crack-plane orientation on the scale of the lath width. Curry examined the possibility that the packet size is the primary microstructural feature controlling the cleavage fracture stress in bainitic steels after showing that the Curry and Knott analysis of the largest eligible particle did not correspond with microstructural measurements. He concluded that the high effective surface energy term required for this model reduced its likelihood. He then suggested that cleavage in bainite proceeds by some dislocation mechanism where dislocation reaction could give easy nucleation necessary for tensile stress controlled fracture.

Tweed and Knott [1982,1983] examined the toughness of C-Mn weld metal with a focus on effects of reheating to maximum temperatures of  $900$  and  $1250^{\circ}\text{C}$  ( $1652$  and  $2282^{\circ}\text{F}$ ) where fine and coarse reheated microstructures were produced. Laboratory weldments of  $25\text{mm}$  (1-inch) thick plate conforming to BS 4360 Gr. 50 D were produced containing a large weld bead at the mid-plane of the weldments where the fatigue crack tip was to be placed.

Simulated reheating of specimens was accomplished using induction coils. Reheating temperatures included 900°C and 1250°C (1652 and 2282°F) where at the latter, some specimens were held at 700°C (1292°F) for 60 seconds during cooling to enhance the amount of equiaxed ferrite in the steels. COD tests were performed at 22, 0 and -40°C (72, 32 and -40°F). Micrographic examination of specimens showed that on cooling, the original austenite transforms to ferrite of two distinct morphologies. Relatively equiaxed ferrite grains occurred at prior austenite grain boundaries, while acicular ferrite was found intergranularly. Where little equiaxed ferrite was present, it outlined the grain and was termed grain boundary ferrite. Results of the COD tests showed that the reheated materials had substantially increased fracture toughness over the as-welded material. The refined microstructure resulting from the 900°C (1652°F) reheat cycle had the highest fracture toughness, and the microstructure consisting of large equiaxed ferrite gave results of a similar range to those for a mixed microstructure derived from the 1250°C (2282°F) reheat. Fractographic and metallographic examination showed the crack paths tended to follow grain boundary ferrite. Microcracks subsidiary to the main crack front were absent and in general, the unit crack length was much greater in grain boundary ferrite. Cracking in acicular ferrite involved much stopping and crack reinitiation. In most cases, fracture initiation was associated with non-metallic inclusions lying on a large brittle

facet. Microhardness of the as-welded microstructure indicated that the grain boundary ferrite was notably softer than accicular ferrite. This led Tweed and Knott to postulate a tentative model for the as-welded microstructure where plasticity is initially localized in the grain boundary ferrite. Dislocations pile up against or around non-metallic inclusions, leading to cracking, where at a critical combined stress level, one or more cracks grow to brittle fracture. Factors favoring brittle fracture include large grain size, high yield stress and work hardening exponents, and large inclusions. This model suggests that fracture is independent of the amount of accicular ferrite present except so far as it constrains the ferrite and effects the yield properties.

Rosenfield, et al. [1983] conducted fractographic examination of cleavage initiated in the ductile-brittle transition region of ASTM A 508 steel. Six 1T compact specimens each were tested at 22°C and 82°C (72 to 180°F), and in all but one, distinct cleavage origins could be located near the fatigue or ductile rupture crack fronts. A significant fraction of the cleavage fractures initiated at MnS inclusions of the order of 1  $\mu\text{m}$  instead of at carbides. The MnS-triggered cleavage appeared to dominate the higher temperature tests.

Bowen and Knott [1984] conducted measurements of microscopic cleavage fracture stress and fracture toughness of ASTM A 533 B steel in an autotempered martensite condition. Heat treatments involved austenitization in the temperature range 900 to 1250°C

(1652 to 2282°F) followed by oil quenching. Fracture toughness was obtained from four-point bend tests over the temperature range 196 to -60°C (-320 to -76°F). Notched bend tests were also performed in the temperature range -196 to -100°C (-320 to -148°F). The microscopic cleavage fracture measurements showed no significant variation with autotempered martensite packet size and prior austenite grain size. The critical stress was independent of temperature in the range -100 to -160°C (-148 to -256°F), but values obtained at -196°C (-320°F) were slightly below those at -160°C (-256°F). The values of  $K_{IC}$  for the coarse grained condition were generally superior, although occasionally low values were obtained. The variation of fracture toughness at -120°C (-184°F) with austenitization temperature was minimal. The mode of fracture for all austenitization treatments was transgranular quasi-cleavage. At -60°C (-76°F), catastrophic brittle fracture was preceded by ductile tearing in the coarse grained material, whereas the fine grained material exhibited only a stretch zone. Inclusions were occasionally observed in the fracture surfaces.

Bowen and Knott suggested that the observed temperature independence of critical fracture stress was strong evidence for a tensile stress propagation controlled fracture process. Possible critical steps were identified as propagation of a microcrack the size of an autotempered packet, carbide, or lath width. The packet and lath mechanisms were discounted for a variety of reasons, and consideration of the role of the inclusions in a

martensite matrix was made. The authors concluded that the distribution of autotempered carbide widths showed no significant variations with prior austenite grain size, and thus it was not probable that cracking of these very thin carbides could control the cleavage fracture. An inclusion controlled fracture mechanism was proposed as the most consistent with the experimental results.

Evans [1983] developed a weakest link cleavage fracture statistical model based on the concepts of crack growth from cracked carbides. This model predicts that the maximum elemental failure probability occurs ahead of the crack tip and provides a natural definition of the critical distance which depends on size, distribution and volume fraction of cracked carbides, and on flow stress. The dependence of fracture toughness was also predicted based on the temperature dependence of flow stress. The most important microstructural property was seen as the size distribution of the cracked carbides.

Lin, et al. [1985] recently developed a model for brittle fracture by transgranular cleavage based on application of weakest link statistics to the critical microstructural mechanism. Particles located in the plastic zone were considered to be cracked, and these microcracks were considered to be non-interacting. Using a modified Griffith criterion, the size distribution of the particles was related to their fracture strength, and strength distribution. The survival probability of the structure was calculated from quantitative measurements of particle size distribution and by approximating the fraction of particles



which participate in the fracture process in response to their location, orientation in the microstructure, and orientation of the local grains. This model was applied to 1008 mild steel which had austenitized and spheroidized to obtain a ferritic matrix with primarily grain boundary carbides. Plane strain fracture toughness and elastic plastic toughness as well as tensile tests were performed over a range of temperatures. Using the measured flow stress, work hardening exponent variation, and carbide size distribution, with various crack tip stress field formulations resulted in predictions which closely matched the fracture toughness measurements. This model was seen to provide a definition of the characteristic distance as the critical radial dimension from the crack tip where the cracking event is most probable. These authors pointed out that this model is inappropriate for a rate limiting step involving coalescence of cracks for unstable fracture versus microcrack propagation into the matrix.

Several recent reviews of the micromechanisms of cleavage crack growth in steels have been produced, most notably by Curry [1980b], Pineau [1981], Knott [1981,1982, 1983], Hahn [1984], and Ritchie and Thompson [1985]. Pineau concluded that although the critical stress criterion explains many cleavage results, for the case of very low carbon alloy steels and in lath martensite microstructures of Fe-Ni alloys containing no carbides, cleavage fracture is controlled by some form of dislocation mechanism rather than cracking of second phase

particles. Hahn [1984] concluded that the microstructural feature controlling brittle fracture for a particular steel is that with the combination of eligible particle size and arrest toughness producing the largest brittle fracture stress value. Particles whose boundaries resist microcrack extension include carbide particles, carbide films at grain boundaries, carbide lamellae in pearlite, hard inclusions, ferrite grains, pearlite colonies or grains, bainite packets and martensite packets. Hahn further concluded that the brittle fracture stress depends on the size of the microcrack and the resistance experienced in attempting to cross boundaries, hence a boundary crack arrest concept was deemed appropriate. Finally, Hahn suggested that the small number of the very largest particles had a disproportionate influence on fracture toughness below the transition temperature.

## DUCTILE FRACTURE

The fracture process in steels changes from cleavage to fibrous as the temperature is increased. The topic of ductile fracture has been most recently reviewed by Rosenfield [1968], Hahn [1976], Hahn and Flanagan [1980], Knott [1978,1980,1982,1983], Pineau [1981], Ritchie and Thompson [1985], Wilsdorf [1983] and Van Stone, et al. [1985]. These and other authors describe this fracture process in terms of three stages including nucleation of voids or cavities, growth of cavities with continued deformation, and coalescence of voids comprising rupture or crack growth. Description of ductile fracture is distinct from cleavage in that it incorporates an intermediate step of void growth. Additionally, plasticity on a local and macro scale must be included in describing this fracture process. This has precluded the valid use of linear elastic fracture mechanics. The development of the COD and J-integral approaches has led to fracture mechanics descriptions of the ductile fracture process. In this section, a review of the stages of the ductile fracture process from a fracture mechanics perspective will be presented with a discussion of experimental observations and measurements, and theoretical aspects particular to each.

### Void Nucleation

Puttick [1959] conducted tensile tests of Tough Pitch High Conductivity (TPHC) copper and ingot iron. The copper material contained small non-metallic inclusions, and was tested in the as rolled and annealed condition. The ingot iron was vacuum annealed

and air cooled. Manually operated tensile tests were performed where load was lowered rapidly after yield had taken place. Metallographic examination of deformed copper specimens showed the existence of large central cavities surrounded by numerous smaller holes. These were found to originate at inclusions by decohering of the interface, or by cracking of the inclusion. The fracture surface was observed to grow by opening and linking of inclusion holes. The iron specimens also contained cavities associated with inclusions. Puttick also observed cracks running from one inclusion site to another even though cavities had not grown appreciably.

Rogers [1960] studied the tensile fracture of OFHC copper through metallographic examination of partially fractured tensile bars. The grain size of the copper was coarsened by heat treatments which were performed in hydrogen, dry nitrogen, and vacuum. The hydrogen atmosphere was intended to induce embrittlement at grain boundaries. Metallographic examination of hydrogen-treated specimens revealed the presence of many grain boundary voids. Some boundaries were free of voids at a particular stress level, where adjacent areas were saturated. After extensive necking, voids were initiated in interiors of grains in highly deformed regions. In specimens heat treated in dry nitrogen, the voids were similar in number to the hydrogen-treated specimens, but not associated with grain boundaries. These voids were a factor of ten larger than those observed away from grain boundaries following hydrogen treatment, and were

postulated to result from inhomogeneous deformation.

Chin [1969] produced welds with different deoxidizer contents in a low carbon alloy steel giving rise to different populations of inclusions in each of the welds. A relationship between impact energy and inclusion population was developed, and metallographic and fractographic examinations were conducted to determine the density of inclusions in the fracture surface compared with the bulk of the weld metal. Chin observed that the propagation of fracture across the Charpy V-notch specimen followed a preferred path between inclusions rather than the shortest geometrical path. This author associated inclusions with dimples on the fracture surface, and it was shown that fracture toughness was governed by conditions where a high density of large inclusion was observed.

Knott [1971] examined the role of second phase particles on the toughness of structural steels. He employed crack opening displacement (COD) tests with free machining steels, and showed that void formed around inclusions, but not pearlite colonies. Knott concluded that in mild steels, the fibrous fracture was controlled by the distribution of non-metallic inclusions.

Smith and Knott [1971] and Ritchie, et al. [1975] evaluated the effects of test piece design and microstructure including grain size and non-metallic inclusion dispersion on the COD of free cutting mild steel at room temperature. Longitudinal and transverse specimens orientations were examined and showed that

the former developed significantly higher COD and upper shelf Charpy toughness values. Fibrous fracture surfaces were examined in the scanning electron microscope and inclusions were identified in the dimples. Metallographic examination showed that voids formed around inclusions, but not around carbide particles.

Dolby and Knott [1972] examined toughness of a 2.5 Ni-Cr-Mo steel which was heat treated to vary the austenitic grain size. COD measurements were taken over a broad temperature range. Little change in upper shelf, ductile fracture toughness was observed in response to changes in prior austenite grain size. Metallographic examination showed that microvoids were not associated with particular features of the microstructure such as martensite colony size. Rather, inclusions believed to be sulphides and possibly large carbides were the initiation sites for these voids. It was also observed that martensite of highest strength showed smaller microvoid diameter, implying that more inclusions (or carbides) were initiating such defects.

Cox and Low [1974] studied mechanisms of plastic fracture in high purity and commercial 18 Ni, 200 grade maraging steels, and quenched and tempered AISI 4340 steels. In the maraging steels, fracture took place through void initiation caused by fracture of titanium carbo-nitride inclusions. The 4340 steel fracture occurred by nucleation and growth of voids formed by fracture of the interface between Mn-sulphide inclusions and the matrix. Void nucleation was observed to

occur more readily at the larger inclusions.

Chipperfield and Knott [1975] evaluated the effects of notch acuity, inclusion content and strength level on the COD of several ductile steels. Free machining mild steel, several steels containing differing volume fractions of manganese sulphide, silicate and alumina inclusions respectively, one carbon-manganese steel containing elongated MnS inclusions, and a high strength Cr-Mo steel (HY-130). In the low strength steels, the fracture path was observed to involve void growth and coalescence from large inclusions. In the case of higher strength steels fracture followed a zig-zag path where shear fracture joined major inclusions.

Clayton and Knott [1976] evaluated the COD on prestrained Q1N (HY-80) low alloy steel. Specimens were transversely prestrained in direct compression to nominal prestrain levels of 0 to 20%. Examination of the fracture surface showed that the primary sites for void initiation were large and small sulphide particles separated in many areas by fine voids formed at carbide particles. Increasing levels of prestrain produced only minor differences in fracture topography.

Fisher and Gurland [1981] conducted a quantitative study of void initiation in low- and medium-carbon spheroidized steels deformed uniaxially in tension. Metallographic examination was performed in both longitudinal and transverse sections, and the areal density of voids was determined by scanning electron microscopy on transverse sections. Voids were

observed to nucleate preferentially at interfaces of large cementite particles located on ferrite grain boundaries. In the high carbon steel, voids were observed to occur by particle fracture where cracks occurred preferentially at large irregular particles with large aspect ratios in the tensile direction. For low and medium-carbon steels, these voids were generally associated with particles of greater than average size, and were rarely observed to form at very small particles. These voids were observed to form often by decohesion of the interfaces of the particles.

The roles of sulphides, oxides and pearlite in the ductile fracture of a Nb microalloyed steel were examined by Melander and Steninger [1982]. Tensile specimens of a 0.2% C, 1.31% Mn, 0.025% Nb steel containing 21% by volume pearlite were produced in the short transverse and longitudinal directions. Intermittent tensile tests were performed to various strain levels beyond maximum load. Void growth was studied on axial metallographic sections from these tests. Results showed that voids were nucleated at pearlite nodules both through shear fracture of the nodule itself, and through decohesion at the interface where the void nucleation strain was approximately 1.1. Voids at elongated sulphides were nucleated by breaking up the particles into segments, and the nucleation strain was on the order of 0.2-0.5. Voids at equiaxed inclusions were usually present after hot rolling, or were initiated early in the tensile test.



Gurland and Plateau [1963] examined the role of inclusions in ductile fracture through describing the stresses which develop around inclusions. They conducted metallographic examinations of the polished convex bend surface of thin plate of an aluminum alloy containing 13% Si, Armco iron, and a pearlitic steel with 0.32% C. In the aluminum alloy, the first cracks opened simultaneously with the first plastic deformation, and appeared to be preferentially located in the larger inclusions. In Armco iron, initiation was observed to occur by decohesion of the matrix and particle along the interface at the site of maximum stress. In the steel specimen, microcracks were observed at the pearlite-ferrite interface, and within the matrix itself near the edges of pearlite of pearlite colonies. From these observations, Gurland and Plateau developed a model using a combination of factors related to the required stress concentration, triaxiality in plastic constraint, and the coherent strength of the inclusion, interface and matrix respectively. Their model required that the strain energy at the inclusion be sufficient to provide the surface energy of the newly formed crack faces. Assuming that the stress field of the particle has dimensions of the same order of magnitude of the particle, and the dimensions of the resulting crack is equal to that of an inclusion, an approximate expression for the critical stress to initiate a void was suggested as follows:

$$\sigma = \frac{1}{q} \left[ \frac{E\gamma}{a} \right]^{1/2} \quad (8)$$

Where:  $q$  = average stress concentration factor at inclusions;

- $\sigma$  = Applied uniaxial stress;
- $\gamma$  = Specific surface energy of crack;
- $E$  = Weighted average of elastic moduli of inclusion and matrix;
- $a$  = Dimension of inclusion.

Gurland and Plateau showed that estimation of the critical stress agreed approximately with the stress at which first cracks appeared in the Al-Si alloy, and this expression accounted for initiation at larger particles.

Argon, et al. [1975] modelled cavity formation from equiaxed inclusions which were approximated as rigid, and plastically non-deformable. They developed a critical stress criterion based on dislocation models for very small inclusions where the radius was less than 100 angstroms, and large inclusions where the radius exceeded this dimension. They postulated that the critical elastic energy conditions are necessary, but not sufficient for cavity formation. Additionally, the interface strength must also be reached on part of the boundary. This analysis suggested that small inclusions cannot form stable cavities because on reaching the interfacial strength, small inclusions will separate from the matrix a certain distance of atomic dimensions to relieve part of the elastic energy, but long range forces will still act across the interface. For larger inclusions, calculations showed that the energy condition is always reached when the interfacial strength is reached, and cavities form by a critical interfacial stress

condition. Argon, et al. [1975] also examined the interaction of inclusions in cavity formation. When the volume fraction of the second phase is small and the secondary plastic zones do not touch, then the interfacial strength is independent of the particle size and depends only on the local flow stress and the long-range triaxial stress. When the volume fraction is large or shear strain is large so that secondary plastic zones touch, then particles interact. Where particles are of a uniform size and have quasi-uniform spacing, the interfacial stress also becomes dependent on the volume fraction of the second phase, but remains independent of particle size. The interfacial stress becomes particle size dependent only when significant local variations of volume fraction of second phase particles exist from point to point for a given average second phase volume fraction.

Goods and Brown [1979] reviewed the literature concerning cavity nucleation, including nucleation around particles. Their criteria for nucleation included the energy release mechanism for surface separation, and the critical stress at the interface or inside the particle. Employing the continuum plasticity solution of Brown and Stobbs [1976], they determined that the critical radius of a particle above which a continuum mechanics description applied is 1-3  $\mu\text{m}$ , depending on the rate of work hardening. Goods and Brown then proposed that the critical strain for cavity nucleation from particles less than 1  $\mu\text{m}$  is:

$$\epsilon_c \approx \left( \frac{\sigma_0}{\mu} \right) \frac{r}{b} \quad (9)$$

Where:  $r$  = Particle radius;

$b$  = Burgers vector;

$\mu$  = Shear modulus.

Here it was shown that the critical stress is a linear function of particle size. Goods and Brown then tried to express this criterion in terms of strain even though it was derived on the basis of critical stress, because such a stress is produced by the local work hardening at the particle, and is a function of the plastic strain in the matrix. They concluded that at low temperatures, the nucleation of cavities around non-deforming particles smaller than approximately  $1 \mu\text{m}$  appeared to be controlled by the build up of internal stresses as a result of incomplete plastic relaxation due to local dislocation tangles, hence local work hardening around particles. Further, in materials which undergo coarse slip, plastic relaxation is not found, and cavities nucleate at low plastic strain. At high temperatures, when dislocation mobility is high, plastic relaxation is easy and local work hardening is small, cavity nucleation becomes very difficult.

Fisher and Gurland [1981] recently developed a model for void nucleation in spherodized steels. This is a double criterion based on a combined critical normal stress condition and a critical elastic energy release requirement. Here, the components of elastic energy release include the elastic energy associated

with the applied loading, the stored energy resulting from the unrelaxed plastic incompatibility between the elastically deforming particle and plastically deforming matrix, and the energy or interaction between internal stress fields and applied stress fields. From this model and analysis of experiments with spherodized carbon steels, the energy criterion for void nucleation is not always satisfied for inclusions in the sub-micrometer size range. They also suggested that inclusion size effects may not be inherently associated with individual particles. Finally, Fisher and Gurland concluded that the factors which favor void nucleation include particle size, low work of adhesion, high flow stress, high triaxiality, large plastic strain, small grain size and location of particles on grain boundaries.

In reviewing the current state of modelling of void nucleation, Van Stone, et al. [1985] suggested that the existing models have not kept pace with experimental results where increasing yield strength lowers the plastic strain for void formation, and void nucleation can be retarded by reduction in particle size. They pointed up that void nucleation is apparently influenced by stress, strain and energy criteria, and is highly dependent on the deformation modes of the particle and matrix.

#### Void Growth and Coalescence

From the fracture mechanics perspective, void growth and coalescence defines the fracture process in that their occurrence

comprises crack initiation and growth. Here the presence of the crack tip introduces a complexity not found in describing tensile testing because of the steep stress and strain gradients in its vicinity. A discussion of experimental observations regarding growth and coalescence of voids principally associated with existence of a preexisting crack will now be presented. Then models describing the ductile fracture process will be discussed.

The observations of Puttick [1959] regarding the nucleation of voids also included observations of the fracture surfaces of copper and ingot iron. He found that in the case of the tensile fracture of copper, the fracture surface was observed to grow by opening and linking of inclusion holes. The iron specimens also contained cavities associated with inclusions, but cracks were also observed to run from one inclusion site to another, even though the cavities had not grown appreciably. Subsequently, Rogers [1960] observed two modes of tensile fracture on OFHC copper. He first observed the joining of voids in the central portion of the test bar to form a crack. The growth of the crack followed bands of shear stress concentration on angles of 30 to 40 degrees from the tensile axis. In these shear band regions of very heavy local deformation, a large number of void sheets were nucleated, and subsequently failed under the applied tensile stress. Fracture then extended out of the plane of minimum cross section, and following the formation of shear bands at the new crack tip, the crack propagated back toward the plane

of maximum stress, thus resulting in a zig-zag pattern across the maximum tensile stress plane as it propagated radially.

Beachem [1965] and Beachem and Meyn [1968] conducted careful electron fractographic studies of the fracture process in ductile metals. Three kinds of microvoid coalescence were identified including normal dimpled rupture where a void grows until it impinges on a neighboring void. Under the influence of shear stresses, voids are seen to elongate in the shear direction and coalesce. Under a strain gradient, voids also are observed to join by tearing.

Floreen and Hayden [1970] investigated void growth during tensile deformation of an 18% Ni (280 Grade) maraging steel. Void initiation was observed by cracking of Ti (C,N) particles. Tensile tests of annealed, and annealed and aged specimens were conducted at room temperature. Several specimens were unloaded and polished metallographically short of failure, and void sizes were measured. They observed no linking up of neighboring voids, even for cases where specimens were unloaded just prior to fracture. The average length and width of the ten largest voids for each steel condition were seen to increase linearly with strain level. These authors suggested that toughness in this steel was dictated primarily by the void growth stage of deformation since it occurred over most of the tensile strain range.

Beachem and Yoder [1973] developed a description of elastic-plastic fracture by homogeneous microvoid coalescence

tearing along alternating shear planes. This addressed observed fracture surfaces of alternating ridges and valleys on a scale considerably larger than that of the dimples. A 13% Cr-8% Ni-2% Mo precipitation hardened stainless steel was tested with precracked cantilever beams in bending in a 3-1/2% NaCl solution while under cathodic charging. An 18% Ni (Grade 200) maraging steel was similarly tested in air. A major portion of the fracture surfaces of both steels consisted of alternating ridges and valleys, the length of which was perpendicular to the direction of local crack propagation. Key observations indicated that the fractures were totally microvoid coalescence, with only 15% equiaxed dimples. The remainder of the dimples pointed either toward or away from these regions. Additionally, there was usually a rim of tear dimples at the peaks of the ridges on the side facing the crack origin. This observed alternating shear mechanism was described by a tension-compression model with a constrained plastic zone in four stages, with each stage occurring by a blend of tearing and shearing on shear planes following a zig-zag course in a continuous manner to form a macroscopically flat crack.

Cox and Low [1974] in their studies of plastic fracture of 4340 and 18% Ni (200 Grade) maraging steels observed both void growth and coalescence in tensile bars and notched tensile specimens. Void growth was observed to be more rapid from larger inclusions, and it was demonstrated that void growth rates were also increased substantially by increasing



the level of triaxiality in the tension tests. In the 18Z-Ni maraging steel, void coalescence occurred by impingement of voids on one another. In the 4340 steel, crack-like features similar to the void sheets described by Rogers [1960] linked the voids before full growth and coalescence. These voids formed at the carbide particles in these shear bands, and were used to explain the observed difference in toughness of the two steels.

Hahn and Rosenfield [1975] evaluated metallurgical factors affecting fracture toughness of aluminum alloys. They observed that the fracture process included the breaking of Fe-, Si-, and Cu-bearing inclusions, and the growth of voids at the cracked particles. The linking of the voids was accomplished by the rupture of the intervening ligaments which was affected by the fine precipitate particles which strengthened the matrix. These authors attributed the substantial loss in fracture toughness with increasing yield strength level to the reduction in work necessary to link voids in the higher strength alloys.

Ritchie, et al. [1975] evaluated the effects of test piece thickness with a normalized free cutting mild steel containing a high volume fraction of manganese sulphide inclusions. COD tests were carried out at 20°C (68°F) with 20 mm (0.79-inch) wide four point bend bars where thickness varied from 2 to 17mm (0.08 to 0.67-inch). The critical COD value was substantially greater in the thin test pieces where thickness was below 5mm (0.20-inch). In these tests, cracking was observed to occur by the linking of voids ahead of the crack tip. The

elevation of fracture toughness in the thinner specimens was ascribed to the ability of the test piece to absorb deformation in a larger volume of material around a crack tip so that the crack requires more displacement per unit crack growth than seen with thicker specimens.

Chipperfield and Knott [1975] evaluated the effects of notch acuity, inclusion content and strength level on the fracture toughness of a variety of C-Mn steels, and one Cr-Mo-V (HY-130) steel. Three- and four-point bend tests of 20mm (0.79-inch) wide bend bars were accomplished at room temperature. In four of the low strength steels, the ductile fracture was observed to involve void growth and coalescence mechanisms from large inclusions. In higher strength steels, or those which initiated fibrous fracture only at large crack tip strain, metallographic sections indicated that fracture followed a zig-zag path. Chipperfield and Knott found, however, that the major inclusions in these intervals were always found to be positioned in troughs or peaks on the fracture surfaces, and metallographic sections of test pieces of HY-130 indicated that the mean shear crack length was comparable with the mean inclusion spacing. Metallographic section also indicated that the continuing shear crack propagation caused very little opening displacement, suggesting that crack propagation between major inclusions was particularly rapid.

Hancock and Mackenzie [1976] conducted tensile tests with circumferentially-notched round tension specimens produced

from three low alloy, quench and tempered steels including Q1, HY-130 and an electro-slag remelted version of HY-130. Metallographic examination was conducted on specimens removed from test after different plastic strains. In the Q1 steel tested in the short transverse direction, the mechanism of failure initiation was microcracking between large elliptical holes, whereas in the long transverse direction, the tendency was for groups of larger holes to grow to almost complete coalescence. In HY-130 in the short transverse direction, fracture initiation occurred by microcracking between inclusion colonies, whereas in the long transverse direction, there was very much more extensive growth of the large holes. The electro-slag remelted steel showed similar hole growth in both the short transverse and long transverse directions.

Green and Knott [1976] conducted COD measurements of HY-130 steel and two C-Mn normalized steels. Specimens were produced with cracks in three orthogonal orientations. The inclusion content and work hardening capacity were shown to have a significant effect on the crack initiation COD measurement. In HY-130, the deformation associated with the crack tip followed the logarithmic spiral of shear lines directed toward voids found at the focus of the spiral. Thus the contribution to COD from the coalescence stage was seen to be small. In the low strength steels with high work hardening capacity, voids were extensively and uniformly distributed below the notch, and extensive void growth was required before the ligament

between the crack tip and void became unstable.

Clayton and Knott [1976] examined the modes of fibrous fracture in prestrained HY-80 steel. Specimens were prestrained in direct compression in the range 3 to 20% where the strain level refers to the average value over the central 6mm of the test piece. The general effect of prestrain was to decrease the critical initiation values of COD, even though no transition to cleavage was noted. At prestrain levels below 17%, no significant reduction in COD was noted, while above 17%, the COD was reduced and a zig-zag fracture process developed. In the non-prestrained material, fracture occurred by shear decohesion along the spiral slip lines joining the blunted crack to nearby inclusions. At the higher prestrain levels, decohesion took place along straight slip lines at an angle to the crack.

Clark, et al. [1982] determined the COD of several cast and wrought steels including HY-80, HY-100, HY-130, ASTM A 533B, and several experimental welds. All of the steels exhibited fibrous fracture. In steels with a clean matrix of high work hardening capacity, the fracture process was one of internal necking linking voids, giving a fracture surface consisting of a number of dimples centered on inclusions. If the hardening capacity of the necking ligament was limited, localized shear fracture was shown to occur following one of the logarithmic spiral slip lines emanating from the blunted crack tip.

King and Knott [1981] evaluated the effects of temper embrittling heat treatments on the ductile fracture of EN 30A low alloy

steel. COD tests of materials in an embrittled and unembrittled condition were conducted at room temperature, and 250°C (482°F). The morphology and distribution of the tempered carbides were identical for the two heat treatment conditions. At 250°C (482°F), the embrittled material exhibited a COD of 0.075mm<sup>9</sup> (0.003-inch) versus 0.03mm (0.001-inch) for the unembrittled material. The fracture surface of both materials was composed of large voids around MnS inclusions linked by fine voids which nucleated at matrix carbides. In the embrittled specimen, the fine voids occupied a larger proportion of the fracture surface than on the unembrittled specimen. King and Knott also produced evidence that the fine voids are just slightly larger than the matrix carbides, and some of the larger carbides in the embrittled steel decohered from the matrix.

Slatcher and Knott [1981] evaluated air-melted and vacuum-remelted versions of EN 25 (0.3%C) steel heat treated to give yield strengths in the range 950-1650 MPa (138-239 ksi). COD measurements were performed with a variety of experimental techniques. There was little difference between the fracture toughness in the air-melted and vacuum-remelted conditions except at the higher yield strength levels, where the air-melted version was tougher, had coarser dimples, and a coarser microstructure. At the lower yield strength levels, the fracture path showed more "zig-zag" type of growth, and there were large relatively featureless areas on the fracture surfaces. These areas corresponded to fine cracks seen just ahead of the crack

in the two lowest strength heat treatments. There was also evidence that carbides nucleated voids, and that the fine cracks may advance by void coalescence along microstructurally predetermined paths.

You and Knott [1982] evaluated the ductile fracture toughness of HY-80 and HY-130 steels using COD tests performed at room temperature. The HY-80 specimens were seen to fail by a void coalescence process which was curtailed by a shear decohesion between the voids when the hardening capacity of the material was exhausted. HY-130 exhibited a similar mechanism, however, it failed in a manner more dominated by shear. HY-130 also exhibited distinct shear steps, the length of which was the same magnitude as the inclusion spacing.

#### Models of Void Coalescence and Fracture

Krafft [1964] postulated a relationship between fracture performance and strain hardening, and investigated this model with a series of fracture toughness tests, and tests of plastic flow properties considering effects of adiabaticity, straining speeds and temperature. This model was based on the premise that the fracture process is considered as tensile rupture occurring in small elemental fracture "cells" lying along the crack front. These cells act as ductile ligaments which form the last connecting links along the crack front. Deformation of these links occurs in response to the stress gradient at the crack tip where it is most intense near the crack tip. The crack growth criteria was based on establishment of sufficient

strain for ductile rupture of a cell a given distance away from the crack tip. Krafft suggested the following correlation between plane strain fracture toughness and strain hardening exponent:

$$K_{Ic} = E\sqrt{(2\pi d_T)^n} \quad (11)$$

where  $d_T$  is a material constant and  $n$  is the work hardening exponent which is a function of temperature and strain rate estimated at a distance  $d$  from the crack tip. Experiments with low, medium and high strength steels to evaluate the tensile instability zone size ( $d_T$ ) showed widely differing values, but for each class of steels they appeared to be constant regardless of temperature and compressive loading rate. Using this model, Krafft suggested that fracture performance would be favored by a large tensile instability zone size and by high relative strain hardening.

McClintock and Irwin [1965] proposed that fracture would occur when the average strain in the plastic zone within a small distance from the crack tip exceeded the true fracture strain of the material. This analysis was based on Mode III anti-plane shear stress application. Here the structural length factor again enters and is intended to incorporate microstructural details and various mechanisms of fracture.

McClintock [1969] developed an analysis of the plastic fracture process for the case of equally spaced cylindrical holes parallel to the leading edge of the crack and lying in the plane of the crack, where interaction of the holes with

each other and logarithmic spiral slip lines associated with the crack tip were neglected. The fracture criterion employed the displacement required to join holes, and explicit expressions were proposed to relate this displacement to dimple size and particle spacing.

Rice and Johnson [1970] employed rigid plastic slip line theory to model void growth and coalescence. They proposed that ductile fracture occurs when some critical fracture strain is achieved at a point a given distance from the crack tip which is related to grain size or mean spacing of second phase particles. They concluded that the crack tip opening displacement should be on the order of 1 to 2.3 times the particle spacing. Employing the results of Rice and Tracey [1969], Rice and Johnson calculated the crack opening displacement at fracture from a simple model of a spherical cavity positioned ahead of the crack tip. From this analysis, they developed numerical results for critical crack tip opening displacements which depended strongly on the choice of the particle distance and diameter. However, the critical distance was shown to increase with particle spacing.

Green and Knott [1976] applied the model of Rice and Johnson [1970] to model fibrous fracture in steels. Slip line field analysis was employed, and the basis for their analysis was that the ligament between the crack tip and nearest inclusion must be strained sufficiently for a void to be nucleated, grow and coalesce with the crack tip. In non-hardening materials, this was held to begin when the logarithmic spirals first



enveloped the inclusion. The critical crack tip opening displacement was predicted to be on the order of 0.5 times the inclusion spacing. Where work hardening occurs, strain distribution ahead of the crack tip is more widespread, which in turn results in critical crack tip opening displacement values which are predicted to be from 0.5 to 2.5 times the inclusion spacing. This model was used to qualitatively address the effects of work hardening and inclusion content and spacing on the the ductile fracture toughness of structural steels.

Green and Knott [1976] and Clark, et al. [1978] examined the predictions from the model of Rice and Johnson for a wide variety of steels assuming an internal necking mechanism. Some steels conformed to the prediction of critical COD, but many were substantially below prediction in measured toughness. These authors ascribed this to the fact that localized shear fracture occurred following the logarithmic slip lines, and thus retarded void formation.

As pointed out by Ritchie and Thompson [1985], the models of McClintock, and Rice and Johnson imply that fracture toughness increases with yield strength. This led to further modelling of the fracture process. Mackenzie, et al. [1977] evaluated four high strength steels varying in yield strength from 360 to 910 MPa (80-130 ksi) where they determined the effective plastic strains necessary to initiate failure under different stress states using notched tensile specimens. Three parameters of stress and strain state including the effective stress, mean

stress and effective plastic strain were defined in terms of the principal stress and increments of plastic strain. Correlation of the stress state parameters and effective plastic strain at failure initiation showed that the effective plastic strain to initiate failure was strongly dependent on the state of stress in the high strength steels. This is in agreement with the conclusions of McClintock regarding the importance of stress state in the void growth and coalescence process. Mackenzie, et al. [1977] then addressed fracture from cracks or notches and suggested a modified initiation criterion based on attainment of some critical fracture strain at some distance below the surface of the crack or notch. This distance is a measure of the minimum amount of material in which the fracture mechanism can operate.

Ritchie, et al. [1979] proposed an expression for fracture toughness under small scale yielding conditions which combined stress and strain as suggested by Mackenzie, et al. [1977]. This model predicted fracture toughness as:

$$K = \text{constant } (\bar{\epsilon}_f^* \cdot l_o^* \cdot \sigma_y \cdot E)^{1/2} \quad (12)$$

where:  $\bar{\epsilon}_f^*$  = critical fracture strain;  
 $l_o^*$  = characteristic distance;  
 $\sigma_y$  = yield stress;  
 $E$  = Elastic modulus.

The value of the critical distance parameter was found to be some small multiple of interparticle spacing as ductile fracture was observed to proceed by shear localization between a number of voids nucleated at the largest particles in the steels investigated. This model was evaluated for SA 302 Gr B and SA 533B-1 steels where the critical distance was varied. These authors concluded that the characteristic distance in the stress modified critical strain model depended on the microstructure and number of major voids which coalesce with the main tip at fracture initiation.

Stout and Gerberich [1978] applied mathematical models to describe opening mode ductile fracture in Inconel 718 using the concept of the critical strain being reached over a particular distance for voids to grow. Their results indicated that fracture initiated at carbide and nitride packets by formation of delaminations. For the case of lower strength conditions where void growth and coalescence prevailed, the width of the carbide packets was the distance most applicable to the model. Where void formation was interrupted by shear steps, the inner carbide spacing distance was seen to be applicable.

#### CRACK ARREST

Unlike the cleavage fracture and ductile tearing processes, the description and modelling of the micro-mechanisms of crack arrest are relatively limited. Hahn, et al. [1970] conducted a series of crack arrest experiments utilizing a Fe-3%Si steel model material. Double cantilever beam specimens were wedge

loaded at 0°C (32°F), and rapid propagation occurred followed by arrest. Plastic zones which recorded plastic deformation up to 5% strain were observed at the surface and on the midsections by etching techniques. For the case of cleavage initiation, a large plastic zone existed near the original machined slot tip consistent with the loading required to initiate fracture. However, the unstable cleavage crack proceeded with no evidence of continuous deformation on either side of the crack. Deformation was associated almost exclusively with unbroken ligaments left behind the crack front. Subsequent metallographic sectioning revealed that all cracked segments were connected. Upon arrest, deformation at the crack tip was again observed. Hahn, et al. speculated that all or part of the deformation attending arrest may have been produced by elastic energy stored in the testing system which was released after the crack had arrested, and was possibly unrelated to factors causing arrest. The role of the unbroken ligaments in the fracture process was discussed, and it was suggested that such ligaments can reduce the stress intensity of the crack tip by a factor of two.

Hoagland, et al. [1972] conducted unstable crack propagation and arrest tests of plain carbon steel, 3%Si steel, A 517 and 4340 steels. Unstable fractures were initiated in double cantilever beam specimens using wedge loading where the strain energy stored in the specimen at the onset of propagation was varied systematically by varying the radius of the starting slot. Detailed metallographic examination was carried out,

and for the case of the Fe-3Si steel included etching studies to reveal the extent of plastic deformation associated with fracture.

In both the Fe-3Si and mild steel, the fractographic examination showed that the fracture mode was predominantly cleavage, but a few small isolated areas showing evidence of dimples were also observed. The crack profiles of the mild steel specimens showed that the cleavage path was quite discontinuous, and numerous unbroken ligaments were left behind as the crack extended. These unbroken regions existed on the order of 12mm (0.5-inch) behind the arrested crack tip, and had grain size dimensions. They were also more numerous near the crack tip, indicating that the opening of the crack involved rupturing of these ligaments. The occurrence of isolated dimpled regions was related to the ductile rupture of these ligaments. Progressive sectioning of the crack profiles showed that no microcrack was completely isolated. Etching studies of the Fe-3Si steel showed that deformation was confined almost entirely to ligaments left behind by the advancing crack front. Ligaments became thicker and more numerous as the test temperature was raised from -75 to 100°C (-103 to 212°F).

In the quenched and tempered A 517 steel, crack propagation was also by cleavage at the test temperature of -196°C (-321°F), but the cleavage facets were smaller and more irregular than those in the mild steel and Fe-3Si. Areas of ductile tearing were also present, and in profile the crack path was also

discontinuous over the entire length. Near the crack tip, the path became quite discontinuous. Rupture of these ligaments apparently occurred at a relatively small crack opening displacement since they were confined to the crack tip region. Similar behavior was noted in the 4340 steel.

Hoagland, et al. [1972] developed an estimate of the energy dissipated by the ligaments in the fracture process. The ligamented crack was treated as a crack in an infinite elastic plate with a portion of the crack loaded by a regular array of point forces which represented the ligaments. Using average dimensions of the unbroken ligament size, spacing, and crack length, calculation of dissipation energy showed that these ligaments can substantially reduce the crack tip stress intensity, and afford the principal energy sink during propagation.

Bullock and Smith [1977] evaluated effects of grain size and temperature on fracture propagation and arrest in mild steel. Charpy specimens were nitrided to eliminate shear lip formation and produce crack initiation sites. Mechanical tests were carried out in four-point bending at temperatures ranging from  $-128$  to  $-23^{\circ}\text{C}$  ( $-198$  to  $-9^{\circ}\text{F}$ ), and tests were terminated at the point of load drop. Specimens were slit longitudinally at midsection to allow metallographic and fractographic examination. All specimens fracture by cleavage irrespective of the initial  $K$  level or test temperature. Arrested cracks showed unruptured links in the vicinity of the crack tips. In specimens with initially short cracks, more extensive linking was observed as

temperature was increased, while specimens containing longer cracks showed decreasing ligament size as temperature was increased, and also showed evidence of kinked arrest fronts.

Hahn, et al. [1980b] conducted crack propagation and arrest measurements using four plates of A 533B steel, two A 508-2 forgings and a submerged arc weldment. These materials were tested with duplex specimens with stiff wedge loading. Prominent unbroken ligaments were observed on the fracture surfaces of the A 508 and A533B steels, and microscopic examination showed ductile areas interrupted with cleavage in these steels. Very large shear strains were evident in failed ligaments which joined non-coplanar sheets of cleavage. The failure of these ligaments was brought about by formation and linking of voids originating at cementite particles. Shear walls were observed perpendicular to the crack and their length oriented parallel to the direction of crack propagation was much greater than their height. An evaluation of the plastic work term due to shear wall fracture was developed using the stress-strain properties of the steels, measurements of the thickness of the deformed regions adjacent to the shear walls, and areal fraction of ductile rupture.  $K_a$  values were estimated from the plastic work term and showed good agreement with the crack arrest toughness measurements. This led Hahn, et al. to conclude that the crack arrest toughness was determined to a large extent by the process of formation and rupture of shear walls normal to the crack plane.

## EXPERIMENTAL DESIGN

## MATERIALS

The HY-80 plate used in this investigation was produced in the form of 31.8mm (1.25-inch) thick plate which was rolled to widths of 2438mm (96-inches). The mill production schedule of this particular heat of steel was not available. The chemical composition of this plate is given in Table 2. Here it can be seen that this plate meets the specification requirements of HY-80 steel.

The ASTM A710 Grade A Class 3 steel plate was produced by Lukens Steel Corporation. Heat D6873 was produced in a 150 ton capacity electric furnace using a cold metal charge, and subsequently vacuum degassed using the Dortmund Hörter process. Calcium treatment for sulphide shape control was also accomplished using argon blowing. The melts were continuously cast into slabs of cross section 2159mm x 229mm (85 x 9-inches). Heating for rolling was performed in a soaking pit furnace to approximately 1177°C (2150°F), and plates were air cooled after rolling. Heat treating was accomplished in a continuous gas fired furnace, and water quenching was accomplished by spray methods. This plate was austenitized at 904°C (1660°F) for one hour, then water quenched, and aged at 593°C (1100°F) for a period of 60 minutes, then water quenched. The plate was supplied at a thickness of 25.4mm (1-inch), and in a width of 2438mm (96-inches). The chemical composition of the ASTM A710 Grade A Class 3 steel plate used in this investigation is shown in Table 2. Here



it can be seen that the carbon content is near the upper limit of the specification, but all other constituents are well within the specification limits.

#### MECHANICAL PROPERTIES TESTS

##### Room Temperature Tensile Tests

Room temperature tensile tests were performed with standard 1.28mm (0.505-inch) diameter round bar specimens shown in figure 10. Specimens were oriented transverse to the rolling direction of the plates, and were removed from the quarter points of the plate thickness. Triplicate tests were performed according to ASTM E 8-81. A Southwerk Emery hydraulic test machine and Satec model PS2M 1052 extensometer with a gage length of 50.8mm (2-inches) were employed for these tensile tests. Although the ASTM A710 Grade A Class 3 steel exhibited a distinct yield point, the 0.2% offset yield stress was evaluated for both steels.

##### True Stress-True Strain Tests

The evaluation of true stress versus true strain was carried out with "hourglass" specimens shown in Figure 11. Specimens were oriented transverse to the rolling direction, and were removed from the quarter points of the plate thickness. These tests were performed over the temperature range 22 to -132°C (72 to -205°F) in an Instron screw-type test machine. Diametral contraction was monitored through use of a clamp-on device placed at the narrowest part of the specimen neck which produced two simultaneous measurements of displacement from capacitance signals. This diametral extensometer was calibrated at room temperature

prior to testing over a displacement range of 1.5 mm (0.060-inch) using a HITEC Proximic 3201 SP amplifier. During testing, simultaneous load and diametral contraction signals were digitized using Fluke Model 8860A digital volt meters and stored on Tektronix Model 4907 flexible disks. All reduced temperature tests were conducted in closed chamber cooled by a jet of liquid nitrogen which was sprayed into the volume surrounding the specimen. A Type T thermocouple was peened into the lower specimen grip, and was used to monitor test temperature. Control of temperature was achieved through manually controlling the flow of liquid nitrogen into the chamber through a needle valve, and was found to be within 2.0°C (3.6°F) throughout the actual test period. All tests were conducted at a constant crosshead displacement rate of 0.63 cm/min (0.025in/min) to the point of maximum load, upon which the displacement rate was increased. Because of the limited travel capacity of the diametral extensometer, data acquisition was terminated at approximately 1.5mm (0.60-inch) of diametral contraction, but loading was continued to the point of fracture, and the fracture load was recorded. True stress versus true strain was calculated from measurements of actual minimum diameter and load. However, the fracture stress was not corrected for specimen necking. A typical test involved the storage of 200 pairs of load/diametral contraction data, and all of this data was analyzed. The yield stress was calculated using the 0.2% offset point from the stress strain plot, or in the case of low temperature tests

where a yield point was observed, from the lower yield point. The strain hardening exponent was calculated from the least squares fit of data from yield stress to the maximum load point plotted in terms of the logarithm of true stress versus true strain.

#### Charpy V-notch Impact Toughness Tests

Impact toughness over the temperature range 22 to  $-129^{\circ}\text{C}$  (72 to  $-200^{\circ}\text{F}$ ) using standard Charpy V-notch specimens shown in Figure 12. Specimens were removed from the quarter points of the plates, and notches were placed in the T-L orientation as shown in Figure 13. All tests were conducted following ASTM E 23-82 using a RIEHLE Model PI-2 test machine, and at least duplicate tests were conducted at each test temperature.

#### 5/8-inch Dynamic Tear Impact Toughness Tests

Additional impact toughness tests using the 5/8-inch dynamic tear specimen (Figure 14) were conducted over the same temperature range as the Charpy impact toughness tests. Specimens were removed from the surfaces of the plates. All tests were conducted following ASTM E-604-80 using a Southwest Research Institute Mark III double-pendulum test machine. Duplicate tests were performed at most test temperatures.

#### Fracture Toughness Testing

Fracture toughness tests were performed with modified 1T compact specimens shown in Figure 15. These allow load-line displacement measurements which are amenable to both  $J_{IC}$  and  $K_{IC}$  calculations. All specimens were side-grooved prior to precracking

to a total depth of 20 percent of the thickness. Cracks were placed in the T-L orientation, Figure 13. Specimens were fatigue precracked according to ASTM E-813-81, to a crack depth of approximately  $0.6 a/W$  where  $a$  is the crack length and  $W$  is the specimen width. The maximum stress intensity range employed in precracking was  $33 \text{ MPa}\sqrt{\text{m}}$  ( $30 \text{ ksi}\sqrt{\text{in.}}$ ).

J-integral tests in this investigation were conducted using the computer-interactive unloading compliance test procedure of Joyce and Gudas [1978]. This involved a series of approximately 10% unloadings during the course of a conventional fracture mechanics test. For all tests, the values of crack length and changes in crack length were calculated from elastic compliance measurements using the expression of Saxena and Hudak [1978].  $J$  was calculated according to the expression of Ernst, et al. [1981] utilizing incremental area under the load displacement record between lines of constant displacement. Load and displacement data were digitized using Fluke model 8860A digital voltmeters, and this data was stored on Tektronix Model 4907 flexible disks.

Fracture toughness tests were performed over the temperature range 22 to  $-168^{\circ}\text{C}$  ( $72$  to  $-271^{\circ}\text{F}$ ). The tests were performed in an Instron screw-type test machine, and as in the case of the true stress-true strain tests, utilized a closed chamber cooled by liquid nitrogen spray for temperature reduction. Thermocouples were attached to the back face of the specimens, and the leads were directed out of the chamber through an access port. Tempera-

ture was manually controlled throughout the test using a needle valve to within 1.5°C (2.7°F).

For tests exhibiting stable crack extension,  $J_{IC}$  values were computed according to ASTM E 813-81 from the intersection of the blunting line with the least squares fit of data points which fell at least 0.15mm (0.006-inch) beyond this line, and did not exceed 1.5mm (0.06-inch) in crack growth from the blunting line. Valid J and crack extension data points were fit sequentially through this region of crack growth, and the  $J_{IC}$  point was selected as that which showed the first peak in correlation with the straight line fit. In certain tests, the development of the resistance curve was terminated by the onset of cleavage fracture. Here the  $J_I$  value was estimated from the limited data, or if no tearing occurred, the J value at the point of initiation was recorded. All  $J_{IC}$  values and  $J_I$  values for initiation of cleavage were converted to values through the following expression:

$$K(J) = (J \times E)^{1/2} \quad (13)$$

where E is the elastic modulus.

#### CRACK ARREST TESTING

The approach to evaluate crack arrest toughness in these steels was a modification of that employed in the ASTM Cooperative Test program in that large, split-pin wedge-loaded compact crack arrest specimens were tested with a linear temperature gradient. The purpose of the gradient was to provide crack tip conditions which would lead to cleavage crack initiation under controlled

conditions, and provide variable toughness throughout the range of crack growth. Figure 16 shows the specimen which was used for these tests, and Figure 17 shows the arrangement of the split pins and wedge employed for all tests. Two tests of HY-80 steel were carried out with similar specimens where the thickness was 31.8mm (1.25-inches), and the ligament was 356mm (14-inches) and 406mm (16-inches) respectively, and the side-groove depth was 25% of the maximum specimen thickness. These tests were used for developing the specific test procedures employed in these experiments.

The compact crack arrest specimens were produced with cracks placed in the T-L orientation. Each specimen was fatigue pre-cracked prior to testing using the remote holes in the load line. An MTS servo hydraulic test machine was used for precracking, and fatigue cracks were typically 4mm (0.16-inch) in length. The maximum stress intensity reached in precracking was 39  $\text{MPa}\sqrt{\text{m}}$  (35  $\text{ksi}\sqrt{\text{in.}}$ ). In several of the tests, a chevron was saw-cut into the specimen at the crack tip to reduce the area of crack front intended to trigger cleavage, hence reduce the applied stress intensity for crack initiation.

Prior to testing, thermocouples were placed along the face on one side of the specimens parallel to the side groove. Iron-Constantan (Type-T) thermocouples were peened into holes drilled 25.4mm (1-inch) away from the side-groove. Holes for containing the thermocouples were drilled to a depth of 2.5mm (0.1-inch), and had a diameter of 3.2mm (0.125-inch). After peening

into the specimen, the area surrounding the individual thermocouples was covered with an epoxy resin which served to protect the positioning during testing. A minimum of 7 thermocouples were placed from the machined notch tip to within 5mm (0.2-inch) of the back wall of the specimen. The thermocouples were placed 38.1mm (1.5-inches) apart.

After placement of thermocouples, heater strips were placed along the back edge of the specimens. The entire test section of each specimen was then covered with styrofoam insulation. The front end of the specimen was left uncovered so that the specimen could be placed in a liquid nitrogen bath to a level which reached to within 50mm (2-inches) of the crack tip.

Instrumentation for crack arrest tests consisted of a temperature sampling and graphical plotting system, and displacement and load transducers for measuring crack opening displacement and force on the wedge during loading. The thermocouples were led to a Hewlett-Packard temperature compensating junction, and then individually read with a Hewlett-Packard Model 3495A scanner. Measurements of temperature were then plotted on a Tektronix 4051 micro-computer, and the least-squares linear regression of the slope of the temperature gradient at the time of the sampling was calculated, and the straight line was fitted through the actual data, and copied with a Tektronix 4631 copy unit. Analysis of temperature data was typically carried out at 5-minute intervals during specimen cooling, then 30 second intervals when the actual crack arrest test was conducted. The stress

intensities for initiation and arrest of cracks were calculated from the solution produced by Crosley, et al. [1983], and subsequently recommended for use in the ASTM Round Robin Test program. This expression which allows calculation of K from measurements of crack opening displacement is as follows:

$$K = E \delta f(a/W) \sqrt{B/B_n} / \sqrt{W} \quad (14)$$

where:

E = Elastic modulus;

B = Maximum specimen thickness;

B<sub>n</sub> = Minimum specimen thickness across side grooves;

W = Specimen width;

a = Initial crack length or length of arrested crack

δ = Initial clip gage displacement or arrest clip gage displacement;

$$f(a/W) = \frac{2/24(1.72-0.9(a/w)+(a/w)^2)(1-a/W)^{1/2}}{(9.85-0.17(a/W)+11(a/W)^2)}$$

This K expression is valid for crack mouth opening displacement measurements obtained a distance 0.25W in front of the load line. For these tests, crack opening displacement measurements were taken at a location 76.2mm (3.0-inches) behind the load line, and the extrapolation of this displacement to the point 0.25W in front of the load line was made with the Saxena and Hudak [1978] expression which allows calculation of crack opening displacement at any location on a compact specimen. Displacements at crack initiation and arrest were then converted to front face displacements, and these calculated values of displacement were used in



the  $K_0$  and  $K_a$  calculations.

Crack arrest tests were carried out essentially according to recommended procedures in the current ASTM Crack Arrest Round Robin Test Program. Specimens were placed vertically in a bath of liquid nitrogen, and temperature along the specimen width was monitored. When the target temperature for crack initiation was reached (or typically exceeded), the heaters were energized, and the slope of the temperature gradient was linearized. The specimen was then placed on the bed of a Tinius Olsen Model test machine where the flange of the split pins was below the specimen, and the surface of the specimen was not in contact with the test bed. The front face of the specimen previously in the liquid nitrogen bath was insulated with styrofoam sheets, and the wedge was inserted into the split "D" arrangement. The flanges of the split pins rested on a 50mm (2-inch) thick, plate containing a slot for the wedge. For tests of HY-80, the loading platen, split pins and loading wedge were chilled in liquid nitrogen prior to placement. The wedge was then wrapped in Teflon sheet, and seated carefully between the split pins. During placement of the wedge, a Kamen model KP 2300-2S displacement gage was seated firmly on phenolic spacers which were previously attached to the specimen at a location 76.2mm (3.0-inches) behind the load line. The aluminum target plate for this eddy current transducer was placed in position prior to cooling, and any accumulated frost was carefully removed. The wedge was then loaded at a constant rate, and both load and

crack opening displacement were monitored. An X-Y recorder was used to record these signals in the analog mode, and these same signals were digitized as previously described in the fracture mechanics testing and stored on flexible disk. A digital load versus displacement record was also obtained during the test. Following crack initiation and arrest, the appropriate displacement values were obtained from the digital record of the test, and compared to the analog record to verify the accuracy of these measurements. The displacement transducers, thermocouples and heater strips were then quickly removed, and the specimen was placed in a furnace at 149°C (300°F) for 1 hour to preclude moisture condensation on the fresh crack surfaces.

Following successful testing of the crack arrest specimen, the bulk of the specimen surface area was cut away from the crack plane. Typically, the crack was contained in a sub-specimen whose height measured 76mm (3-inches), and where the side grooves were centered approximately 38mm (1.5-inch) from the top and bottom edges. The length of this sub specimen depended on the length of the crack jump, but was typically 50mm (2-inches) longer than the surface measurement of crack jump length. The front end of this sub-specimen was cut 12mm (0.5-inch) in front of the machined notch. This sub-specimen containing the arrested crack was then saw-cut longitudinally to produce two specimens of equal thickness. In one of these specimens, two 12mm (0.5-inch) holes were drilled on either side of the crack plane toward the front of the specimen away from the arrested crack tip, and

this sub-specimen was then placed in an MTS servo-hydraulic test machine. This double cantilever beam type sub-specimen was then loaded in fatigue at a high mean load to separate the crack faces and mark the extent of crack growth during the run arrest event. After it was thus broken open, the maximum crack length was measured, and measurements of the fatigue precrack at three equally spaced points along the crack front were also obtained, and these values were used to calculate  $K_0$  and  $K_a$  from the appropriate crack opening displacement measurements obtained during test. The actual crack length at arrest was also then used with the temperature gradient measurements to establish the arrest temperature. In this case, linear extrapolation between the thermocouple measurements obtained on either side of the arrest point was used to establish the arrest temperature at the point of maximum crack extension. The remaining sub-specimen from the crack arrest tests was used for metallographic analysis of the crack path. Samples which were 19mm (0.75-inch) in length were removed along the crack path, and specimens across the crack path were also removed and mounted for metallographic examination. These specimens allowed examination of the actual fracture path and the arrest event at the crack tip without disturbing the metal comprising the crack path.

#### METALLOGRAPHIC AND FRACTOGRAPHIC EXAMINATIONS

Both metallographic and fractographic examinations of many of the specimens tested in this investigation were conducted. Metallographic samples from fracture toughness specimens were

obtained by longitudinally cutting the compact specimens, and then removing the area of the specimen half containing the crack tip. These specimens were then vacuum impregnated with epoxy resin, and polished for examination. Other metallographic specimens from a variety of tests were conventionally mounted in hot presses, and polished for examination. Metallographic polishing was accomplished in ABPRAPOL automatic polishing equipment, but hand polishing of the ASTM A710 steel was required to successfully examine ferrite grain size and morphology. Two etchants used in this investigation included 2% Nital and 4% Picral. Metallographic examination was conducted on a Zeiss AXIOMAT light metallograph. Measurements of grain size and particle size were accomplished using a Zeiss Videoplan Measurement Tablet. Fractographic examination of etched metallographic specimens and fractured specimens were conducted on a JEOL Model JSM 35 scanning electron microscope.

## RESULTS AND DISCUSSION

### MECHANICAL PROPERTIES

#### Microstructure of High Strength Steels

Figure 18 presents optical photomicrographs of HY-80 steel where a 2% Nital etch was used after polishing. Here it can be seen that this steel possesses a fine tempered martensite structure, where the estimated mean prior austenite grain size is ASTM classification 9. Although dominated by tempered martensite laths, ferrite grains on the order of 2 to 10  $\mu\text{m}$  in diameter are observable. Figure 19 presents optical photomicrographs of ASTM A710 Gr. A Cl. 3 steel. Here the microstructure is polygonal ferrite with an average grain size of 6.2  $\mu\text{m}$ , and an ASTM grain size classification of 12. The high magnification photomicrographs show distinct dark regions which predominantly reside at grain boundaries or triple points, and which are clearly smaller than the typical grain size. These have been described by Jesseman and Murphy [1979, 1984] as lower bainite, the proportion of which is dependent on plate thickness (and by inference cooling rate from quenching). Cutler and Krishnadev [1982] identified this constituent in as-rolled plate as decomposed pearlite, lower bainite or autotempered martensite, and heavily twinned martensite. Krishnadev, et al. [1983] later identified this constituent as martensite-austenite (M-A).

#### Tensile Tests

The results of the room temperature tensile tests are

presented in Table 3. Here it can be seen that the HY-80 steel exhibits an average yield strength of 584 MPa (85 ksi) which places it in the lower end of the specification range. On the other hand, the ASTM A 710 Gr. A Cl. 3 steel displayed an average yield strength of 639 MPa (91 ksi), versus the specification minimum of 515 MPa (75 ksi). This yield strength level is likely the result of the carbon level in this heat which is just below the maximum allowed within this specification. According to the supplier, this heat was intended to obtain a minimum yield strength of 551 MPa (80 ksi), and the carbon content and heat treatment schedule are consistent with that objective.

Table 4 presents the results of the tensile tests performed over a range of temperatures in which true stress and true strain were measured. In examining yield stress, both steels showed a similar elevation as temperature was decreased to approximately  $-105^{\circ}\text{C}$  ( $-157^{\circ}\text{F}$ ). This is shown in Figure 20 where the yield strength of HY-80 and ASTM A710 Gr. A Cl. 3 steels is plotted against test temperature. This yield strength elevation is on the order of 22% over this temperature range, and for HY-80 tested at  $-132^{\circ}\text{C}$  ( $-205^{\circ}\text{F}$ ), the yield elevation is 34%. There is no published data regarding the temperature dependence of yield strength for ASTM A710 Gr. A Cl. 3 steel, but Harding [1977], and Hasson and Joyce [1981] performed such measurements with HY-80. The data from these two references is included in Figure 21, and it can be seen that the results

developed in this investigation coincide with these two studies. The results of Harding are below those of the current study over the range of common test temperatures, but this is likely the result of the lower yield strength of this particular heat as evidenced by the room temperature results.

One distinct difference in the steels is the change in fracture strain measured from diametral contraction over the test temperature range. Here HY-80 steel shows a progressive decrease as temperature is lowered, whereas the ASTM A710 Gr. A Cl. 3 steel exhibits essentially constant values. Furthermore, the ASTM A710 Gr. A Cl. 3 steel exhibits substantially higher levels of true fracture strain, ranging up to 28% greater than HY-80 at  $-106^{\circ}\text{C}$  ( $-159^{\circ}\text{F}$ ).

Calculations of strain hardening exponents were carried out for a stress-strain expression of the form:

$$\left(\frac{\bar{\epsilon}}{\bar{\epsilon}_0}\right) = \alpha \left(\frac{\bar{\sigma}}{\bar{\sigma}_0}\right)^n \quad (15)$$

where  $\bar{\epsilon}_0$  and  $\bar{\sigma}_0$  are the yield strain and yield strength respectively,  $\alpha$  is a material constant, and  $n$  is the strain hardening exponent. These results show that both steels have similar strain hardening behavior at room temperature, but HY-80 is shown to systematically increase its strain hardening as temperature is lowered, although the order of this increase is moderate. ASTM A710 Gr. A Cl. 3 steel shows an overall decreasing trend with temperature, but the order of change was

small, and obscured by scatter.

#### Impact Toughness Tests

Tables 5 and 6 present the results of the Charpy V-notch impact toughness tests performed in this study for HY-80 and ASTM A710 Gr. A Cl. 3 steels respectively. Figure 22 presents the impact toughness results versus test temperature for both alloys, Figure 23 presents the percentage of shear fracture, and Figure 24 presents the lateral expansion measurements. In these figures, the trend lines are placed at the lower bounds of the data. Figure 22 shows that while ASTM A710 Gr. A Cl. 3 steel has a distinctly higher impact energy on upper shelf, the temperature at which this alloy departs from upper shelf behavior is on the order of 25°C (45°F) higher than HY-80. This point is also made in Figure 23 where the departure from 100% shear fracture for HY-80 is 25°C (45°F) lower than ASTM A710 Gr. A Cl. 3 steel. This crossover in toughness properties where the ASTM A 710 Gr. A Cl. 3 steel is clearly superior on upper shelf, and HY-80 is seen to remain on upper shelf at lower temperatures and exhibit higher toughness in transition, presents the principal metallurgical and fracture mechanics center of interest for this investigation.

These impact toughness values for HY-80 are within the range of data reported by Heller, et al. [1965], Pellini [1977], and Rolfe and Barsom [1977]. The Charpy impact toughness of the 25.4 mm (1.0-inch) thick ASTM A 710 Gr. A Cl. 3 plate used in this investigation can be compared with results developed



in several recent studies of this alloy. Hydrean, et al. [1972] presented Charpy transition curves for IN-787 steel plate in thicknesses of 32mm (1.25-inch) and 50.8mm (2.0-inch). These showed upper shelf impact energies of approximately 238 J (175 Ft-lb) compared to 235 J (173 Ft-lb) average upper shelf energy of the steel in this study. Hydrean, et al. observed departure from upper shelf at  $-18^{\circ}\text{C}$  ( $0^{\circ}\text{F}$ ) which was similar to results obtained in this investigation. Jesseman and Murphy [1979] reported the temperature at which the CVN energy was 68 J (50 ft-lb) for quenched and aged 19 mm (0.75-inch) plate in the range  $-105$  to  $-115^{\circ}\text{C}$  ( $-157$  to  $-175^{\circ}\text{F}$ ) depending on aging temperature above  $600^{\circ}\text{C}$  ( $1112^{\circ}\text{F}$ ). Plate in 85mm (3.25-inches) thickness displayed 68 J (50 ft-lb) transition temperatures in the range  $-70$  to  $-80^{\circ}\text{C}$  ( $-94$  to  $-112^{\circ}\text{F}$ ) where the aging temperature ranged from  $590$  to  $650^{\circ}\text{C}$  ( $1094$  to  $1202^{\circ}\text{F}$ ) for specimens removed from the quarter thickness position of the plate. In this study, the 68 J (50 ft-lb) transition temperature was between  $-101$  and  $-84^{\circ}\text{C}$  ( $-150$  and  $-120^{\circ}\text{F}$ ), in agreement with the thicker plate data of Jesseman and Murphy [1979]. Cutler and Krishnadev [1982] reported the 27 J (20 ft-lb) temperature for as-rolled 19 mm (0.75-inch) plate in the overaged condition as  $-60^{\circ}\text{C}$  ( $-76^{\circ}\text{F}$ ). The 27 J temperature in this study was approximately  $-100^{\circ}\text{C}$  ( $-76^{\circ}\text{F}$ ). Jesseman and Murphy [1984] reported  $-46^{\circ}\text{C}$  ( $-50^{\circ}\text{F}$ ) Charpy impact toughness values from 83 mm (3.25-inch) plate aged in the temperature range  $620$  to  $675^{\circ}\text{C}$  ( $1150$  to  $1250^{\circ}\text{F}$ ) to be from 114 to 148 J (84 to 109 ft-lb) depending on aging

time. At this test temperature, the Charpy impact toughness of the ASTM A710 Gr. A Cl. 3 steel plate used in this study ranged from 148 to 196 J (109 to 144 ft-lb), indicating slightly higher toughness at this temperature. Hicho, et al. [1984] varied the precipitation temperature of 32 mm (1.25-inch) ASTM A710 steel plate. At an aging temperature of 593°C (1100°F), the Charpy impact energy was 175 J (129 ft-lb) when tests were performed at -17°C (0°F). Results from this study showed values in the range 250 J (184 ft-lb) at that test temperature. Finally, Montemarano, et al. [1984] reported results of Charpy impact toughness tests for 32 mm (1.25-inch) thick plate of ASTM A710 Gr. A Cl. 3 steel. Here the reported impact energies were slightly above those obtained in this study at -84 and -51°C (-120 and -60°F), and equivalent at room temperature. These results then point to the conclusion that this Class 3 ASTM A710 plate used in this investigation possesses typical Charpy impact toughness properties in comparison to other studies of this alloy.

Table 7 presents results of the 5/8-inch dynamic tear impact toughness tests, and the impact energy measured with both steels is plotted versus test temperature in Figure 25. Here it can be seen that the attainment of upper shelf with HY-80 occurs at approximately -60°C (-76°F), whereas the attainment of upper shelf in the ASTM A 710 Gr. A Cl. 3 steel is achieved somewhat below room temperature. Again there is a distinct elevation of upper shelf energy noted with ASTM A710 Gr. A Cl. 3

steel, and a distinct inversion of toughness level as temperature is lowered. These differences are consistent with the Charpy impact toughness results, and typical results with dynamic tear testing where the increased test section size contributes to a typically larger spread in impact toughness data for steels of varying toughness. Also as in the Charpy impact toughness measurements, the distinct elevation of upper shelf toughness of ASTM A710 Gr. A Cl. 3 steel is noted when compared to HY-80.

These dynamic tear impact toughness results for ASTM A710 Gr. A Cl. 3 steel are substantially different than those reported by Montemarano, et al. [1984] for 32 and 19 mm (1.25 and 0.75-inch) plate which was produced using inclusion shape control. Their dynamic tear impact toughness results showed impact energies of approximately 952 J (700 ft-lb) at  $-51^{\circ}\text{C}$  ( $-60^{\circ}\text{F}$ ) compared to values in the range 449 to 911 J (330 to 670 ft-lb) at  $-40^{\circ}\text{C}$  ( $-40^{\circ}\text{F}$ ) obtained in this study. As temperature was raised to  $-18^{\circ}\text{C}$  ( $0^{\circ}\text{F}$ ), the results of Montemarano, et al. were a factor of two higher than those measured in these impact toughness tests. Here the elevated yield strength and high carbon content of the alloy used in this investigation may have led to the steep drop in impact toughness observed in these tests.

#### FRACTURE TOUGHNESS TESTS

Figure 26 presents load versus load-line deflection results for three compact specimens of HY-80 which exhibited fully ductile tearing, tearing interrupted by cleavage, and cleavage

respectively in tests performed at different temperatures. The corresponding J-integral resistance curves which developed to varying degrees of crack extension are shown in Figure 27. Similar information for ASTM A710 Gr. A Cl. 3 steel is shown in Figures 28 and 29 respectively. As discussed earlier, the  $J_{IC}$  values for cases of full resistance curve development were calculated according to ASTM E 813. Where only limited tearing was observed followed by cleavage, an approximate extrapolation to the blunting line was used to identify the  $J$  value for initiation of tearing, and the  $J_I$  value for cleavage was calculated from the point of cleavage instability.

Table 8 presents results of fracture toughness tests performed with HY-80 steel, and similar results for ASTM A 710 Gr. A Cl. 3 Steel are presented in Table 9. These tables include information on test temperature, the mode of crack extension observed during the test, the elastic-plastic fracture toughness  $J_{IC}$  calculated from resistance curve measurements, and  $J$  values for initiation of tearing followed by cleavage, or initiation of cleavage without tearing.

Several investigators have reported results of fracture toughness measurements of HY-80 steel. Little plane strain fracture toughness ( $K_{IC}$ ) data is available due to the large section size required to validly test this very tough steel. Shoemaker and Rolfe [1971] evaluated  $K_{IC}$  over a broad temperature range, and reported valid measurements of 68 and 61  $\text{MPa}\sqrt{\text{m}}$  (62 and 55  $\text{ksi}\sqrt{\text{in.}}$ ) at  $-196^\circ\text{C}$  ( $-320^\circ\text{F}$ ). Clayton and Knott [1976]

evaluated the crack opening displacement of HY-80 plate in relation to the level of prestrain. They converted the COD measurements to equivalent K values using a small scale yielding solution, and reported fracture toughness of  $182 \text{ MPa}\sqrt{\text{m}}$  ( $163 \text{ ksi}\sqrt{\text{in.}}$ ) for steel tested without prestrain. Hasson and Joyce [1981] conducted static and accelerated loading rate  $J_{Ic}$  tests of HY-80 over a broad temperature range. They showed that as temperature was decreased from room temperature to  $-140^\circ\text{C}$  ( $-220^\circ\text{F}$ ), fracture toughness first increased for the case of ductile tearing, then fell abruptly as temperature was further lowered, and cleavage fracture without prior ductile tearing occurred. A 44% elevation in fracture toughness was noted prior to the reduction associated with cleavage fracture. Room temperature fracture toughness was  $133 \text{ kJ/m}^2$  ( $757 \text{ in-lb/in}^2$ ). Vassilaros, et al. [1982] evaluated tearing instability concepts employing J-integral resistance curve measurements with HY-80 steel, and reported room temperature fracture toughness as  $176 \text{ kJ/m}^2$  ( $1000 \text{ in-lb/in}^2$ ). Most recently, Joyce and Hackett [1984] conducted static and dynamic J-integral resistance curve measurements using HY-80. The average quasi-static fracture toughness from unloading compliance measurements was  $168 \text{ kJ/m}^2$  ( $956 \text{ in-lb/in}^2$ ).

Three studies of the dynamic fracture toughness of HY-80 steel have been reported. Shoemaker and Rolfe reported results of impact tests of bend bars where  $K_{Ic}$  was determined over the temperature range  $-196$  to  $-94^\circ\text{C}$  ( $-320$  to  $-138^\circ\text{F}$ ) [1971]. Over this

range,  $K_{Ic}$  increased from 31 to 70  $\text{kPa}\sqrt{\text{m}}$  (28 to 64  $\text{ksi}\sqrt{\text{in.}}$ ), with substantial scatter in the data. The accelerated loading rate tests of Hasson and Joyce [1981] showed  $J_{Ic}$  increasing from 14  $\text{kJ/m}^2$  (80  $\text{in-lb/in}^2$ ) at  $-192^\circ\text{C}$  ( $-314^\circ\text{F}$ ) to a plateau in the range 98 to 149  $\text{kJ/m}^2$  (555 to 848  $\text{in-lb/in}^2$ ) where test temperature exceeded  $-140^\circ\text{C}$  ( $-229^\circ\text{F}$ ). Joyce and Hackett [1984] reported impact rate fracture toughness values for HY-80 in the range 343 to 383  $\text{kJ/m}^2$  (1952 to 2179  $\text{in-lb/in}^2$ ) for tests conducted at room temperature.

In examining the results of fracture toughness tests performed with HY-80 steel presented in Table 8, it can be seen that the ambient temperature results fell within scatter of previously published data. Figure 30 is a plot of  $J_{Ic}$  or  $J_I$  versus test temperature which includes results of this study and those of Hasson and Joyce which are the only other systematic data developed over this temperature range. Here it is seen that the fracture toughness increases as test temperature is lowered for the cases where ductile tearing occurs, and then decreases as cleavage fracture occurs. The temperature for initiation of cleavage fracture appears to be the same in both studies, but Hasson and Joyce did not explicitly note this in their discussion.

Fracture toughness measurements for ASTM A710 Gr. A C1. 3 steel are less numerous than seen with HY-80 due to the relatively recent development of this steel, and its very high level of fracture toughness on the upper shelf. Here again the

use of elastic-plastic fracture mechanics is necessary to validly characterize fracture toughness. Cutler and Krishnadev [1982] reported fracture toughness for overaged as-rolled class 1 plate in the range  $190 \text{ kJ/m}^2$  ( $1081 \text{ in-lb/in}^2$ ) at temperatures above  $-20^\circ\text{C}$  ( $-4^\circ\text{F}$ ). Below this temperature, the fracture toughness fell abruptly. Miglin, et al. [1983] reported low temperature  $K_{Ic}$  and room temperature J values for initiation of tearing of ASTM A710 Gr. A steel in the quenched and overaged condition. At  $-196^\circ\text{C}$  ( $-320^\circ\text{F}$ ), the  $K_{Ic}$  of this steel was  $33 \text{ MPa}\sqrt{\text{m}}$  ( $30 \text{ ksi}\sqrt{\text{in.}}$ ). At room temperature, J for initiation was approximately  $465 \text{ kJ/m}^2$  ( $2646 \text{ in-lb/in}^2$ ) for both overaged conditions tested. These authors pointed out that these values were clearly invalid for the 19 mm (0.75-inch) thick specimen tests. Most recently, Montemarano, et al. [1984] reported room temperature, static load rate J-integral resistance curve measurements for a selection of ASTM A710 Gr. A Cl. 3 steels. For plate in the thickness range 32 to 16 mm (1.25 to 0.625-inches) where inclusion shape control treatment was used,  $J_{Ic}$  ranged from 394 to 234  $\text{kJ/m}^2$  (2243 to 1330  $\text{in-lb/in}^2$ ).

Figure 31 presents results of the J-integral fracture toughness tests versus test temperature which were performed with ASTM A710 Gr. A Cl. 3 steel and which are detailed in Table 9. Here the average room temperature fracture toughness of  $260 \text{ kJ/m}^2$  ( $1453 \text{ in-lb/in}^2$ ) is below the values reported by Miglin, et al. [1983] for quenched and overaged plate, and is equal to the lower bound of data reported by Montemarano, et al. [1984] for

Class 3 plates which received inclusion shape control processing. This level of fracture toughness measured in this study is consistent with the fact that the yield strength of the plate (630 MPa) is higher than those reported by these authors, and is significantly above the specification minimum for this alloy.

Figure 32 presents the results of the fracture toughness tests performed with both HY-80 and ASTM A710 Gr. A Cl. 3 steels over the full range of temperatures tested. This figure very clearly shows the distinct fracture differences which were indicated by the impact toughness test results. Here the upper shelf fracture toughness of ASTM A710 Gr. A Cl. 3 steel is 2.2 times that of HY-80 when comparing values at temperatures just above which cleavage initiation was observed, and 1.8 times higher than HY-80 when comparing values at room temperature. This figure also shows that ASTM A710 Gr. A Cl. 3 steel exhibits cleavage fracture at a temperature of  $-19^{\circ}\text{C}$  ( $-3^{\circ}\text{F}$ ), whereas HY-80 first was shown to cleave at  $-118^{\circ}\text{C}$  ( $-180^{\circ}\text{F}$ ). This 100 deg shift in cleavage initiation temperature leads to a distinct inversion in ranking of fracture toughness. That is, at any given temperature below approximately  $25^{\circ}\text{C}$  ( $-13^{\circ}\text{F}$ ), ASTM A 710 Gr. A Cl. 3 steel fracture toughness is always below that of HY-80. Further, the mode of fracture with HY-80 in these quasistatic tests is ductile tearing down to approximately  $-104^{\circ}\text{C}$  ( $-156^{\circ}\text{F}$ ), whereas all tests of ASTM A710 Gr. A Cl. 3 steel exhibit cleavage fracture in this temperature



range. The slopes of the cleavage fracture toughness versus temperature curves (filled points in Figure 32) are similar for both alloys, but offset by approximately 75°C (135°F).

Another result from these tests relates to the elevation of ductile fracture toughness with decreasing temperature prior to the point of cleavage initiation. Shih [1981] developed a relation for  $J$  and crack tip opening displacement for small scale yielding which is as follows:

$$J = n\sigma_y\delta \quad (16)$$

where  $n$  is a proportionality factor which depends on yield strength, work hardening exponent and the assumption of plane stress or plane strain conditions,  $\delta$  is the crack tip opening displacement, and  $\sigma_y$  is yield strength. If the assumption is made that the strain hardening change is negligible over this temperature range of interest, and that the critical crack tip opening displacement is constant for initiation of tearing at all temperatures, then the increase in ductile fracture toughness should be totally related to yield strength elevation. To test this hypothesis, ratios of yield strength versus yield strength at 22°C (72°F), and  $J_{Ic}$  versus  $J_{Ic}$  at 22°C (72°F) were calculated. These are plotted in figure 33. In this case, the upper bounds of the data were fitted with trend lines. Here it can be seen that the elevation of fracture toughness of HY-80 increases at a rate somewhat higher than yield strength as temperature is lowered to -103°C (-153°F). Although the data is over a much more limited range, the elevation of fracture

toughness of ASTM A710 Gr. A Cl. 3 steel bears little correlation with the yield strength elevation, and is substantially higher in rate of increase. This indicates that the large strain component of plasticity plays a major role with the ASTM A 710 Gr. A Cl. 3 steel in elevating fracture toughness.

#### CRACK ARREST TOUGHNESS

Table 10 presents results of compact crack arrest specimen tests of NY-80 steel, and Table 11 presents results obtained with ASTM A710 Gr. A Cl. 3 steel. These tables include the specimen dimensions, temperature gradient slope, test measurements related to crack length and displacements for calculating values of  $K$  at cleavage crack initiation and arrest, and temperature at the tip of the arrested crack.

The conduct of these crack arrest tests was an iterative process where results from one test were used to set the parameters for the next. The overall approach was directed to obtaining crack arrest values over several different temperatures for each steel in order to compare the  $K_a$  versus temperature curve with that obtained in the static fracture toughness tests. The key test variables which were controlled were the  $K$  value at initiation, and the slope of the temperature gradient which was imposed along the specimen width. The  $K_0$  values were changed by changing the depth of chevron placement at the crack tip, and by the temperature at the crack tip at the instant of cleavage crack initiation. The key point here was to obtain a  $K_0$  level sufficient to drive the crack a distance of at

least twice the specimen thickness prior to arrest, and which was not so high as to induce crack branching. The length of crack jump at a given  $K_0$  level was then dependent on the slope of the temperature gradient, where a long crack jump was expected for a shallow gradient, and a shorter jump for the steeper gradient. The temperature gradient slope was controlled during the tests by the proximity of the liquid nitrogen bath to the crack tip, and sequencing and amount of heating applied to the back wall of the specimen.

Figure 34 presents plots of test temperature versus crack position for typical high and low temperature gradient tests, where trend lines were fit from least squares linear regression analysis. Here it is seen that the temperature gradients were quite linear. For the HY-80, because of the very low temperatures for crack initiation, the specimen was tested within 5 minutes after removal from the liquid nitrogen bath. The maximum temperature for crack initiation was  $-131^{\circ}\text{C}$  ( $-204^{\circ}\text{F}$ ). The ASTM A710 Gr. A Cl. 3 steel specimens were in position in the tensile test machine for as much as 15 minutes prior to establishment of the target crack tip temperature and gradient. Figure 35 is a plot of load versus crack opening displacement for one HY-80 and one ASTM A710 Gr. A Cl. 3 steel test. These are typical of the data obtained from the digital data acquisition system, and which were compared with the signals obtained from the analog recording system. The HY-80 showed substantially higher crack opening displacement increases with crack jump

than the ASTM A 710 Gr. A Cl. 3 steel. All HY-80 specimens initiated cracking on the first load application. One ASTM A710 Gr. A Cl. 3 specimen (GGO-4) was first loaded at a crack tip temperature of  $-21^{\circ}\text{C}$  ( $-5^{\circ}\text{F}$ ), and after no crack initiation was observed, unloaded and cooled to a crack temperature of  $-48^{\circ}\text{C}$  ( $-54^{\circ}\text{F}$ ), where a cleavage crack was initiated upon reloading.

Table 10 presents results for five CCA specimen tests of HY-80 steel. The first two were conducted using full plate thickness (32 mm) specimens, and the remaining tests were conducted with 25.4 mm (1-inch) thick specimens. This was done to provide geometric similarity with tests of ASTM A710 Gr. A Cl. 3 steel which was supplied in a thickness of 25.4 mm (1-inch). Specimen FYB CCA-2 had a width of 406 mm (16-inches), but the remaining specimens were all 356 mm (14-inches) wide. The temperature gradients achieved in the HY-80 tests ranged from 0.21 to  $0.44^{\circ}\text{C}/\text{mm}$  (9.9 to  $20.3^{\circ}\text{F}/\text{inch}$ ). In this test series, specimen FYB CCA-1 was loaded to a K level of  $301 \text{ MPa}\sqrt{\text{m}}$  (274 ksi/in.) at initiation, and crack branching occurred. Because a dominant branch progressed parallel to the crack plane, a crack arrest value was calculated. This value is artificially high in both crack arrest temperature and crack arrest toughness because much of the fracture energy was consumed in the branching process. The occurrence of branching led to the use of the saw-cut chevron to reduce initiation fracture toughness. The remaining four HY-80 CCA specimens all

resulted in long crack jumps with little or no crack branching. Figures 36 through 39 are photographs of the crack path of the four successful HY-80 crack arrest tests. These specimens were obtained by cutting the full scale specimen longitudinally, then opening the remaining crack in fatigue. The photographs in Figures 36 to 39 include only one-half of the thickness of the specimen. The cracks were seen to remain substantially within the plane of the side groove, or just displaced slightly from this plane for the entire crack jump event. Where cracks were out of the plane of the side grooves (specimens FYB 1A and 3A), a moderate degree of tunnelling was observed at the arrest crack tip associated with pinning the crack tip at the root of the side groove, and continued growth of the crack in the center of the specimen. This tunnelling was confined to the outer 20% of the specimen thickness.

Figure 40 presents results of the crack arrest tests of HY-80 steel plotted versus test temperature. This figure also includes the results of the fracture toughness tests which were introduced earlier, plotted in this case in terms of  $K(J)$ , where scatter bands to encompass the upper and lower range of measured and expected transition data were drawn. Here it can be seen that the  $K_a$  versus temperature data follows the same trend as the fracture toughness results. However, the  $K_a$  data is displaced to the right of the static fracture toughness curve by approximately 60 to 70°C (108 to 126°F). This result is expected as crack arrest toughness is a lower bound measurement

of the dynamic fracture toughness.

Because these are the first measurements of the crack arrest toughness of HY-80, there were no direct comparisons with other results. However, the results of dynamic fracture toughness measurements of this steel from Shoemaker and Rolfe [1971] and the accelerated load rate measurements of Hasson and Joyce [1981] provide some basis for assessment of dynamic effects. The static fracture toughness and crack arrest toughness measurements obtained in this study are plotted in Figure 41 with results of Shoemaker and Rolfe, and Joyce and Hasson. Again, the comparison is based on  $K$  (J) calculations for the static fracture toughness results. Here a clear rate effect is shown where the  $K$  versus temperature curves for the various loading rates are clearly displaced from one another. The results from static fracture toughness tests are displaced farthest to the left (low temperature regime), and the  $K_{IC}$  and impact-loading  $K_{IC}$  tests of Shoemaker and Rolfe are farthest to the right (high temperature regime) but clearly merge with the results produced in these crack arrest tests. The accelerated loading rate tests of Hasson and Joyce also are seen to fall within the range of data for the crack arrest and impact loading tests, suggesting that at these temperatures and  $K$  levels, such loading rates can approximate fully dynamic loading.

Barsom [1975] suggested an expression to approximate the magnitude of the temperature shift between slow bend and impact loading of steels as follows:

$$T_{\text{Shift}} = 215 - 1.5 \sigma_y$$

(17)

This expression was intended for steels in the yield strength range 248 to 965 MPa (36 to 140 ksi). A predicted temperature shift of 23°C (41°F) is calculated for the highest temperature where cleavage of HY-80 occurred in these tests, and this shift is negligible at the lowest test temperature because of the continued elevation of yield strength. Figure 41 contains bands within which the scatter of the cleavage fracture toughness measurements of HY-80 lie. This figure also shows a shift of the highest temperature scatter band of 23°C, and it can be seen that with the exception of the single point calculated from a branched crack, the crack arrest data are outside of the predicted range. Because this branch crack calculation is artificially high in both crack arrest toughness and arrest temperature as discussed earlier, the predicted dynamic temperature shift is non conservative when considering full constraint crack arrest toughness as developed with HY-80 steel.

Figure 41 also points up one of the limitations of crack arrest testing using the method developed in this study. Because it is a decreasing K test, the arrest K measurement is limited by the initiation K (and slope of the temperature gradient), which is in turn limited by the tendency toward crack branching. Thus the  $K_a$  value and arrest temperature cannot be taken much higher up the HY-80  $K_a$  resistance curve using this specimen dimension. Some additional elevation of  $K_a$  and arrest

temperature can be accomplished with a steeper temperature gradient, but this is likely to be only moderately higher than the results obtained herein.

The results of compact crack arrest tests with ASTM A710 Gr. A Cl. 3 steel are presented in Table 11. Because of the broad range of toughness available, and steepness of the fracture toughness transition curve, tests of this steel proved more difficult than with HY-80. Specifically, the  $K_0$  level was very sensitive to temperature, and could achieve very high levels prior to initiating cleavage. Specimen GGO-1 was loaded to an initial  $K$  level of  $320 \text{ MPa}\sqrt{\text{m}}$  ( $291 \text{ ksi}\sqrt{\text{in.}}$ ), and severe branching occurred as seen with an HY-80 specimen at a similarly high level of  $K_0$ . Specimen GGO-2 was loaded to a very low  $K_0$  level at a reduced crack tip temperature, and the resultant crack jump was on the order of 23 mm (0.9-inch). This is below the minimum crack jump length being considered by ASTM for valid crack arrest testing, but it is considered an acceptable measurement in light of the rather low  $K_0$  value. Specimen GGO-4 underwent warm prestress as discussed earlier, and substantial branching occurred in this test as well. Here the dominant branch which proceeded parallel to the side grooves but out of their plane was used to estimate  $K_a$ . The final two tests (GGO-5 and GGO-3) utilized chevron notches in an attempt to reduce the  $K$  value corresponding to initiation. Nevertheless, both specimens exhibited branched cracks. Specimen GGO-3 exhibited a single crack in the plane of the side grooves.



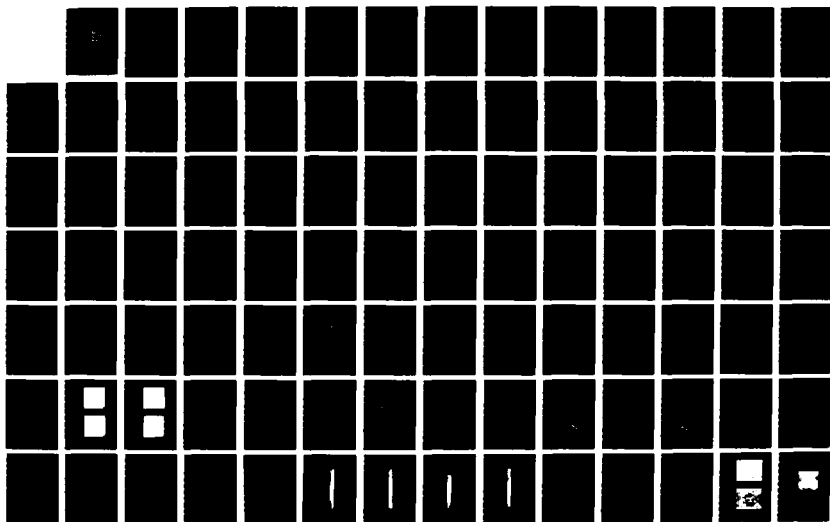
AD-A181 324

MICROMECHANISMS OF FRACTURE AND CRACK ARREST IN TWO  
HIGH STRENGTH STEELS(U) DAVID W TAYLOR NAVAL SHIP  
RESEARCH AND DEVELOPMENT CENTER ANN J P GUDAS FEB 87  
DTNSRDC/SME-87-28 F/G 11/6 1

3/4

UNCLASSIFIED

NL





of 45 mm (1.75-inch), then sent out a single major branch parallel to the crack plane. Specimen GGO-3 bifurcated immediately after crack initiation, even at a  $K_0$  level of 252 MPa $\sqrt{m}$  (229 ksi $\sqrt{in.}$ ).

From these five tests,  $K_a$  values were calculated for one planar crack jump case, and two cases where dominant crack branches were employed to calculate the crack arrest temperature and crack arrest  $K$  value. These are plotted in Figure 42 with  $K(J)$  results from the fracture toughness tests. Here there is no dynamic fracture toughness data for comparison, but again the crack arrest toughness values are displaced to the right of the static fracture toughness curve. In this case the order of this displacement is approximately 25°C (45°F), which is smaller than seen with HY-80. Additional data are required to clarify the magnitude of this temperature shift due to dynamic effects.

The crack branching behavior of ASTM A710 Gr. A Cl. 3 steel itself warrants further discussion. The occurrence of crack branching is tied to the attainment of a maximum crack velocity. From the earlier discussion of the  $\dot{a}$ - $K$  relationship for metals, it was shown that there is a regime where a large increase in  $K$  results in only a slight increase in crack velocity. When  $K$  is further increased, branching is an attempt to balance the driving force and the energy dissipation rate. Although no crack velocity measurements were attempted in this study, the results of the crack arrest experiments suggest that the ASTM A710 Gr. A Cl. 3 steel plate used in this study is much less

able to dissipate elastic energy associated with the dynamic fracture event than HY-80. Further, there appears to be a substantially lower level of driving force in this configuration which will lead to crack branching, and thus crack arrest testing of this steel requires more precise adjustment of the crack initiation parameters, and the slope of the temperature gradient.

#### Summary of Mechanical Property Tests

The objective of this series of mechanical property and fracture mechanics tests was to quantify the levels of fracture toughness of the two steels under conditions where loading rate, temperature, and degree of constraint were varied. A key element of the evaluation of these steels was the development of a crack arrest test method which allowed the simultaneous evaluation of effects of full constraint (full plate thickness) dynamic crack propagation at various temperatures.

The results of these tests first pointed up the fact that the HY-80 and ASTM A710 Gr. A Cl. 3 steel consistently switched order of fracture performance as temperature was lowered. HY-80 displayed lower upper shelf fracture toughness, but higher temperatures where transition from ductile to brittle fracture occurred. As the degree of test specimen constraint was increased, the temperatures for departure from upper shelf fracture were increased. The largest separation between fracture properties occurred in the fracture toughness tests performed with 25.4 mm (1-inch) thick specimens.

The second key finding of these tests was that the compact crack arrest toughness test developed in this investigation appears to be a feasible method to evaluate the crack arrest properties of high toughness, low transition temperature steels. The control of the test variables led to production of results which can describe significant portions of the  $K_a$  versus temperature curve. Although the results of tests of ASTM A710 Gr. A Cl. 3 steel were limited, and the occurrence of crack branching was difficult to eliminate, this type of testing is seen to be useful in assessing the dynamic fracture performance of such steels from a qualitative standpoint.

The results of the crack arrest tests with HY-80 steel showed that the  $K_a$  versus temperature curve developed from this test series merges closely with previous results from impact loading tests, and significantly extends the range of dynamic fracture toughness measurements upward and to higher temperatures. These results also showed that the  $K_a$  measurements are not substantially lower than accelerated loading rate tests for fixed temperatures at the low test temperature and low  $K$  level. Finally, these tests showed that dynamic effects in these two steels are manifested in clear differences in the ability to sustain dynamic crack propagation under similar crack driving force conditions without crack branching.

#### METALLURGICAL EXAMINATION

The results of the impact toughness, fracture toughness and crack arrest toughness measurements reported in this study

showed distinctly different properties of these steels depending on temperature, degree of constraint and loading rate. For the case where both steels exhibited upper shelf behavior and ductile fracture occurred, the ASTM A710 Gr. A Cl. 3 steel showed substantially higher toughness than HY-80 steel. As temperature was lowered in all tests of fracture properties, the ASTM A710 Gr. A Cl. 3 steel was seen to fracture in a cleavage-dominated mode at temperatures where the HY-80 was still in a predominantly fibrous fracture mode, and measures of impact toughness or fracture toughness fell below those of HY-80. In this section of this study, results of metallurgical examinations of the micromechanisms of fracture will be detailed, and explanations of the fracture performance of the two steels will be developed. Finally, micromechanisms of crack arrest will be described in relation to the specific arrest toughness/arrest temperature data developed in this investigation.

#### Microstructure of Steels

Figure 18 presented typical optical micrographs of HY-80 steel. As stated earlier, the microstructure of this steel retains much of the original martensite lath structure, but the tempering has caused formation of some larger ferrite grains which tend to be equiaxed. This predominant lath structure is shown in scanning electron micrographs in Figure 43 which includes specimens which were lightly etched in 2% Nital. Here the lath spacing is observed to be on the order of 1-3  $\mu\text{m}$ .

This partially recrystallized microstructure is typical of low carbon steels tempered in the range 600-700°C (1112-1292°F). These micrographs also show that carbides are precipitated at lath boundaries and ferrite boundaries as discussed by Speich [1972]. Cementite is also present within martensite laths. According to Krauss [1984], these particles originally formed as fine platelets in (110)<sub>m</sub> habit planes.

Because the size and distribution of carbides is seen to be a key element in the cleavage fracture process, HY-80 specimens were examined after 4% Picral etchant had been applied. Figure 44 is an optical micrograph which shows the typical carbide distribution in this steel. Figure 45 presents scanning electron micrographs of similarly etched specimens. These figures show that the carbides are dispersed uniformly through the microstructure, with some segregation at grain boundaries as seen earlier. These are predominantly in the form of spheroidal Fe<sub>3</sub>C particles as discussed by Speich [1972, 1973] and Krauss [1984]. The distribution of carbide sizes indicates that some coarsening has taken place, but not to a great extent. The maximum width or diameter of these carbide particles is 0.38 μm, and the average particle diameter is 0.22 μm.

The microstructure of the ASTM A 710 Gr. A Cl. 3 steel is distinctly different than HY-80. Figure 19 shows this to be a polygonal ferrite microstructure with an average grain size of 6.2 μm. Figure 46 presents scanning electron micrographs produced with specimens which were etched in 2% Nital solution.

Here the morphology, distribution and location of the second phase which is present as isolated dark islands on the optical micrographs is clearly evident. This constituent is seen to reside principally at the boundaries of ferrite grains, or triple points, but is also seen within larger ferrite grains. It possesses a mottled appearance, which in some cases includes aligned, parallel platelets.

Optical and scanning electron micrographs of ASTM A710 Gr. A Cl. 3 steel which were etched in 4% Picral solution are shown in Figures 47 to 49. Here only the carbides are highlighted, and they are seen to be segregated at grain boundaries, and within the constituent present at grain boundaries and triple points. These areas contain colonies of cementite particles which if not continuous, are highly clustered. The mean diameter of these colonies is 3.55  $\mu\text{m}$ , and the range of measured diameters is 0.4 to 8.4  $\mu\text{m}$ . Within these colonies, the maximum cementite particle diameter (or width) measured is 0.81  $\mu\text{m}$ , and average particle size is 0.37  $\mu\text{m}$ . Additionally, these micrographs show that most of the ferrite grains are carbide free. Table 12 presents a summary of carbide particle measurements for both steels including the mean values, standard deviation of the sample, and range of measurements for a given sample.

The second constituent in the ASTM A710 Gr. A Cl. 3 steel has been identified as lower bainite, decomposed pearlite, autotempered martensite, heavily twinned martensite, and martensite-austenite (M-A) as discussed earlier. The clear



identification of this constituent is made difficult by the high aging temperature employed with this plate which tends to spheroidize these carbides, and the lack of a published continuous cooling transformation diagram for this alloy. During cooling from the austenite, ferrite grains form initially, and carbon is rejected. Eventually, these carbon-enriched areas transform as either bainite, M-A or possibly martensite depending on the cooling rate. The precise identification of this constituent is possible with transmission electron microscopic studies which were not undertaken in this investigation. The importance of this constituent lies in the size and distribution of cementite particles which it contains. These are significantly larger and coarser than seen with HY-80, even though the ASTM A710 Gr. A Cl. 3 steel contains only 39% as much carbon as HY-80. These carbide particles are also seen in many cases to be closely packed with one another.

The role of inclusions in the ductile fracture process has been introduced earlier. Because of the large difference in measured sulphur contents in these steels (0.013% for HY-80 versus 0.004% for ASTM A710 Gr. A Cl. 3), and due to the special sulphide shape control treatment used with ASTM A710 Gr. A Cl. 3 steel, there is expected to be a large difference in manganese sulphide particle size, shape and distribution. This is born out in the optical micrographs of Figure 50 which were taken from unetched specimens of each steel. Here the HY-80 is seen to have essentially a bimodal distribution of manganese sulfide

inclusions which includes large stringers elongated in the rolling direction which are typically 5 to 50  $\mu\text{m}$  in length, and 2 to 25  $\mu\text{m}$  in width, and smaller, more spherically shaped particles distributed throughout the microstructure. The ASTM A710 Gr. A Cl. 3 steel contains a more uniform size distribution of inclusions, all of which are in the spherical shape, with no orientation favoring the rolling direction. The size of these particles is much smaller than the large inclusion stringers, but larger than many of the spherical inclusions in HY-80.

To further classify the size of inclusions in the subject steels, measurements of their diameters were made from fracture surfaces of specimens which failed in ductile tearing. This means of measurement was suggested by Widgery and Knott [1978], and was shown to be valid in comparison to replica and electropolishing techniques. The distribution of inclusion sizes was seen to be related to the interaction distance, which was proportional to the size of the nucleating microvoid, and dependent on strain hardening behavior of the matrix. Several scanning electron fractographs of ductile fracture toughness specimens of each steel were used in the sampling of inclusion size. The mean inclusion size in the HY-80 was 1.49  $\mu\text{m}$ , where only the smaller, spherical inclusions were measured. This compared to an average inclusion size of 4.65  $\mu\text{m}$  for ASTM A710 Gr. A Cl. 3 steel. Here it is seen that the manganese sulphide inclusion size in the low carbon ferritic steel is larger than the small-particle population of HY-80. These measurements of

inclusion size for both steels are summarized in Table 12.

#### Micromechanisms of Ductile Fracture

The results of the J-integral fracture toughness tests which are presented in Tables 8 and 9 showed that the fracture toughness of ASTM A710 Gr. A Cl. 3 steel was between 1.8 to 2.2 times that of HY-80 at similar temperatures. The source of this difference can be determined from examination of the fracture path and fracture surfaces generated by stable tearing of each alloy. Figures 51 to 53 show optical metallographic views of the profile of tearing-mode cracks which existed in several HY-80 specimens. Here, the fracture path is typically zig-zag in nature with evidence of interrupted void growth and the fast shear process. The cracks were seen to initially grow along spiral slip lines which emanated from the blunted fatigue crack tip. However, they were seen to join larger voids which had opened ahead of the crack tip. In many cases, the crack paths contained large voids which were elongated in the rolling direction, some of which still contained manganese sulphide inclusions in the plane of polish. The mechanism of joining these voids was typically one of shear decohesion, or zig-zag growth between larger voids. Figure 52 (specimen FYB-57) shows large voids which had just coalesced, and specimen FYB-44 in this figure shows a distinct shear band between two elongated voids. Figure 53 shows the tip of a crack of a specimen which was adjacent to a large elongated void, and which had not yet connected in this plane of polish.

These metallographic observations are in agreement with those of Clayton and Knott [1976], Green and Knott [1976] and You and Knott [1982] who also examined the ductile fracture of HY-80 steel. Knott [1980] suggested that such shear fracture ran from carbide to carbide, decohering the carbide/matrix interfaces. During plastic strain, dislocations pile up producing work hardening and increasing the stress on the carbide/matrix interface as the strain is increased. At a critical strain, the interface (or particle) fractures, and the localized shear fracture becomes rapid until it arrests at an inclusion-centered void.

To further examine the mechanism of ductile fracture in HY-80, scanning electron fractographic examinations of surfaces of specimens which had failed in this mode were conducted. Figure 54 shows a low magnification view of ductile crack growth where large inclusion-related voids are coincident with the direction of crack growth. The opening of these voids is the dominant micromechanism of failure along the crack front in that they locally reduce the constraint ahead of the crack tip, and allow large local strains to occur. Figures 55 and 56 show that the regions between these large voids contain equiaxed dimples which contain the spherical manganese-sulphide inclusions at their bases. There are also many instances of fine scale microcracks which are spaced similarly to the carbide particle spacing seen in HY-80. These areas have fractured by shear decohesion of the carbides, and the fine scale is in agreement

with the metallographic observations where crack opening along the shear band is limited. These fractographs also show that shear walls of reduced dimple size often connect adjacent planes of inclusion-related hole joining.

The fracture paths observed with ASTM A710 Gr. A Cl. 3 steel are distinct from those of HY-80. Figures 57 and 58 present metallographic sections through several specimens which exhibited ductile tearing through the entire test. Here the cracks grew only by the zig-zag fracture mode, and with little or no evidence of shear band formation. The crack tip opening displacement for equivalent amounts of crack growth is seen to be significantly higher than HY-80, as predicted from the J-integral measurements. Also, for this steel, cracking was seen to emanate from the blunted crack tip along straight slip lines for a short distance. This type of tearing would also serve to elevate the fracture toughness as it increases the amount of external displacement required to achieve a critical crack tip opening displacement for void growth and joining.

The scanning electron fractographic examination of ASTM A710 Gr. A Cl. 3 steel specimens which failed in ductile tearing showed a fracture mode which was much coarser than seen with HY-80. That is, the fracture surface was dominated by the existence of large, equiaxed voids, many of which contained spherical inclusions (Figure 59). In many cases, these voids coalesced as shown in Figure 60. The next order of smaller dimples between these voids were in many cases associated with

particles which appeared to be angular in shape, and were likely small inclusions. The finest scale dimples did not contain particles which were resolvable at scanning electron microscope magnifications. In many cases, these dimples (Figure 61) were elongated in the principle direction of crack growth as seen by Beachem [1965]. The spacing of these dimples does not appear to be associated with the carbides in this steel because of their coarseness. Miglin [1982] also observed such voids and attributed them to vanadium carbonitride precipitates which were not resolvable in fractographic examination. Further analysis is required to explore this hypothesis and the role of dislocation cells in the finest scale microvoid formation in this steel.

These metallographic and fractographic observations verify the strong role that the manganese-sulphide inclusion content, size and distribution plays in the initiation of ductile fracture. Here the HY-80 fracture was dominated by the elongated stringers, and the mechanism of crack tip linkage was greatly affected by the fine dispersion of carbides throughout the matrix. These factors led to high strains at the crack tip for a given stress or load level. Crack initiation and growth proceeded at crack tip opening displacement levels which were reduced from the case of complete void coalescence by the interruption of void growth due to the shear band instability between growing voids. For the ASTM A710 Gr. A Cl. 3 steel which contained significantly less sulphur, crack initiation and growth was associated with spherical manganese-sulphide

inclusion. In this case, these voids were seen to grow to large size and coalesce. Here the carbon level of the alloy and distribution of carbide particles at grain boundaries and triple points precluded localized shear decohesion of the carbide/ferrite matrix interfaces over any significant distance. Hence, the crack growth mechanism was principally one of void coalescence.

#### Micromechanisms of Cleavage Fracture

The most significant difference in properties between the HY-80 and ASTM A710 Gr. A Cl. 3 steels was seen in the temperature at which the fracture mode changed from ductile tearing to brittle cleavage. In the introductory review of the mechanisms of cleavage fracture, the important role of the carbide particles was seen. Briefly, cleavage fracture ahead of a crack occurs when the maximum value of the tensile stress in the volume of metal adjacent to the crack tip exceeds the critical fracture stress. Because the maximum stress occurs ahead of a sharp crack tip, models were formulated which require that local tensile stress must exceed the fracture stress over a microstructurally significant distance [Ritchie, et al. 1973]. The cleavage fracture process is seen as one of competition between cracked carbides of different sizes, or as recently stated, the largest eligible particles [Hahn, 1984]. The most recent analyses Curry and Knott [1979], Evans [1983], and Lin, et al. [1985] produced statistical treatments of the cleavage fracture process, including fully quantitative weakest link

models.

To attempt to explain the cleavage fracture temperature differences observed in this study, careful scanning electron microscopic examination of specimens which had failed in cleavage was conducted. This was done in an attempt to identify the possible role of inclusions in initiating cleavage cracking as has been seen recently by Tweed and Knott [1982, 1983], Rosenfield, and Shetty [1983], Bowen and Knott [1984], and Rosenfield, et al. [1985]. These are the largest particles in the microstructure of each alloy, and provide the first opportunity for stress controlled fracture. It should be recalled that in the HY-80 steel, inclusions displayed a bimodal distribution with large stringers on the order of 2 to 25  $\mu\text{m}$  in width, and smaller particles averaging 1.49  $\mu\text{m}$  in diameter. The distribution of inclusions in the ASTM A710 Gr. A Cl. 3 steel was seen to have a larger range than seen with discrete inclusions in HY-80, and the average inclusion diameter was 4.65  $\mu\text{m}$ . The manganese-sulfide inclusions are significantly larger than the carbide particles observed in either steel.

The results of this fractographic examination of the fractured specimens were negative in that there was no instance where an inclusion or any other identifiable particle could be linked to the start of cleavage fracture in either steel. In the HY-80 specimens, cleavage initiated apparently sympathetically across the crack front as there were no "river" markings pointing to a source. Rather, the texture of the cleavage



crack was uniform across the width of the specimen. Figure 62 presents typical scanning electron fractographs of cleavage fracture in HY-80 steel which occurred in the quasi-static fracture toughness tests. Here the cleavage facets are fluted, and are seen to exist on multiple planes. Linkage of planes of cleavage was frequently seen to occur by a void sheet mechanism where the dimple size is related more to the carbide spacing rather than inclusion spacing and distribution. The fluted appearance of the cleavage fracture facets suggests that substantial energy is required to produce this mode of fracture, and this supports the relatively high fracture toughness of this steel seen after the tearing mode of fracture has ceased to operate.

Optical examination of the ASTM A710 Gr. A Cl. 3 steel compact specimens which failed in cleavage showed several cases where potential sources of cleavage fracture were identified by river patterns. These were located on the order of 150 to 400  $\mu\text{m}$  ahead of the fatigue crack tip. Figure 63 shows two scanning electron fractographs of 1TCT specimen GGO-2 which was tested at  $-52^{\circ}\text{C}$  ( $-62^{\circ}\text{F}$ ) where the fracture pattern emanated from a distinct area or point on the fracture surface. High magnification views of this area shows this point to be a ferrite grain intersection with other grains. Here the cleavage fracture is seen to proceed with much less surface relief and over many contiguous ferrite grain boundaries with minimal reorientation. With this steel, there was much less evidence of multiple

cleavage crack paths, and ductile hole joining mechanism between crack planes. Figure 64 shows another example where the cleavage fracture emanated apparently from a focused source. Examination of this area showed it to be a large, contiguous cleavage facet which incorporated approximately 20 ferrite grains. Again no trigger particle was observed in this area associated with cleavage initiation. This initiation site suggests that the trigger for the major cleavage crack across the specimen was the successful propagation of a microcrack across several grain boundaries. This has been proposed as a cleavage initiation criteria for fine-grained materials by Groom and Knott [1975].

The lack of identified inclusion trigger particles then directs attention to the next finer sized particles in the microstructures of the two steels, which are the carbides. Distinct differences in carbide particle size and distribution were seen in each steel as previously discussed. The HY-80 contains a uniform dispersion of 0.22  $\mu\text{m}$  diameter cementite particles (Table 12). Although some carbide segregation occurs on ferrite grain boundaries, and martensite lath boundaries, there is no evidence of clustering of these particles. On the other hand, the ASTM A710 Gr. A Cl. 3 steel displayed individual carbide particles which were larger than those observed in the HY-80, and which were mostly concentrated in the M-A or bainite constituent which exists at the grain boundaries and triple points. Table 12 presents a summary of

carbide particle measurements taken for both steels, and includes measurements of the average colony size of carbides in the ASTM A710 Gr. A Cl. 3 steel. Here the colonies include the area of M-A or bainite constituent which contains evidence of linked carbides. Their mean diameter is 3.55  $\mu\text{m}$ , with a large spread in the measurements. Because the carbides in the grain boundary and triple-point regions of M-A or bainite are in many cases packed close to each other, these colonies can be thought of as having an effective particle size which ranges from the diameter of individual carbide particles, to the dimensions of the colony itself.

Because cleavage fracture has been shown to be a stress controlled phenomenon as described earlier, it is convenient to analyze the role of the carbide particles in terms of the critical fracture stress. This has been shown to be essentially temperature independent, and allows for introduction of particle size into the analysis. Curry and Knott [1978] restated the Smith [1966] fracture stress model in terms of the grain size dependence of the effective shear stress (Equation 5). If the dislocation term is neglected as has been suggested by Knott for the case of mild steels [1981], this expression can be reduced to the Griffith model, treating the microcrack nucleus as a penny-shaped crack in a spheroidal particle equal to the particle diameter. Thus, following Curry and Knott [1978] the critical fracture stress can be approximated as:

$$S = (\pi E \gamma_p / (1 - \nu^2) C_0)^{1/2} \quad (18)$$

The ratio of critical fracture stress for the two steels then can be related to the ratio of the effective surface energy terms, and the inverse square roots of the particle size. The values of the effective surface energy in ferrite have ranged from 14 to 6 kJ/m<sup>2</sup> [Curry and Knott, 1978; Bowen and Knott, 1985]. Setting this term equal for both steels seems reasonable to a first approximation as the only wide variation in this value exists in the case of bainitic steels. The ratio of the fracture stresses then becomes that of the inverse square root of the particle diameters. Using the mean values from Table 12, the critical fracture stress for HY-80 is 1.29 times that of ASTM A710 Gr. A Cl. 3 steel if only individual carbides are considered, and 4.0 times that of this ferritic steel if the entire colony of carbides is seen to operate as a single particle in initiating a Griffith crack. The actual ratio lies in this range, probably closer to the individual carbide value, as the colonies of carbides are not likely to act as simple single particles. This difference in fracture stress can be seen to account for the higher temperature initiation of cleavage as the yield properties of the two steels are similar over the temperature range of interest. This difference in critical stress will be increased when the dislocation term is included in the Smith expression. Earlier it was noted that carbides are present principally on ferrite grain boundaries or at triple points in the ASTM A710 Gr. A Cl. 3 steel. These carbides are presented with potentially large

slip bands over which dislocation sources can act to further reduce the critical fracture stress.

This comparison of critical fracture stress for slip-initiated low temperature cleavage fracture is only a first order approximation to determine the effects of carbide size and distribution differences in these two steels. However, this does suggest that the differences in cleavage fracture performance of the two steels are likely due to the observed differences in carbide size and distribution. Prediction of the fracture toughness versus temperature trends with these steels will require more statistically complete measurements of the particle size distribution and elemental strength distribution, as well as determination of the effective surface energy of the ferrite in both steels.

This postulated role of the carbide particles in the cleavage fracture process is at variance with previous investigations of ASTM A710 Gr. A steel. Miglin [1982] and Miglin, et al. [1983] observed that  $K_{IC}$  at  $-196^{\circ}\text{C}$  ( $-321^{\circ}\text{F}$ ) was independent of ferrite grain size changes induced by different heat treatments. These authors reasoned that neither copper particles nor carbo-nitrides could have triggered cleavage at this temperature because both would have responded to the heat-treatments used. Because sulfides are affected minimally by heat treatment, these authors suggested that they appeared to play a key role in the cleavage fracture initiation. However, no fractographic evidence was obtained which identified

sulphides as seen in other studies of cleavage initiation.

Cutler and Krishnadev [1982] evaluated the cleavage fracture toughness of as-rolled and aged ASTM A710 Gr. A steel. They postulated that slip bands have similar orientations over many ferrite grains in the aged condition, and low temperature fracture occurs by ductile tearing between ligaments between microcracks of similar orientation. The copper precipitates were seen to blunt the microcracks which formed leading to the ligament tearing mechanism. In this study, the evidence of tearing in cleavage fracture was limited. Further, the model of Cutler and Krishnadev relies totally on slip formation of cleavage initiation sites, even though large carbide particles were known to exist within the matrix.

These metallographic and fractographic observations lead to the conclusion that the relatively high temperature for cleavage fracture initiation in ASTM A710 Gr. A Cl. 3 steel is attributable directly to the relatively large carbide particle size, and their distribution in the M-A or bainite islands which are located at grain boundaries and triple points. This is consistent with the many observations which relate the ductile-brittle transition temperature to carbide size and content in steels. Essentially, these carbides act as Griffith microcrack nuclei either singly or in concert with adjacent particles. Cleavage fracture is then likely controlled by the ability of the ferrite grains to arrest such cracks which are operating in a steep stress gradient. Observation of one case of a multiple-grain

cleavage source suggests that the controlling microstructural parameter is that of the several ferrite grain boundaries which must be crossed by the cleavage microcrack to trigger sympathetic cleavage crack growth across the entire crack front.

#### Micromechanisms of Crack Arrest

After completion of each crack arrest test, metallurgical samples were removed in such a manner as to allow for metallographic examination of the crack path as it existed at the instant of arrest, and fractographic examination of the crack surfaces. The focus of these examinations was the determination of the mode of cracking which occurred up to and including the arrest event.

Figure 36 is a photograph of the crack path which occurred in HY-80 compact crack arrest specimen FYB CCA-2. This specimen was tested with a mild temperature gradient, and the crack jump was the longest of this test series. The arrest temperature calculated from the central length of the crack tip was  $-103^{\circ}\text{C}$  ( $-154^{\circ}\text{F}$ ). In this figure it can be seen that the crack path was relatively flat, and limited tunnelling was evident at the point of arrest.

Figure 65 is an optical photomicrograph of the arrested crack tip. Here the point of crack arrest is associated with cleavage fracture as evidenced by the microcracks which emanate from the crack path, and the apparently unconnected crack branches at the very crack tip. However, approximately 700

$\mu\text{m}$  (0.03-inch) behind the arrested crack tip, there was a region of cracking which exhibited zig-zag path without the secondary cracks, and minor evidence of shear banding. Figure 66 presents scanning electron fractographs taken in the vicinity of the arrested crack tip. These show that the predominant mode of fracture at arrest was cleavage, but there was also evidence of dimple formation on connecting planes. One large region which includes an elongated manganese sulphide artifact which is surrounded by dimpled fracture is shown. Figure 67 is a scanning electron fractograph of a section of the crack path which was removed from the arrested tip by 12 mm (0.5-inch). Here it can be seen that the fracture is nearly entirely cleavage, with limited evidence of micro-plasticity. This is typical of the fracture path of this crack prior to the arrest point.

Figure 37 is a photograph of HY-80 CCA specimen FYB-1A. This specimen had a temperature gradient of  $0.21^{\circ}\text{C}/\text{mm}$  ( $9.9^{\circ}\text{F}/\text{inch}$ ) which was the lowest of this test series. The crack arrest temperature was  $-117^{\circ}\text{C}$  ( $-179^{\circ}\text{F}$ ), which again was the lowest observed. Because the initial K level was relatively low, this specimen formed the lower bound of the crack arrest toughness results. From Figure 37, it can be seen that the crack path showed a slight tendency to branch out of plane about midway through the crack jump, but then returned to the plane of the side grooves toward the arrest point. Figure 68 is an optical photomicrograph of the arrested tip of the crack showing



that the entire run-arrest event was accomplished in the cleavage fracture mode. That is, micro-branching along the crack path occurred up to and including the point of crack arrest. Figure 69 presents scanning electron fractographs from the crack tip region showing the dominant cleavage fracture which occurred at the arrest point.

HY-80 CCA specimen FYB-1B was subjected to a steep thermal gradient, and provided an intermediate combination of arrest toughness and temperature in this series. In this case, the surface roughness of the crack path near the arrest portion of the crack jump was increased over the specimens discussed previously (Figure 38). The arrest temperature was  $-106^{\circ}\text{C}$  ( $-159^{\circ}\text{F}$ ), and as shown in the optical photomicrograph in Figure 70, the arrest occurred in a cleavage mode. This was verified by scanning electron fractographic examination of the crack tip area, and Figure 71 presents evidence of the cleavage fracture path at the arrest point.

The last HY-80 crack arrest test conducted (specimen FYB-3A) was aimed toward obtaining a high value of arrest toughness and temperature. Here the temperature gradient was  $0.44^{\circ}\text{C}/\text{mm}$  ( $20.3^{\circ}\text{F}/\text{inch}$ ), and the initiation K level was quite high. Figure 39 shows that the crack ran a significant distance and arrested without branching. Again, the surface roughness was increased over previous tests. Figures 72 and 73 present two magnifications of the arrested crack tip in specimen FYB-3A. Here it can be seen that the fracture mode at the point of arrest

was not associated with the cleavage microcracks as seen in other specimens. Rather the crack seemed to open uniformly along a line of inclusions, as seen earlier in the examination of the ductile fracture specimens.

Figure 74 presents two low magnification scanning electron fractographs of the arrested crack tip. In the upper fractograph taken without specimen tilt, two distinct instances of out-of-plane crack growth are evident up to the point of arrest. A 61-degree tilt exposed the sides of these regions, and they are marked with fatigue striations which were induced in opening this specimen after test. This presents evidence that these ligaments were not fractured at the time of the arrest of this crack.

Figure 75 includes two scanning electron fractographs taken in the vicinity of the arrested crack tip of HY-80 CCA specimen FYB-3A. Here it is seen that regions of predominant cleavage, and cleavage associated with microplasticity were both observed. There was distinctly more evidence of formation of microvoids in connecting cleavage planes than observed in any of the other crack arrest specimens. In attempting to explore this evidence, the specimen was tilted to various degrees and regions of predominantly tearing-mode fracture were observed, as well as regions of predominant cleavage, as shown in Figure 76. One source of such regions of deformation is shown in Figure 77 which is an optical photomicrograph taken across the crack path of this specimen 12mm (0.5-inch) behind the crack tip. Here the multiple planes of the cleavage crack growth are shown clearly,

and shear bands connecting them are also evident. At this point in the specimen, the crack was contiguous across the specimen thickness.

Figure 78 is a photograph of the run-arrest path in the only crack arrest test of ASTM A710 Gr. A Cl. 3 steel specimen which did not branch during the cracking event. Here the short crack jump is evident in comparison with the HY-80 specimens. Because the crack initiated at a relatively low temperature versus the start of cleavage temperature in the fracture toughness tests, the crack jump would not be expected to be great. In this specimen, the crack jumped and arrested entirely in cleavage as is shown in the photomicrograph in Figure 79, and the scanning electron fractograph in Figure 80. This was to be expected from the test conditions of this specimen.

Previous investigations of the micromechanisms of crack arrest emphasized the important role that unbroken ligaments played in damping the cleavage fracture process [Hahn, et al. 1970; Hoagland, et al. 1972; Hahn, et al. 1980b]. In this study, there was evidence of increased surface roughness which these authors attributed to ligation along the crack path. Figure 81 compares three HY-80 crack arrest specimens and shows that for the case of the low toughness, lowest temperature event, the crack tip region was distinctly flatter than observed with the other specimens. However, the degree of ligation observed with these HY-80 specimens was substantially less than observed by previous investigators who evaluated reactor

pressure vessel steels.

Metallographic examination across the crack tips of all specimens which were successfully tested showed that with one exception, the cracks paths were contiguous across the specimen width. Also, as shown in Figure 77, there was evidence of shear wall formation parallel to the direction of crack propagation and perpendicular to the crack plane as seen by Hoagland, et al. [1972] and Hahn, et al. [1980b]. This finding of contiguous crack paths agrees with previous investigations, but provides more conclusive evidence of crack mode in the vicinity of the arrested crack tip.

Because this crack arrest test was designed to allow variation of the driving force to fracture and material resistance to fracture simultaneously, these results point to the likely scenario for crack arrest in the case of a steel which is approaching the upper transition fracture regime. As seen with HY-80 CCA specimen FYB-3A which produced the highest combination of arrest toughness and temperature in this study, the path of fracture takes on a combination of cracking modes near the arrest point. There is evidence of dominant cleavage fracture in close proximity with ductile tearing events. This suggests that the arrest under these conditions occurs because the cleavage crack experiences significant difficulty in simultaneously spreading laterally as well as in the direction of growth. This limitation in lateral spreading is caused by successful initiation of ductile tearing processes which are

associated with local loss of constraint. Thus the running cleavage crack cannot maintain the stress levels across the crack tip required for sympathetic growth. The crack velocity is reduced locally, and local arrest events likely occur. When temperature is raised sufficiently, reinitiation of cleavage is difficult at these arrested points, and formation of cleavage crack on multiple planes is promoted.

The evidence presented here suggests that the termination of cleavage cracking occurs in a manner similar to the initiation of such cracking near the upper shelf. That is the competition between sympathetic cleavage crack growth, and local plastic fracture processes operate simultaneously. In this K decreasing format, arrest occurs when the elastic driving force cannot maintain the rapid cleavage crack propagation. This was seen in several specimens which were seen to arrest in dominant cleavage. Where the driving force is high (as in Specimen FYB-3A), the arrested crack may attempt to reinitiate in response to elastic "ringing" of the specimen, and the observed regions of plastic fracture and ligament shear probably occurred in response to these reinitiation attempts. Additional experimentation is required to establish the crack velocity and crack opening displacement history in this compact crack arrest specimen in order to more accurately address the role of local crack tip plasticity and ductile fracture in the arrest event.

## SUMMARY AND CONCLUSIONS

The objective of this investigation was two-fold. It first included the quantification of fracture properties of two 585 MPa (85 ksi) yield strength steels which obtained their mechanical properties through distinctly different metallurgical mechanisms. These steels were the quenched and tempered martensitic HY-80, and low-carbon, copper precipitation-hardened ferritic alloy ASTM A710 Gr. A Cl. 3. The focus of the mechanical property investigations was on fracture performance through the ductile brittle transition, where both static and dynamic properties were evaluated under varying levels of specimen constraint. To obtain lower bound measurements of fracture toughness, a crack arrest procedure was developed which utilized wedge-loaded compact crack arrest specimens in the presence of a linear temperature gradient over the specimen width.

The second objective was to conduct metallurgical examinations to explain the relative changes in fracture performance of the two steels as fracture mechanics test variables were changed. Metallographic and fractographic studies of fractured specimens were performed to identify the modes of ductile fracture, micro-mechanisms of cleavage crack initiation, and micro-mechanisms of arrest of cleavage cracks.

The results of this study were presented in terms of the fracture properties of the steels, and the metallurgical aspects of the three types of fracture processes which occurred. Impact toughness and fracture toughness tests showed that the ASTM A710

Gr. A Cl. 3 steel displayed superior fracture toughness when compared to HY-80 where the fracture mode occurred by ductile processes. As specimen constraint was increased and temperature lowered, the HY-80 steel was shown to remain in the ductile fracture mode to significantly lower temperatures than the ASTM A710 Gr. A Cl. 3 steel, and displayed higher cleavage fracture toughness throughout the range of test temperatures.

A significant portion of this investigation was devoted to the development of a crack arrest test procedure which could be successfully employed with steels which exhibit substantial low temperature toughness. The approach to this testing included the production of full plate thickness compact crack arrest specimens which had large in-plane dimensions including a maximum crack jump distance of 356 mm (14-inches). The size of the specimen was chosen to allow for the imposition of a linear temperature gradient from the crack tip to the back wall of the specimen. This led to control of the conditions for cleavage crack initiation principally through setting the temperature at the crack tip, and variation of  $K_a$  and crack jump length through control of the slope of the temperature gradient in conjunction with the crack initiation stress intensity. The intent was to use changes in  $K$  level for cleavage crack initiation, slope of temperature gradient, and temperature of crack initiation to produce crack arrest toughness measurements over a range of temperatures.

For the first time, evaluation of the crack arrest tough-

ness of HY 80 steel was accomplished with the compact crack arrest test procedure developed in this study. The range of crack arrest results led to a clear definition of the  $K_a$  versus temperature curve. These data were shown to merge with previous impact toughness data, and significantly extend the  $K$  range for characterization of lower bound dynamic fracture toughness. Results of crack arrest tests with ASTM A710 Gr. A Cl. 3 steel were less successful in that significant crack branching prevented quantification of the crack arrest toughness transition curve except for very low temperatures and  $K_a$  levels. However, this testing clearly displayed the inability of this heat of this alloy, which was significantly over the minimum yield strength, to contain running cleavage cracks in the face of moderate elastic driving force.

The results of the metallurgical examinations showed that the ASTM A710 Gr. A Cl. 3 steel cracked by a microvoid coalescence mode when on upper shelf, whereas the HY-80 ductile fracture was characterized as interrupted microvoid coalescence, with fast shear linking of developing voids. The sulfide inclusions in each steel were seen to control the ductile fracture process. In HY-80, manganese sulphides were distributed as stringers and small spherical particles. The former dominated the tearing fracture mode and caused reduction of local constraint, and tearing fracture at relatively low crack tip opening displacements. The ASTM A710 Gr. A Cl. 3 steel displayed a predominance of void coalescence, with no evidence of shear-band formation



between growing voids. This is attributable to the low sulphur content, sulphide shape control treatment, and lack of carbide particles in the ferrite grains to contribute to shear instabilities.

Cleavage fracture properties of both steels were seen to be dominated by the size and distribution of the cementite particles which existed after tempering or aging. The HY-80 microstructure contained a relatively uniform dispersion of cementite particles which averaged  $0.22\text{ }\mu\text{m}$  in diameter. The ASTM A710 Gr. A Cl. 3 steel contained fewer, but larger carbide particles which resided in bainite or M-A islands which existed on polygonal ferrite grain boundaries and triple points. These cementite particles averaged  $0.37\text{ }\mu\text{m}$  in diameter, and likely acted as effectively larger particles because of interactions with neighboring or adjacent cementite particles. The higher temperature for initiation of cleavage fracture in ASTM A710 Gr. A Cl. 3 steel was ascribed to these measured differences in carbide particle size, and the possible interaction of these particles.

Crack arrest at low temperatures and  $K_{\text{a}}$  values in HY-80 was seen to occur through reduction in driving force, and no evidence of change in micromechanical fracture characteristics was noted. At the highest temperatures and  $K_{\text{a}}$  levels, substantial crack tip plasticity was seen in the form of dimple formation similar to that seen in static ductile tearing. The dominant mode of fracture at the arrest point was still cleavage, but

the attempts to initiate tearing fracture were evidence of competition of fracture processes.

The following conclusions can be drawn from this study:

(1). ASTM A 710 Gr. A Cl. 3 steel displays superior ductile fracture toughness when compared to HY-80 steel. This is due to the low sulphur and carbon contents of this alloy in comparison to HY-80 which promoted full void coalescence for crack initiation;

(2). The micromechanism of ductile fracture in HY-80 steel is dominated by the initiation of large voids at manganese-sulfide stringers, and joining of smaller voids through shear band fracture associated with carbide particles. This interrupted void growth mechanism reduces the crack tip opening displacement required for crack initiation over that seen with a void coalescence mechanism;

(3). Impact toughness measurements showed that HY-80 displays upper shelf ductile fracture performance to significantly lower temperatures than ASTM A710 Gr. A Cl. 3 steel. Fracture toughness tests showed that the temperature of cleavage initiation for ASTM A710 Gr. A Cl. 3 steel is 100°C (180°F) higher than observed with HY-80;

(4). The relatively elevated cleavage initiation temperature of ASTM A710 Gr. A Cl. 3 steel is attributable to the size and distribution of cementite particles. In this alloy, carbides were seen to reside only in islands of tempered M-A or bainite, and their individual size was 68% larger than

those in HY-80 steel, even though the carbon content was significantly reduced from HY-80. Additionally, these carbides are seen to have larger effective sizes because of their clustering and close proximity in colonies on grain boundaries and triple points;

(5). The critical microstructural distance parameter for cleavage in ASTM A710 Gr. A Cl. 3 steel is related to the requirement for a cleavage microcrack to cross several ferrite grain boundaries before large scale instability occurs;

(6). The compact crack arrest test procedure developed in this study appears feasible for evaluation of the crack arrest toughness of steels, particularly those which exhibit substantial low temperature toughness;

(7). The crack arrest toughness of HY-80 steel as a function of increasing test temperature shows an upward sweeping trend, and merges with previous impact toughness measurements. The crack arrest toughness of HY-80 is displaced from static fracture toughness values approximately 60 to 70°C (108 to 126°F) toward higher temperatures. The ability of ASTM A710 Gr. A Cl. 3 steel to sustain dynamic crack propagation without crack branching is reduced from that observed with HY-80;

(8). Arrest of cleavage cracks produced at low temperatures and under low K-applied values occurs in response to reduction of driving force, and does not involve fracture mode change;

(9). At temperatures closer to the upper transition of the  $K_{Ic}$  versus temperature curve, crack arrest occurs in the presence

of mixed modes of cleavage and ductile tearing, and is related to the loss of local constraint due to local plastic deformation.

## REFERENCES

- Y. Akita and K. Ikeda, Report of Transportation and Technical Institute No. 40 Tokyo, Japan, 1959.
- Y. Akita and K. Ikeda, Report of Transportation and Technical Institute No. 56, Tokyo, Japan 1962.
- N.P. Allen, W.P. Rees, B.E. Hopkins and H.R. Tipler, J. Iron St. Inst. 174, 108-120 (1953).
- A.S. Argon, J. Im and R. Safoglu, Metall. Trans A 6A, 825-837 (1975).
- J.M. Barsom, J. Engr. Fracture Mech. 7, 605 (1975)
- H. Baumgardt, H.F. DeBoer and F. Heisterkamp, in NIOBIUM, PROCEEDINGS OF THE INT. SYMPOSIUM, edited by H. Stuart (The Metallurgical Society of AIME, Pittsburgh, 1984), pp. 883-915.
- C.D. Beachem, J. Basic Eng. 87, 299-306 (1965).
- C.D. Beachem and D.A. Meyn, ELECTRON FRACTOGRAPHY, ASTM STP 436, (American Society for Testing and Materials, Philadelphia, PA, 1968), pp. 59-88.
- C.D. Beachem and G.R. Yoder, Metall. Trans 4, 1145-1153 (1973).
- J. Beinert and J.F. Kalthoff, in APPLICATION OF FRACTURE MECHANICS TO MATERIALS AND STRUCTURES, edited by G.C. Sih, E. Sommer and W. Dahl, (Martinus Nijhoff, The Hague, 1983), pp. 493-507.
- W.D. Biggs and P.L. Pratt, Acta Metall. 6, 694-703 (1958).
- P. Bowen and J.F. Knott, Metal Science 18, 225-235 (1984).
- L.M. Brown and W.M. Stobbs, Phil. Mag. 34, 351-372 (1976).
- P. Brozzo, G. Buzzichelli, A. Masconzoni and M. Mirabile, Metal Science 11, 123-129 (1977).
- G. Bullock and E. Smith, in FAST FRACTURE AND CRACK ARREST, ASTM STP 627, edited by G.T. Hahn and M.F. Kanninen, (American Society for Testing and Materials, Philadelphia, 1977), pp. 286-300.
- R.D. Cheverton, D.G. Ball, S.E. Bolt, S.K. Iskander, R.K. Nanstad, ORNL Rept. NUREG/CR-4249, ORNL-6183, 1985.
- L.L-J. Chin, Welding Research Supplement, July, 290-294 (1969).

- C.G. Chipperfield and J.F. Knott, *Metals Tech.* 2, 45-51 (1975).
- G. Clark, S.M. El Soudani, W.G. Ferguson, R.F. Smith, and J.F. Knott, *Inst. Mech. Eng.* 121, 181-198 (1978).
- J.Q. Clayton and J.F. Knott, *Metal Science* 10, 63-71 (1976).
- A.H. Cottrell, *Trans. Am. Inst. Min. Metall. Petrol. Engrs.* 212, 192-203 (1958).
- A.R. Cox and J.M. Winn, *J. Iron Steel Inst.* 203(2), 175-179 (1965).
- T.B. Cox and J.R. Low, *Metall. Trans.* 5, 1457-1470 (1974).
- P.B. Crosley and E.J. Ripling, *J. Basic Eng.* 91, 525-534 (1969).
- P.B. Crosley and E.J. Ripling, *Nuc. Eng. Design* 17, 32-45 (1971).
- P.B. Crosley and E.J. Ripling, in *FAST FRACTURE AND CRACK ARREST*, STP 627 edited by G.T. Hahn and M.F. Kanninen (American Society for Testing and Materials, Philadelphia, 1977), pp 372-391, *ibid.* ., pp. 203-277
- P.B. Crosley and E.J. Ripling, in *PROCEEDINGS OF INTERNATIONAL CONFERENCE ON DYNAMIC FRACTURE TOUGHNESS* (The Welding Institute, Cambridge, U.K. 1977, pp. 339-349.
- P.B. Crosley and E.J. Ripling, in *CRACK ARREST METHODOLOGY AND APPLICATIONS*, ASTM STP 711, edited by G.T. Hahn and M.F. Kanninen (American Society for Testing and Materials, Philadelphia, 1980), pp. 211-227, *ibid.*., pp. 321-337.
- P.B. Crosley, W.L. Fourney, G.T. Hahn, R.G. Hoagland, G.R. Irwin and E.J. Ripling, U.S. NRC Rept. NUREG/CR-3261 April 1983.
- D.A. Curry, *Nature* 276, 50-51 (1978).
- D.A. Curry, *Mat. Sci. Eng.* 43, 134-144 (1980).
- D.A. Curry, *Metal Science* 14, 319-326 (1980).
- D.A. Curry, *Metal Science* 16, 435-440 (1982).
- D.A. Curry and J.F. Knott, *Metal Science* 10, 1-6 (1976).
- D.A. Curry and J.F. Knott, *Metal Science* 12, 511-514 (1978).
- D.A. Curry and J.F. Knott, *Metal Science* 13, 341-345 (1979).

- L.R. Cutler and M.R. Krishnadev, in MICROSTRUCTURAL SCIENCE, (Elvesier Science Pub., New York, 1982), pp. 79-90.
- L. Dahlberg, F. Nilsson and B. Brikstad, in CRACK ARREST METHODOLOGY AND APPLICATIONS, ASTM STP 711, edited by G.T. Hahn and M.F. Kanninen, (American Society for Testing and Materials, Philadelphia, 1980), pp. 29-108.
- A.J. DeArdo, J.M. Gray and I.L. Meyer, in NIOBIUM, PROCEEDINGS OF THE INT. SYMPOSIUM, edited by H. Stuart (The Metallurgical Society of AIME, Pittsburgh, 1984), pp. 685-760.
- R.A. DePaul and A.L. Kitchen, Metall. Trans. 1, 389-393 (1970).
- R.E. Dolby and J.F. Knott, J. Iron and Steel Inst. 210, 857-865 (1972).
- F. Erdogan, in PROCEEDINGS OF WORKSHOP ON DYNAMIC FRACTURE, (California Institute of Technology, Palo Alto, CA., 1983), pp. 72-74.
- H. Ernst, P.C. Paris, and J.D. Landes, in FRACTURE MECHANICS: 13TH SYMPOSIUM, ASTM STP 743, edited by R. Roberts, (American Society for Testing and Materials, Philadelphia, 1981), pp. 476-502.
- A.G. Evans, Metall. Trans. A 14A, 1349-1355 (1983).
- F.J. Feely Jr., D. Hrtko, S.R. Kleppe and M.S. Northrup, Weld. J. Res. Sup. 19, 995-1115 (1954).
- F.J. Feely Jr., M.S. Northrup, M.S. Kleppe and M. Gensamer, Weld. J. Res. Sup. 596-607 (1955).
- J.R. Fisher and J. Gurland, Metal Science 15, 185-192 (1981).
- S. Floreen and H.W. Hayden. Scripta Met. 4, 87-94 (1970).
- W.L. Fournery, R. Chona and R.J. Sanford, in PROCEEDINGS OF WORKSHOP ON DYNAMIC FRACTURE, (California Institute of Technology, Palo Alto, CA., 1983), pp. 75-99.
- P.C. Gehlen, R.G. Hoagland and C.H. Popelar, Int. J. Fracture 15, 69-84 (1979).
- S. Goodman, S.S. Brenner and J.R. Low, Jr., Metall. Trans. 4, 2363-2369 (1973), *ibid.* 4, 2371-2378 (1973).
- S.H. Goods and L.M. Brown, Acta. Met 27, 1-14 (1979).

- G. Green and Knott, J. Eng. Mat. Tech. 98, 37-46 (1976).
- J.D.G. Groom and J.F. Knott, Metal Science 9, 390-400 (1975).
- J. Gurland and J. Plateau, Trans. ASM 56, 442-454(1963).
- Y. Hagiwara and J.F. Knott, in ADVANCES IN FRACTURE RESEARCH (FRACTURE 81), 1981, pp. 704-714.
- G.T. Hahn, Atomic Structure and Mechanical Properties of Metals, 436-490 (1976).
- G.T. Hahn, Metall. Trans. A 15A, 947-958 (1984).
- G.T. Hahn, A.R. Rosenfield and M. Sarrate, INELASTIC BEHAVIOR OF SOLIDS, edited by M.F. Kanninen et al(McGraw-Hill, New York, 1970), pp. 673-690.
- G.T. Hahn, R.G. Hoagland, M.F. Kanninen and A.R. Rosenfield, in DYNAMIC CRACK PROPAGATION, edited by G.C. Sih (Noordhoff Int., Leyden, 1973) pp. 649-677.
- G.T. Hahn, R.G. Hoagland, A.R. Rosenfield and R. Sejnoha, Metall. Trans. 5, 475-482 (1974).
- G.T. Hahn and A.R. Rosenfield, Metall. Trans. A 6A, 653-668 (1975).
- G.T. Hahn, R.G. Hoagland, M.F. Kanninen and A.R. Rosenfield, Eng. Frac. Mech. 7, 583-591 (1975).
- G.T. Hahn, R.G. Hoagland and A.R. Rosenfield, in PROCEEDINGS OF THE CONFERENCE ON DYNAMIC FRACTURE TOUGHNESS, (The Welding Institute, Cambridge, U.K., 1976), pp. 237-247.
- G.T. Hahn and W.F. Flanagan, in PROCEEDINGS OF CONFERENCE ON DISLOCATION MODELLING OF PHYSICAL SYSTEMS, (Gainsville, Fla., 1980), pp. 1-17.
- G.T. Hahn, R.G. Hoagland, A.R. Rosenfield and C.R. Barnes, CRACK ARREST METHODOLOGY AND APPLICATIONS, ASTM STP 711, edited by G.T. Hahn and M.F. Kanninen, (American Society for Testing and Materials, Philadelphia, 1980), pp. 248-269.
- G.T. Hahn, R.G. Hoagland, J. Lereim, A.J. Markworth and A.R. Rosenfield, in CRACK ARREST METHODOLOGY AND APPLICATIONS, ASTM STP 711, edited by G.T. Hahn and M.F. Kanninen, (American Society for Testing and Materials, Philadelphia, 1980), pp. 289-320.



- G.T. Hahn, R.G. Hoagland and R.D. Cheverton, in **ADVANCES IN FRACTURE RESEARCH (ICF5)**, (Pergamon Press, London, 1981), pp. 1043-1050.
- J.W. Hancock and A.C. Mackenzie, *J. Mech. Phys. Solids* 24, 147-169 (1976).
- J. Harding, *Metals Technology*, Jan., 6-18 (1977).
- D.F. Hasson and J.A. Joyce, *J. Eng. Mat. Tech.* 103, 133-141 (1981).
- S.R. Heller, Jr., I. Fioriti and J. Vasta, *Naval Engineers J.* 77, 29-44 (1965).
- G.E. Hicho, S. Singhal, L.C. Smith and R.J. Fields, *J. Heat Treating* 3(3) 205-212 (1984).
- R.G. Hoagland, A.R. Rosenfield and G.T. Hahn, *Metall. Trans.* 3, 123-136 (1972).
- R.G. Hoagland, A.R. Rosenfield, P.C. Gehlen and G.T. Hahn, in **FAST FRACTURE AND CRACK ARREST**, ASTM STP 627, edited by G.T. Hahn and M.F. Kanninen (American Society for Testing and Materials, Philadelphia, 1977), pp. 177-202.
- E. Hornbogen, *Trans. ASM* 57, 120-132 (1964).
- D. Hull, *Acta Metall.* 8, 11-18 (1960).
- J.L. Hurley and C.H. Shelton, *Metals Engineering Quart.* 6(2), 25-31 (1966).
- P.P. Hydrean, A.L. Kitchen and F.W. Schaller, *Metall. Trans.* 2, 2541-2548 (1971).
- P.P. Hydrean, J.E. Chard and C.H. Shelton, presented at 14th Mechanical and Steel Processing Conference, Chicago, 1972.
- G.R. Irwin, in **FAST FRACTURE AND CRACK ARREST**, ASTM STP 627, edited by G.T. Hahn and M.F. Kanninen (American Society for Testing and Materials, 1977), pp. 7-18.
- G.R. Irwin, presented at the CSNI Specialists Meeting on Crack Arrest, Freiburg, W. Germany, 1984, (to be published).
- G.R. Irwin and A.A. Wells, *Metallurgical Rev.* 10(38), 223-270 (1965).
- R.J. Jesseman and G.J. Murphy, *Ind. Heat Treating*, Sept., 27-32(1979).
- R.J. Jesseman and G.J. Murphy, *J. Heat Treating* 3(3), 228-236 (1984).

- R.J. Jesseman and R.C. Smith, Trans. ASME, J. Engr. for Ind., May, 1975, pp. 408-416.
- W. Jolley, Trans. Metall. Soc. AIME 242, 306-314 (1968).
- J.A. Joyce and J.P. Gudas, in ELASTIC PLASTIC FRACTURE, ASTM STP 668, (American Society for Testing and Materials, Philadelphia, 1979), pp. 451-468
- J.A. Joyce and E.M. Hackett, presented at ASTM 17th National Fracture Mechanics Symposium, Albany, New York, August 1984 (to be published).
- J.F. Kalthoff, in PROCEEDINGS OF WORKSHOP ON DYNAMIC FRACTURE, (California Institute of Technology, Palo Alto, 1983), pp. 11-35.
- J.F. Kalthoff, J. Beinert and S. Winkler, in FAST FRACTURE AND CRACK ARREST, ASTM STP 627 (American Society for Testing and Materials, Philadelphia, 1977), pp. 161-176.
- J.F. Kalthoff, J. Beinert, S. Winkler and W. Klemm, in CRACK ARREST METHODOLOGIES AND APPLICATIONS, ASTM STP 711, edited by G.T. Hahn and M.F. Kanninen, (American Society for Testing and Materials, Philadelphia, 1980), pp. 109-127.
- T. Kanazawa, in DYNAMIC CRACK PROPAGATION, edited by G.C. Sih (Noordhoff Int., Leyden, 1973), pp. 565-597.
- T. Kanazawa, S. Machida and M. Matoba, J. Soc. Naval Arch. Japan 115, 77-88 (1964).
- T. Kanazawa, S. Machida and M. Matoba, J. Soc. Naval Arch. Japan 116, 124-135 (1964).
- T. Kanazawa and S. Machida, J. Japan Shipbuilding and Eng., Sept., 21-28 (1967).
- T. Kanazawa, S. Machida and M. Ohyagi, J. Soc. Naval Arch. Japan 122, 201-214 (1967).
- T. Kanazawa, S. Machida and H. Doi, J. Soc. Naval Arch. Japan 124, 321-330 (1967).
- T. Kanazawa, S. Machida and T. Teramoto, in FAST FRACTURE AND CRACK ARREST, ASTM STP 627, (American Society for Testing and Materials, Philadelphia, 1977), pp. 39-58.
- T. Kanazawa, S. Machida and H. Yajima, in FRACTURE MECHANICS TECHNOLOGY APPLIED TO MATERIAL EVALUATION AND STRUCTURAL DESIGN, edited by G.C. Sih, N.E. Ryan and R. Jones, Martinus Nijhoff, The Hague, 1983), pp. 81-100.

- M.F. Kanninen, C. Popelar and P.C. Gehlen, in FAST FRACTURE AND CRACK ARREST, ASTM STP 627 (American Society for Testing and Materials, Philadelphia, 1977), pp. 19-38.
- M.F. Kanninen and C.H. Popelar, in ADVANCED FRACTURE MECHANICS, (Oxford University Press, New York, 1985), pp. 192-280.
- R.E. Kelley, M.S. thesis, University of Texas, El Paso, 1974.
- J.E. King and J.F. Knott, Metal Science 15, 1-6 (1981).
- J.F. Knott, J. Iron Steel Inst. 204, 104-111 (1966).
- J.F. Knott, Proceedings of ISI Conf. on Effect of Second Phase Particles on the Mechanical Properties of Steel, 1971, pp. 44-53.
- J.F. Knott, in PROC. INT. CONF. ON FRACTURE, 4TH, edited by D.M.R. Taplin (Pergamon Press, New York, 1978), pp. 61-92.
- J.F. Knott, Metal Science 14, 327-336 (1980).
- J.F. Knott, Phil. Trans. R. Soc. Lond. A 299, 45-57 (1981).
- J.F. Knott, in PROCEEDINGS OF THE INTERNATIONAL CONFERENCE ON ADVANCES IN THE PHYSICAL METALLURGY AND APPLICATIONS OF STEELS, (The Metals Society, London, 1982), pp. 181-198.
- J.F. Knott, in PROCEEDINGS OF THE CONFERENCE ON STEELS FOR LINE PIPELINE AND FITTINGS, (The Metals Society, London, 1983), pp. 79-89.
- A.S. Kobayashi and S. Mall, Exp. Fracture Mech., Jan., 11-18 (1978).
- T. Kobayashi and J.W. Dally, in FAST FRACTURE AND CRACK ARREST, ASTM STP 627, edited by G.T. Hahn and M.F. Kanninen, (American Society for Testing and Materials, Philadelphia, 1977), pp. 257-273.
- T. Kobayashi and J.W. Dally, in CRACK ARREST METHODOLOGY AND APPLICATIONS, ASTM STP 711, (American Society for Testing and Materials, Philadelphia, 1980), pp. 189-210.
- J.M. Krafft, Applied Materials Research 3, 88-101 (1964).
- G. Krauss, in PHASE TRANSFORMATIONS IN FERROUS ALLOYS, edited by A.R. Marder and J.I. Goldstein (The Metallurgical Society of AIME, Warrendale, PA, 1984), pp. 101-124.

- M.R. Krishnadev, L.R. Cutler, M.C. Cheresh, D.R. Ireland and J.E. Green, in MICROSTRUCTURAL SCIENCE, (Elsevier Science Publishing Co., New York, 1983), pp.63-76.
- T. Lin, A.G. Evans and R.O. Ritchie, Lawrence Berkeley Laboratory Rept. LBL-19673, May, 1985.
- C.H. Lorig, discussion of Smith and Palmer, AIME Trans. 105 165-167, 1933.
- J.R. Low, Jr., Trans. ASM 46A, 163-179 (1954).
- A.C. Mackenzie, J.W. Hancock and D.K. Brown, Eng. Fracture Mech. 9, 167-188(1977).
- F.A. McClintock, PHYSICS OF STRENGTH AND PLASTICITY, edited by A.S. Argon (M.I.T. Press, Cambridge MA., 1969), pp. 307-326.
- F.A. McClintock and G.R. Irwin, FRACTURE TOUGHNESS TESTING AND ITS APPLICATIONS, ASTM STP 381, (American Society for Testing and Materials, Philadelphia, 1965), 84-113.
- C.J. McMahon, Jr. and M. Cohen, Acta Metall. 13, 591-604 (1965).
- C.J. McMahon, Jr. and M. Cohen, in PROCEEDINGS OF 1ST INTERNATIONAL CONFERENCE ON FRACTURE, Vol. 2, 1965, pp. 779-812.
- A. Melander and J. Steninger, Mat. Sci. and Eng. 52, 239-248 (1982).
- METALS HANDBOOK, 1948 ed., (American Society for Metals, Cleveland, 1948), pp. 462-495.
- L. Meyer and W. Mueschenborn, in MICROALLOYING 75, (Union Carbide Corp., New York, 1977), pp. 153-167.
- M.T. Miglin, PhD. Dissertation, the Ohio State University, 1982.
- M.T. Miglin, J.P. Hirth and A.R. Rosenfield, Metall. Trans. 14A, 2055-2061 (1983).
- T.W. Montemarano, B.P. Sack, J.P. Gudas, M.G. Vassilaros and H.H. Vanderveldt, presented to Soc. of Naval Arch. and Marine Engr.(Chesapeake Chapter), September, 1984 (to be published).
- N.F. Mott, J. Iron St. Inst. 183, 233-243 (1956).

- Y. Nakano, presented at 18th Symposium on X-ray Study on Deformation and Fracture and Solids, July 1981 (Society of Mat. Sci., Japan).
- Y. Nakano, presented at the Symposium on Fracture Mechanics, October 1981, (Society of Mat. Sci., Japan).
- Y. Nakano and M. Katayama, J. Soc. Mat. Sci. Japan 30, 241 (1981).
- Y. Nakano and M. Tanaka, Trans. Iron Steel Inst. Japan 22, 147-153 (1982).
- J.P. Naylor, Metall. Trans. A 10A, 861-873 (1979).
- W.J. Nordell and W.J. Hall, Weld. Res. Supp. , 124-134 (1965).
- S.R. Novak, Eng. Fracture Mech. 5, 727-763 (1973).
- J.P. Orton, in MICROALLOYING 75, (Union Carbide Corp., New York, 1977), pp. 334-347.
- W.S. Owen, B.L. Averbach and M. Cohen, Trans. ASM 50, 634-655 (1958).
- W.S. Pellini, in PRINCIPLES OF STRUCTURAL INTEGRITY, (Office of Naval Research, Arlington Va., 1976), pp. 99-105.
- N.J. Petch, J. Iron St. Inst. 173, 25-28 (1953).
- F.B. Pickering, in HIGH STRENGTH LOW ALLOY STEELS-A DECADE OF PROGRESS, (Union Carbide Corp., New York, 1977), pp. 9-31.
- A. Pineau, in ADVANCES IN FRACTURE RESEARCH, edited by D. Francois (Pergamon Press, New York, 1981), Vol. 1, pp. 553-577.
- C.H. Popelar and M.F. Kanninen, in CRACK ARREST METHODOLOGY AND APPLICATIONS, ASTM STP-711, edited by G.T. Hahn and M.F. Kanninen, (American Society for Testing and Materials, Philadelphia, 1980), pp. 5-23.
- K.E. Puttick, Phil. Mag. 4, 964-969 (1959).
- K. Ravi-Chandar and W.G. Knauss, in PROCEEDINGS OF WORKSHOP ON DYNAMIC FRACTURE, (California Institute of Technology, Palo Alto, 1983), pp. 119-128.
- R.E. Reed Hill, PHYSICAL METALLURGY PRINCIPLES, (D. Van Nostrand Co., Inc., Princeton, NJ, 1964), pp. 439-493.

- S.P. Rawal and J Gurland, Metall. Trans. 8A, 691-698 (1977).
- J.R. Rice and D.M. Tracey, J. Mech. Phys. Solids 17, 201-217 (1969).
- J.R. Rice and M.A. Johnson, INELASTIC BEHAVIOR OF SOLIDS, edited by M.F. Kanninen et al (McGraw-Hill, New York, 1970), pp. 641-672.
- R.O. Ritchie, J.F. Knott and J.R. Rice, J. Mech. Phys. Solids 21, 395-410 (1973).
- R.O. Ritchie, R.F. Smith and J.F. Knott, Metal Science 9, 485-492 (1975).
- R.O. Ritchie, W.L. Server and R.A. Wullaert, Metall. Trans. A 10A, 1557-1570 (1979).
- R.O. Ritchie and A.W. Thompson, Metall. Trans. A, 16A, 233-248, (1985).
- V.G. Rivlin, Int. Met. Rev. 29, No. 2, 96-121 (1984).
- T.S. Robertson, J. Iron Steel Inst. 175, 361-374 (1953).
- H.C. Rogers, Trans. Met. Soc. AIME 218, 498-506 (1960).
- S.T. Rolfe and J.M. Barson, FRACTURE AND FATIGUE CONTROL IN STRUCTURES, (Prentice-Hall, New Jersey, 1977), pp. 131-170.
- A.J. Rosakis, J. Duffy and L.B. Freund, in PROCEEDINGS OF WORKSHOP ON DYNAMIC FRACTURE, (California Institute of Technology, Palo Alto, 1983), pp. 100-118.
- A.R. Rosenfield, Met.Rev. 13, 29-40 (1968).
- A.R. Rosenfield, D.K. Shetty and A.J. Skidmore, Metall. Trans. A 14A, 1934-1937 (1983).
- A.R. Rosenfield, P.N. Mincer, C.W. Marshall and A.J. Markworth, in FRACTURE MECHANICS, FIFTEENTH SYMPOSIUM, ASTM STP 833, edited by R.J. Sanford (American Society for Testing and Materials, Philadelphia, 1984), pp. 149-164.
- A.R. Rosenfield and D.K. Shetty, in ELASTIC PLASTIC FRACTURE TEST METHODS, THE USER'S EXPERIENCE, ASTM STP 856, (American Society for Testing and Materials, Philadelphia, 1985), pp. 196-209.
- T. Saario, K. Wallin and K. Torronen, J. Eng. Mat. Tech. 106, 173-177 (1984).

- A. Saxena and S.J. Hudak, *Int. J. Fracture* 14, 453-468 (1978).
- C.F. Shih, *J. Mech. Phys. Solids* 29, 305-330 (1981).
- A.K. Shoemaker and S.T. Rolfe, *Eng. Fracture Mech.* 2, 319-399 (1971).
- S. Slatcher and J.F. Knott, *FRACTURE AND THE ROLE OF MICROSTRUCTURE, VOL. 1* (Engineering Materials Advisory Services Ltd., U.K., 1982), pp. 176-181.
- C.S. Smith and E.W. Palmer, *Trans. AIME* 105, 133-168 (1933).
- E. Smith, in *PROCEEDINGS OF CONFERENCE ON 'PHYSICAL BASIS OF YIELD AND FRACTURE'*, (Institute for Physics and Physical Soc., Oxford, 1966), pp. 36-46.
- E. Smith, *Int. J. Frac. Mech.* 4, 131-145 (1968).
- R.F. Smith and J.F. Knott, *Inst. Mech. Engr.* 9, 65-75, (1971).
- G.R. Speich, *Metall. Trans.* 3, 1043-1053 (1972).
- G.R. Speich, in *METALS HANDBOOK, 8th EDITION* (American Society for Metals, Metals Park, Ohio, 1973), pp. 202-204.
- F.N. Speller, discussion of C.S. Smith et al, *AIME Trans.* 105, 164-168, 1933.
- M.G. Stout and W.W. Gerberich, *Metall. Trans. A* 9A, 649-658 (1978).
- A.N. Stroh, *Proc. R. Soc. A* 223, 404-414 (1954).
- A.N. Stroh, *Philos. Mag.* 46, 968-972 (1955).
- A.N. Stroh, *Adv. Phys.* 6, 418-434 (1957).
- T. Tanaka, T. Furukori, M. Ueda, J. Tsuboi, T. Yasuda and C. Uehashi, in *MICROALLOYING 75*, (Union Carbide Corp, New York, 1977), pp. 399-409.
- J.H. Tweed and J.F. Knott, in *FRACTURE AND THE ROLE OF MICROSTRUCTURE, VOL.1* (Engineering Materials Advisory Services Ltd., U.K., 1982) pp. 127-133.
- J.H. Tweed and J.F. Knott, *Metal Science* 17 (2), 45-54 (1983).
- R.H. Van Stone, T.B. Cox, J.R. Low, Jr., and J.A. Psoida, *Int. Metals Rev.* 30; 4, 157-179 (1985).

- M.G. Vassilaros, J.P. Gudas and J.A. Joyce, U.S. Nuclear Regulatory Commission Report NUREG/CR-2570, April 1982.
- K. Wallin, T. Saario and K. Torronen, Metal Science 18, 13-16 (1984).
- W. Werchniak, Eng. Fracture Mech. 4, 841-851 (1972).
- D.J. Widgery and J.F. Knott, Metal Science 12, 8-11, (1978).
- H.G.F. Wilsdorf, Mat. Sci. and Eng. 59, 1-39 (1983).
- M. Yoshiki and T. Kanazawa, J. Soc. Naval Arch. Japan 102, 39-45 (1957).
- M. Yoshiki, T. Kanazawa and S. Machida, J. Soc. Naval Arch. Japan 118, 192 (1965).
- C.P. You and J.F. Knott, FRACTURE AND THE ROLE OF MICROSTRUCTURE, VOL. 1, (Engineering Materials Advisory Services Ltd., U.K., 1982), pp. 23-29.
- C. Zener, Trans. ASM 40A, 3-31 (1948).



Table 1. SPECIFICATION COMPOSITIONS AND PROPERTIES OF HY-80 AND ASTM A 710  
Gr. A Cl. 3 STEELS

ALLOY	CHEMICAL COMPOSITION WEIGHT PERCENT											
	C	Mn	P	S	Ni	Cr	Mo	Cu	Si	Nb	V	Ti
HY-80	0.18 max.	0.10 – 0.40	0.025 max.	0.025 max.	2.00 – 3.25	1.00 – 1.80	0.20 – 0.60	0.25 max.	0.15 – 0.35	—	0.03 max.	0.02 max.
ASTM A710 Gr A Cl 3	0.07 max.	0.40 – 0.70	0.025 max.	0.025 max.	0.70 – 1.00	0.60 – 0.90	0.15 – 0.25	1.00 – 1.30	0.40 max.	0.02 min.	—	

ALLOY	TENSILE PROPERTY MEASUREMENT			
	0.2% Yield Strength MPa	Yld. Strength ksi	Ult. Tensile Strength MPa	Elong. % in 50.8 mm
HY-80	551-689	80-100	—	19 min.
ASTM A710 Gr A Cl 3	515 min.	75 min.	585 min.	20 min.

Table 2. CHEMICAL COMPOSITION OF HY-80 AND ASTM A 710 Gr. A Cl. 3 STEELS

ALLOY	CHEMICAL COMPOSITION, WEIGHT PERCENT												
	C	Mn	P	S	Ni	Cr	Mo	Cu	Si	Al	Nb	V	Ti
HY-80 Material Code FYB	0.153	0.33	0.012	0.013	2.55	1.66	0.37	0.033	0.18	—	—	0.003	<0.001
HY 80 Specification Allowables	0.18 max.	0.10 — 0.40	0.025 max.	0.025 max.	2.00 — 3.25	1.00 — 1.80	0.20 — 0.60	0.25 max.	0.15 — 0.35			0.03 max.	0.02 max.
ASTM A710 Gr A Cl 3 Material Code GGO	0.06	0.50	0.013	0.004	0.88	0.75	0.21	1.16	0.28	0.030	0.039	—	—
ASTM A710 Gr A Cl 3 Specification Allowables	0.07 max.	0.40 — 0.70	0.025 max.	0.025 max.	0.70 — 1.00	0.60 — 0.90	0.15 — 0.25	1.00 — 1.30	0.40 max.	—	0.02 min.	—	—

Table 3. ROOM TEMPERATURE MECHANICAL PROPERTIES OF HY-80 AND ASTM A 710  
Gr. A Cl. 3 STEELS

	TENSILE PROPERTY MEASUREMENT					
	0.2% Yield Strength MPa	Yield Strength ksi	Ult. Tensile Strength MPa	Tensile Strength ksi	Elongation % in 50.8 mm	Reduction of Area %
HY 80 Material Code FYB Specification	588.4 576.7 587.7 Avg. 584.3 551-689	85.4 83.7 85.3 Avg. 84.8 80-100	706.2 693.1 704.8 Avg. 701.4 —	102.5 100.6 102.3 Avg. 101.8 —	28 27 25 Avg. 27 19 min.	68 68 67 Avg. 68 —
ASTM A710 Gr A Cl 3 Material Code GGO Specification	626.3 631.8 631.1 Avg. 628.7 515 min.	90.9 91.7 91.6 Avg. 91.4 75 min.	719.3 721.4 720.0 Avg. 720.2 585 min.	104.4 104.7 104.5 Avg. 104.5 85 min.	29 28 29 Avg. 29 20 min.	74 74 74 Avg. 74 —

Table 4. RESULTS OF TRUE STRESS/TRUE STRAIN TESTS OF HY-80 AND ASTM A 710  
Gr. A Cl. 3 STEELS

Material	Specimen	Test Temp.		0.2% Yield Str.		Lower Yield Str.		True Fracture Stress		True Fracture Strain	Strain Hardening Exponent
		°C	°F	MPa	ksi	MPa	ksi	MPa	ksi		
HY-80 Steel	FYB-37	22	72	634	92			909	132	1.087	0.155
	FYB-36	-23	-9			668	97	1233	179	1.021	0.169
	FYB-35	-49	-57			690	100	1309	190	1.008	0.169
	FYB-34	-78	-109			723	105	1344	195	0.961	0.165
	FYB-32	-103	-153			744	108	1385	201	0.992	0.187
	FYB-31	-132	-205			847	123	1399	203	0.855	0.264
ASTM A 710 Gr. A Cl. 3 STEEL	GG0-45	22	72	634	92			1371	199	1.339	0.140
	GG0-49	-9	16	668	97			1371	199	1.315	0.114
	GG0-42	-19	-2			668	97	1330	193	1.255	0.130
	GG0-43	-47	-53			682	99	1385	201	1.247	0.138
	GG0-47	-77	-108			737	107	1468	213	1.270	0.100
	GG0-48	-106	-159			758	110	1523	221	1.263	0.099

Table 5. CHARPY V-NOTCH IMPACT TOUGHNESS TEST RESULTS FOR HY-80 STEEL  
MATERIAL CODE FYB

Spec. No.	Test Temperature		Absorbed Impact Energy		Shear Fracture %	Lateral Expansion	
	°C	°F	J	Ft-Lb		mm	inch
64	22	72	97	71	100	1.30	0.051
65	22	72	99	73	100	1.47	0.058
66	22	72	94	69	100	1.52	0.060
67	-18	0	94	69	100	1.42	0.056
68	-18	0	84	62	100	1.07	0.042
69	-18	0	106	78	100	1.45	0.057
74	-46	-50	90	66	100	1.17	0.046
75	-46	-50	88	65	100	1.19	0.047
70	-46	-50	105	77	100	1.55	0.061
80	-84	-120	80	59	80	1.17	0.046
81	-84	-120	94	69	60	1.30	0.051
82	-84	-120	72	53	70	1.14	0.045
77	-101	-150	53	39	20	0.76	0.030
78	-101	-150	54	40	20	0.84	0.033
79	-101	-150	68	50	20	0.91	0.036
83	-129	-200	39	29	10	0.51	0.020
84	-129	-200	38	28	10	0.53	0.021
85	-129	-200	46	34	10	0.58	0.023

Table 6. CHARPY V-NOTCH IMPACT TOUGHNESS TEST RESULTS FOR ASTM A 710  
Gr. A CL. 3 STEEL, MATERIAL CODE GGO

Spec. No.	Test Temperature		Absorbed Impact Energy		Shear Fracture %	Lateral Expansion	
	°C	°F	J	Ft-Lb		mm	inch
22	22	72	242	178	100	2.36	0.093
23	22	72	231	170	100	2.41	0.095
24	22	72	230	169	100	2.34	0.092
8	-18	0	249	183	100	2.21	0.087
9	-18	0	246	181	100	2.26	0.089
00	-18	0	253	186	100	1.73	0.068
25	-47	-53	148	109	60	1.83	0.072
26	-47	-53	189	139	75	2.11	0.083
27	-47	-53	196	144	70	2.11	0.083
31	-62	-80	159	117	60	1.91	0.075
36	-62	-80	192	141	70	2.51	0.099
33	-62	-80	178	131	70	2.13	0.084
23	-84	-120	139	102	60	1.75	0.069
24	-84	-120	148	109	60	1.83	0.072
25	-84	-120	133	98	50	1.73	0.068
17	-101	-150	132	97	30	1.68	0.066
18	-101	-150	22	16	10	0.36	0.014
20	-101	-150	136	100	60	1.75	0.069
21	-118	-180	75	55	20	0.94	0.037
22	-118	-180	22	16	0	0.30	0.012

Table 7. RESULTS OF 5/8-INCH DYNAMIC TEAR TESTS OF HY-80 AND ASTM A 710  
Gr. A Cl. 3 STEELS

Material/ Code	Spec. No.	Test Temperature		Absorbed Impact Energy		Shear Fracture %
		°C	°F	J	Ft-Lb	
HY80 FYB	1	22	72	857	630	100
	3	22	72	1088	800	100
	4	22	72	898	660	100
	9	-18	0	816	600	100
	10	-18	0	789	580	100
	11	-40	-40	802	590	100
	12	-40	-40	884	650	100
	15	-84	-120	326	240	20
	16	-84	-120	326	240	20
	17	-101	-150	218	160	15
	18	-101	-150	218	160	10
	19	-62	-80	802	590	100
ASTM A710 Gr. A Cl. 3  GGO	20	-62	-80	748	550	100
	68	21	70	1972	1450	100
	58	-18	0	884	650	25
	66	-18	0	734	540	35
	54	-40	-40	449	330	15
	55	-40	-40	911	670	20
	65	-62	-80	286	210	10
	67	-62	-80	190	140	10
	56	-84	-120	150	110	0
	57	-84	-120	150	110	0

Table 8. FRACTURE TOUGHNESS TEST RESULTS FOR HY-80 STEEL

Specimen	Test Temp		Crack Extension Description	$J_{IC}$		$K(J_{IC})$		$J_I$ (cleavage)		$K(J_I)$ (cleavage)	
	$^{\circ}C$	$^{\circ}F$		$kJ/m^2$	$in-lb/in^2$	$MPa\sqrt{m}$	$ksi\sqrt{in}$	$kJ/m^2$	$in-lb/in^2$	$MPa\sqrt{in}$	$ksi\sqrt{in}$
FYB 42	22	72	Stable Tearing	132	752	162	148	—	—	—	—
43	22	72	Stable Tearing	149	850	173	157	—	—	—	—
57	22	72	Stable Tearing	153	871	175	159	—	—	—	—
44	-19	-2	Stable Tearing	168	955	183	166	—	—	—	—
56	-24	-12	Stable Tearing	158	897	177	161	—	—	—	—
46	-48	-55	Stable Tearing	182	1039	191	174	—	—	—	—
58	-49	-57	Stable Tearing	165	939	182	165	—	—	—	—
45	-77	-106	Stable Tearing	199	1133	199	181	—	—	—	—
59	-80	-112	Stable Tearing	212	1210	206	187	—	—	—	—
57	-104	-156	Stable Tearing	225	1281	212	193	—	—	—	—
60	-103	-154	Stable Tearing	173	988	186	169	—	—	—	—
51	-118	-180	Cleavage	—	—	—	—	127	722	159	145
49	-129	-201	Slight Tearing $\rightarrow$ Cleavage	176	1000	187	170	270	1538	232	211
52	-132	-205	Slight Tearing $\rightarrow$ Cleavage	203	1155	201	183	226	1287	213	193
50	-130	-202	Slight Tearing $\rightarrow$ Cleavage	193	1100	196	179	268	1524	231	210
48	-132	-211	Slight Tearing $\rightarrow$ Cleavage	193	1100	196	179	214	1216	207	188
38	-143	-225	Cleavage	—	—	—	—	137	778	165	150
40	-157	-250	Cleavage	—	—	—	—	121	687	155	141
62	-171	-276	Cleavage	—	—	—	—	74	419	121	110



Table 9. FRACTURE TOUGHNESS TEST RESULTS FOR ASTM A710 Gr. A Cl. 3 STEEL

Specimen	Test Temp		Crack Extension Description	$J_{Kc}$		$K(J_{Kc})$		$J_I$ (cleavage)		$K(J_I)$ (cleavage)	
	°C	°F		$\text{kJ/m}^2$	$\text{in-lb/in}^2$	$\text{MPa}\sqrt{\text{m}}$	$\text{ksi}\sqrt{\text{in}}$	$\text{kJ/m}^2$	$\text{in-lb/in}^2$	$\text{MPa}\sqrt{\text{in}}$	$\text{ksi}\sqrt{\text{in}}$
GGO-3	22	72	Stable Tearing	238	1354	218	198	—	—	—	—
GGO-9	21	70	Stable Tearing	282	1607	237	216	—	—	—	—
GGO-1	9	49	Stable Tearing	414	2355	287	261	—	—	—	—
GGO-4	-4	24	Stable Tearing	443	2522	298	271	—	—	—	—
GGO-6	-12	11	Stable Tearing	500	2845	316	287	—	—	—	—
GGO-5	-19	-3	Tearing → Cleavage	439	2500	296	269	555	3160	333	303
GGO-11	-23	-9	Cleavage	—	—	—	—	248	1412	223	202
GGO-2	-52	-61	Cleavage	—	—	—	—	122	697	156	142
GGO-10	-74	-101	Cleavage	—	—	—	—	192	1092	196	178
GGO-18	-76	-105	Cleavage	—	—	—	—	156	886	176	160
GGO-16	-103	-154	Cleavage	—	—	—	—	12	67	48	44
GGO-7	-106	-158	Cleavage	—	—	—	—	34	193	82	75

Table 10. CRACK ARREST TOUGHNESS RESULTS FOR HY-80 STEEL

Spec.	Crack Arrest Specimen Dimensions					
	Thickness B		Net Thickness B <sub>n</sub>		Width W	
	mm	in	mm	in	mm	in
FYBCCA-1	31.8	1.25	25.4	1.00	356	14
FYBCCA-2	31.8	1.25	25.4	1.00	406	16
FYB-1A	25.4	1.00	20.3	0.80	356	14
FYB-1B	25.4	1.00	20.3	0.80	356	14
FYB-3A	25.4	1.00	20.3	0.80	356	14

CRACK ARREST TEST PARAMETERS AND RESULTS																					
Spec	Avg Temp Grad		Orig Crack Length, $a_i$		Crack Init COD, $a_0$		Temp Init $T_0$		$K_{max}$ $K_{IC}$		Final Crack Length, $a_f$		Crack Jump Length, $\Delta a$		Crack Arr COD, $a_f$		$K_0$		Temp. Arr. $T_a$		Comments
	Cross	Face	min	in	min	in	°C	°F	MPa $\sqrt{m}$	$\text{ksi} \sqrt{\text{in}}$	min	in	min	in	min	in	MPa $\sqrt{m}$	$\text{ksi} \sqrt{\text{in}}$	°C	°F	
FYB CCA 1	0.34	16.6	120	5.1	1.07	0.042	-137	-216	201	274	226	8.90	114	4.00	1.32	0.062	146	133	-103	-164	Branch cracks. Dominant branch evolution.
FYB CCA 2	0.23	16.6	120	5.06	0.96	0.008	-146	-226	227	262	328	12.90	168	7.00	1.76	0.067	96	87	-103	-164	Chorron crack starter.
FYB- 1A	0.21	9.9	124	4.06	0.88	0.027	-160	-236	200	190	240	9.70	124	4.00	1.00	0.043	100	91	-117	-178	Chorron crack starter; slight branch.
FYB 1B	0.41	16.6	124	4.07	0.86	0.006	-146	-234	200	182	224	8.70	98	3.00	0.96	0.038	111	101	-106	-160	Chorron crack starter.
FYB 3A	0.44	26.3	124	4.02	0.86	0.004	-131	-204	206	242	228	9.00	104	4.10	1.24	0.040	126	123	-96	-138	Chorron crack starter.

Table 11. CRACK ARREST TOUGHNESS RESULTS FOR ASTM A 710  
Gr. A Cl. 3 STEEL

CRACK ARREST TEST PARAMETERS AND RESULTS																					
Spec.	Avg Temp Grad		Orig Crack Length, a <sub>o</sub>		Crack Init. COD, b <sub>o</sub>		Temp. Init. T <sub>o</sub>		K <sub>max</sub> K <sub>IC</sub>		Final Crack Length, a <sub>f</sub>		Crack Jump Length, Δa		Crack Ar. COD, b <sub>f</sub>		K <sub>IC</sub>		Temp. Ar. T <sub>a</sub>		Comments
	°C/min	°F/hr	mm	in	mm	in	°C	°F	MPa√m	ksi√in	mm	in	mm	in	mm	in	MPa√m	ksi√in	°C	°F	
QGO-2	0.26	16.1	124	4.9	1.33	0.013	-62	-79	90	90	147.3	5.80	22.9	0.90	0.41	0.061	95	95	-48	-56	Severely branched crack.  Branched crack dominant branch calculations. Branched crack dominant branch calculations. Severely branched crack.
QGO-1	0.21	9.8	124	4.9	1.07	0.042	-34	-29	326	281	—	—	—	—	—	—	—	—	—	—	
QGO-4	0.26	12.6	124	4.9	0.97	0.036	-46	-54	290	264	214.6	8.46	90.2	3.55	1.14	0.045	141°	128°	-24	-11	
QGO-6	0.32	16.2	124	4.9	1.19	0.047	-43	-46	360	326	9.16	0.36	110.5	4.35	1.47	0.058	166°	142°	-3	27	
QGO-3	0.26	17.5	124	4.86	0.94	0.033	-53	-64	266	233	—	—	—	—	—	—	—	—	—	—	

\*Non-valid  $K_{IC}$  calculations from dominant branch measurements

NOTE: Specimen Thickness B = 25.4 mm (1.0-inch)  
Specimen Net Thickness  $B_N$  = 20.3 mm (0.80-inch)  
Specimen Width = 356 mm (14-inches)

Table 12. SUMMARY OF INCLUSION AND CARBIDE SIZE MEASUREMENTS  
IN HY-80 AND ASTM A 710 Gr. A Cl. 3 STEELS

Particle Description	Mean Particle Size		Standard Deviation		Range of Particle Size		Measurement Source
	$\mu\text{m}$	$\frac{\text{in}}{(\times 10^{-5})}$	$\mu\text{m}$	$\frac{\text{in}}{(\times 10^{-5})}$	$\mu\text{m}$	$\frac{\text{in}}{(\times 10^{-5})}$	
Discrete, spherical HY-80 MnS inclusions	1.50	5.85	0.55	2.15	0.71-3.3	2.77-12.87	SEM: Ductile fracture spec.
HY-80 Tempered Carbide	0.22	0.86	0.05	0.20	0.10-0.38	0.39-1.48	SEM: 4% Picral etched spec.
ASTM A 710 Gr. A Cl. 3 MnS inclusions	4.65	1.83	0.18	0.70	0.16-0.87	0.62-3.39	SEM: Ductile fracture spec.
ASTM A 710 Gr. A Cl. 3 Carbide	0.37	1.44	0.14	0.55	0.05-0.81	0.20-3.16	SEM: 4% Picral etched spec.
ASTM A 710 Gr. A Cl. 3 Carbide Colony	3.55	13.85	1.38	5.38	0.41-8.41	1.60-32.80	SEM: 4% Picral etched spec.

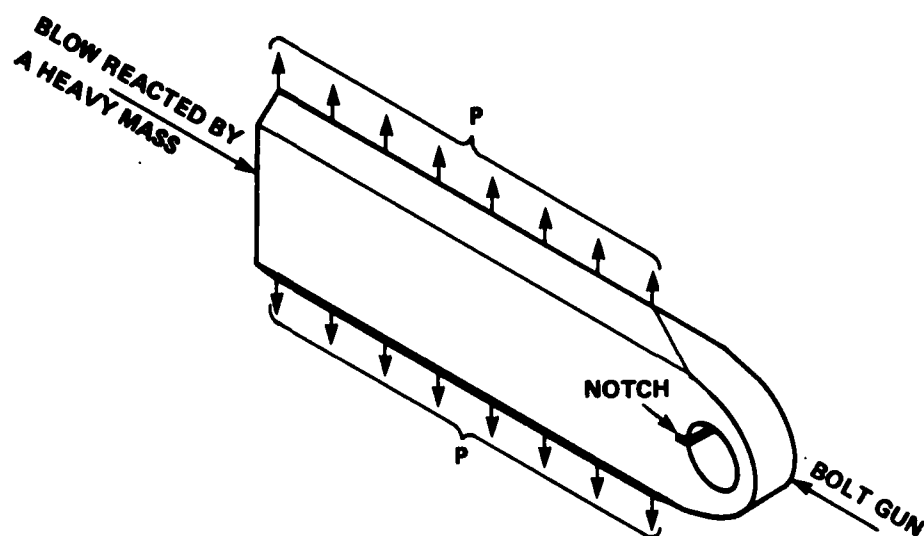


Figure 1. Robertson Crack Arrest Test Specimen  
[Robertson, 1953]

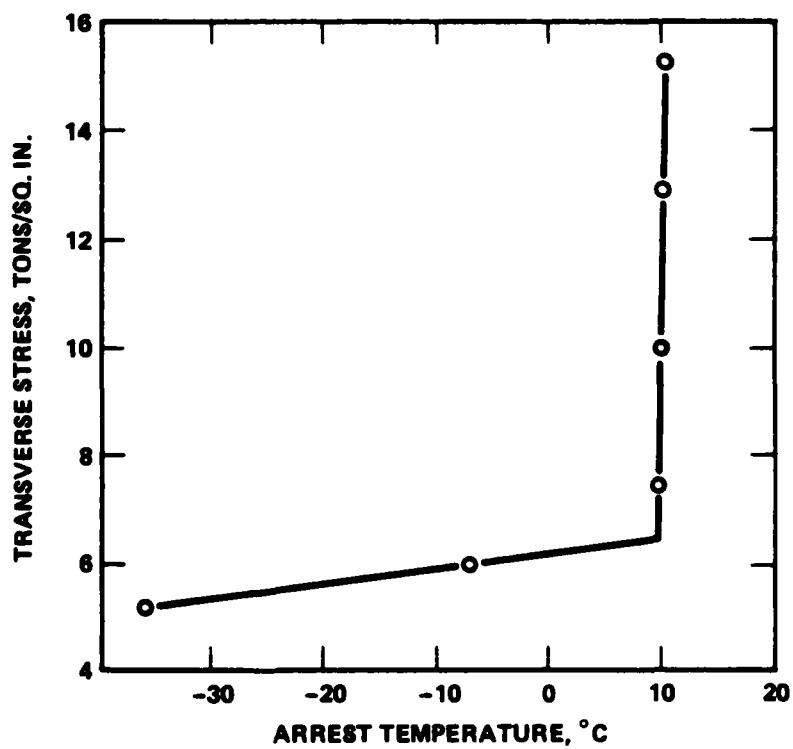


Figure 2. Typical Results of Robertson Crack Arrest Test  
[Robertson, 1953]

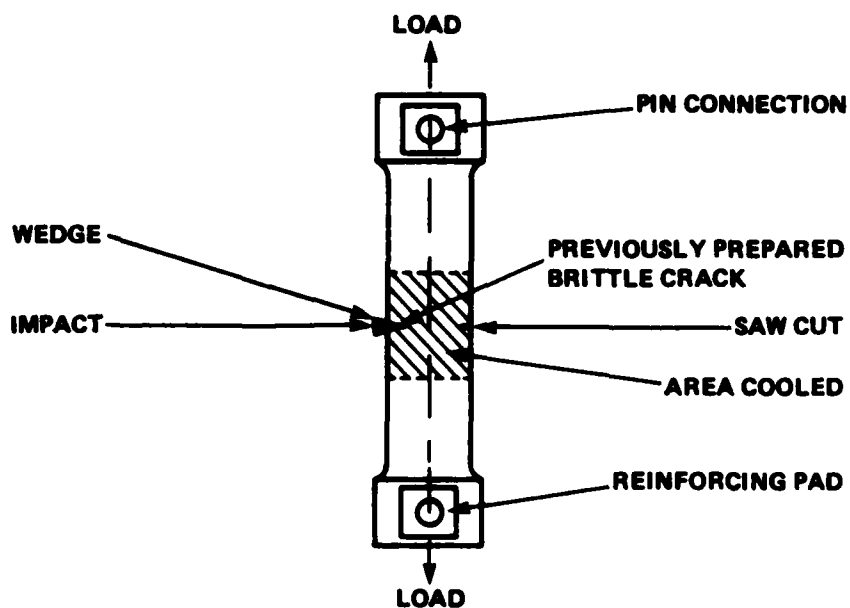


Figure 3. Wide Plate Crack Arrest Specimen Design and Test Arrangement [Feely et al, 1954]

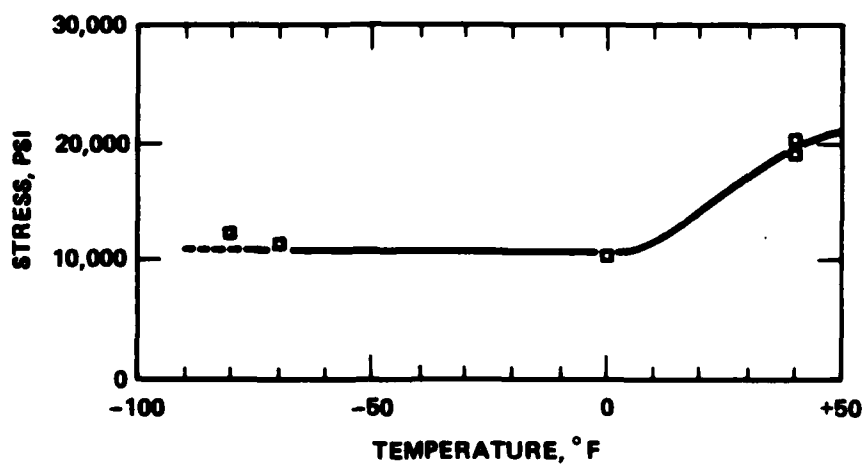


Figure 4. Typical Results of SOD (ESSO) Wide Plate Crack Arrest Tests, ASTM-A285 Gr. C Steel [Feely et al, 1954]

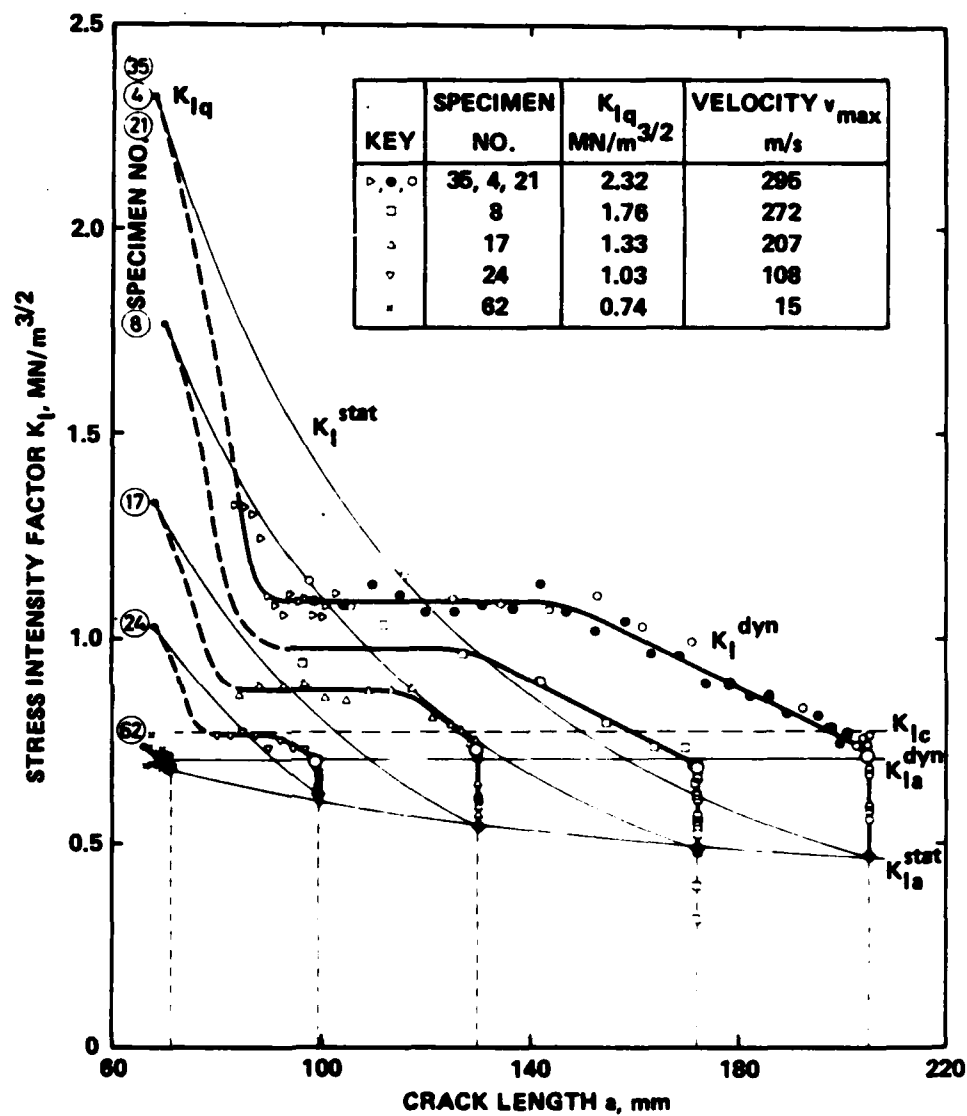


Figure 5. Crack Arrest Toughness Values for ARALDITE B Double Cantilever Beam Specimens From Optical Method of Caustics Measurements [Kaltoff et al, 1977]

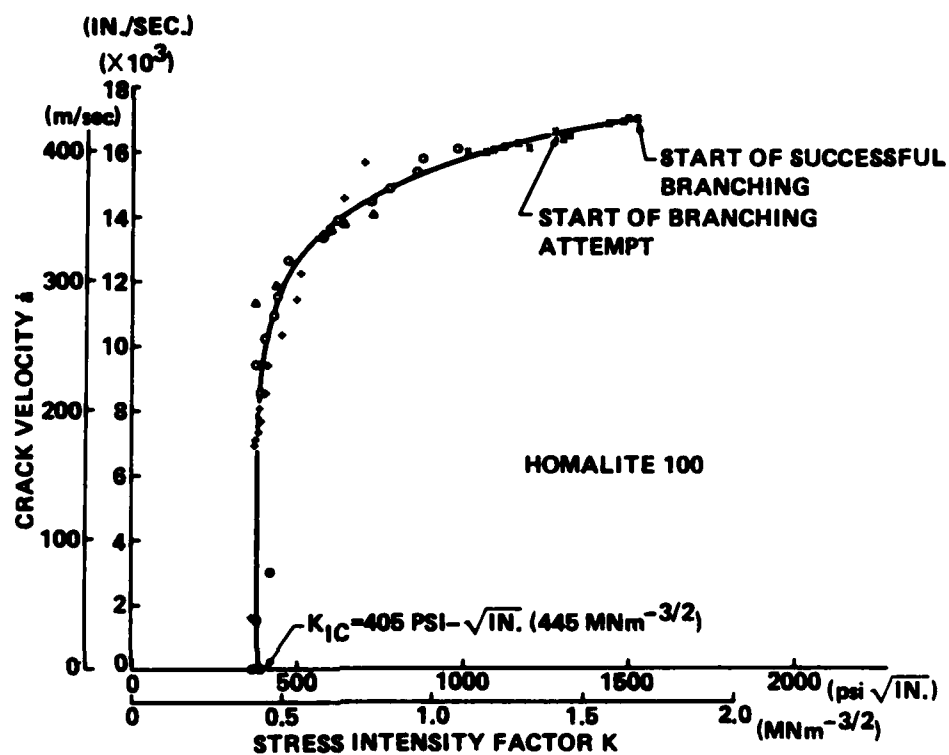


Figure 6 Crack Velocity As a Function of the Instantaneous Stress Intensity Factor for HOMALITE-100 [Kobayashi and Dally, 1977]



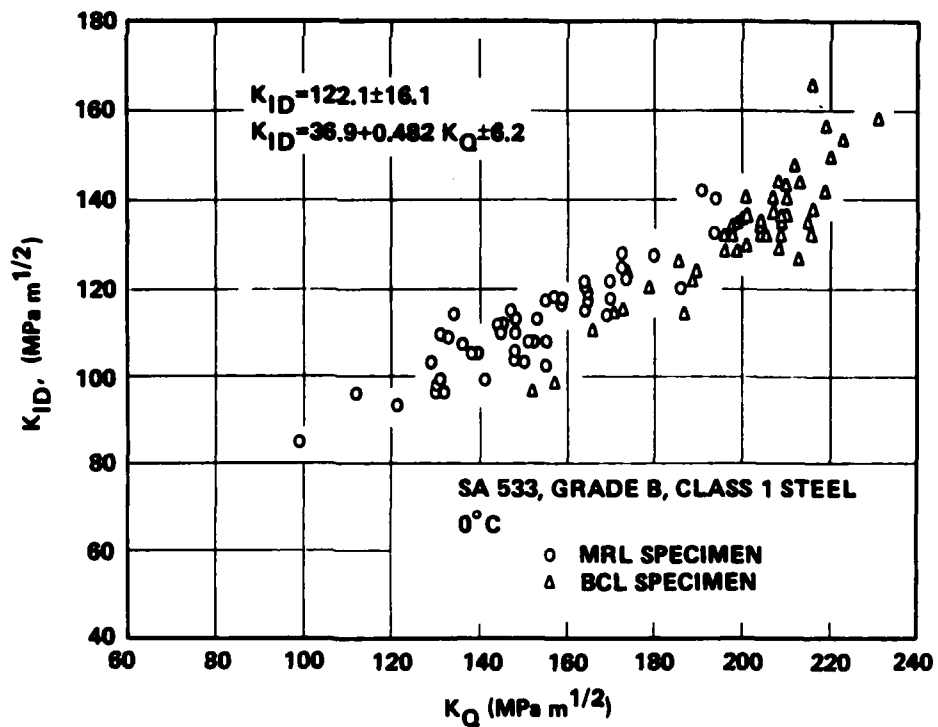
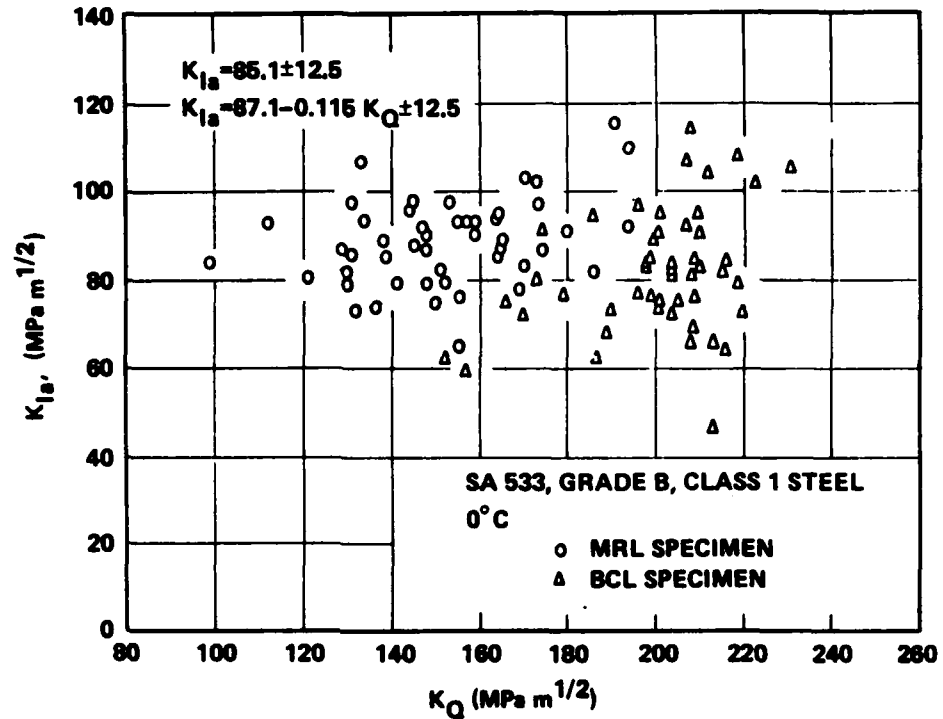


Figure 7. Crack Arrest Toughness Plotted as a Function of Initiation Toughness for MRL and BCL Specimens of SA533 B-1 Steel Tested at 0°C (32°F) [Crosley et al, 1983]

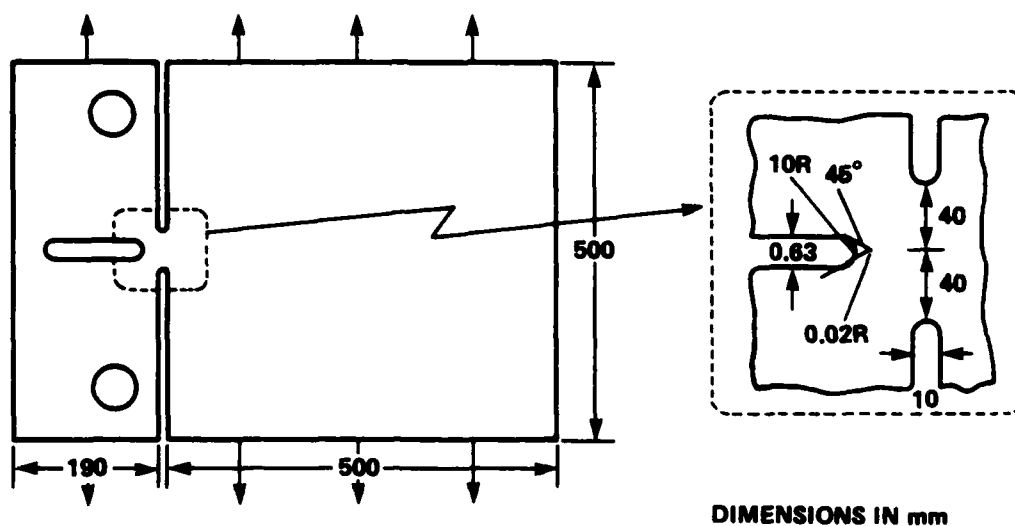


Figure 8 Double Tension Test Specimen Geometry

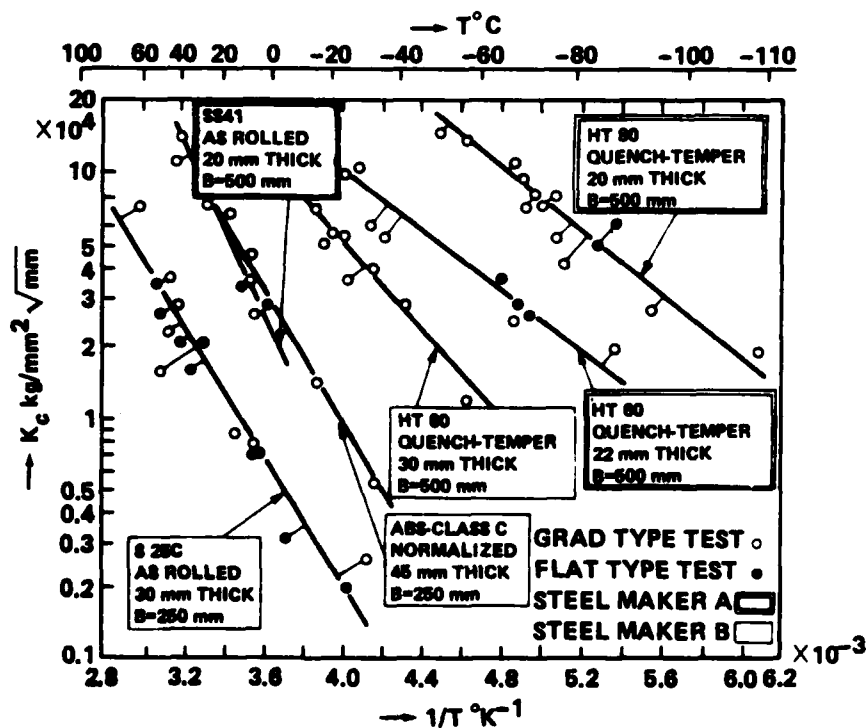
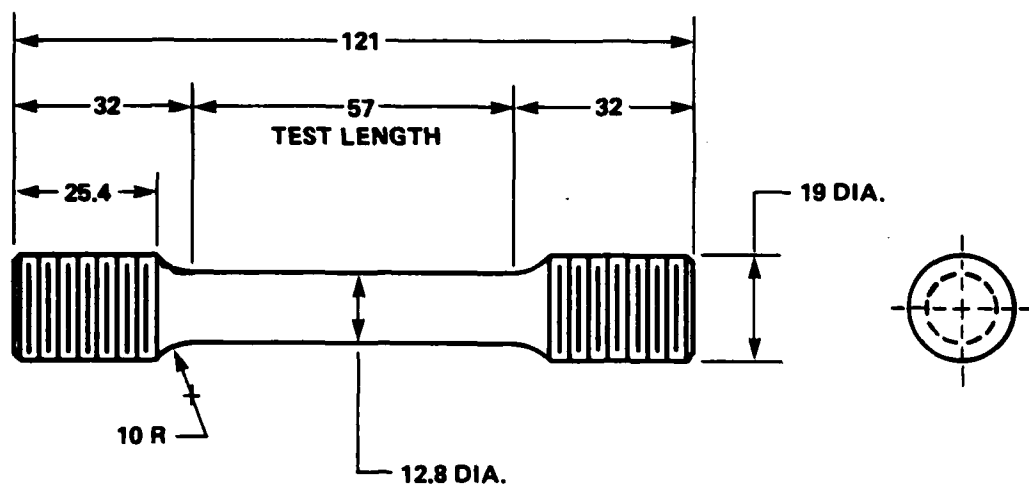
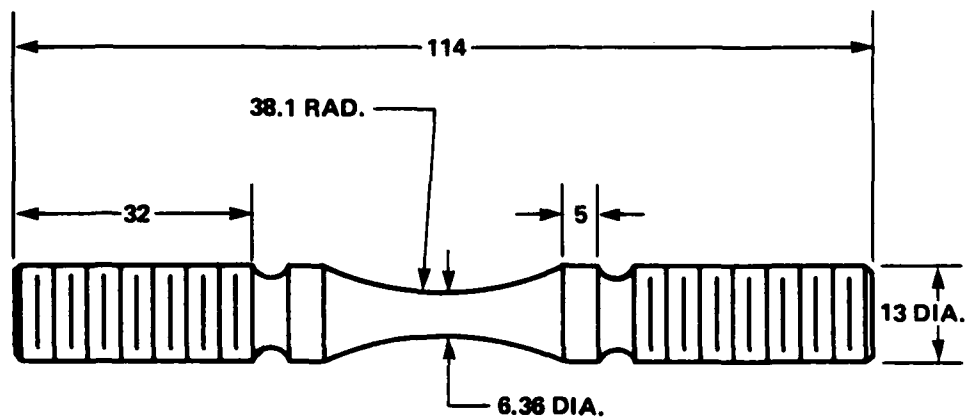


Figure 9. Results of Double Tension Crack Arrest Tests  
[Kanazawa, 1973]



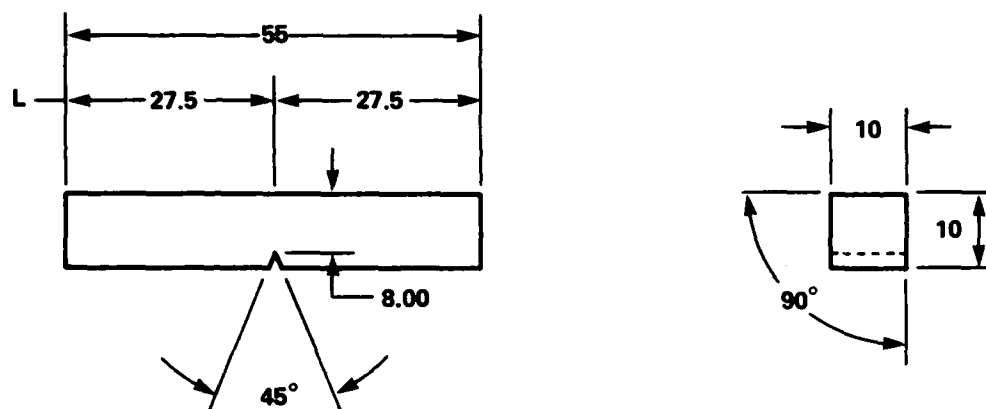
DIMENSIONS IN mm

Figure 10. Tensile Specimen Used for Room Temperature Tests



DIMENSIONS IN mm

Figure 11. Tensile Specimen Used for True Stress/True Strain Tests



DIMENSIONS IN mm

Figure 12. Charpy V-Notch Test Specimen

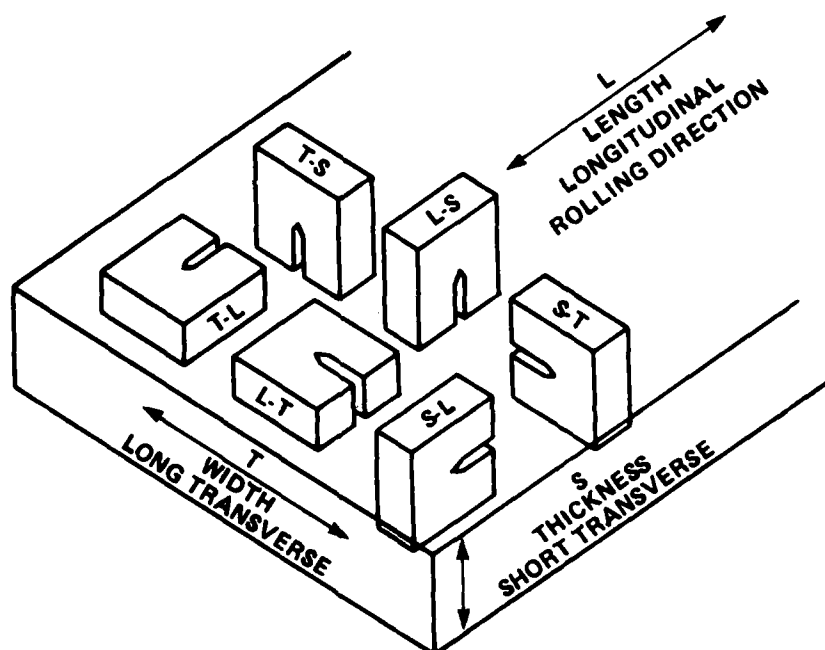


Figure 13. Schematic Drawing of Plate Showing Specimen Orientations

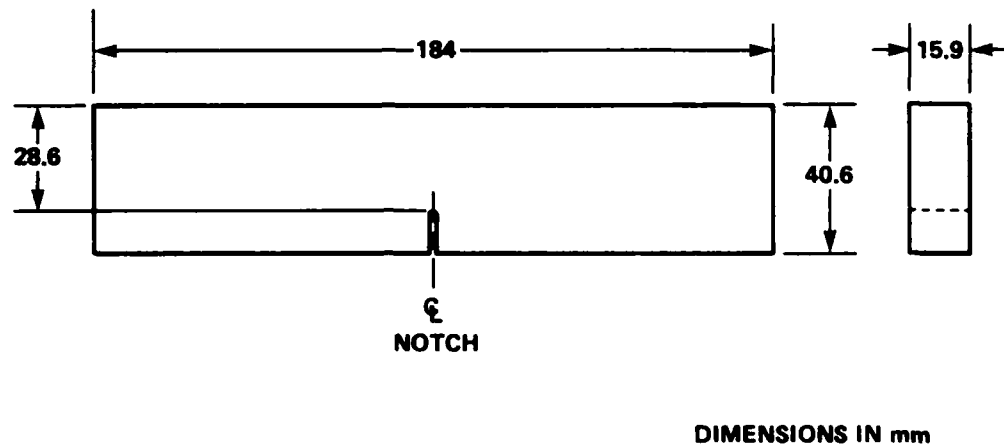


Figure 14. 5/8-Inch Dynamic Tear Impact Toughness Specimen

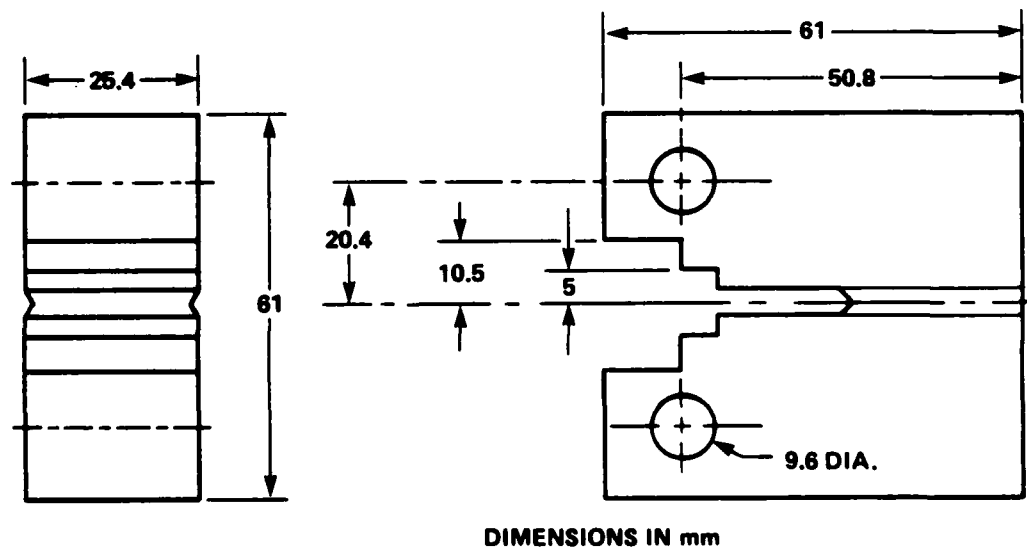
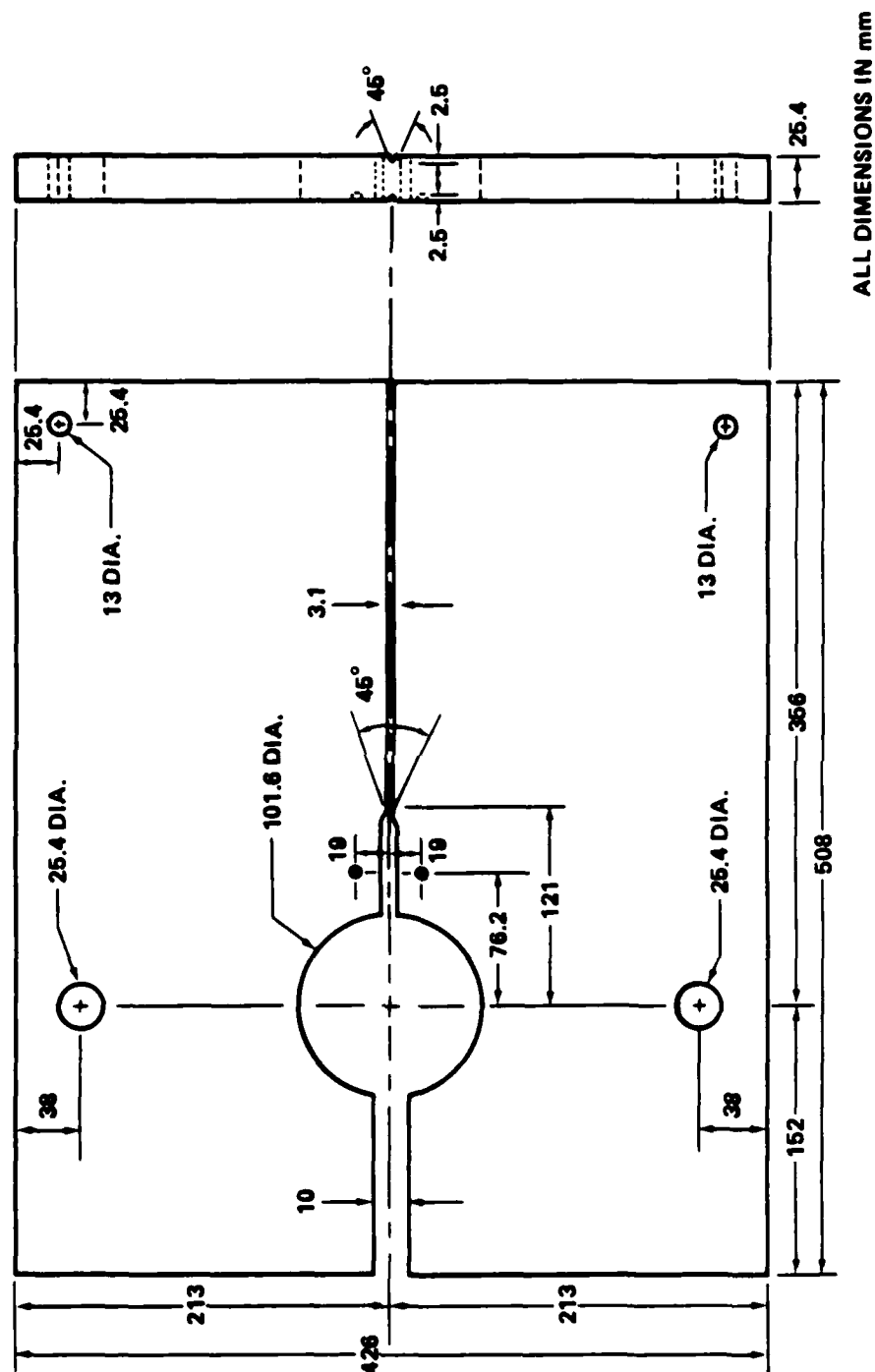


Figure 15. Modified 1T Compact Specimen for Fracture Toughness Tests



**Figure 16. Compact Crack Arrest Test Specimen**

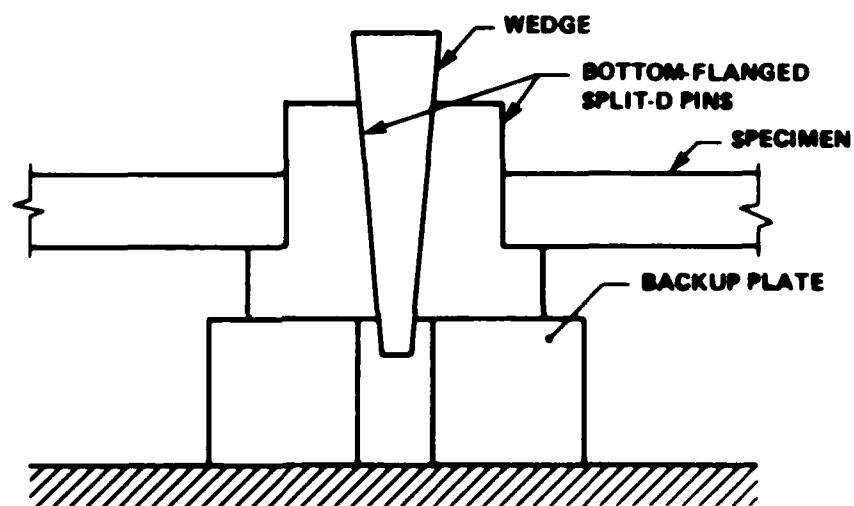


Figure 17. Compact Crack Arrest Specimen Test Arrangement

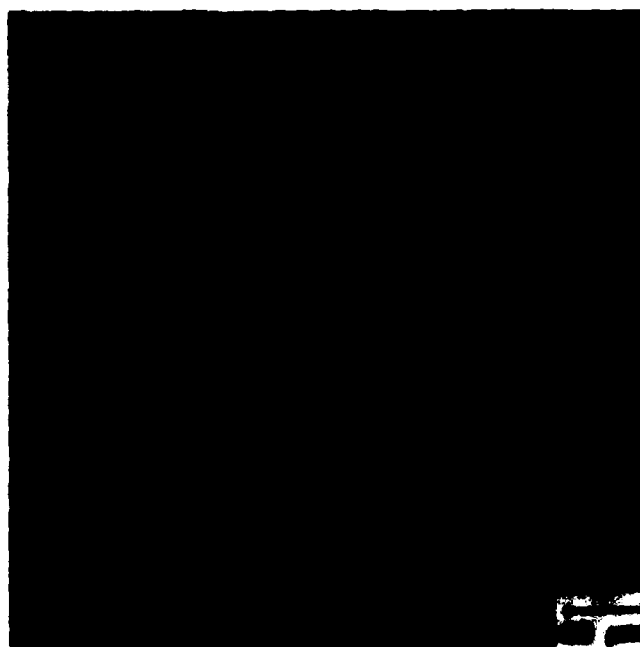


Figure 18. Optical Photomicrographs of HY-80 Steel  
(2% Nital etch)



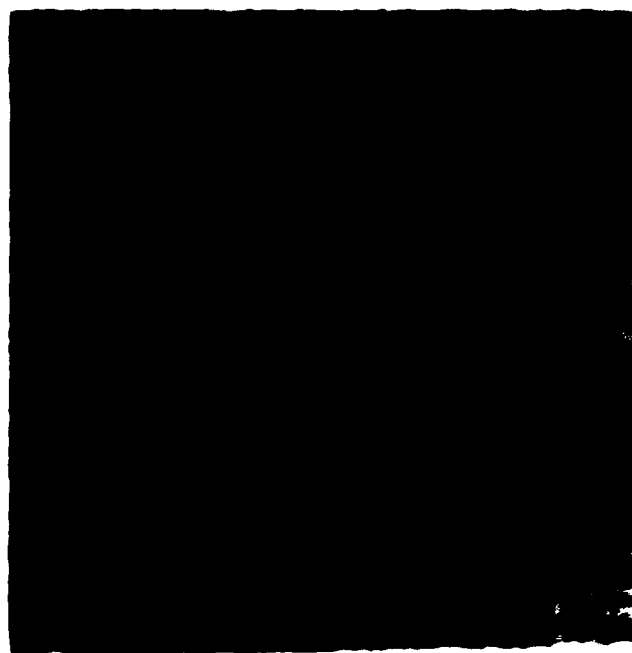
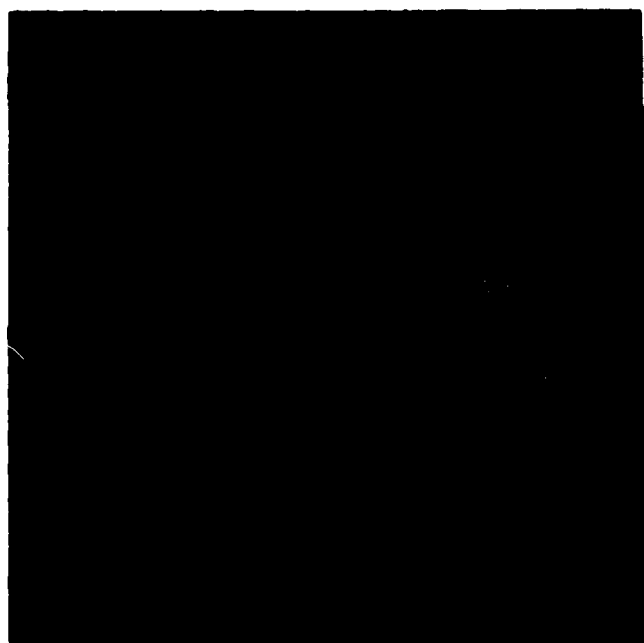


Figure 19. Optical Photomicrographs of ASTM A 710  
Gr. A Cl. 3 Steel (2X Nital etch)

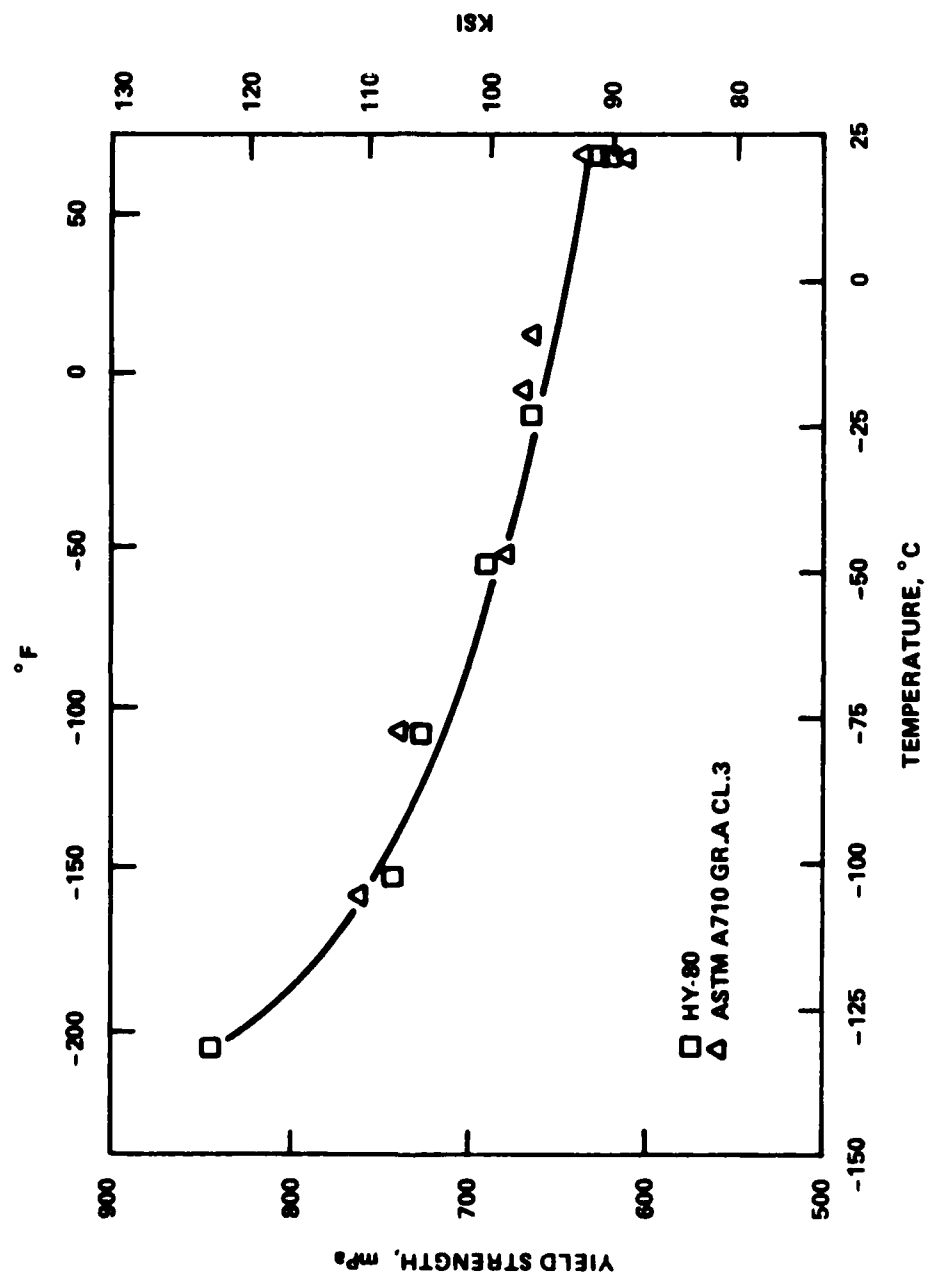


Figure 20. Plot of Yield Strength As a Function of Temperature for HY-80 and ASTM A 710 Gr. A Cl. 3 Steels

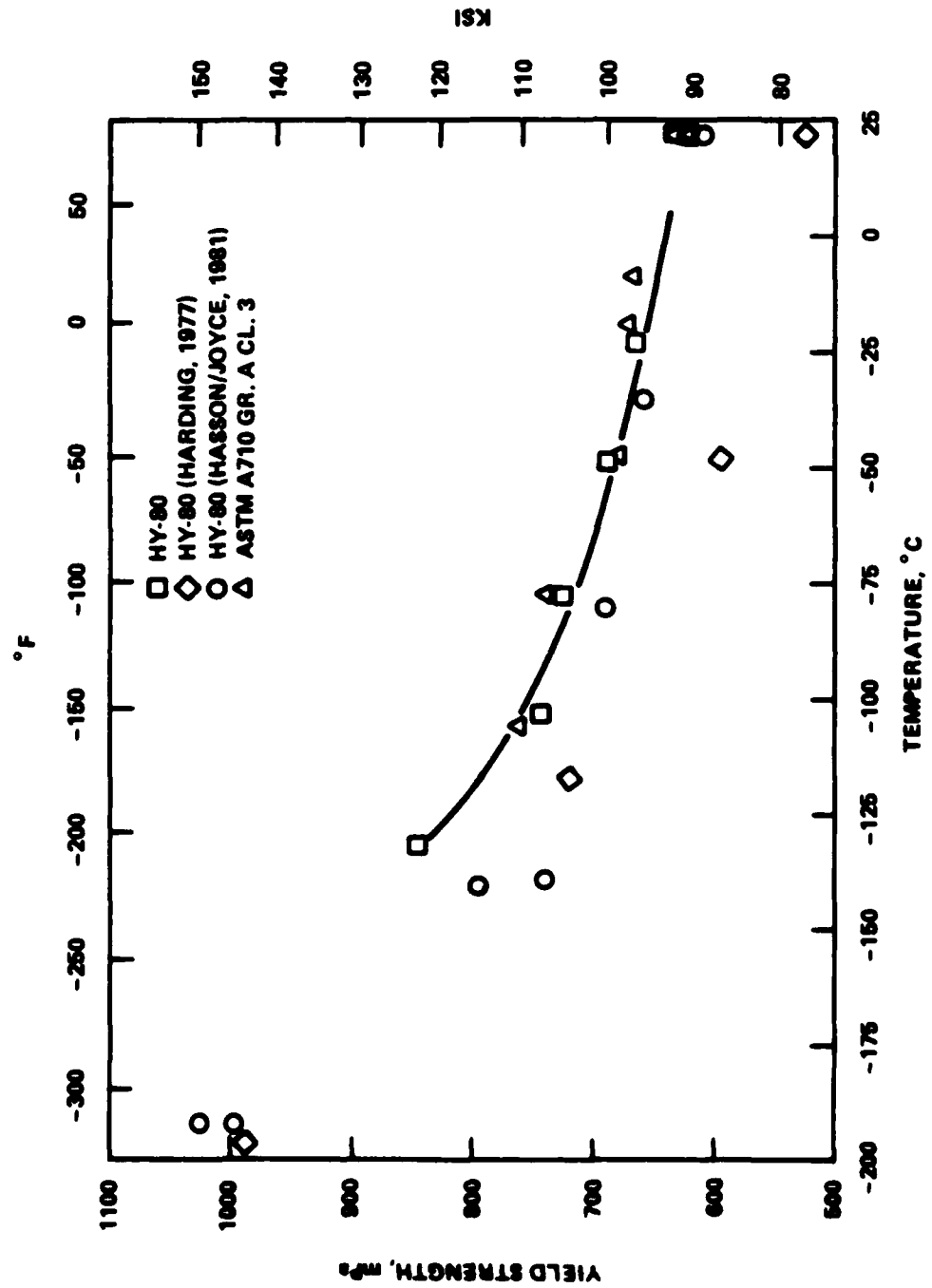


Figure 21. Plot of Yield Strength As a Function of Temperature for HY-80 Steel

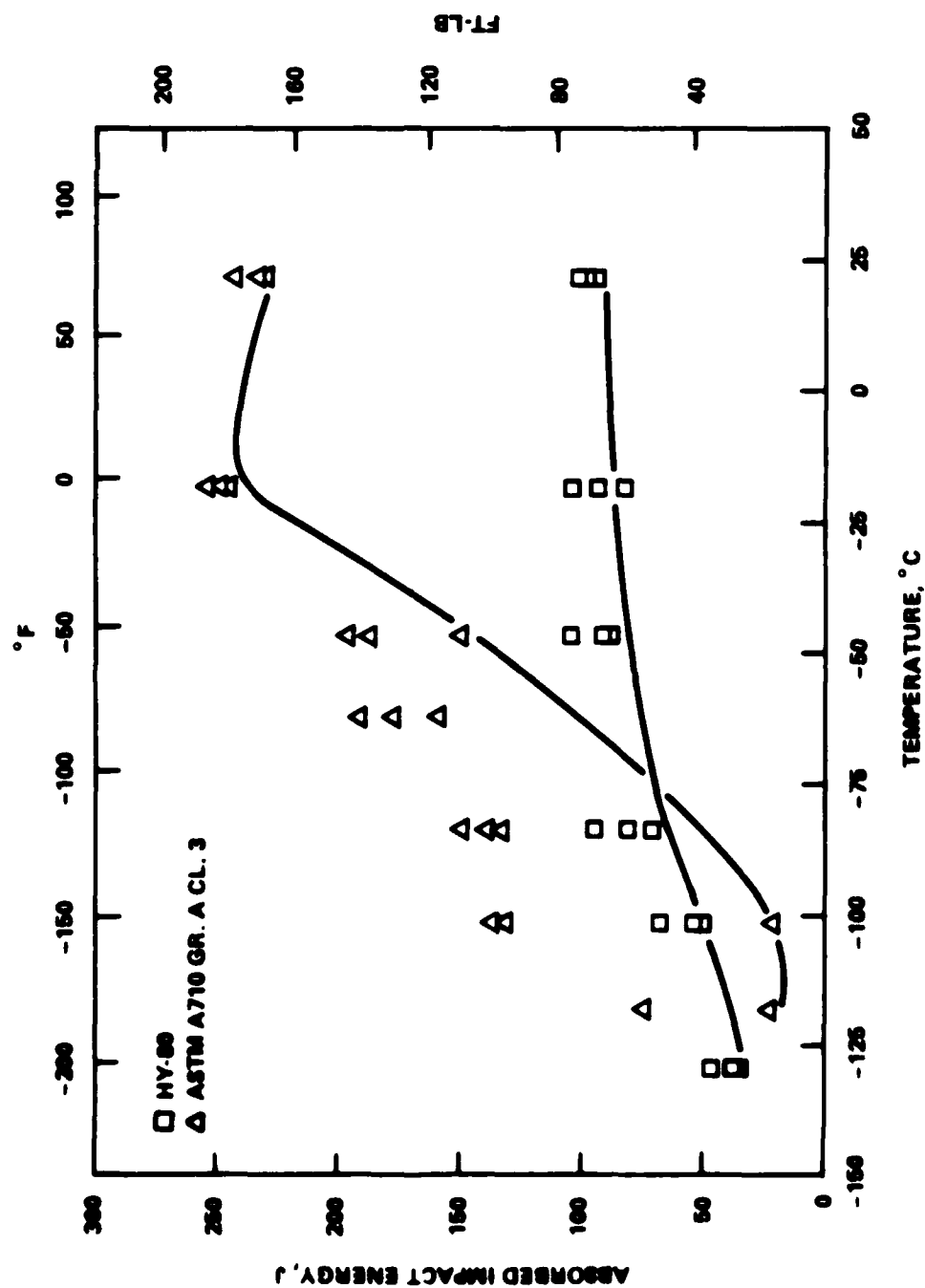


Figure 22. Charpy V-Notch Impact Toughness Results for HY-80 and ASTM A 710 Gr. A Cl. 3 Steels

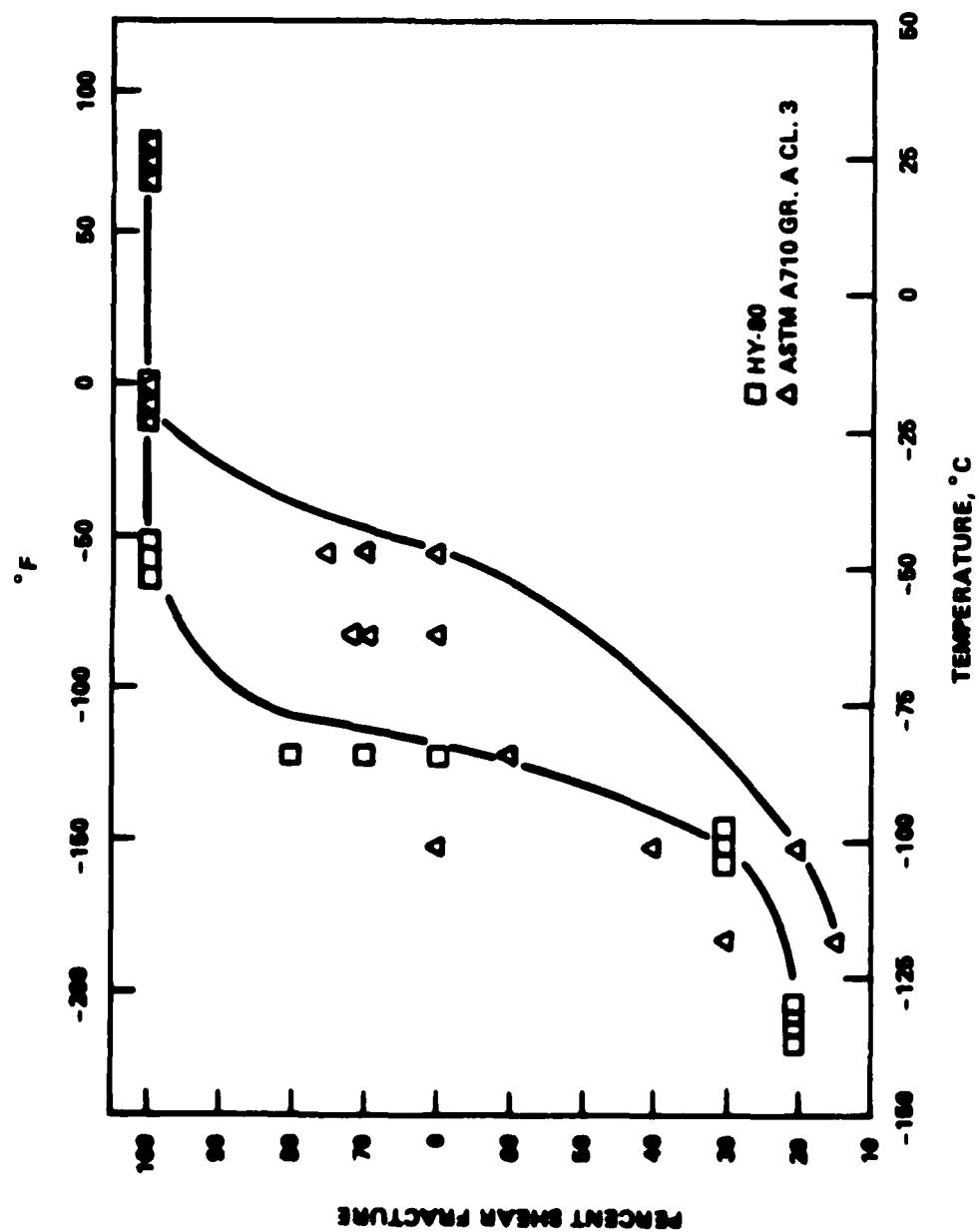


Figure 23. Percent Shear Fracture From Charpy V-Notch Tests of HY-80 and ASTM A 710 Gr. A Cl. 3 Steels

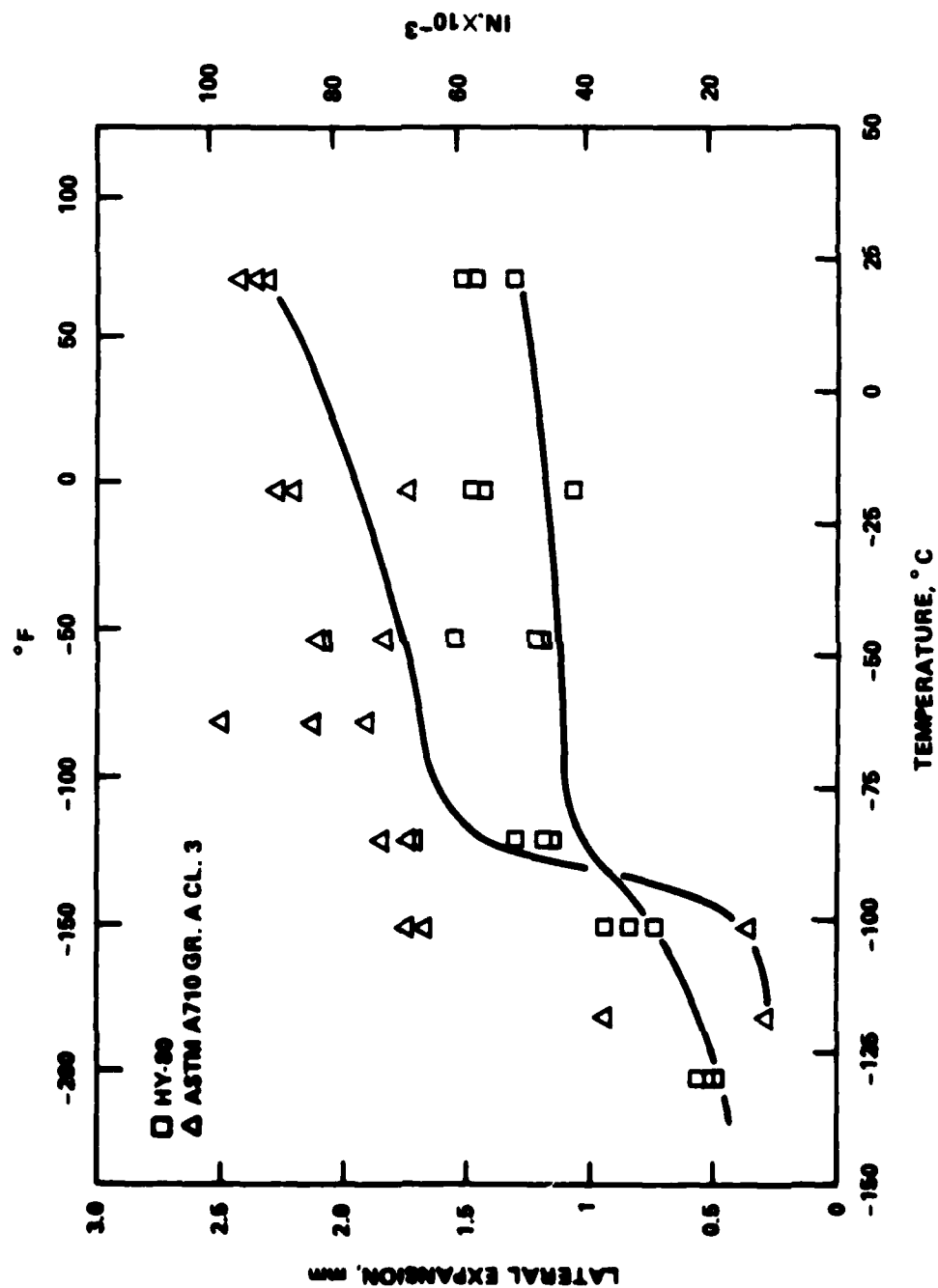


Figure 24. Lateral Expansion From Charpy V-Notch Tests of HY-80 and ASTM A 710 Gr. A Cl. 3 Steels

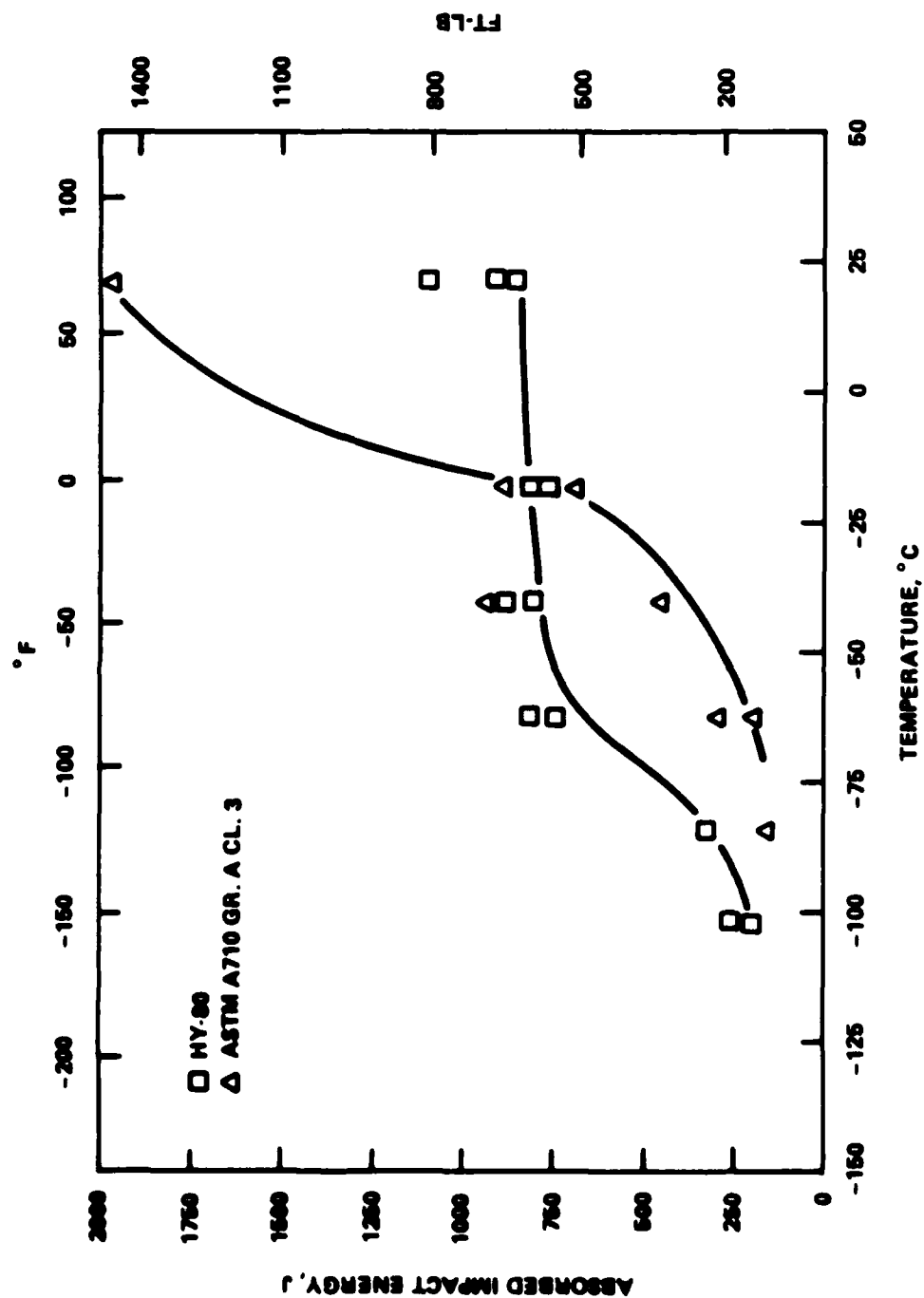


Figure 25. Results of 5/8-Inch Dynamic Tear Tests of HY-80 and ASTM A 710 Gr. A Cl. 3 Steels

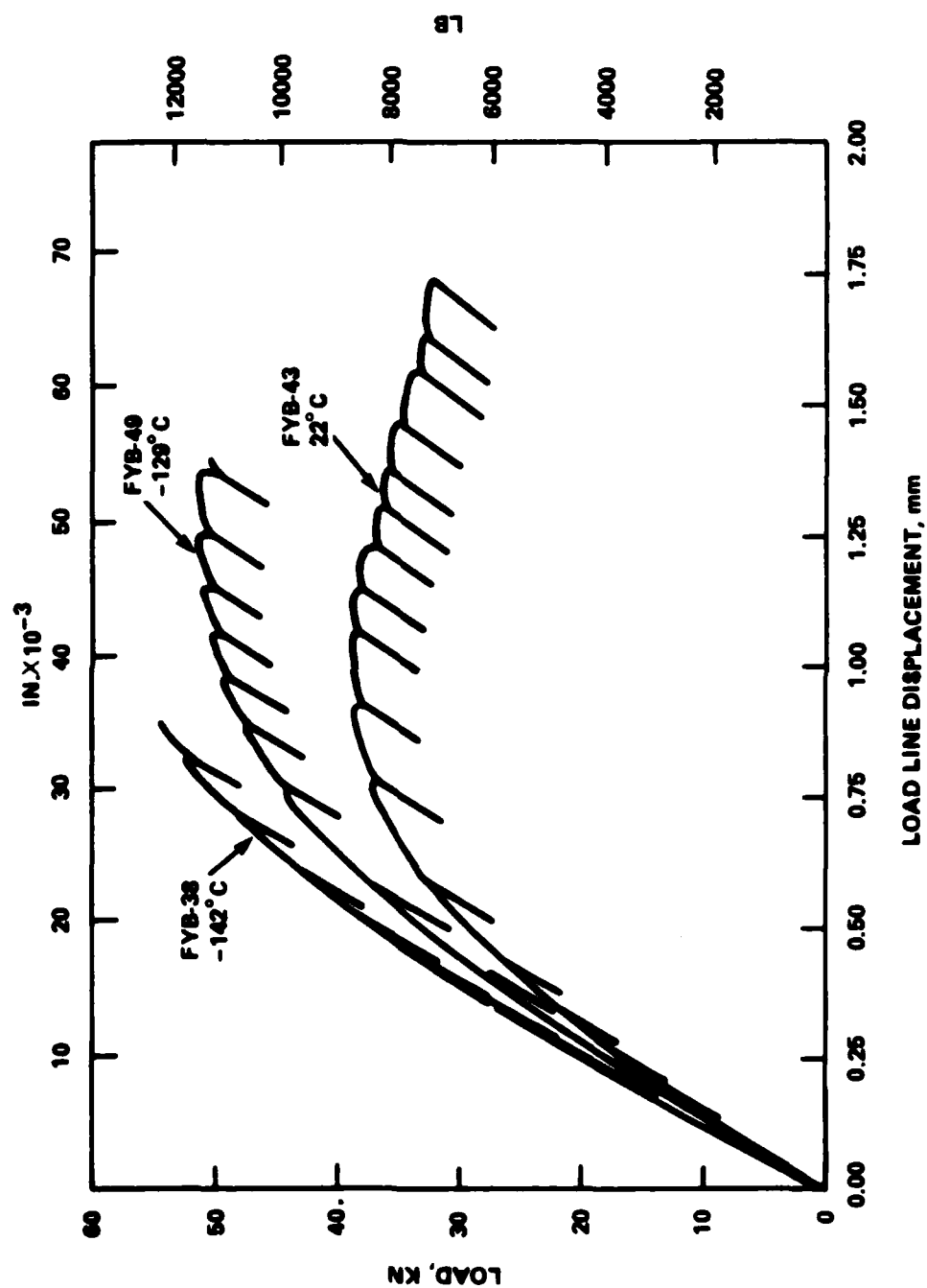


Figure 26. Load Versus Load-Line Displacement Results for 1TCT Specimens of HY-80 Steel



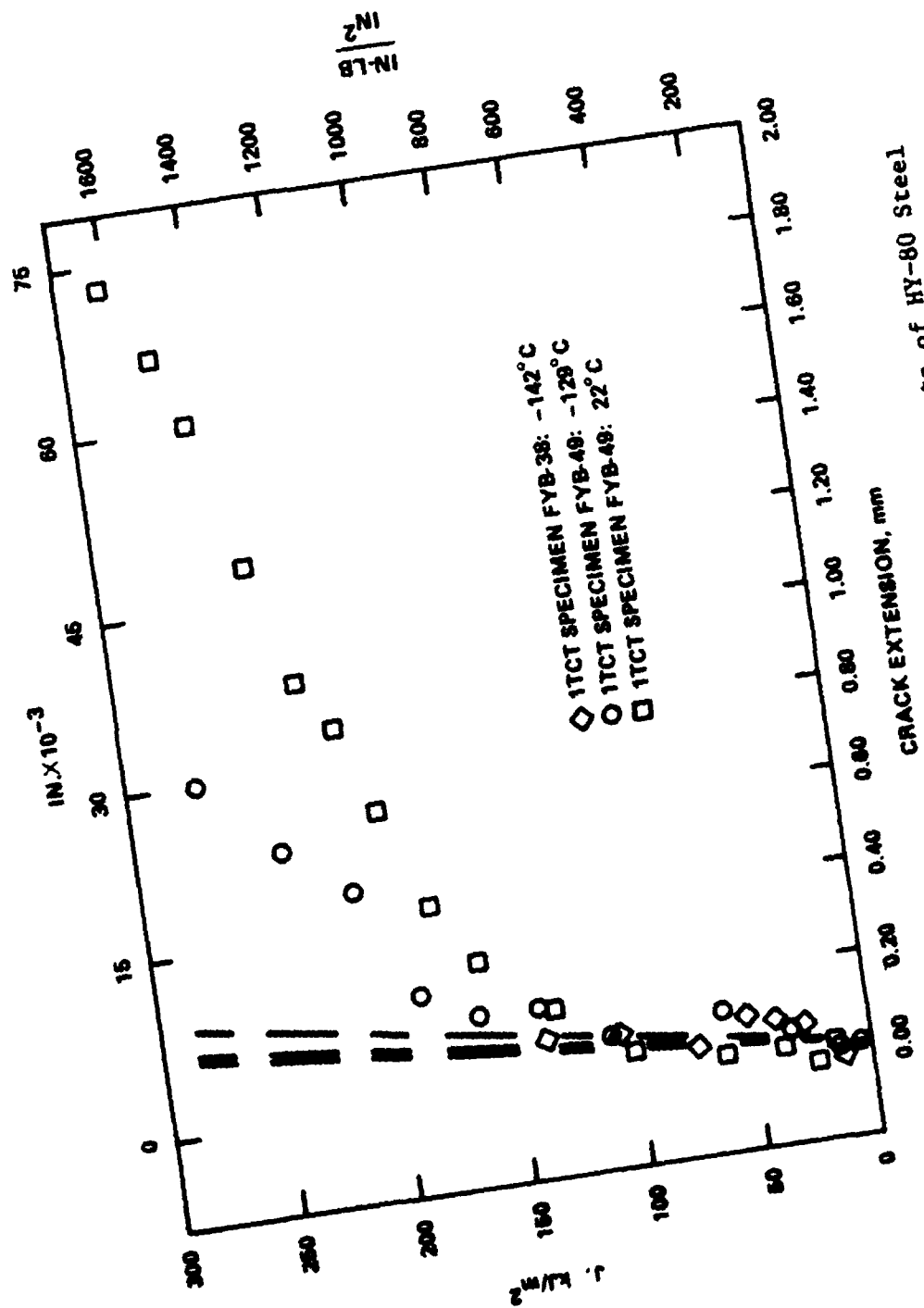


Figure 27. Typical Results of J-Integral Tests of HY-80 Steel

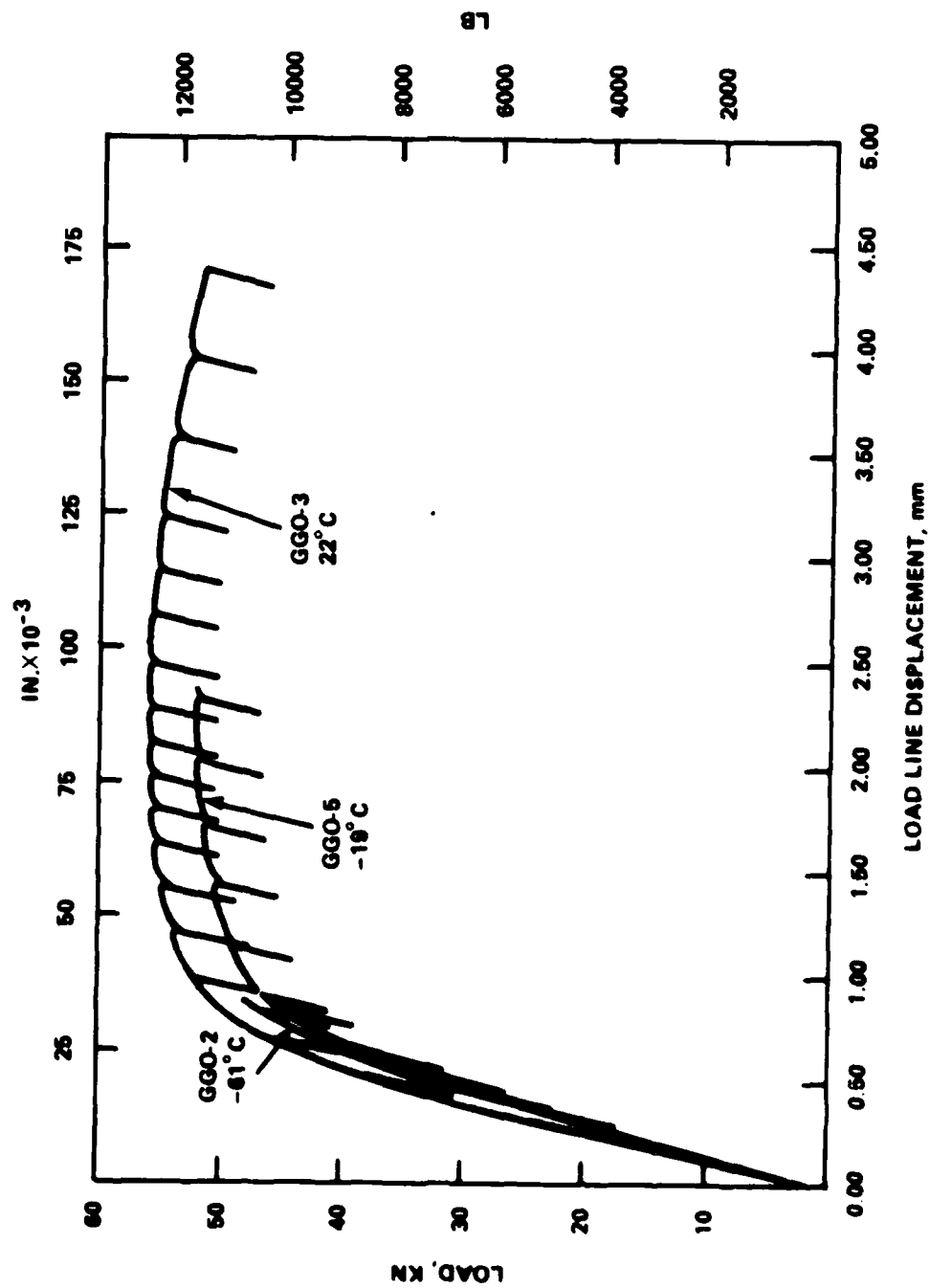


Figure 28. Load Versus Load-Line Displacement Results for ITCT Specimens of ASTM A 710 Gr. A Cl. 3 Steel

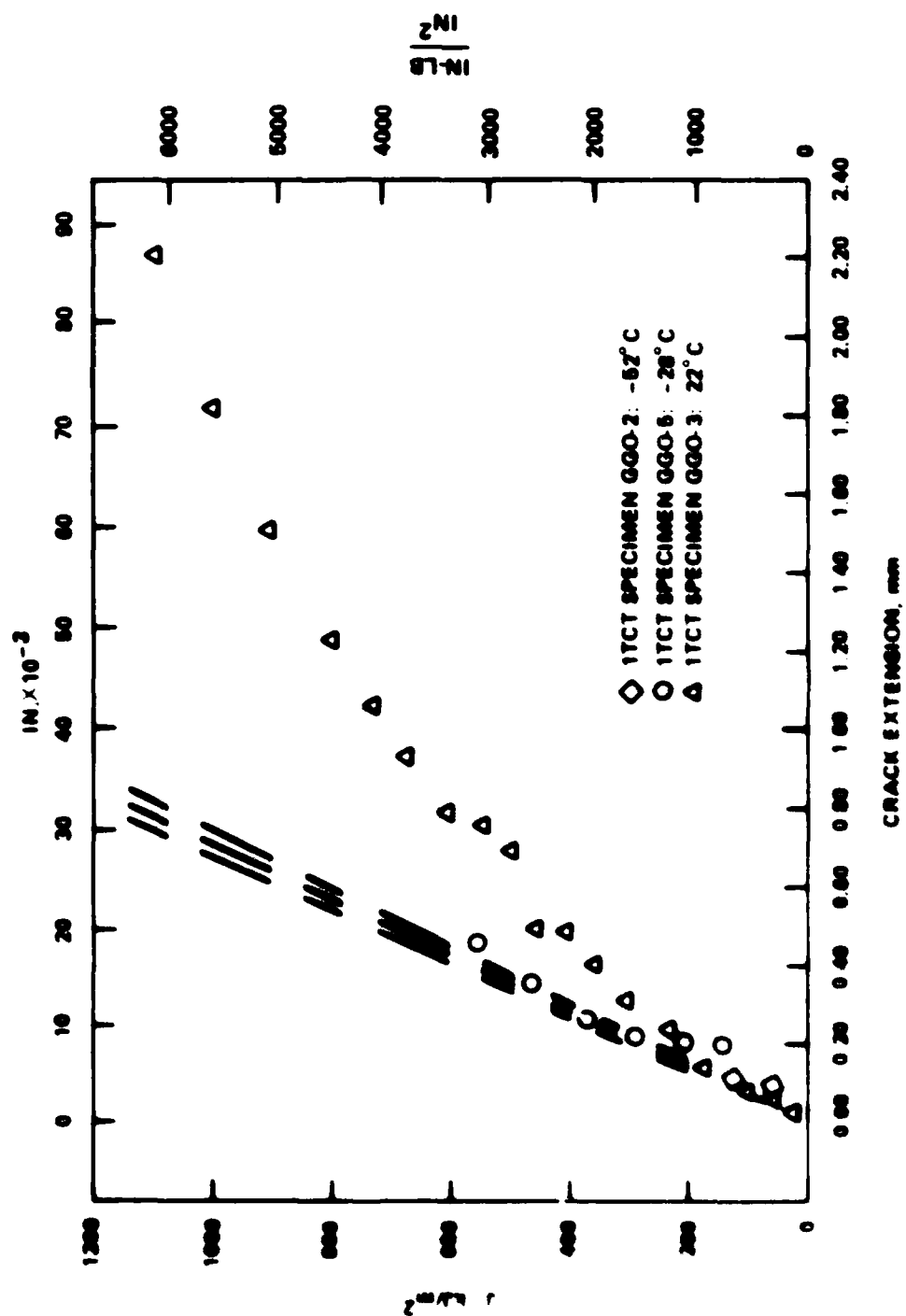


Figure 29. Typical Results of J-Integral Tests of ASTM A 710 Gr. A  
(AISI 5 Steel)

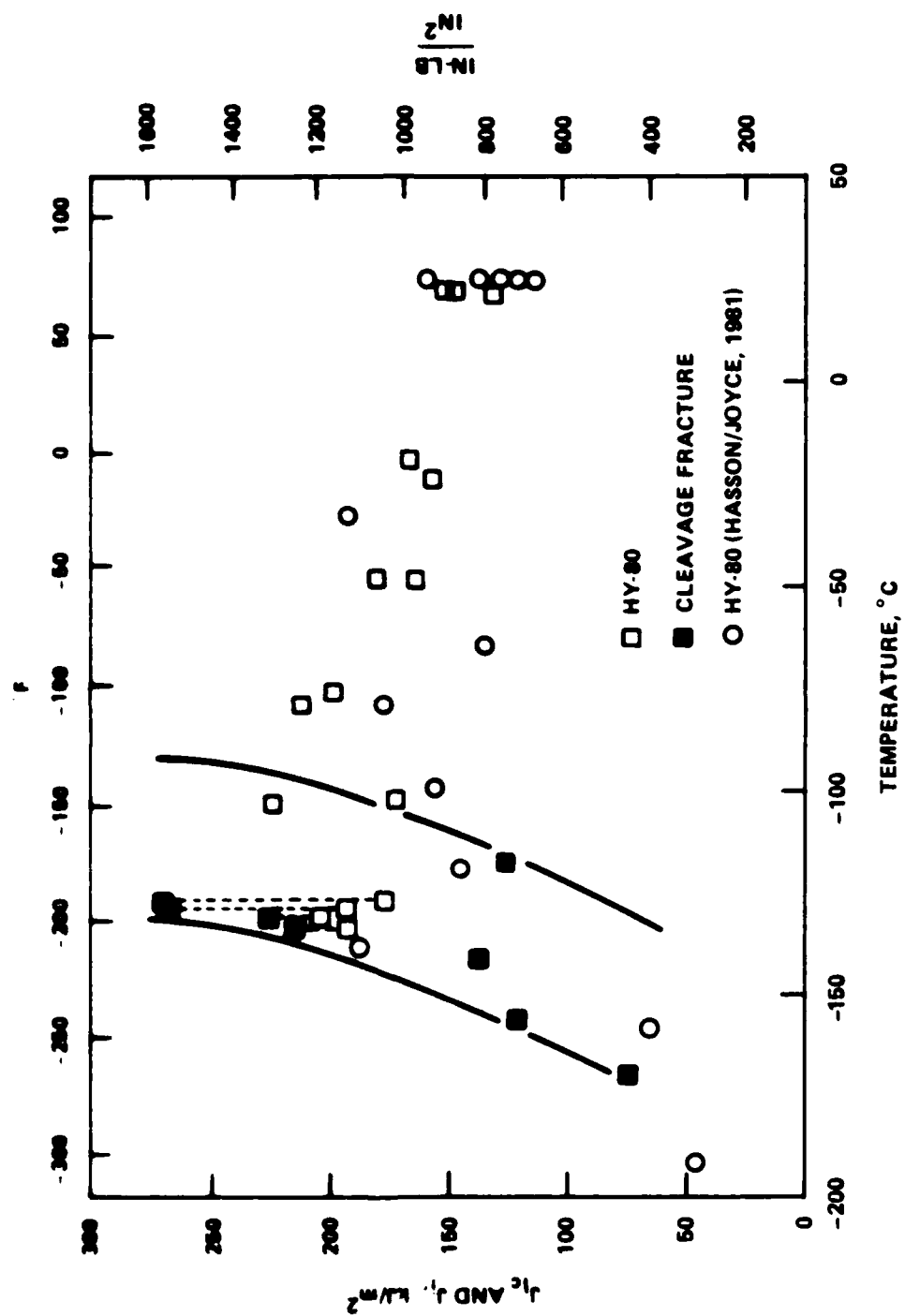


Figure 30. Results of Fracture Toughness Tests of HY-80 Steel

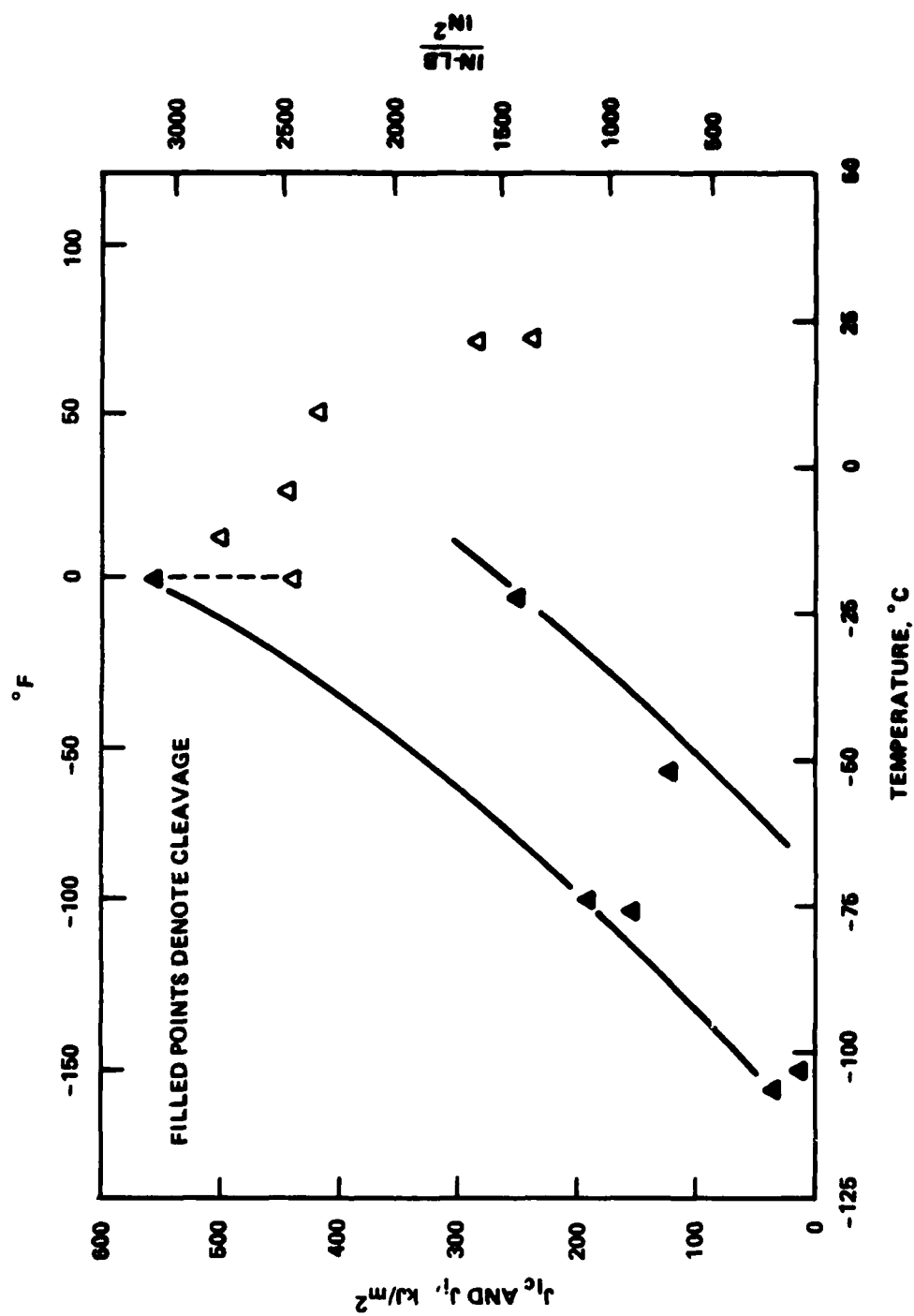


Figure 31. Results of Fracture Toughness Tests of ASTM A 710 Gr. A Cl. 3 Steel

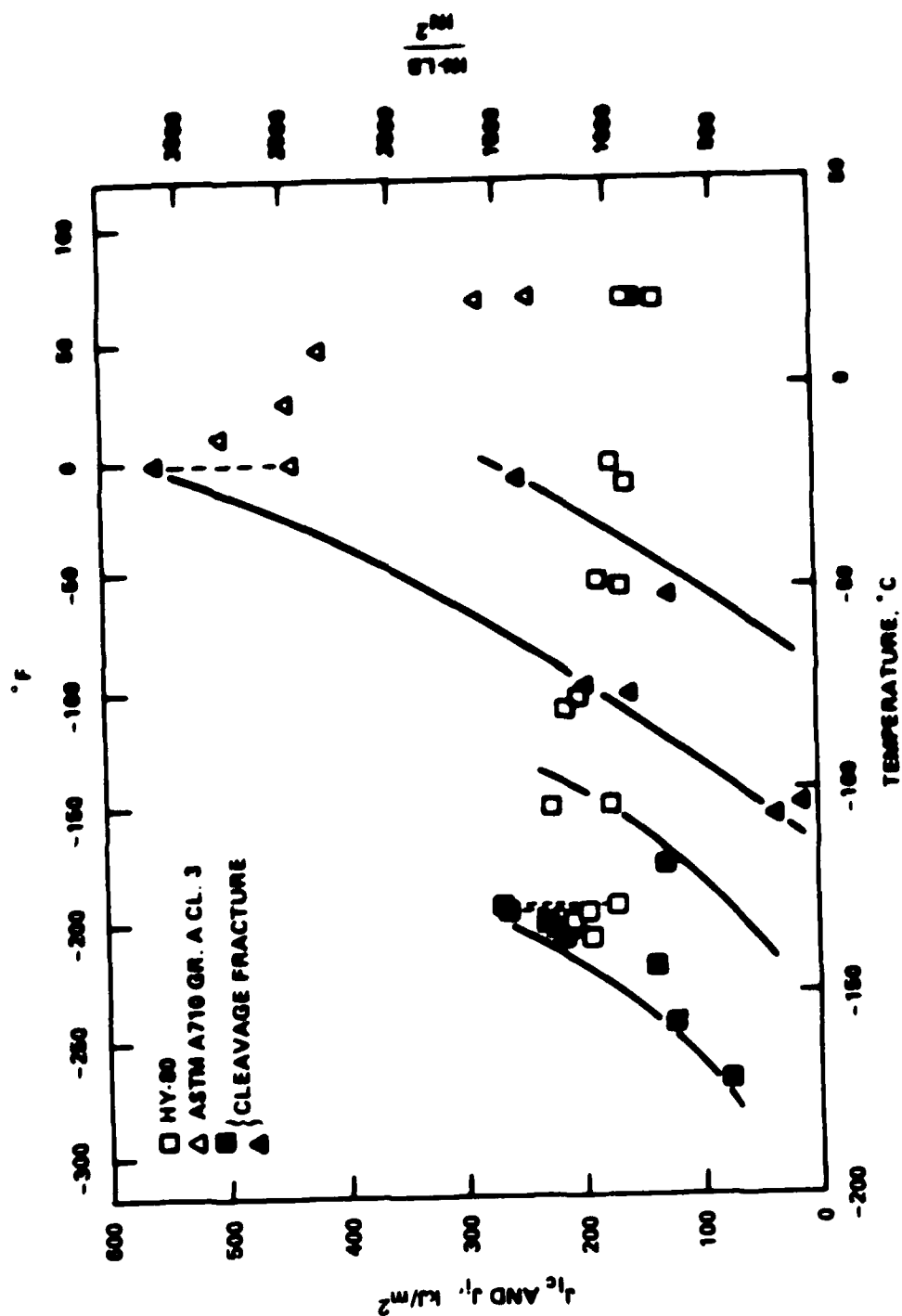


Figure 32. Results of Fracture Toughness Tests of HY-80 and ASTM A 710 Gr. A Cl. 3 Steels

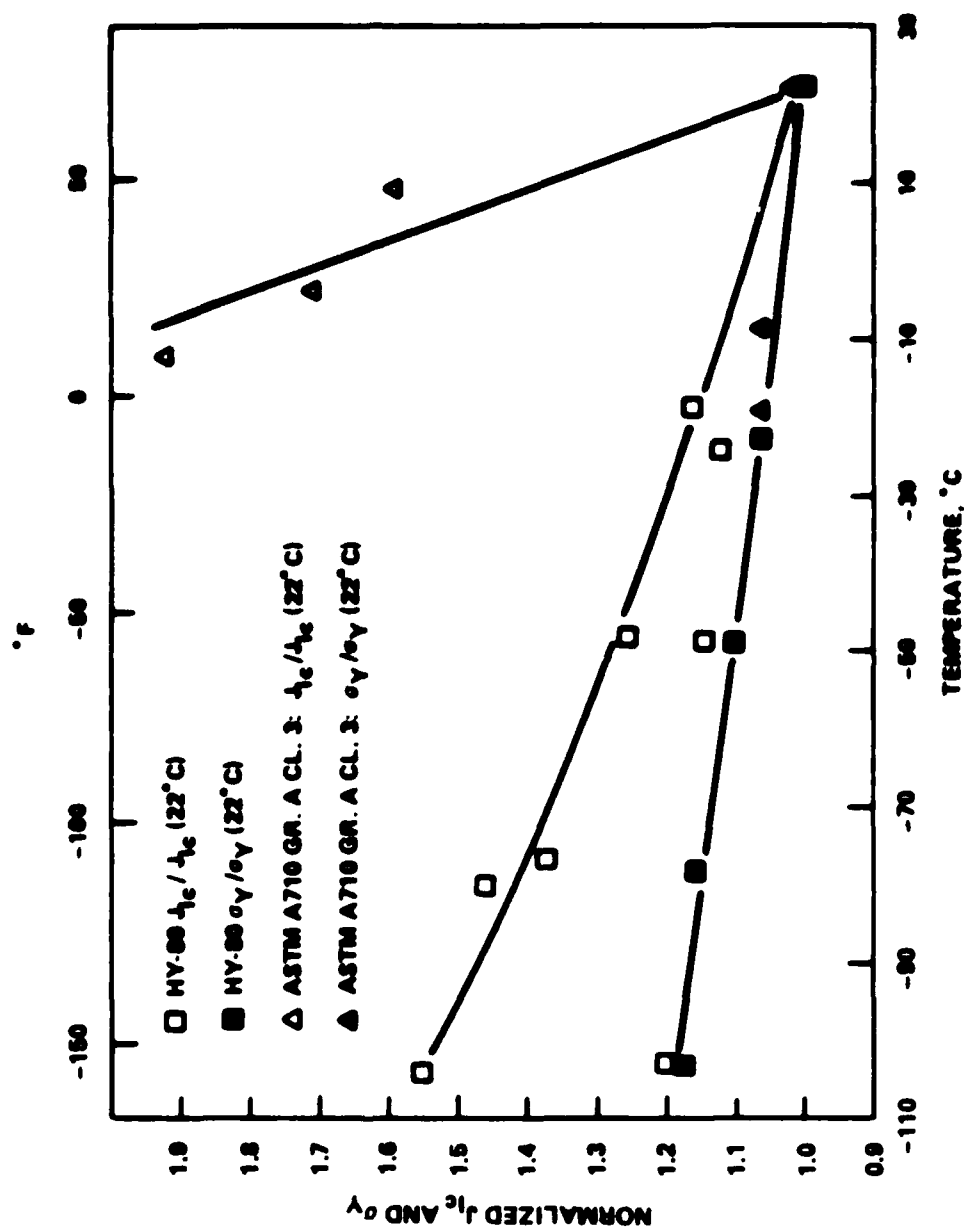


Figure 33. Ratios of Yield Strength and Fracture Toughness Versus Room Temperature Values of These Properties for HY-90 and ASTM A 710 Gr. A Cl. 3 Steels

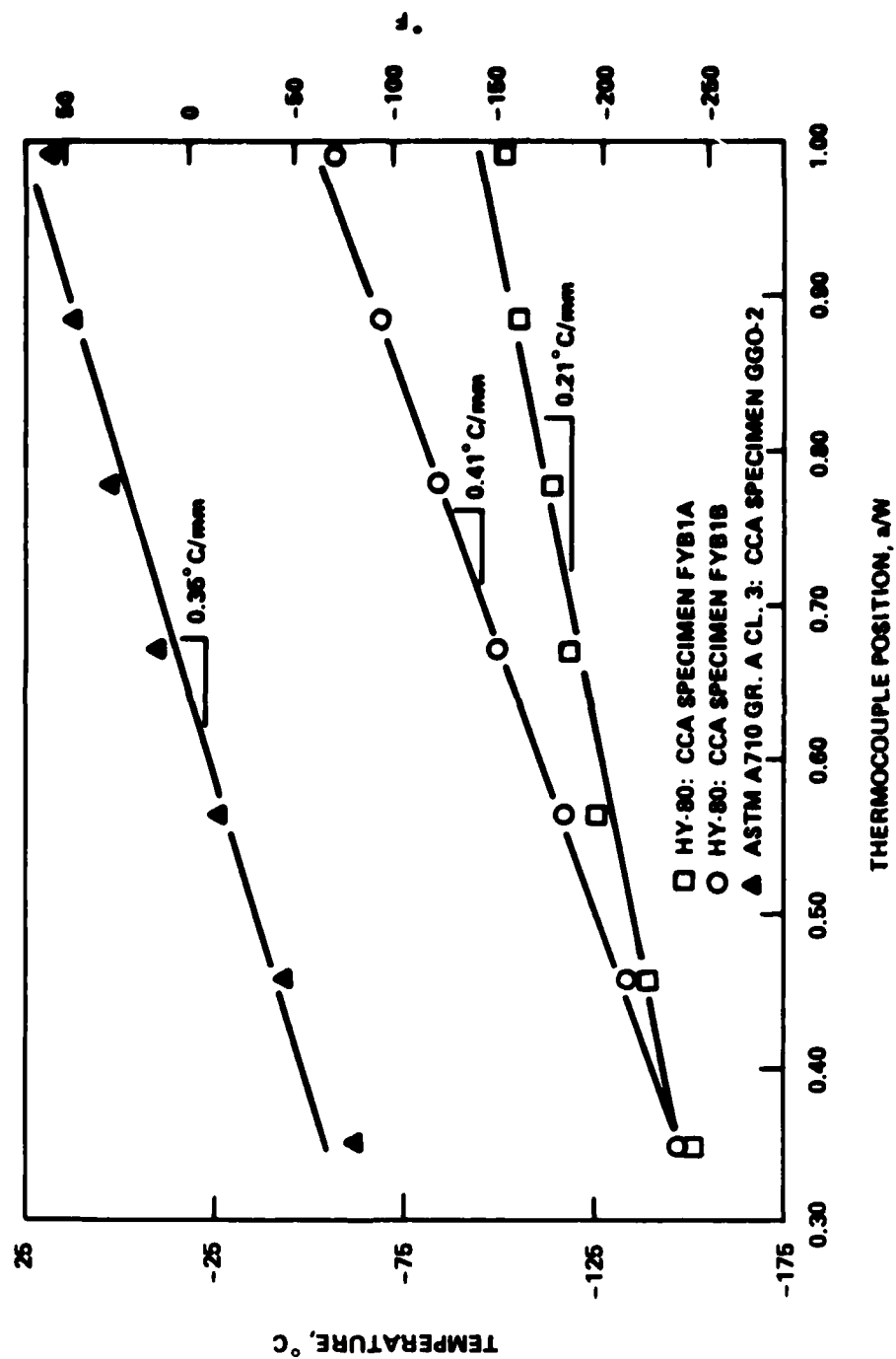


Figure 34. Typical Temperature Gradient Data From Compact Crack Arrest Specimen Tests



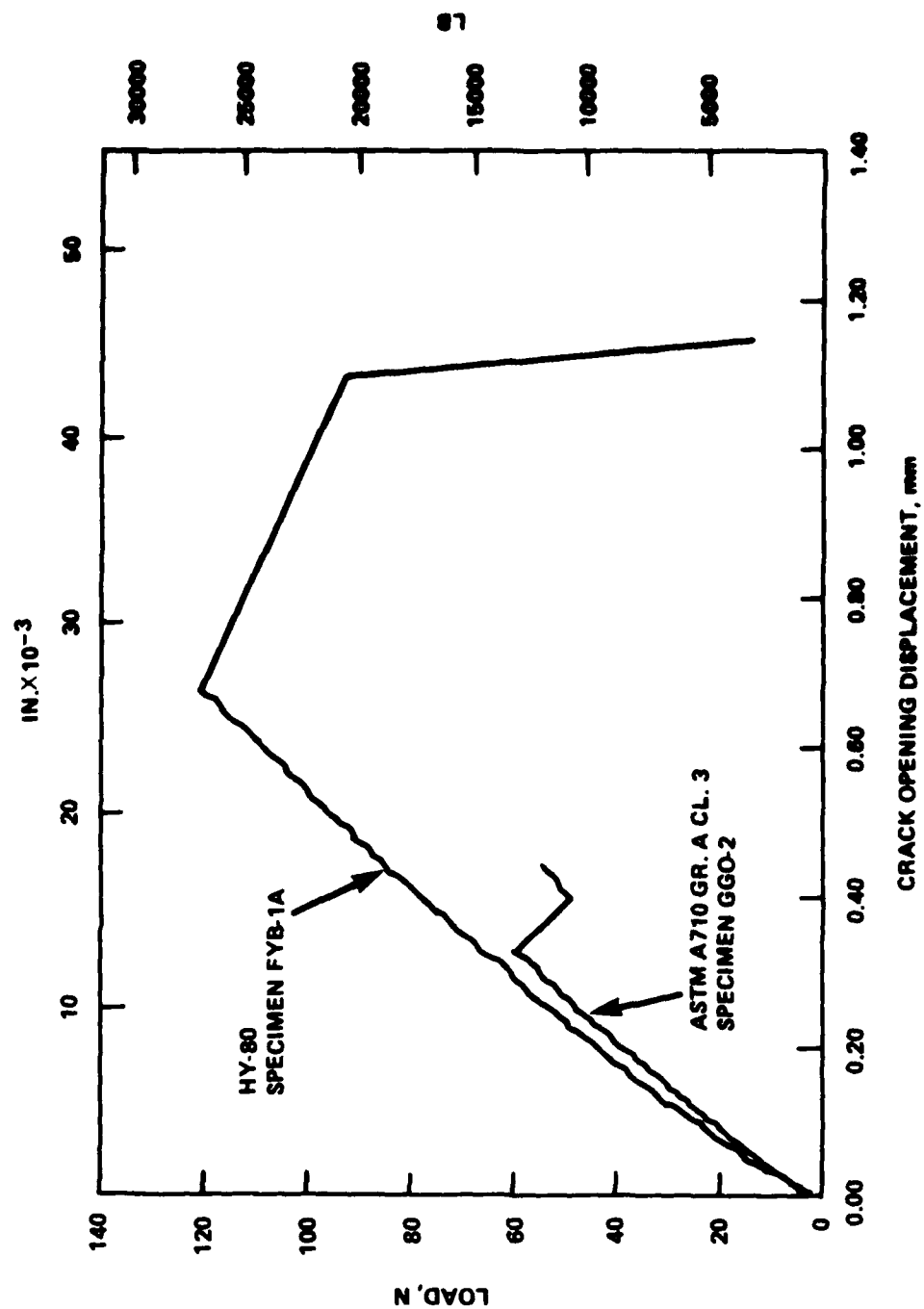


Figure 35. Typical Load Versus Crack Opening Displacement Results From Compact Crack Arrest Specimen Tests

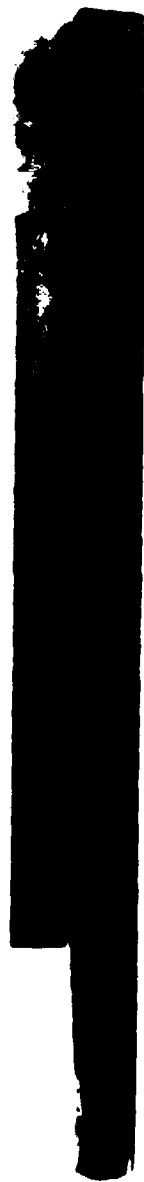


Figure 36. Fracture Surface of HY-80 Compact Crack Arrest  
Specimen FYB CCA-2



Figure 37. Fracture Surface of HY-80 Compact Crack Arrest  
Specimen FYB 1A

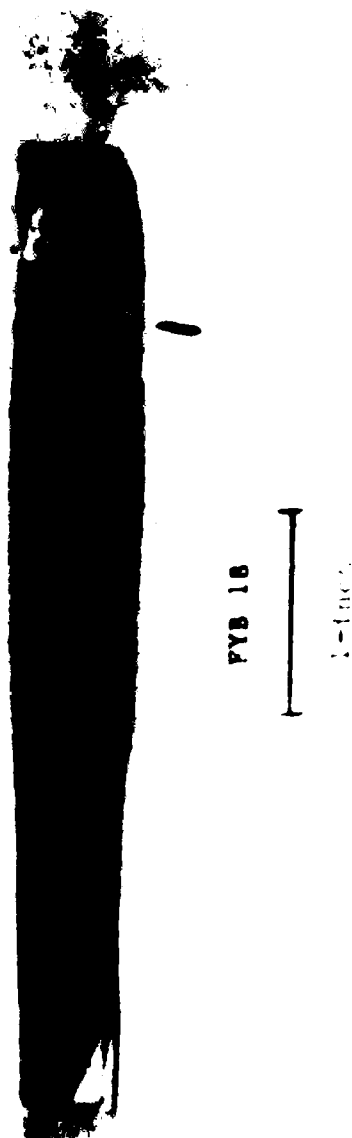


Figure 38. Fracture Surface of HY-80 Compact Crack Arrest  
Specimen FYB 1B



FYB 3A



1-inch

Figure 39. Fracture Surface of HY-80 Compact Crack Arrest  
Specimen FYB 3A

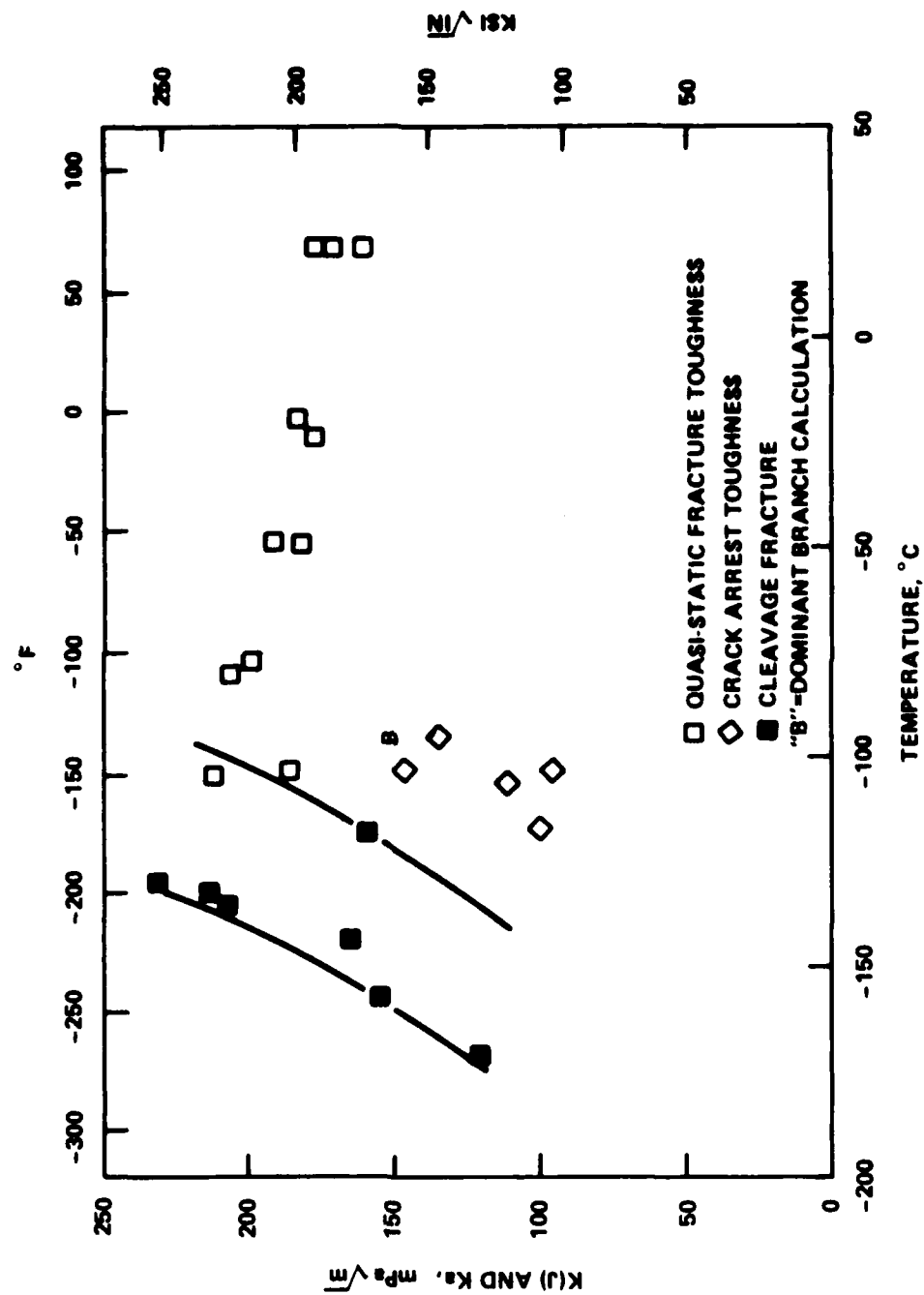


Figure 40. Results of Fracture Toughness and Crack Arrest Toughness Tests of HY-80 Steel

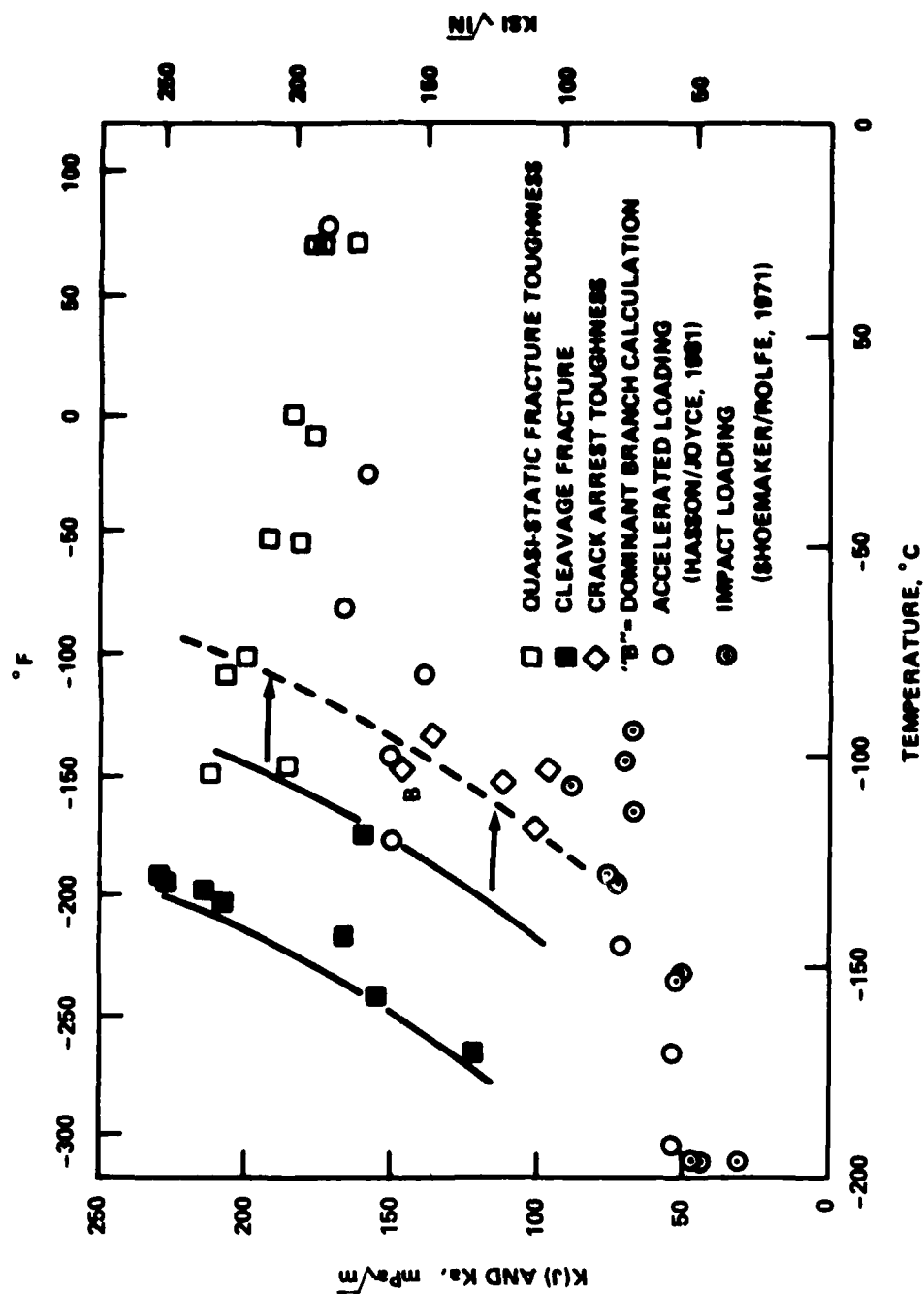


Figure 41. Results of Fracture Toughness, Crack Arrest Toughness, and Reported Dynamic Fracture Toughness Measurements of HY-80 Steel

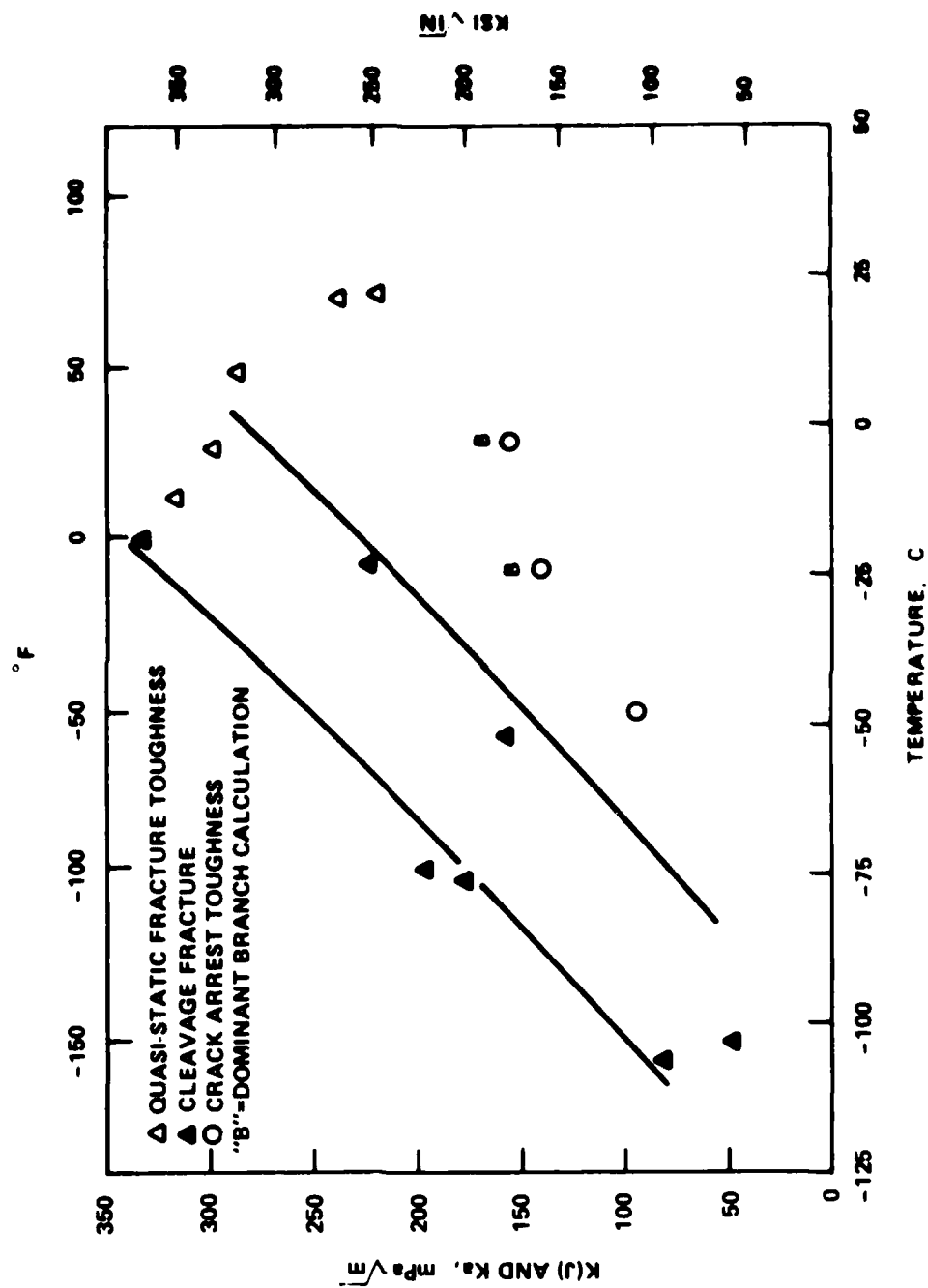


Figure 42. Results of Fracture Toughness and Crack Arrest Toughness Tests of ASTM A 710 Gr. A (1.3 Steel)



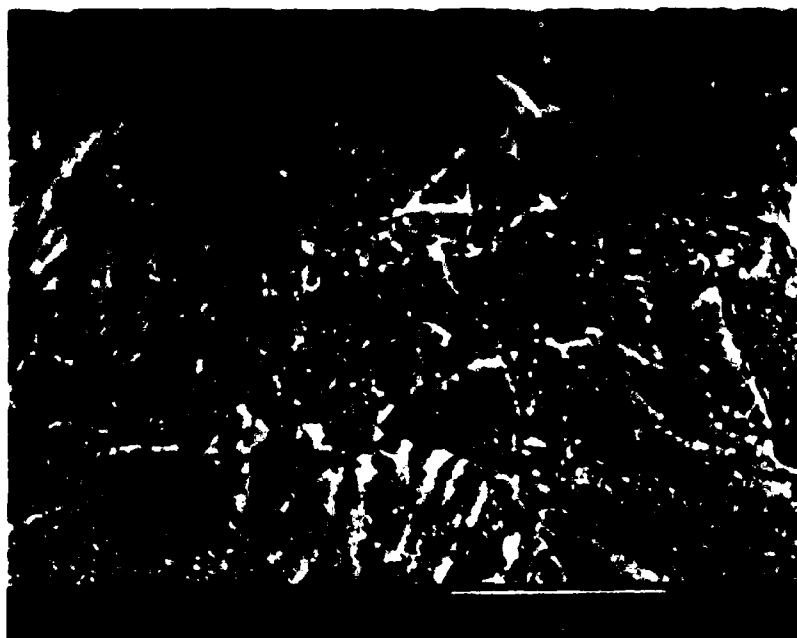
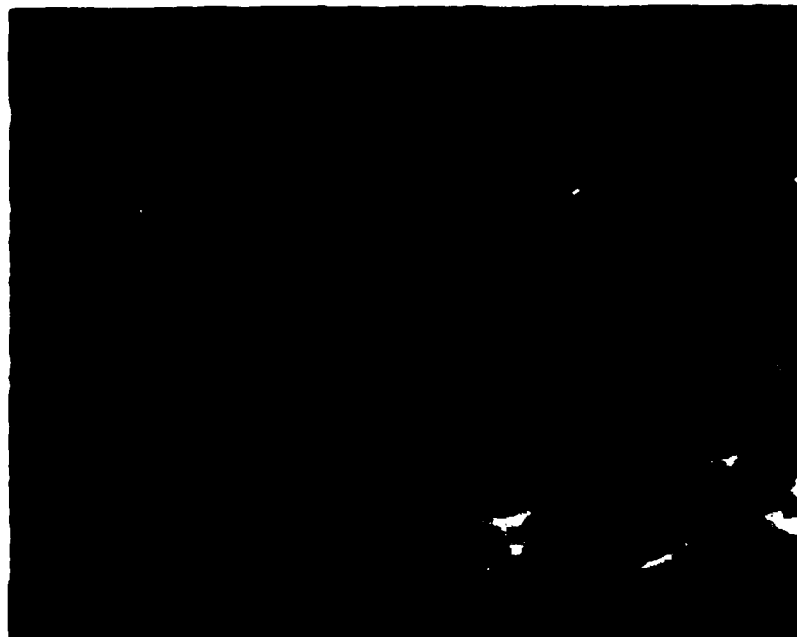


Figure 43. Scanning Electron Micrographs of HY-80 Steel  
(2% Nital etch)

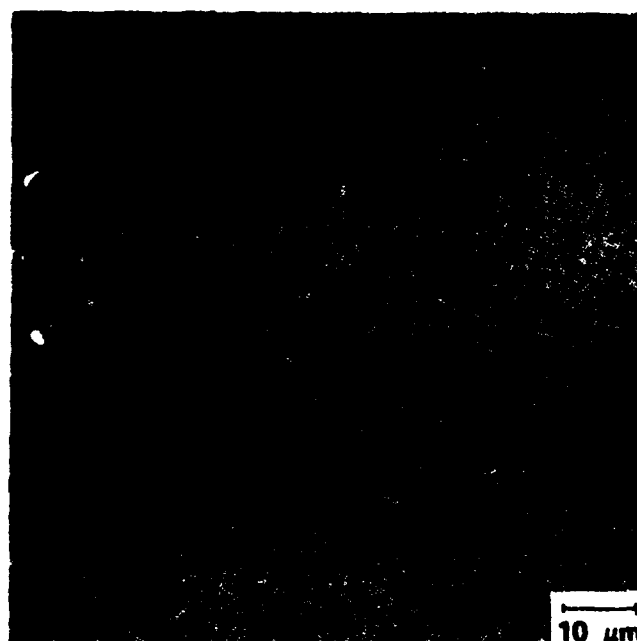


Figure 44. Optical Photomicrograph of HY-80 Steel  
(4% Picral etch)

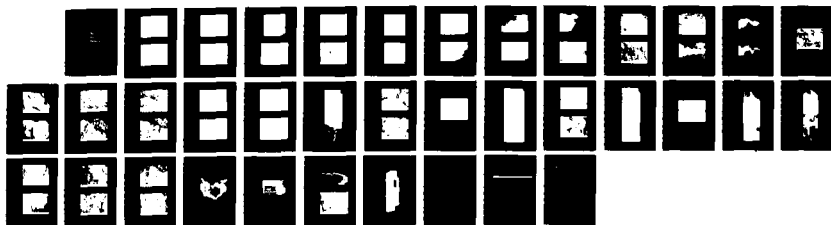
AD-A181 324

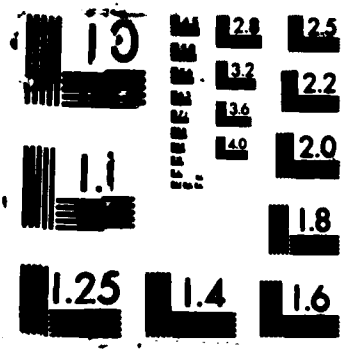
MICROMECHANISMS OF FRACTURE AND CRACK ARREST IN TWO  
HIGH STRENGTH STEELS(U) DAVID W TAYLOR NAVAL SHIP  
RESEARCH AND DEVELOPMENT CENTER ANN J P GUDAS FEB 87  
DTNSRDC/SME-87-28 F/G 11/6 1

4/4

UNCLASSIFIED

NL





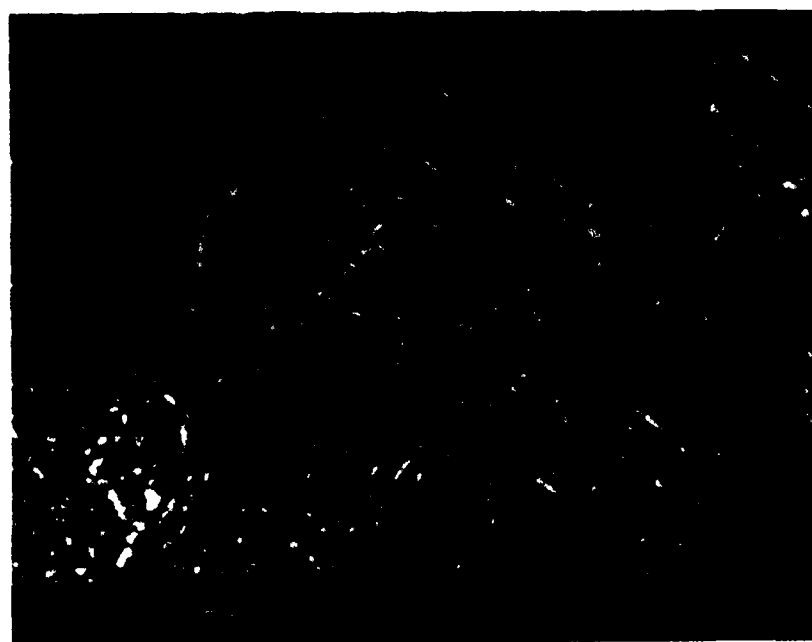
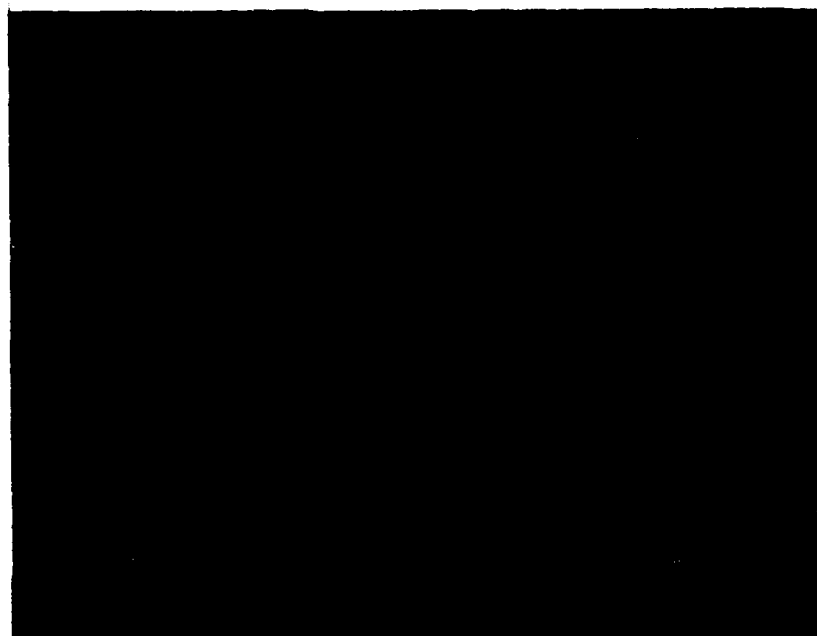


Figure 45. Scanning Electron Micrographs of HY-80 Steel  
(4% Picral etch)

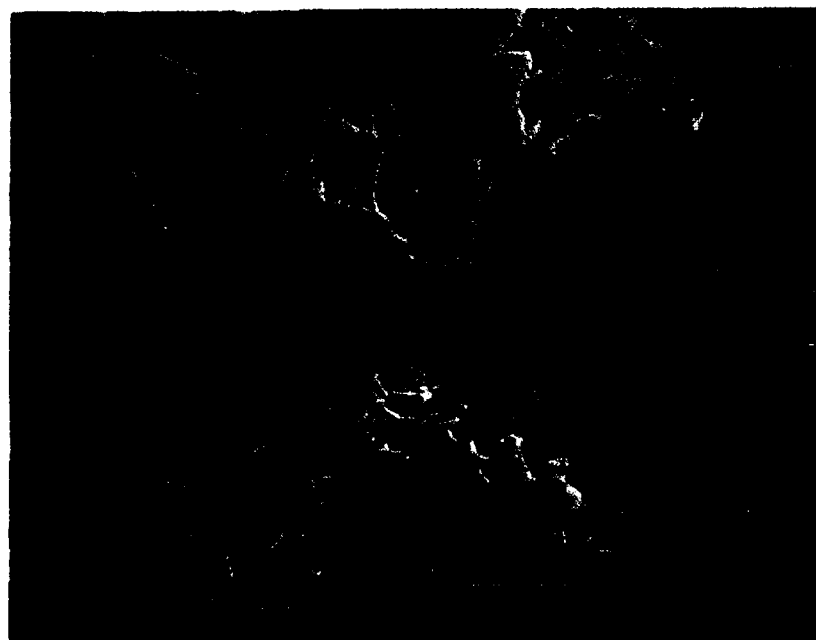
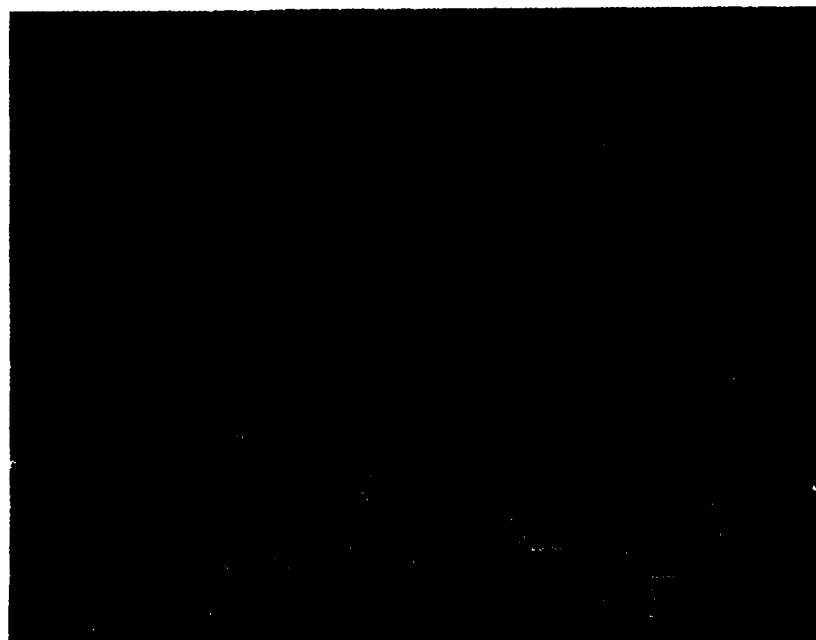


Figure 46. Scanning Electron Micrographs of ASTM A 710  
Gr. A Cl. 3 Steel (2% Nital etch)

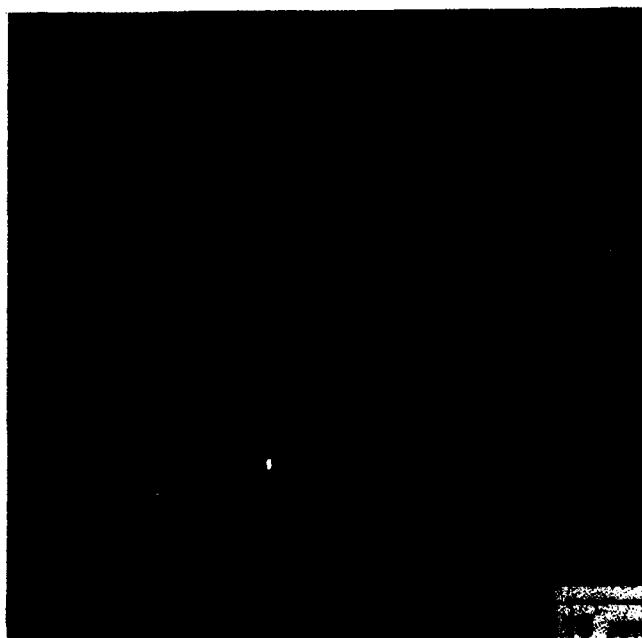


Figure 47. Optical Photomicrograph of ASTM A 710  
Gr. A Cl. 3 Steel (4% Picral etch)

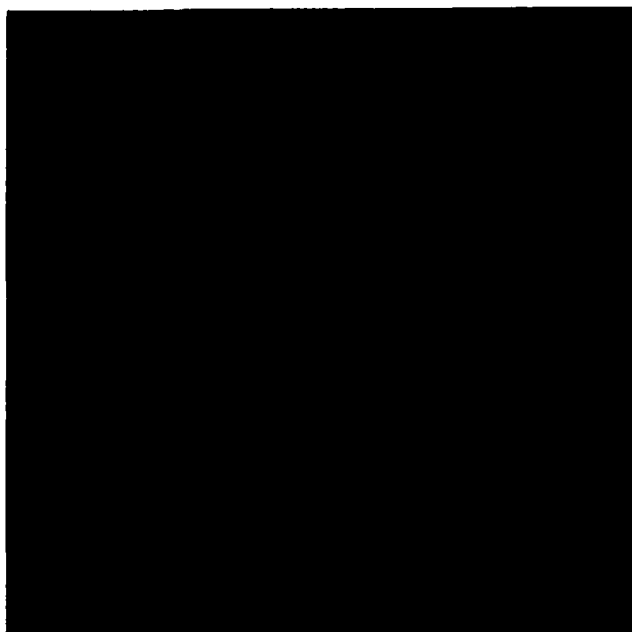


Figure 48. Scanning Electron Micrographs of ASTM A 710  
Gr. A Cl. 3 Steel (4% Picral etch)



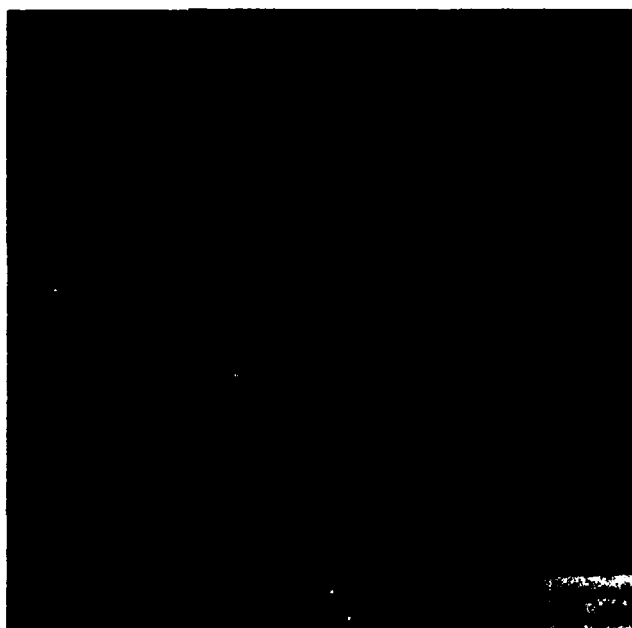
Figure 49. Scanning Electron Micrographs of ASTM A 710  
Gr. A Cl. 3 Steel (4% Picral etch)





(a) HY-80

Rolling Direction



(b) ASTM A 710 Gr. A Cl. 3

Figure 50. Optical Photomicrographs of HY-80 and ASTM A 710 Gr. A Cl. 3 Steels (unetched)



1TCT Specimen FYB 42 (22°C)



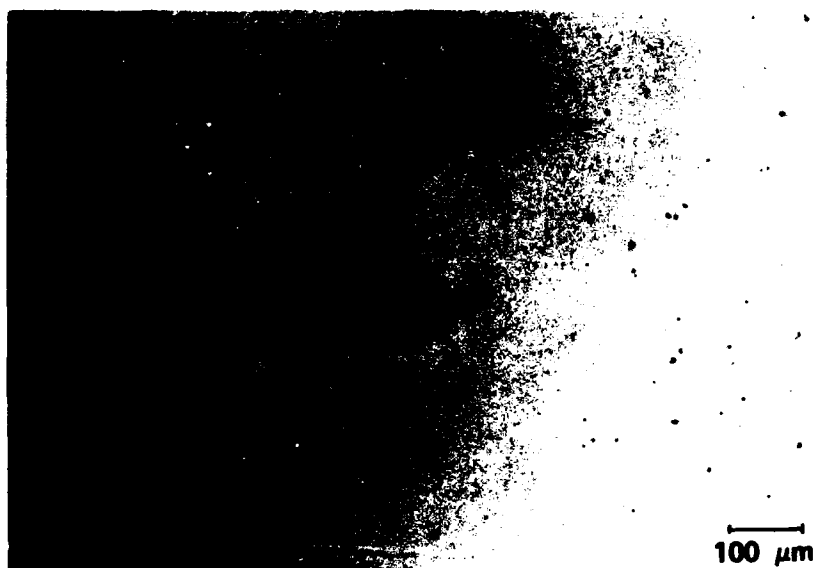
1TCT Specimen FYB 45 (-77°C)

Figure 51. Optical Photomicrographs of Crack Paths in HY-80  
1TCT Specimens FYB 42 and FYB 45 (unetched)



1TCT Specimen FYB 44 ( $-19^{\circ}\text{C}$ )

Figure 52. Optical Photomicrographs of Crack Paths in HY-80  
1TCT Specimens FYB 57 and FYB 44 (unetched)



1TCT Specimen FYB 59 ( $-80^{\circ}\text{C}$ )

Figure 53. Optical Photomicrograph of Crack Path in HY-80 Specimen FYB 59 (unetched)



Figure 54. Scanning Electron Fractograph of HY-80 1TCT Specimen FYB 43 ( $22^{\circ}\text{C}$ )

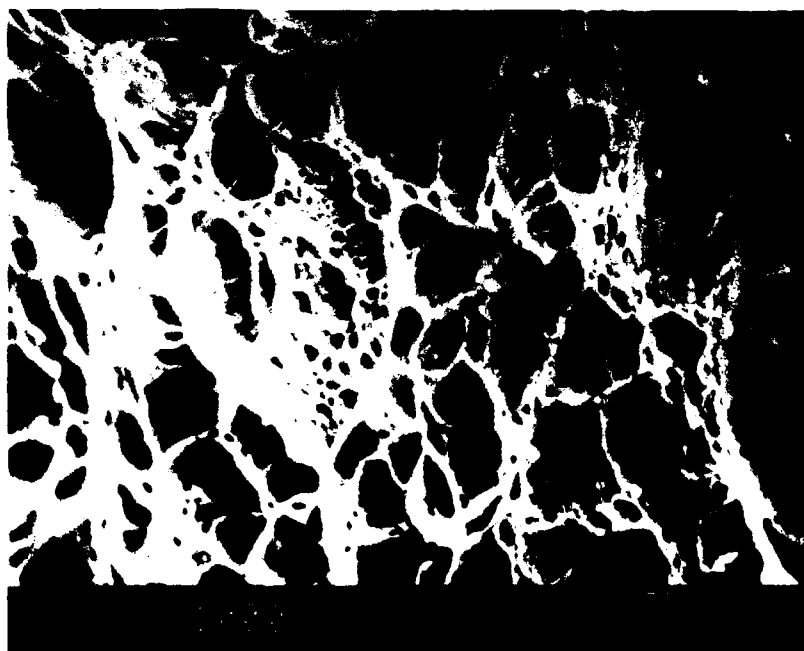
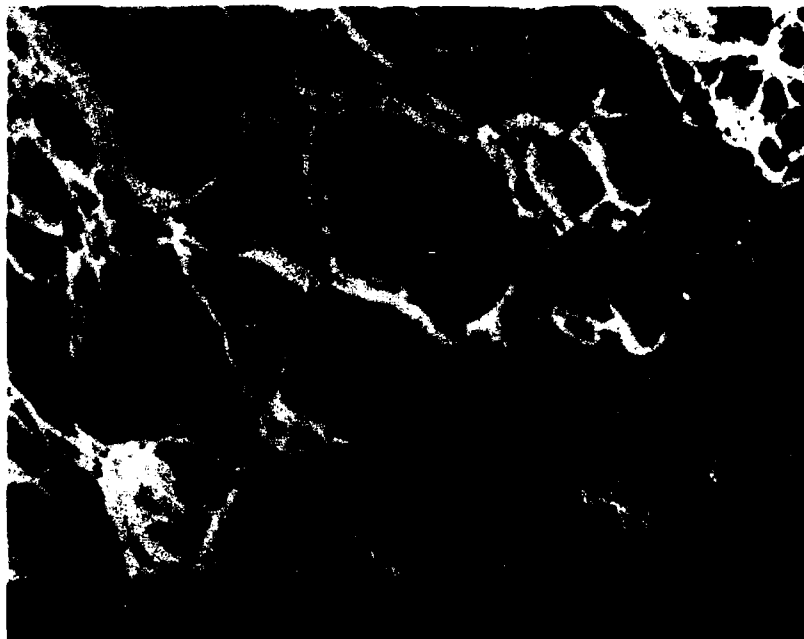


Figure 55. Scanning Electron Fractographs of HY-80 1TCT  
Specimen FYB 42 (22°C)

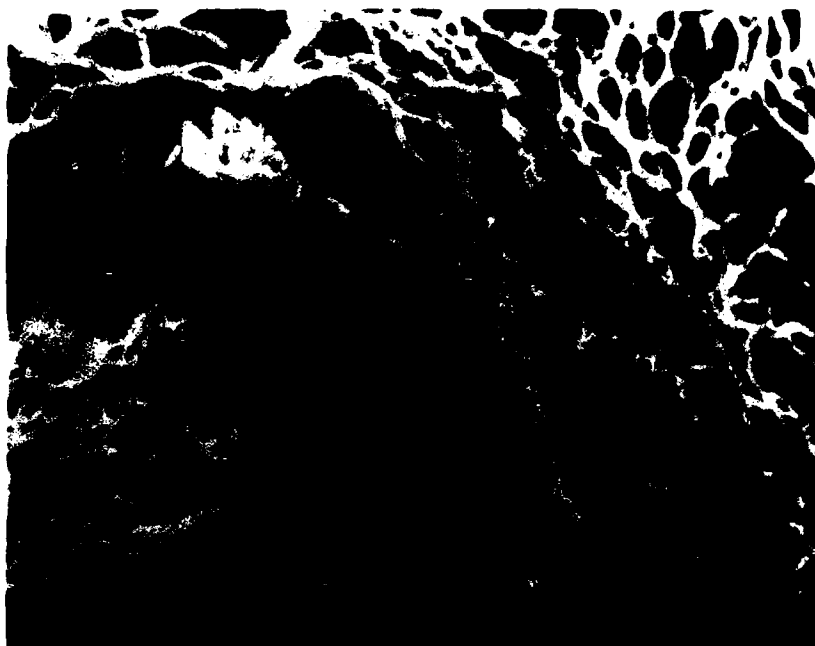
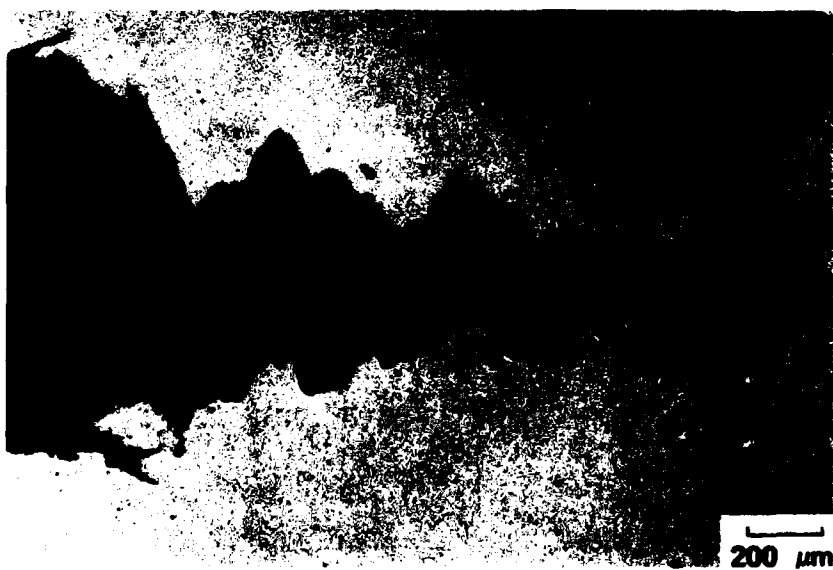


Figure 56. Scanning Electron Fractograph of HY-80 1TCT Specimen FYB 42 (22°C)



1TCT Specimen GGO-4 (-4°C)

Figure 57. Optical Photomicrograph of Crack Path in 1TCT Specimen of ASTM A 710 Gr. A Cl. 3 Steel (unetched)



1TCT Specimen GGO-9 (21°C)



1TCT Specimen GGO-1 (9°C)

Figure 58. Optical Photomicrographs of Crack Path in 1TCT Specimens GGO-9 and GGO-1 of ASTM A 710 Gr. A Cl. 3 Steel (unetched)

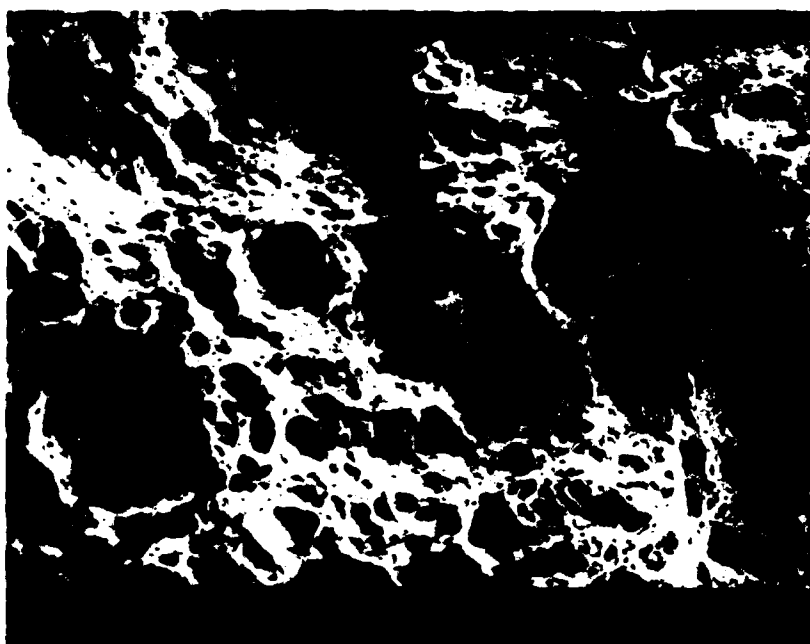
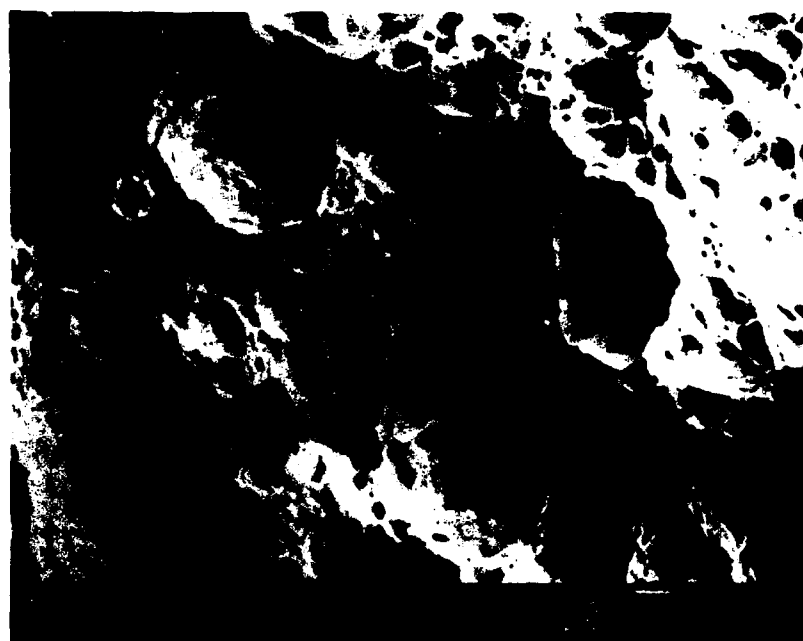


Figure 59. Scanning Electron Fractograph of ASTM A 710  
Gr. A Cl. 3 Steel 1TCT Specimen GGO-3 (22°C)





ITCT Specimen GGO-9 (21°C)



ITCT Specimen GGO-3 (22°C)

Figure 60. Scanning Electron Fractographs of ASTM A 710  
Gr. A Cl. 3 Steel ITCT Specimens GGO-9 and GGO-3

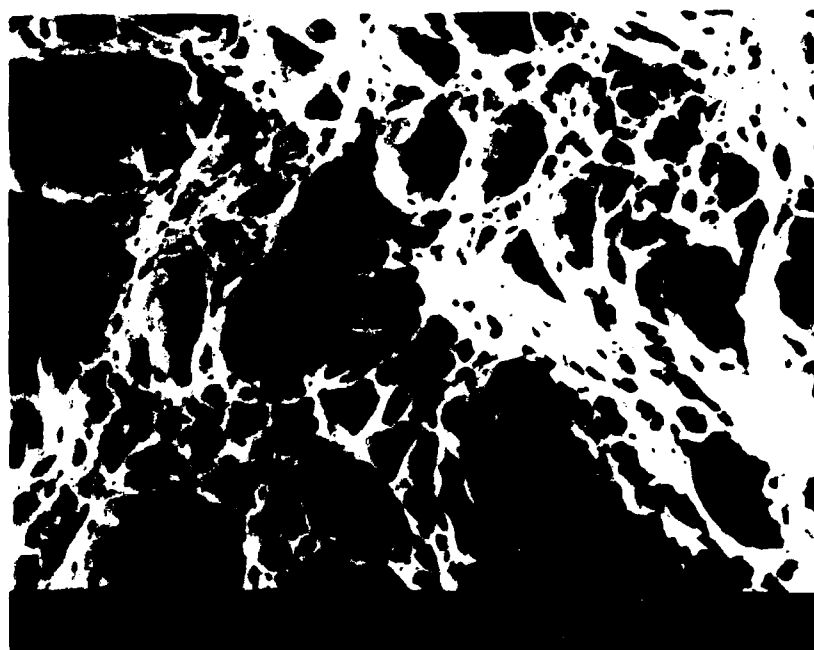
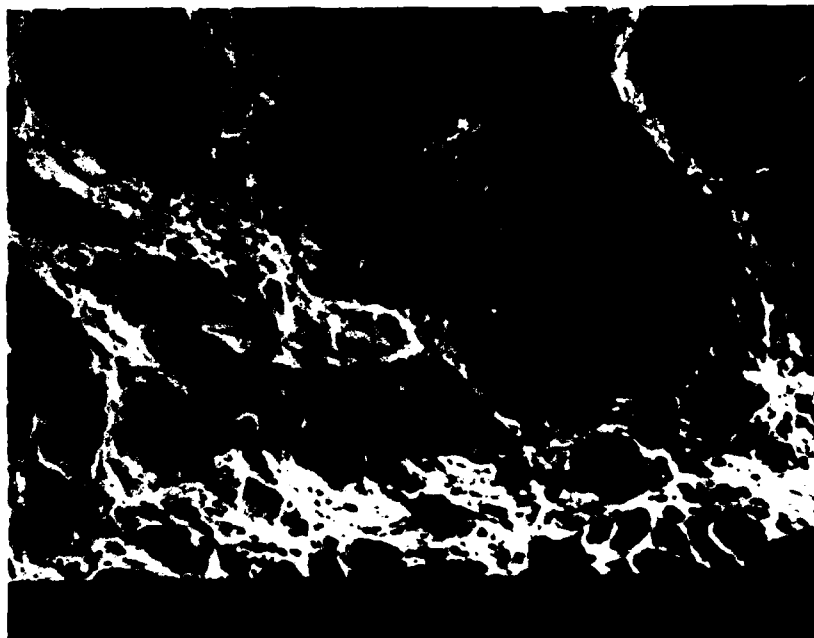


Figure 61. Scanning Electron Fractographs of ASTM A 710  
Gr. A Cl. 3 Steel 1TCT Specimen GGO-3 (22°C)

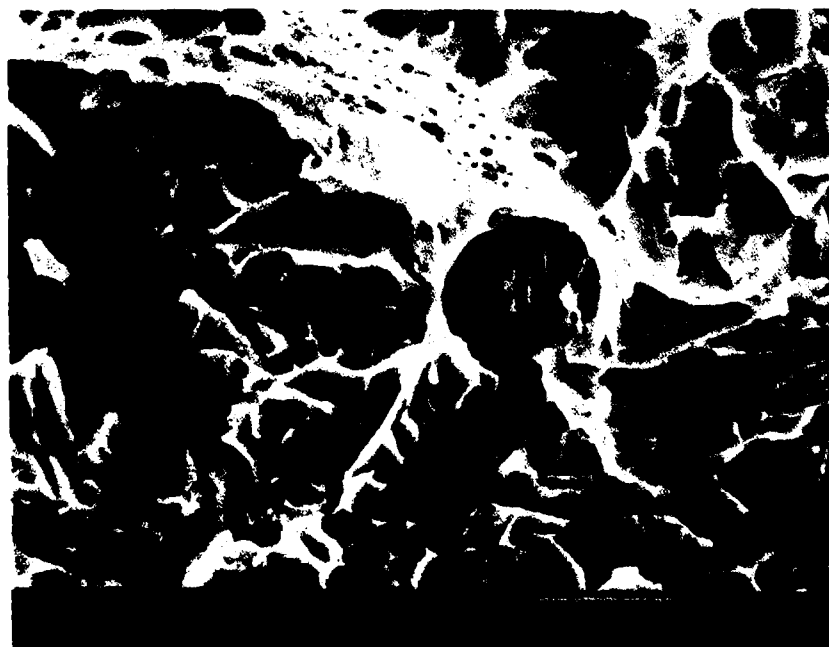
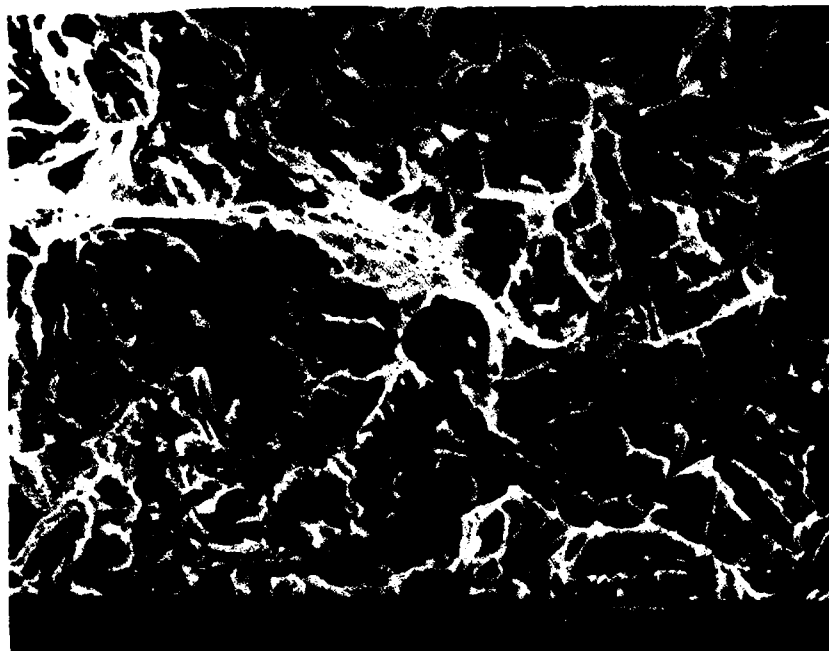


Figure 62. Scanning Electron Fractographs of Cleavage Fracture  
in HY-80 Steel 1TCT Specimen FYB 51 ( $-118^{\circ}\text{C}$ )

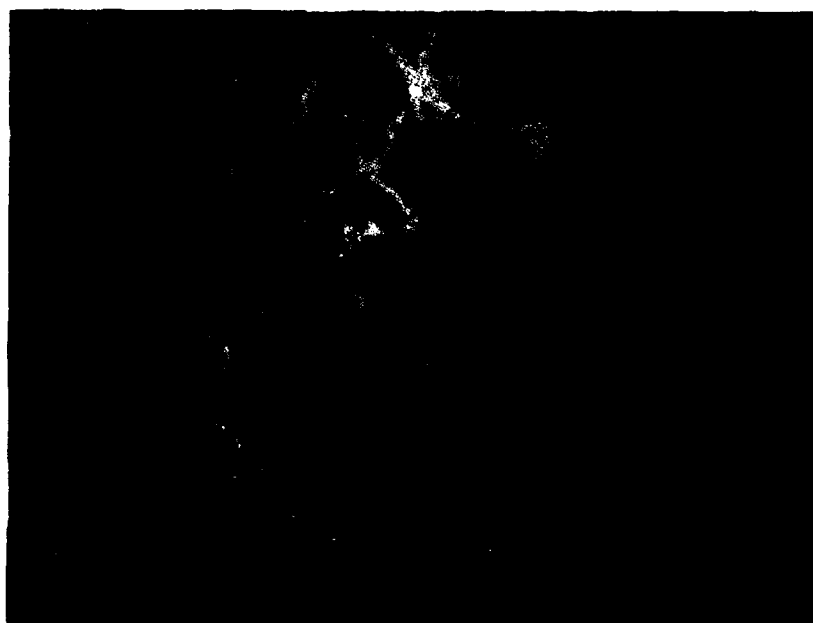
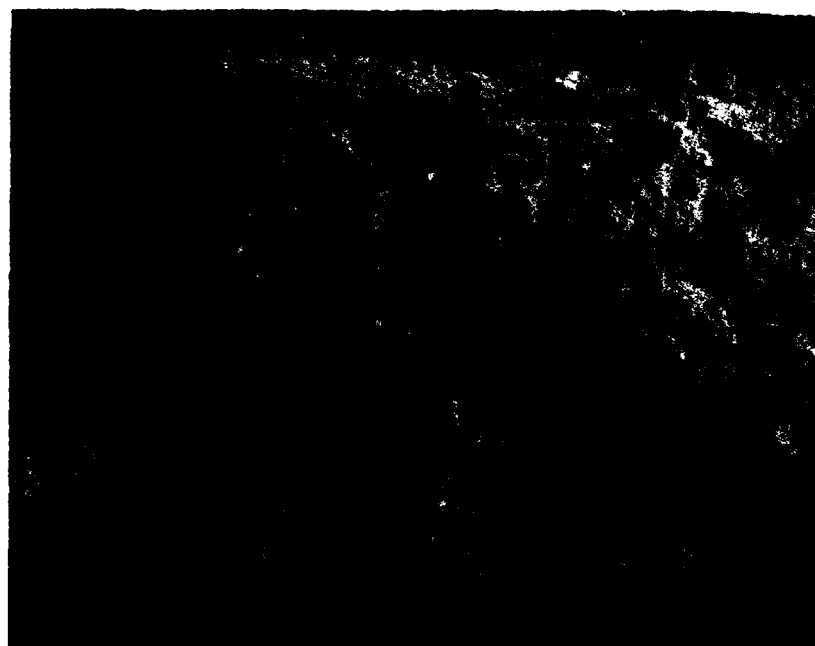


Figure 63. Scanning Electron Fractographs of Cleavage Fracture  
in ASTM A 710 Gr. A Cl. 3 Steel 1TCT Specimen GGO-2 ( $-52^{\circ}\text{C}$ )



Figure 64. Scanning Electron Fractographs of Cleavage Fracture  
in ASTM A 710 Gr. A Cl. 3 Steel 1TCT Specimen GG0-18 ( $-76^{\circ}\text{C}$ )

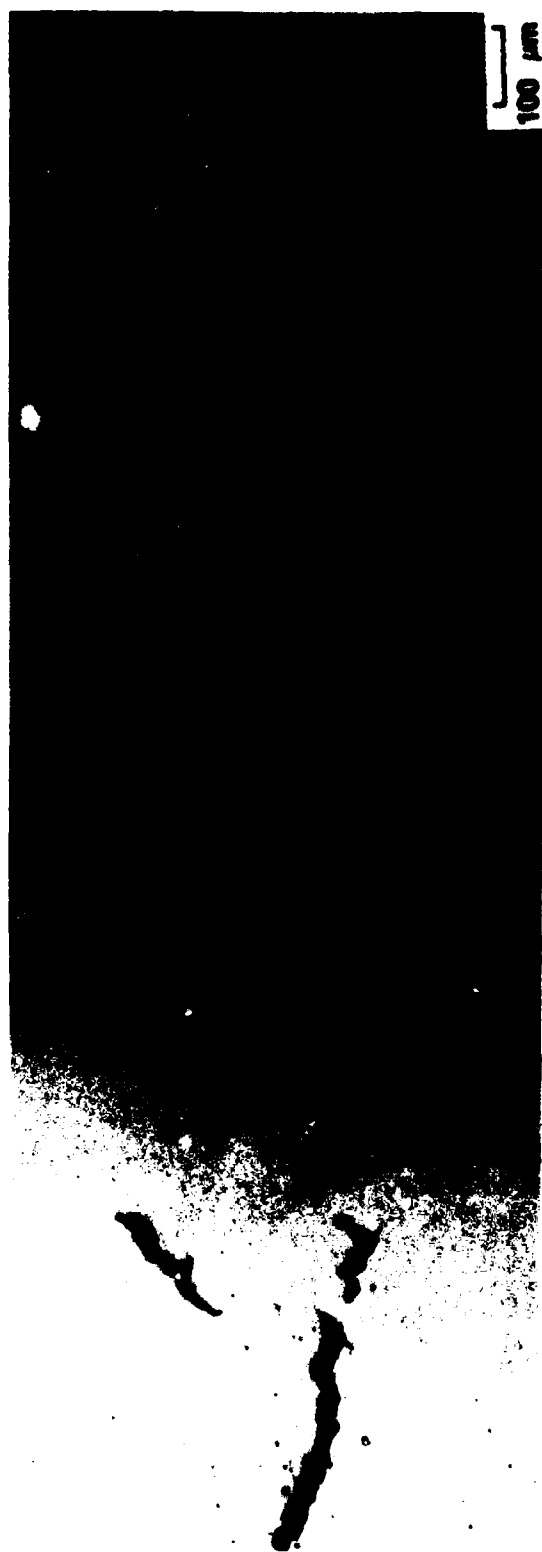


Figure 65. Optical Photomicrograph of Arrested Crack Tip in  
HY-80 Compact Crack Arrest Specimen CCA-2 (unetched)  
 $K_a = 96 \text{ MPa } \sqrt{\text{m}}; T_a = -103^\circ\text{C}$

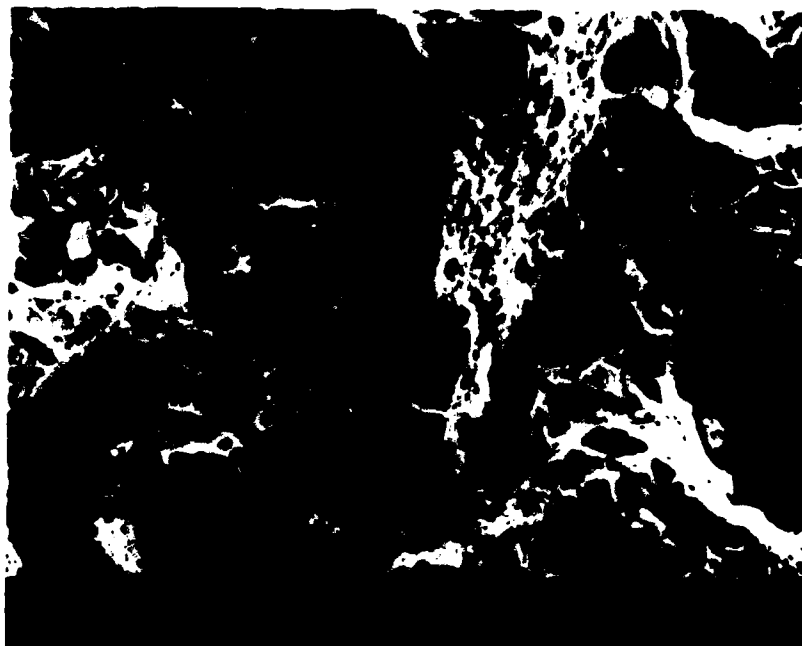


Figure 66. Scanning Electron Fractographs Near Arrested Crack  
Tip in HY-80 Compact Crack Arrest Specimen FYB CCA-2

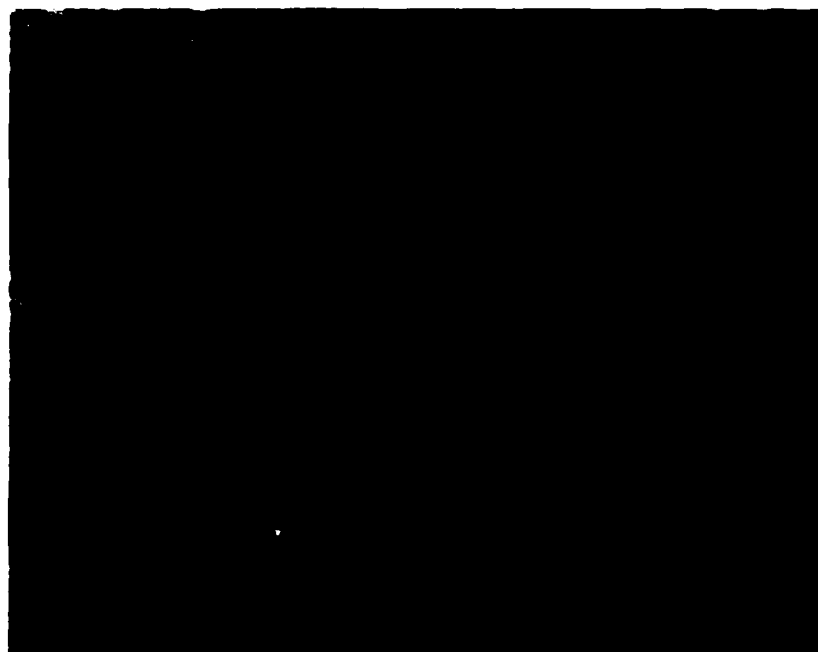


Figure 67. Scanning Electron Fractograph From Crack Path of  
HY-80 Compact Crack Arrest Specimen FYB-2 Located 12mm  
Behind Arrested Crack Tip



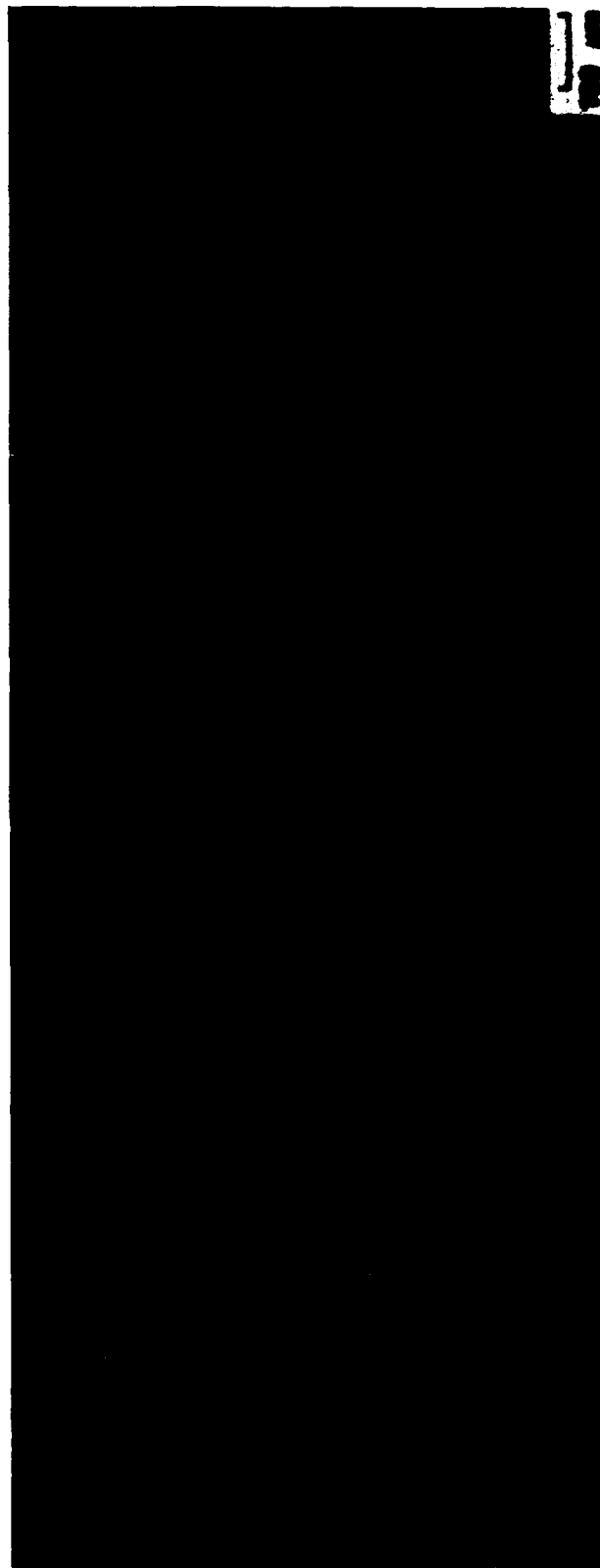


Figure 68. Optical Photomicrograph of Arrested Crack Tip in  
HY-80 Compact Crack Arrest Specimen FYB-1A (unetched)  
 $K_a=100 \text{ mPa } \sqrt{\text{m}}; T_a = -117^\circ\text{C}$

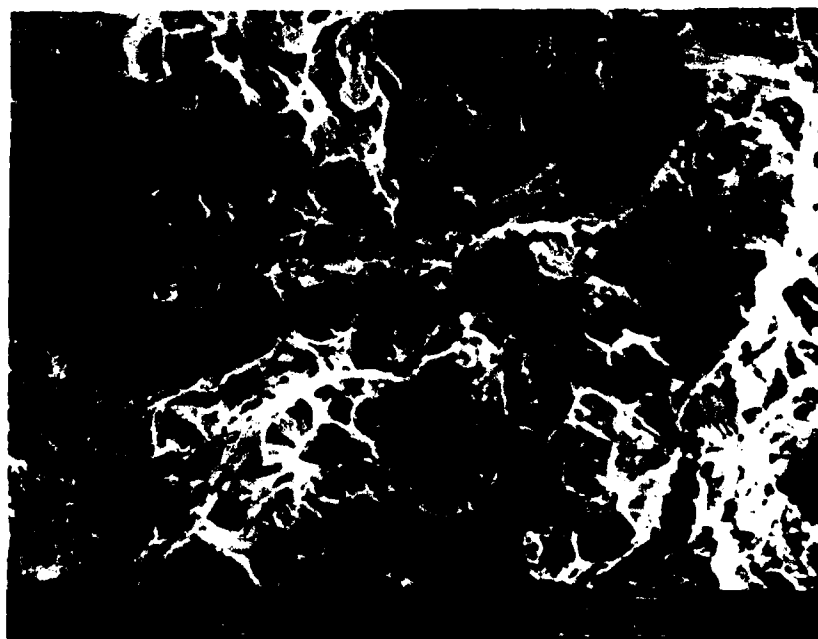


Figure 69. Scanning Electron Fractographs of Arrested Crack Tip  
in HY-80 Compact Crack Arrest Specimen FYB-1A



Figure 70. Optical Photomicrograph of Arrested Crack Tip in  
HY-80 Compact Crack Arrest Specimen FYB-1B (unetched)

$K_d=111 \text{ mPa} \sqrt{\text{m}}; T_d = -106^\circ\text{C}$



Figure 71. Scanning Electron Fractograph at Arrested Crack  
Tip of HY-80 Compact Crack Arrest Specimen FYB-1B

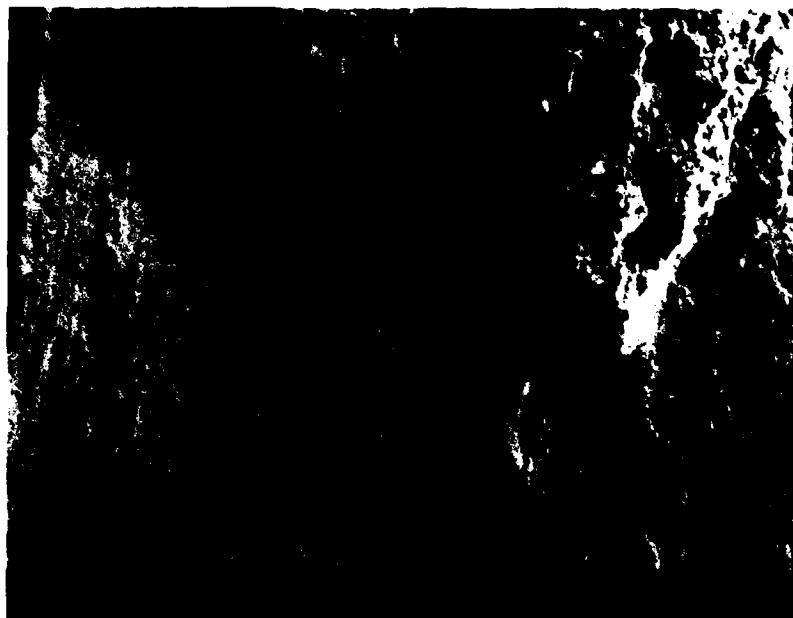


Figure 72. Optical Photomicrograph of Arrested Crack Tip in  
HY-80 Compact Crack Arrest Specimen FYB-3A (unetched)

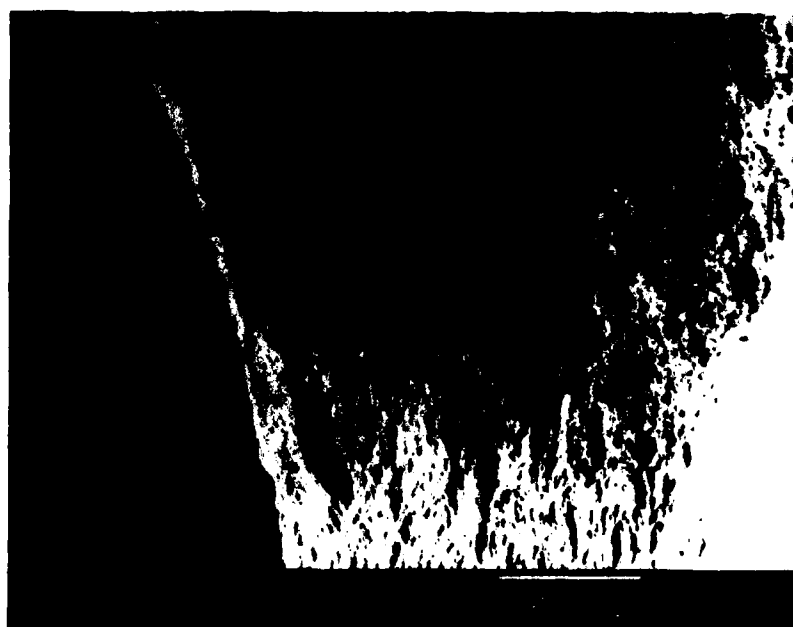
$K_{\text{a}}=135 \text{ mPa} \sqrt{\text{m}}; T_{\text{a}} = -95^{\circ}\text{C}$



Figure 73. Optical Photomicrograph of Arrested Crack Tip in  
HY-80 Compact Crack Arrest Specimen FYB-3A (unetched)



No Tilt



61° Tilt

Figure 74. Low Magnification Scanning Electron Fractographs of  
HY-80 Compact Crack Arrest Specimen FYB 3A

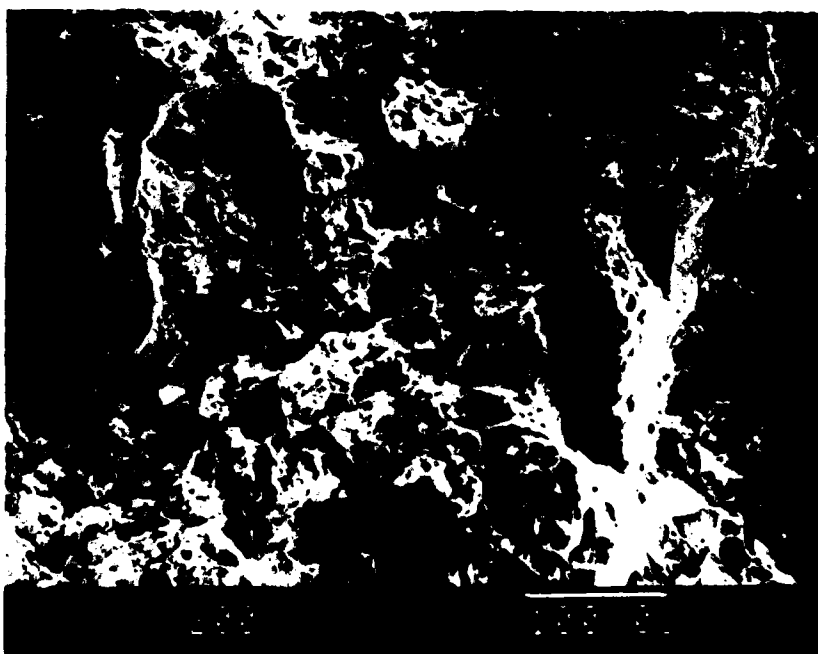
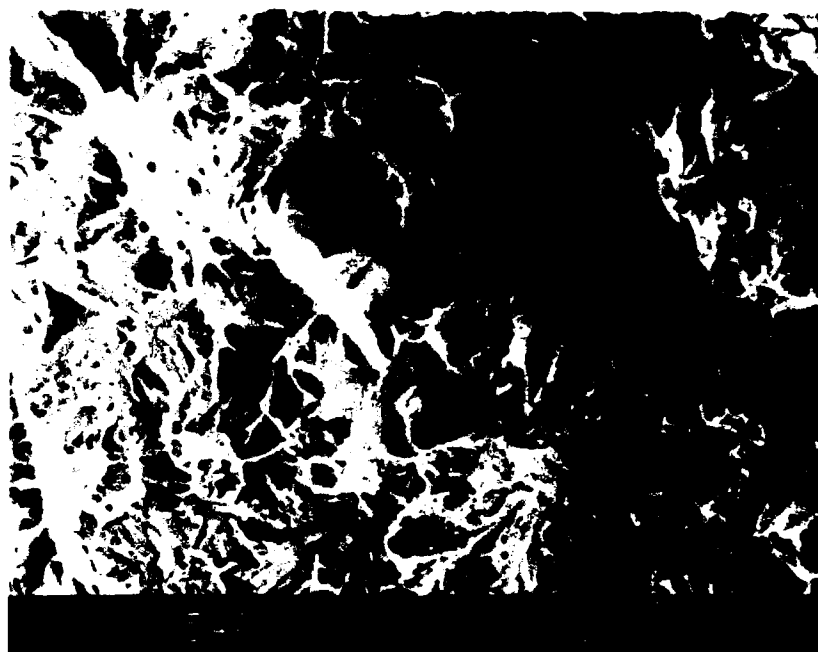
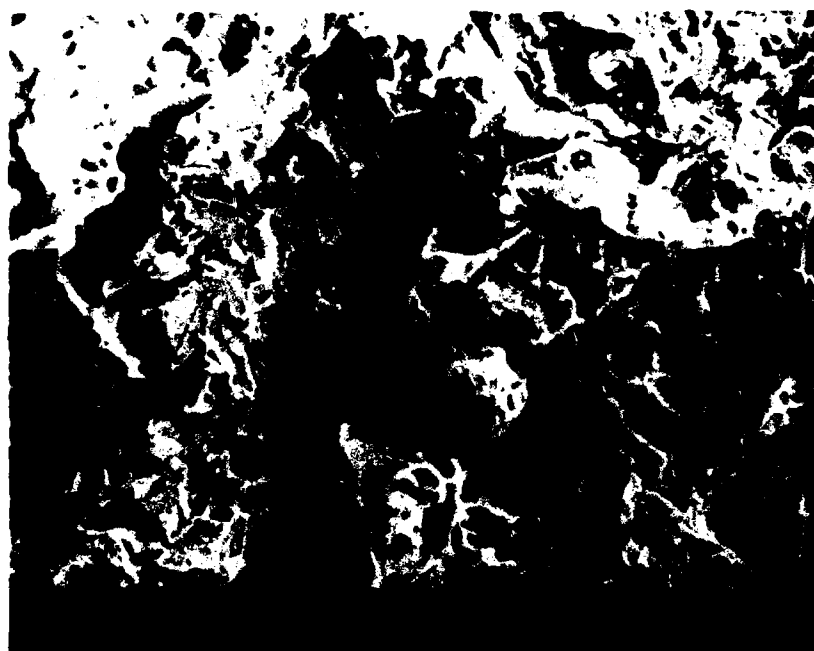
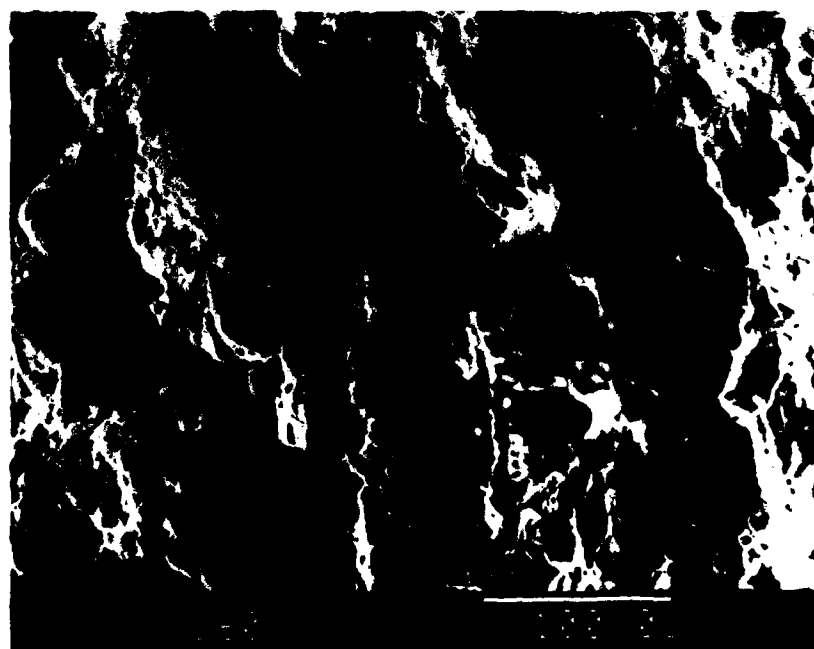


Figure 75. Scanning Electron Fractographs of Arrested Crack Tip  
in HY-80 Compact Crack Arrest Specimen FYB 3A





30° Tilt



60° Tilt

Figure 76. Scanning Electron Fractographs of Crack Tip of HY-80 Compact Crack Arrest Specimen FYB 3A at Various Tilt Angles

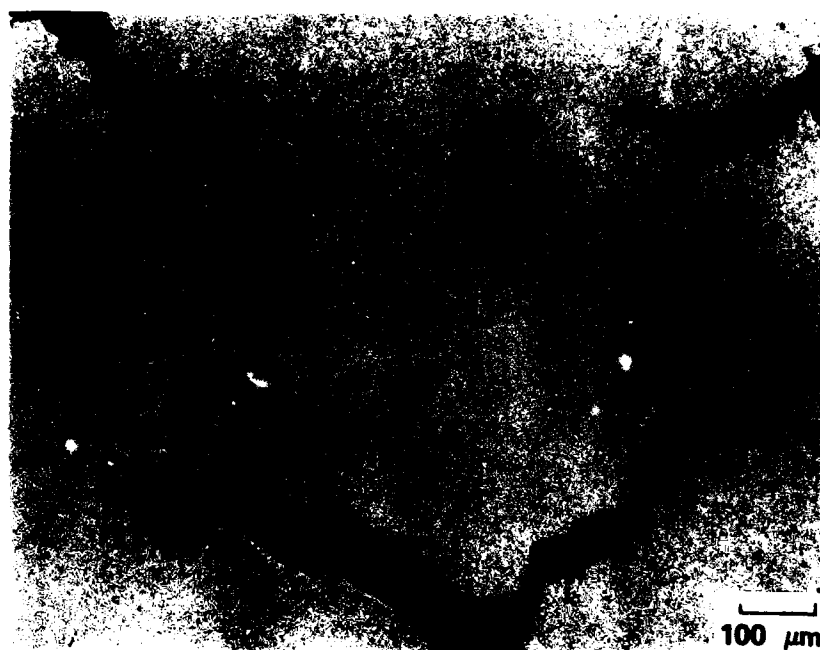


Figure 77. Optical Photomicrograph Across Crack Path of HY-80  
Compact Crack Arrest Specimen FYB-3A on Plane Located  
12mm Behind Arrested Tip



**Figure 78. Fracture Surface of ASTM A 710 Gr. A Cl. 3 Compact  
Crack Arrest Specimen GG0-2**



Figure 79. Optical Photomicrograph of Arrested Crack Tip of  
ASTM A 710 Gr. A Cl. 3 Compact Crack Arrest Specimen  
GG0-2 (unetched)

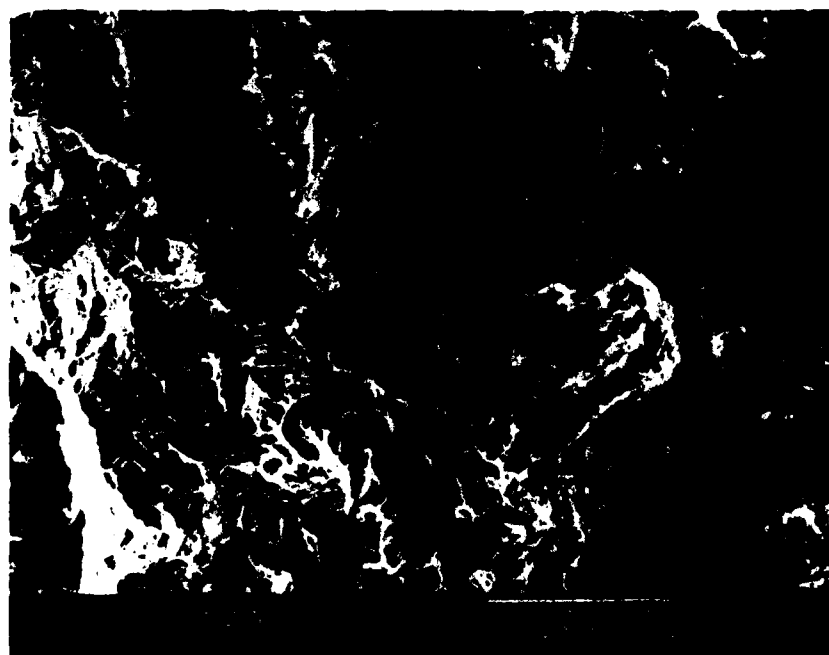


Figure 80. Scanning Electron Fractograph of Arrested Crack  
Tip of ASTM A 710 Gr. A Cl. 3 CCA Specimen GG0-2

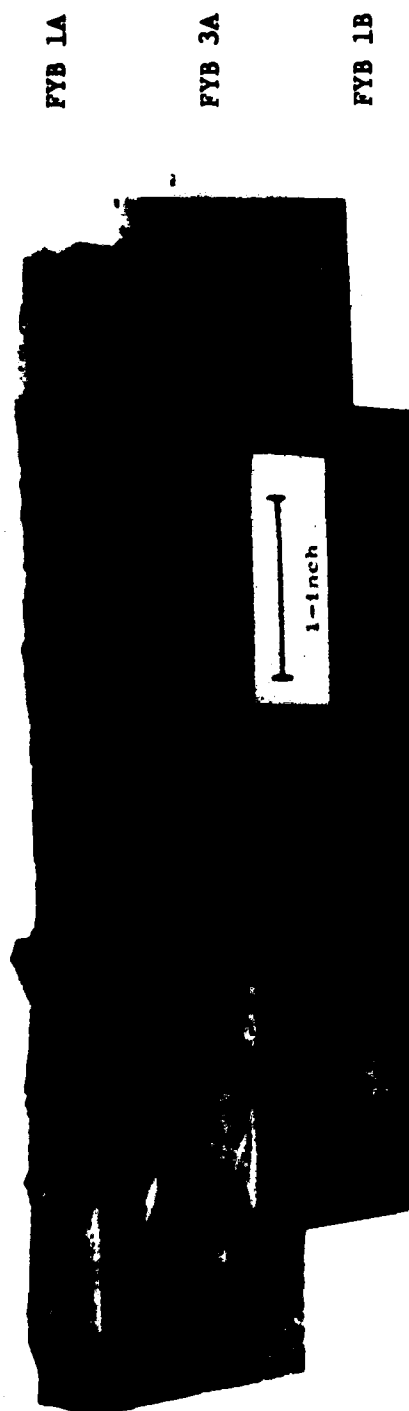


Figure 81. Comparison of Fracture Surfaces of HY-80 Compact Crack Arrest Specimens FYB 1B, FYB 1A and FYB 3A

# INITIAL DISTRIBUTION

## Copies

1 OCNR Code 225 (Kelly)

2 ONR  
1 Code 1132-SM  
1 Code 11-D

4 NRL  
1 Code 6000  
1 Code 6380  
1 Code 6320  
1 Code 6396

10 NAVSEA  
1 05M  
1 08  
1 55Y  
1 092  
1 323  
1 393  
1 395  
1 396  
1 5013  
1 99612

1 NISC Code 369

12 DTIC

## CENTER DISTRIBUTION

Copies	Code	Name
1	012.5	Caplan
1	17	Krenske
1	173	Beach
1	1720.4	Wiggs
1	28	Wacker
1	2801	Crisci
1	2803	Hardy
10	281	Gudas
4	2814	Montemarano
1	2814	Kirk
1	522.1	TIC
1	5231	Office Service

### DTNSRDC ISSUES THREE TYPES OF REPORTS:

1. **DTNSRDC reports, a formal series**, contain information of permanent technical value. They carry a consecutive numerical identification regardless of their classification or the originating department.
2. **Departmental reports, a semiformal series**, contain information of a preliminary, temporary, or proprietary nature or of limited interest or significance. They carry a departmental alphanumerical identification.
3. **Technical memoranda, an informal series**, contain technical documentation of limited use and interest. They are primarily working papers intended for internal use. They carry an identifying number which indicates their type and the numerical code of the originating department. Any distribution outside DTNSRDC must be approved by the head of the originating department on a case-by-case basis.

END

7-87

DTIC